



## Durham E-Theses

---

# *Multicomponent Solid Forms in Pharma, Hair Care and Dental Care*

CHAMBERS, LUKE, IAN

### How to cite:

---

CHAMBERS, LUKE, IAN (2022) *Multicomponent Solid Forms in Pharma, Hair Care and Dental Care*, Durham theses, Durham University. Available at Durham E-Theses Online:  
<http://etheses.dur.ac.uk/14344/>

### Use policy

---

The full-text may be used and/or reproduced, and given to third parties in any format or medium, without prior permission or charge, for personal research or study, educational, or not-for-profit purposes provided that:

- a full bibliographic reference is made to the original source
- a [link](#) is made to the metadata record in Durham E-Theses
- the full-text is not changed in any way

The full-text must not be sold in any format or medium without the formal permission of the copyright holders.

Please consult the [full Durham E-Theses policy](#) for further details.

---

Academic Support Office, Durham University, University Office, Old Elvet, Durham DH1 3HP  
e-mail: [e-theses.admin@dur.ac.uk](mailto:e-theses.admin@dur.ac.uk) Tel: +44 0191 334 6107  
<http://etheses.dur.ac.uk>



# Multicomponent Solid Forms in Pharma, Hair Care and Dental Care

A thesis submitted in fulfilment of the requirements for the  
degree of

*Doctor of Philosophy*

In the Department of Chemistry at Durham University

By

Luke Chambers

November 2021

## Abstract

This work covers multicomponent solid forms including co-amorphous solid forms with active pharmaceutical ingredients (APIs) and, co-crystals, salts, hydrates and solvates to help model intermolecular interaction taking place in larger systems including polymers and proteins. A new prediction model was created to help identify which combinations of APIs and small molecule co-formers were likely to form co-amorphous systems. The prediction model suggests co-amorphous formation is related to the average molecular weight of the two components and the strength of the intermolecular interactions formed. A new co-amorphous screen containing mebendazole with 29 co-formers was performed and compared to the predicted results, which showed a predictive hit rate of 90%.

The dimer of vinylcaprolactam (bisVCap) was used in a co-amorphous screen with 13 APIs. The experimental results were compared to the predicted results with 11 out of 13 systems correctly predicted. The co-amorphous systems found were analysed by FTIR which identified new intermolecular interactions formed between bisVCap and the APIs, stabilising the co-amorphous state.

Crystals of a hydrogenated dimer of vinylpyrrolidone and hydrogen peroxide were grown by cooling crystallisation and characterised by SXRD. The structures were used to identify the bonding models present in a polyvinylpyrrolidone hydrogen peroxide complex. The crystal structures were combined with DFT calculations to produce two new proposed structures of the hydrogen bonding in the polyvinylpyrrolidone hydrogen peroxide complex.

A hair care mixture formed from a gluconamide and a gluconate and 3-hydroxypropyl ammonium salt, is known to strengthen hair fibres; however, the process is unknown. To identify potential interactions between the mixture and hair fibres, a range of crystals were grown. The crystals were identified by SXRD as two polymorphic forms of the gluconamide and three salts of 3-hydroxypropylammonium with sulfuric acid, methane sulfonic acid and oxalic acid. The new crystal structures and structures from the Cambridge structural database were used to speculate potential interactions formed. The gluconamide was identified to be a supramolecular gelator in aniline and benzyl alcohol. The gels were characterised by rheology, scanning electron microscopy,  $^1\text{H}$  NMR, FTIR and XRPD.

## Declaration

The work described in this thesis was undertaken in the Department of Chemistry at Durham University (UK) between April 2018 and October 2021, under the supervision of Professor Jonathan W. Steed of Durham University and Dr Osama M. Musa of Ashland LLC. This work has not been previously submitted for a degree at this or any other University.

All X-ray structures were collected and process by Dr Dmitry Yufit, apart from **1** form I (Chapter 5) which was collected and processed by Dr James Smith. All solid-state NMR data was collected by Dr David Apperly. DSC data (Chapter 3) was collected by Mr Douglas W. Casrwell and Mr Philip Robinsons. DFT calculations (Chapter 4) were performed by Dr Mark A. Fox. XRPD data was collected by the author and Mr Gary Oswald. External supervision was provided by Professor Thomas Rades, Dr Holger Grohganz and Dr Korbinian Löbmann for Chapter 2. SEM characterisation of the supramolecular gels (Chapter 6) was carried out by Dr James Smith.

## Statement of Copyright

The copyright of this thesis rests with the author. No quotation from it should be published without the author's prior written consent and information derived from it should be acknowledged.

## Funding

This work was funded by the Engineering and Physical Sciences Research Council (EPSRC), through the Soft Matter and Functional Interfaces Centre for Doctoral Training (SOFI CDT) and Ashland LLC.

## Publications

### Scientific papers

1. **“Predictive Identification of Co-formers in Co-amorphous Systems”**, L. I. Chambers, H. Grohganz, H. Palemlund, K. Löbmann, T. Rades, O. M. Musa and J. W. Steed, *Eur. J. Pharm. Sci.*, 2021, **157**, 105636
2. **“Structure of the Polyvinylpyrrolidone-Hydrogen Peroxide Complex”**, L. I. Chambers, D. S. Yufit, M. A. Fox, O. M. Musa and J. W. Steed, accepted by *Chemical Communications*

### Book Chapters

1. **“Hydration Behaviour of Polylactam Clathrate Hydrate Inhibitors and their Small-Molecule Model Compounds”**, L. I. Chambers, A. V. Hall, O. M. Musa and J. W. Steed in *Handbook of Pyrrolidone and Caprolactam Based Materials*, O. M. Musa ed., Wiley, Chichester, UK, 2021
2. **“Cocrystals. Coamorphous Phases and Coordination Complexes of  $\gamma$ - and  $\epsilon$ -Lactams”**, A. V. Hall, L. I. Chambers, O. M. Musa and J. W. Steed in *Handbook of Pyrrolidone and Caprolactam Based Materials*, O. M. Musa ed., Wiley, Chichester, UK, 2021

## Acknowledgements

At the start of my PhD during the SOFI CDT training period I had to choose who I wanted to work with for my PhD. It was a difficult decision, but I can say with certainty that I made the right choice to work with Professor Jonathan Steed. Jon has been a very big help in my PhD and has read countless drafts of books chapters, papers and now thesis chapters and he has always provided brilliant feedback. If I ever had a problem, I always knew Jon would be happy to help.

I'm very grateful for the support and guidance that Dr Osama Musa and all the people I met from Ashland LLC have provided throughout my PhD. I was always surprised by Osama's dedication to science with him putting aside time to discuss my PhD whilst working as the CTO for a global company. I would like to thank the technical staff at Durham especially Gary Oswald for his support with my hundreds of XRPD measurements and Dr Dmitry Yufit for his expertise in always finding a good single crystal from my questionable samples.

I would like to thank the people I worked with during my short visit to the University of Copenhagen including Professor Thomas Rades, Dr Korbinian Löbmann and Dr Holger Grohgan for their supervision and guidance. I am also grateful for the warm welcome I received from everyone in the Pharmacy department especially Henrik Palmelund, Mikkel Herzburg, Troels Pedersen, Tobias Holm, Hannah Plappert, Nele-Johanna Hempel and Heidi Öblom.

I was very lucky to join the Steed group where I was surrounded by wonderful people who were always happy to help and usually more than happy to have the occasional pub session after a long day. I would especially like to thank Dr James Smith, Dr Amy Hall, Dr Matthew Mulvee, Alan Braschinsky, Dr Jessica Andrew, Mike Walters and JungSik Shin for making the office the fun place I will remember it as. I would also like to thank the Steed group for their constant determination to do well even in the face of countless lab floods, a fire, and a global pandemic.

Outside of the Chemistry Department, I would like to thank my parents Sue and Ian Chambers for their constant support. I would also like to give a massive thanks to Mila Popova who has always been there to cheer me up, support me and helping me switch off

after a long day in the lab. I am also grateful for my cat Timmy for providing me with lots of entertainment and stopping me from going too crazy whilst writing up my PhD.



# Table of Contents

Abstract.....	i
Declaration.....	ii
Statement of Copyright.....	ii
Funding .....	ii
Publications.....	iii
Scientific papers .....	iii
Book Chapters.....	iii
Acknowledgements.....	iv
Table of Contents.....	vi
Abbreviations .....	xii
List of Figures .....	
List of Tables .....	v
List of Schemes.....	vii
1 Introduction .....	1
1.1 Crystallisation .....	1
1.1.1 Nucleation and Growth.....	1
1.1.2 Crystal Engineering .....	9
1.1.3 Cambridge Structural Database.....	12
1.1.4 Polymorphism .....	13
1.2 Multicomponent Solid Forms.....	14
1.2.1 Overview .....	14
1.2.2 Co-crystals.....	16
1.2.3 Hydrates and Solvates .....	18
1.2.4 Salts.....	19
1.2.5 Amorphous Forms.....	20

1.2.6	Co-amorphous Phases .....	22
1.3	Characterisation of Solid Forms .....	24
1.3.1	Crystallographic Analysis .....	24
1.3.2	Spectroscopic Analysis .....	25
1.3.3	Thermal Analysis .....	27
1.4	Production Methods for Solid Forms .....	28
1.4.1	Crystallisation Methods .....	28
1.4.2	Preparation of Co-amorphous Systems .....	31
1.5	Small Molecule Models .....	31
1.5.1	Introduction .....	31
1.5.2	Povidone-iodine .....	32
1.5.3	Co-amorphous Pharmaceutical Phases .....	33
1.6	Project Aims and Overview .....	36
1.7	References.....	36
2	Predictive Identification of Co-formers in Co-amorphous Systems .....	43
2.1	Introduction.....	43
2.2	Results and Discussion .....	45
2.2.1	Correlation of $\Delta H_{mix}$ and $\Delta \log P$ with Co-amorphisation .....	45
2.2.2	PLS-DA.....	54
2.2.3	Model .....	56
2.2.4	Prediction of Co-amorphous Formation by Mebendazole with 29 Co-formers	60
2.3	Conclusion .....	63
2.4	Experimental .....	64
2.4.1	Materials .....	64
2.4.2	X-ray Powder Diffraction (XRPD) .....	64
2.4.3	Mebendazole Co-former Screening.....	64

2.4.4	Film Casting Mebendazole – Gallic acid.....	65
2.4.5	COSMOquick Calculations.....	65
2.4.6	Partial Least Squares – Discriminant Analysis.....	65
2.5	References.....	66
3	Prediction and Preparation of Co-amorphous Phases of a Bislactam.....	69
3.1	Introduction.....	69
3.2	Results and Discussion .....	71
3.2.1	Testing Model with Literature Co-amorphous Screen .....	71
3.2.2	Testing Model with the New BisVCap Co-amorphous Screen.....	73
3.2.3	Analysing the Stabilising Interactions in COAM Systems .....	89
3.2.4	Stability Study at Different Temperatures.....	96
3.2.5	Increasing the Ratio of Furosemide to BisVCap.....	103
3.2.6	Stability Study on BisVCap and Furosemide at Different Humidities .....	105
3.3	Conclusion .....	109
3.4	Experimental .....	110
3.4.1	Materials .....	110
3.4.2	Analytical Methods .....	110
3.4.3	COSMOquick Calculations.....	111
3.4.4	Synthesis of BisVCap .....	111
3.4.5	HSM Method for Co-amorphous Systems.....	112
3.4.6	Co-melting for Co-amorphous Systems.....	112
3.4.7	RSE for Co-amorphous Systems.....	113
3.4.8	Stability Test at Different Temperatures .....	113
3.4.9	Varying Humidity Stability Test.....	113
3.5	References.....	113
4	Structure of the Poly(vinylpyrrolidone)-Hydrogen Peroxide Complex.....	116

4.1	Introduction.....	116
4.2	Results and Discussion .....	118
4.2.1	Polymer Analysis .....	118
4.2.2	Small Molecule Model .....	125
4.2.3	DFT Calculated Models .....	129
4.2.4	Peroxydone Structure .....	131
4.3	Conclusion .....	132
4.4	Experimental .....	133
4.4.1	Materials .....	133
4.4.2	Analytical Methods .....	133
4.4.3	Titration.....	134
4.4.4	H <sub>2</sub> bisVP H <sub>2</sub> O <sub>2</sub> cocrystal synthesis.....	135
4.4.5	Computations.....	136
4.5	References.....	137
5	Understanding the Interaction of Gluconamides and Gluconates with Amino Acids in Hair Care .....	140
5.1	Introduction.....	140
5.2	Results and Discussion .....	142
5.2.1	Cambridge Structural Database Search .....	142
5.2.2	Gluconamide Structures .....	144
5.2.3	Amino Acid Salt Screen .....	148
5.2.4	Potential Interactions of <b>1</b> , <b>2</b> and <b>3</b> with Hair Protein.....	155
5.3	Conclusion .....	158
5.4	Experimental .....	159
5.4.1	Materials .....	159
5.4.2	Analytical Methods .....	159

5.4.3	CSD Search .....	160
5.4.4	The Crystallisation of <b>1</b> form I.....	161
5.4.5	Crystallisation of D-GLA <b>1</b> form I .....	161
5.4.6	Crystallisation of <b>1</b> form II.....	161
5.4.7	Cosmoquick Screen .....	162
5.4.8	<b>2</b> ·HSO <sub>4</sub> <sup>-</sup> salt .....	162
5.4.9	<b>2</b> ·CH <sub>3</sub> SO <sub>3</sub> <sup>-</sup> salt .....	162
5.4.10	<b>2</b> ·HC <sub>2</sub> O <sub>4</sub> <sup>-</sup> salt.....	163
5.4.11	Guanidine Carbonate Methanol Solvate .....	163
5.4.12	N,N'-ethylene bis- <i>L</i> -gluconamide.....	163
5.4.13	<i>L</i> -Cysteic acid dimethylsulfoxide solvate synthesis.....	164
5.4.14	4,4'-Biphenol·Morpholine (1:2) co-crystal synthesis.....	164
5.5	References.....	164
6	Supramolecular Gelation Properties of Hydroxypropyl- <i>L</i> -gluconamide.....	167
6.1	Introduction.....	167
6.2	Results and Discussion .....	169
6.2.1	Initial Gel Screen .....	169
6.2.2	Gel Formation Conditions .....	170
6.2.3	Gel Screen of Aniline and Amine Derivatives .....	172
6.2.4	Rheology .....	174
6.2.5	Xerogel Analysis .....	176
6.3	Conclusion .....	180
6.4	Experimental .....	181
6.4.1	Materials .....	181
6.4.2	Analytical Methods .....	181
6.4.3	Gel Screening Procedure.....	182

6.4.4	The Temperature of Gel Formation Study.....	182
6.4.5	Sonication Study .....	182
6.4.6	Critical Gelling Concentration Study .....	183
6.4.7	Gel Breakdown Temperature .....	183
6.4.8	Xerogel Formation .....	183
6.5	References.....	183
7	Concluding Remarks.....	186
7.1	Conclusion .....	186
7.1.1	Introduction .....	186
7.1.2	Section One – Co-amorphous Systems in Pharma .....	186
7.1.3	Section Two – Solvates and Hydrates in Dental Care .....	188
7.1.4	Section Three – Salts, Polymorphs and Supramolecular Gels in Hair Care .....	189
7.2	Future Work .....	190
7.2.1	Section One – Co-amorphous Systems in Pharma .....	190
7.2.2	Section Two – Solvates and Hydrates in Dental Care .....	190
7.2.3	Section Three – Salts, Polymorphs and Supramolecular Gels in Hair Care .....	191
7.3	References.....	192
8	Appendices.....	193
8.1	Full Crystallographic Information for Structures in Chapter 4.....	193
8.2	Full Crystallographic Information for Structures in Chapter 5.....	196

## Abbreviations

2,4-DHBA – 2,4-dihydroxybenzoic acid	CARI – Carisoprodol
3,5-DHBA – 3,5-dihydroxybenzoic acid	CATEC – Catechol
3-ABA – 3-aminobenzoic acid	CBZ – Carbamazepine
3AP – 3-amino-1-propanol	$C_{eq}$ – Equilibrium concentration
4-ABA – 4-aminobenzoic acid	CHPD – Chlorpropamide
4-AS – 4-aminosalicylic acid	CHPL – Chloramphenicol
5-AS – 5-aminosalicylic acid	CM – Co-melting
AFM – Atomic force microscopy	COAM – Co-amorphous
ALA – <i>L</i> -Alanine	COSMO-RS – Conductor-like Screening Model for Real Solvents
API – Active pharmaceutical ingredient	CSD – Cambridge structural database
ARG – <i>L</i> -Arginine	CYS – <i>L</i> -cysteine
ASCA – Ascorbic acid	DFT – Density functional theory
ASN – <i>L</i> -asparagine	DMSO – Dimethyl sulfoxide
ASP – <i>L</i> -Aspartic acid	DOPA – Dopamine
ASPR – Aspirin	DSC – Differential scanning calorimetry
<i>AV. MW</i> – The average molecular weight of the API and the co-former.	DVS – Dynamic vapour sorption
BENZ – Benzocaine	FAMO – Famotidine
BIPY – 4,4'-Bipyridine	FLURB – Flurbiprofen
BisVCap – Bisvinylcaprolactam	FTIR – Fourier-transform infrared
BisVP – Bisvinylpyrrolidone	FUMA – Fumaric acid
CAF – Caffeine	FUR – Furosemide
CAR – Carvedilol	$G'$ – Elastic storage modulus

G'' – Elastic loss modulus	NICO – Nicotinamide
GALA – Gallic acid	NIR – Near-infrared
GLA – L-Gluconic acid	NMR – Nuclear magnetic resonance
GLN – L-Glutamine	Not COAM – Not co-amorphous
GLU – L-Glutamic acid	OXA – Oxalic acid
GLY – L-Glycine	PARA – Paracetamol
GLYA – Glycolic acid	PASD – Polymeric amorphous solid dispersion
H <sub>2</sub> bisVP – Hydrogenated bisvinylpyrrolidone	PEX – Peroxydone
HIS – L-Histidine	PHB – Phenobarbital
HSM – Hot-stage microscopy	PHE – L-Phenylalanine
ILE – L-Isoleucine	PHENA – Phenazine
IMID – Imidazole	PIP – Piperazine
IND – Indomethacin	PIRA – Piracetam
INICO – Isonicotinamide	PIRO – Piroxicam
ISON – Isoniazid	PLS-DA – Partial least squares-discriminant analysis
KETO – Ketoprofen	PRO – L-Proline
LEU – L-Leucine	PVCap – Polyvinylcaprolactam
LV – Latent variables	PVP – Polyvinylpyrrolidone
LYS – L-Lysine	PYROG – Pyrogallol
MALA – Maleic acid	RH – Relative humidity
MEB – Mebendazole	ROY – 5-Methyl-2-[(2-nitrophenyl)amino]-3-thiophenecarbonitrile
MET – L-Methionine	
MIR – Mid-infrared	



RSE – Rapid solvent evaporation

SALCA – Salicylic acid

SEM – Scanning electron microscopy

SER – *L*-Serine

SIM – Simvastatin

SS-NMR – Solid state nuclear magnetic resonance

SUCA – Succinic acid

SXRD – Single crystal X-ray diffraction

TARTA – Tartaric acid

$T_g$  – Glass transition temperature

TGA – Thermogravimetric analysis

THEO – Theophylline

THR – *L*-Threonine

$T_m$  – Melting temperature

TRP – *L*-Tryptophan

TYR – *L*-Tyrosine

UREA – Urea

VAL – *L*-Valine

VALS – Valsartan

VL – Viscous liquid

VP – Vinylpyrrolidone

wt % – Weight percent

XRPD – Powder X-ray diffraction

$\Delta(\delta h)$  – The difference between the Hansen parameter for hydrogen bonding in MPa0.5 of the API and the co-former.

$\Delta\mu$  – The difference between the pseudo chemical potential of the pure solute of the API and the co-former.

$\Delta G$  – Gibbs free energy of the system

$\Delta G^*$  – Nucleation barrier

$\Delta G_{mix}$  – Gibbs energy of mixing

$\Delta H_{hb}$  – Excess enthalpy of hydrogen bonding

$\Delta H_{mix}$  – Excess enthalpy of mixing

$\Delta \log P$  – The difference in lipophilicity

$\Delta TPSA$  – The difference between the topological polar surface area of the API and the co-former.

$\Sigma HBC_{self}$  – The sum of the difference of hydrogen bond donors to hydrogen bond acceptors for the individual components, for both the API and co-former. To represent the hydrogen bonding present in the individual components.

## List of Figures

Figure 1.1: A solubility curve showing how the increase in temperature or concentration affects solubility. <sup>9</sup> .....	2
Figure 1.2: A graph of the Gibbs free energy of the system ( $\Delta G$ ) vs the radius of the nucleus ( $r$ ) showing how $\Delta G$ increases until reaching the nucleation barrier ( $\Delta G^*$ ) where it starts to decrease. The $\Delta G$ contribution from the interfacial energy is shown in red and the volume energy is shown in blue. Reproduced with permission from reference 12. ....	3
Figure 1.3: The different models of nucleation. Classical nucleation involves the formation of small crystal nuclei which grow into larger crystals. Two-step nucleation involves the formation of crystal nuclei within a disordered precursor. Barrier-free nucleation involves the formation of a nucleus from one or very few molecules. Non-equilibrium nucleus shape involves the formation of nuclei with the correct crystal structure but with a non-equilibrium shape, the shape converts to the equilibrium shape during crystal growth. Dynamic diffuse interface involves the formation of crystal nuclei which varies in shape over time due to diffuse interfaces. Reproduced with permission from reference 14.....	4
Figure 1.4: A three-dimensional crystal surface showing the three different types of crystal growth with F being the flat face, K the kinked face and S the step face. <sup>36</sup> .....	6
Figure 1.5: The three different layer growth mechanisms continuous growth (a) occurs on stepped or kinked faces when these surface sites are favourable for attachment. Surface nucleation (b) occurs when stepped growth occurs at high supersaturations causing the formation of layers. Spiral growth (c) is also a stepped growth mechanism occurring at low supersaturation. <sup>40</sup> .....	7
Figure 1.6: A general phase diagram to show how the temperature and pressure affect the state of a material. The blue line is the sublimation line, the red line is the vaporization line, and the green line is the fusion line. The dashed green line shows the behaviour of water. ..	8
Figure 1.7: Binary phase diagrams. Eutectic (a) shows how mixing two components lowers their melting point. Co-crystals contain multiple eutectic points (b) with varying mole fraction affecting the melting point. Solid solutions (c) show a gradual change in melting point related to the change in mole fraction of the components with the solid line showing the liquidus line and the dashed line showing the solidus line. Above the liquidus line the system is in a liquid state, below the solidus line the system is in a solid state and between the solidus and liquidus lines the system is a mix of solid and liquid. <sup>42</sup> .....	8
Figure 1.8: Example of a ternary phase diagram showing the changes of active pharmaceutical ingredient (API), co-former and solvent affect solubility. The axes are from 0-100%. <sup>42</sup> .....	9
Figure 1.9: Examples of representative supramolecular synthons. ....	11
Figure 1.10: The Gibbs free energy diagrams for (a) monotropic and (b) enantiotropic conditions. For (a) polymorph B is the most stable across the temperature range. For (b) below the transition temperature polymorph B is the stable polymorph, however, above the transition temperature polymorph A is more stable. Reproduced with permission from reference 61.....	14

Figure 1.11: A scheme showing the division of solid forms. Modified from reference 69. ....	15
Figure 1.12: Simplified images of the different solid forms of APIs including an amorphous form, two different polymorphic forms, a solvate/hydrate, a salt, and a co-crystal. Reproduced with permission from reference 70. ....	16
Figure 1.13: A graph of drug concentration against time showing the “spring” and “parachute” effects. (1) The crystalline powder is stable and has low solubility. (2) The “spring” effect shows a rapid increase in drug concentration which quickly drops to the equilibrium concentration ( $C_{eq}$ ). (3) The “spring” effect is followed by the “parachute” effect, showing a rapid increase in drug concentration which gradually drops over a long time. Reproduced with permission from reference 79. ....	17
Figure 1.14: Enthalpy and volume of a drug in both a crystalline and amorphous state as a function of temperature. Reproduced with permission from reference 96. ....	21
Figure 1.15: The structure of a PASD with the API represented as a red hexagonal and the polymer as curvy lines. Image (A) shows the ideal structure with the API molecularly dispersed in the polymer matrix, (B) shows the phase separation and crystallisation of the API, and (C) shows the phases separation into amorphous API rich domains. Reproduced with permission from reference 98. ....	22
Figure 1.16: The advantages and structure of co-amorphous systems. <sup>114, 115</sup> Reproduced with permission from reference 115. ....	23
Figure 1.17: Chemical structures of bisVP, H <sub>2</sub> bisVP and bisVCap. ....	32
Figure 1.18: Originally proposed structure of povidone-iodine. <sup>161</sup> ....	33
Figure 1.19: Revised structure of povidone-iodine showing bridging between two PVP chains. <sup>161</sup> ....	33
Figure 1.20: Microscopy images of APIs and the co-formers, showing the stabilisation effects. <sup>154</sup> The bisVCap is shown to stabilise more APIs when compared with bisVP and no co-former. Reproduced with permission from reference 154. ....	35
Figure 2.1. Relationship between the formation of COAM systems from Kasten et al. <sup>53</sup> , $\Delta H_{mix}$ and $\Delta \log P$ . Green markers indicate COAM systems were formed and red markers indicate not COAM systems. The red dotted line is the expected boundary line between COAM and not COAM systems <sup>48</sup> ....	48
Figure 2.2: XRPD results of equimolar mixtures of mebendazole and 29 different cofomers after ball milling. ....	53
Figure 2.3. Relationship between the formation of COAM systems of mebendazole with 29 co-formers, $\Delta H_{mix}$ and $\Delta \log P$ . Green markers indicate COAM systems were formed and red markers indicate not COAM systems were formed. The red dotted line is the expected boundary line between COAM and not COAM systems based on previous research by Mizoguchi et al. <sup>48</sup> Abbreviations of the cofomers are shown in Table 2.2. ....	54
Figure 2.4. PLS-DA score scatter plot of latent variables (LV) 1 and 2. The red markers indicate not COAM systems and the green markers show COAM systems. The APIs are displayed with different markers with carvedilol (CAR) displayed as an X, carbamazepine (CBZ) as a triangle, furosemide (FUR) as a hollow square, indomethacin (IND) as a cross, mebendazole (MEB) as a circle and simvastatin (SIM) as a hollow diamond. The dashed blue	

line shows the predicted separation between COAM and Not COAM systems for visualization purposes.....	57
Figure 2.5. PLS-DA loading weights scatter plot of the latent variables (LV) 1 and 2. The responses are shown with orange circles and the variables with blue circles. The responses show how the two groups are related to the variables. ....	59
Figure 2.6. Score scatter plot of the predicted scores for the mebendazole-co-former combinations. COAM samples are shown in green, not COAM samples are shown in red. The hollow circles indicate samples which have been predicted incorrectly. The blue dashed line shows the predicted separation line for visualization purposes. ....	61
Figure 2.7: XRPD results of an equimolar mixture of mebendazole and gallic acid after film casting. ....	63
Figure 3.1: PLS-DA score scatter plot of latent variables (LV) 1 and 2. The colour of the markers displays the results of the experimental screen by Goodwin <i>et al.</i> <sup>21</sup> with red markers indicating not COAM systems and green markers indicating COAM systems. Samples incorrectly predicted by the prediction model are shown as hollow circles. <sup>19</sup> The blue dashed line shows the predicted separation line between COAM and not COAM systems for visualization purposes. ....	73
Figure 3.2: PLS-DA score scatter plot of latent variables (LV) 1 and 2. The colour of the markers displays the results of the experimental screen with red markers indicating not COAM systems and green markers indicating COAM systems. Samples incorrectly predicted by the prediction model are shown as hollow circles. <sup>19</sup> The blue dashed line shows the predicted separation line for visualization purposes. ....	77
Figure 3.3: The heat/cool/heat DSC thermograms of 1:1 mixtures of the APIs with bisVCap with exotherms up. The different APIs are a) aspirin, b) chloramphenicol, c) chlorpropamide, d) flurbiprofen, e) furosemide, f) indomethacin, g) ketoprofen, h) paracetamol, i) phenobarbital and j) simvastatin. The black trace displays the initial heat cycle, followed by the cooling cycle in red and the second heat cycle in green. The $T_g$ is highlighted with a blue box on each thermogram. ....	84
Figure 3.4: The XRPD diffractograms for the COAM screen (Table 3.2) of bisVCap with 13 APIs. The CM samples are shown in black and the RSE samples are in red. The different APIs are a) aspirin, b) chloramphenicol, c) chlorpropamide, d) famotidine, e) flurbiprofen, f) furosemide, g) indomethacin, h) ketoprofen, i) mebendazole, j) paracetamol, k) phenobarbital, l) piroxicam, and m) simvastatin. Famotidine, mebendazole and piroxicam only have an RSE trace due to the system decomposing when undergoing CM. ....	89
Figure 3.5: The FTIR spectra for the COAM screen Table 3.2 of bisVCap with 13 APIs. BisVCap is shown in black, the pure API in red, the CM sample in blue and the RSE sample in green. The different APIs are a) aspirin, b) chloramphenicol, c) chlorpropamide, d) famotidine, e) flurbiprofen, f) furosemide, g) indomethacin, h) ketoprofen, i) mebendazole, j) paracetamol, k) phenobarbital, l) piroxicam, and m) simvastatin. The famotidine, mebendazole and piroxicam spectra only display an RSE sample due to the system decomposing when undergoing CM. ....	96

Figure 3.6: The XRPD traces of COAM samples of bisVCap with a) indomethacin, b) simvastatin and c) paracetamol. The initial COAM sample made by RSE is shown in black. The XRPD traces are shown after two weeks when stored at ~20 °C (red) and 3 °C (green). 98	
Figure 3.7: The FTIR spectra of COAM samples of bisVCap with a) indomethacin, b) simvastatin and c) paracetamol. The initial COAM sample made by RSE is shown in black. The FTIR spectra are shown after two weeks when stored at ~20 °C (red) and 3 °C (green). 99	
Figure 3.8: The XRPD traces of COAM samples of bisVCap with a) simvastatin and b) paracetamol. The XRPD traces are shown after one week when stored at ~20 °C (black) and 3 °C (red). .....	101
Figure 3.9: The FTIR spectra of COAM samples of bisVCap with a) simvastatin and b) paracetamol. The initial FTIR spectra after RSE is shown in black. The FTIR spectra are shown after one week when stored at ~20 °C (red) and 3 °C (green). .....	102
Figure 3.10: XRPD traces of bisVCap with furosemide after RSE in a 1:1 (black), 1:2 (red), 1:3 (blue) and 1:4 ratio (green). Pure furosemide after RSE is shown in purple.....	104
Figure 3.11: FTIR spectra for the increased ratio study of bisVCap and furosemide showing the carbonyl and alcohol region. The spectra display pure bisVCap (black) and pure furosemide (red). The bisVCap furosemide systems were made via RSE at different ratios with 1:1 in blue, 1:2 in green, 1:3 in purple and 1:4 in light brown. The furosemide systems which underwent RSE is also shown in cyan. ....	104
Figure 3.12: The XRPD traces of a COAM bisVCap furosemide system made via RSE. The initial system is shown in black. The system was stored for seven days at 0% RH (red), 11% RH (green), 33% RH (blue), 75% RH (cyan) and 100% RH (pink). ....	106
Figure 3.13: The FTIR spectra of a COAM bisVCap furosemide system made via RSE. Pure bisVCap is shown in black, pure furosemide in red and the initial bisVCap furosemide COAM system in green. The system was stored for seven days at 0% RH (blue), 11% RH (cyan), 33% RH (pink), 75% RH (yellow) and 100% RH (brown). ....	106
Figure 3.14: The XRPD traces of a COAM bisVCap furosemide system made via RSE. The initial system is shown in black. The system was stored for 28 days at 0% RH (red), 11% RH (green), 33% RH (blue), 75% RH (cyan) and 100% RH (pink). ....	108
Figure 3.15: The FTIR spectra of a COAM bisVCap furosemide system made via RSE. Pure bisVCap is shown in black, pure furosemide in red and the initial bisVCap furosemide COAM system in green. The system was stored for 28 days at 0% RH (blue), 11% RH (cyan), 33% RH (pink), 75% RH (yellow) and 100% RH (brown). ....	108
Figure 4.1: Suggested models of the bonding between hydrogen peroxide and PVP. <sup>28</sup> .....	117
Figure 4.2: The chemical structure of H <sub>2</sub> bisVP. ....	117
Figure 4.3: The FTIR spectra of PVP K-25 (black) and PEX K-30 (red).....	120
Figure 4.4: The FTIR spectra of PVP K-90 (black) and PEX K-90 (red).....	120
Figure 4.5: The FTIR spectra of PVP XL-10 (black) and PEX XL-10 (red).....	121
Figure 4.6: The MAS solid state NMR spectra of PVP K-25 (black) and PEX K-30 (red).....	122
Figure 4.7: The MAS solid state NMR spectra of PVP K-90 (black) and PEX K-90 (red).....	122

Figure 4.8: The MAS solid state NMR spectra of PVP XL-10 (black) and PEX XL-10 (red). ....	123
Figure 4.9: FTIR spectrum of H <sub>2</sub> bisVP (black), amorphous H <sub>2</sub> bisVP hydrogen peroxide complex (red), H <sub>2</sub> bisVP·H <sub>2</sub> O <sub>2</sub> ·H <sub>2</sub> O (green), H <sub>2</sub> bisVP·1.7H <sub>2</sub> O <sub>2</sub> ·0.3H <sub>2</sub> O (purple) and H <sub>2</sub> bisVP·2H <sub>2</sub> O <sub>2</sub> complex (blue).....	126
Figure 4.10: The X-ray structure of H <sub>2</sub> bisVP·2H <sub>2</sub> O <sub>2</sub> with the two crystallographically independent peroxide sites labelled A and B. ....	127
Figure 4.11: The X-ray structure of H <sub>2</sub> bisVP·H <sub>2</sub> O <sub>2</sub> ·H <sub>2</sub> O showing the localisation of the water molecule at site B.....	128
Figure 4.12: The X-ray structure of H <sub>2</sub> bisVP·1.7H <sub>2</sub> O <sub>2</sub> ·0.3H <sub>2</sub> O showing the disorder in one of the hydrogen peroxide molecules. ....	128
Figure 4.13: The DFT calculated structure of three tetramer models of PVP and twelve molecules of hydrogen peroxide in an alternating A and B hydrogen bonding form. ....	130
Figure 4.14: The DFT calculated structure of a hexamer model of PVP and six hydrogen peroxide molecules all in the A hydrogen bonding form. ....	131
Figure 4.15: The two proposed structures of PEX (a) single type of hydrogen peroxide hydrogen bonded chain (A-type). (b) Hydrogen peroxide cross-linking between PVP molecules (AB-type).....	132
Figure 5.1. The components of the haircare mixture: hydroxypropyl- <i>L</i> -gluconamide ( <b>1</b> ), hydroxypropylammonium <i>L</i> -gluconate ( <b>2</b> and <b>3</b> ). ....	142
Figure 5.2: The X-ray crystal structure of <i>D</i> -gluconic acid monohydrate (CAKZAP) in the (010) crystallographic plane.....	143
Figure 5.3: The X-ray crystal of ammonium gluconate (BAGDOC) showing a single NH <sub>4</sub> <sup>+</sup> interacting with four <b>3</b> anions.....	144
Figure 5.4: The X-ray crystal structure of <b>1</b> form I showing the hydrogen bonding in the a) (100) and b) (001) crystallographic planes. ....	145
Figure 5.5: The X-ray crystal structure of <b>1</b> form II in a) crystallographic plane (120) with the C1-C2 bond highlighted in a blue circle. b) The two crystallographically independent molecules in the asymmetric unit form two separate chains along the end OH group, this is shown in the crystallographic plane (100).....	146
Figure 5.6: The X-ray crystal structure of <i>N,N'</i> -ethylene bis- <i>L</i> -gluconamide showing the amide hydrogen bond chain in the a) (100) and b) (010) crystallographic plane. ....	147
Figure 5.7: XRPD patterns of the <i>N,N'</i> -ethylene bis- <i>L</i> -gluconamide with the pattern calculated from the single crystal structure (black) and the bulk powder (red). ....	148
Figure 5.8: The X-ray crystal structure of a DMSO solvate of <i>L</i> -cysteic acid.....	150
Figure 5.9: The X-ray crystal structure of <b>2</b> ·HSO <sub>4</sub> <sup>-</sup> showing the hydrogen bonding interactions in the a) (100) and b) (010) crystallographic planes. ....	152
Figure 5.10: The X-ray crystal structure of <b>2</b> ·CH <sub>3</sub> SO <sub>3</sub> <sup>-</sup> in the a) (100) and b) (101) crystallographic planes. ....	153
Figure 5.11: The X-ray crystal structure of <b>2</b> ·HC <sub>2</sub> O <sub>4</sub> <sup>-</sup> in the a) (010) and b) (100) crystallographic plane. ....	154

Figure 5.12: The X-ray crystal structure of guanidinium carbonate methanol solvate. a) the asymmetric unit and b) the (310) crystallographic plane.....	155
Figure 5.13: Model structure of the potential intermolecular interactions formed between <b>1</b> and the amino acid substituent groups on a simplified hair structure. ....	156
Figure 5.14: Model structure of the potential intermolecular interactions formed between <b>2</b> and the amino acid substituent groups on a simplified hair structure. ....	157
Figure 5.15: Model structure of the potential intermolecular interactions formed between <b>3</b> and the amino acid substituent groups on a simplified hair structure .....	158
Figure 6.1: Gel formation process. Reproduced with permission from Draper <i>et al.</i> <sup>9</sup> .....	167
Figure 6.2: The structure of hydroxypropyl- <i>L</i> -gluconamide ( <b>1</b> ).....	168
Figure 6.3: Images of the two supramolecular <b>1</b> gels with a) aniline and b) benzyl alcohol.	170
Figure 6.4: The oscillatory frequency sweep for different concentrations of <b>1</b> in aniline at 10 Pa. $G'$ is shown in red and $G''$ is shown in blue. The different concentrations are 0.75 wt% (circle), 1 wt% (square), 1.5 wt% (diamond) and 2 wt% (triangle).....	175
Figure 6.5: The variation of $G'$ at 10 rad/s from the oscillatory frequency sweep for different concentrations of compound <b>1</b> in aniline.....	175
Figure 6.6: The oscillatory stress sweeps for a range of different concentrations of <b>1</b> in aniline at 10 rad/s. $G'$ is shown in red and $G''$ is shown in blue. The different concentrations are 0.75 wt% (circle), 1 wt% (square), 1.5 wt% (diamond) and 2 wt% (triangle).....	176
Figure 6.7: FTIR spectra of <b>1</b> form I (black), form II (green), <b>1</b> aniline xerogel (red) and <b>1</b> benzyl alcohol xerogel (blue). ....	177
Figure 6.8: The XRPD patterns of <b>1</b> form I (black), <b>1</b> form II (red), <b>1</b> aniline xerogel (blue) and <b>1</b> benzyl alcohol xerogel (purple). The calculated patterns from published crystal structures of aniline (green) and benzyl alcohol (orange) are shown. <sup>42, 43</sup> .....	178
Figure 6.9: The labelled diagram of <b>1</b> and the gluconate salt for NMR assignment. ....	178
Figure 6.10: The <sup>1</sup> H NMR spectrum of <b>1</b> (black), <b>1</b> aniline xerogel (red) and <b>1</b> benzyl alcohol xerogel (green). Two peaks are assigned based on the labelling in Figure 6.9 to show the ratio of <b>1</b> to the salt decomposition product. ....	179
Figure 6.11: SEM micrographs of the dried xerogel of <b>1</b> aniline at 1 wt%.....	180
Figure 6.12: SEM micrographs of the dried xerogel of <b>1</b> benzyl alcohol at 5 wt%.....	180

## List of Tables

Table 2.1: Results of experimental COAM screening using ball milling by Kasten et al. <sup>53</sup> N indicates the system is not COAM including crystalline salts or crystalline starting material and Y indicates COAM formation including COAM salts. ....	46
Table 2.2: Results of COAM screening by ball milling with mebendazole. ....	48

Table 2.3: The definitions of all the variables used to find the PLS-DA model. The key parameters identified are in bold. ....	55
Table 2.4. Misclassification table showing the percentage of correctly assigned observations of the 120 API-amino acid combinations. Fisher’s probability of $4.7 \times 10^{-8}$ . ....	60
Table 2.5. Misclassification table showing the percentage of correctly assigned observation of the 29 MEB-co-former combinations. Fisher’s probability of $1.8 \times 10^{-4}$ . ....	61
Table 2.6: Misclassification table showing the percentage of correctly assigned observations of the 29 MEB-co-former combinations after gallic acid was confirmed as being COAM by film casting. Fisher’s probability of $2.4 \times 10^{-5}$ . ....	63
Table 3.1: Results of an experimental co-amorphous screen from Goodwin <i>et al.</i> <sup>21</sup> compared to the predicted result using the prediction model from Chambers <i>et al.</i> <sup>19</sup> .....	72
Table 3.2: The results of the COAM screen including the predicted and experimental results. The prediction includes the predicted COAM value. The experimental COAM screen includes the results from an initial HSM screen, the $T_g$ from DSC, and the XRPD analysis of both CM and RSE samples. Y indicates the samples were COAM, N indicates the samples were not COAM and D indicates the samples decomposed. The predicted result was also compared with the experimental results to determine if the prediction was correct. ....	76
Table 3.3: Optical micrographs of samples melted using an HSM after 24 hours. The first column shows the pure APIs, and the second column shows the APIs in a 1:1 molar ratio with bisVCap. ....	78
Table 4.1: FTIR $\nu$ OH and $\nu$ CO stretching bands for PVP K-25, K-90, XL-10, PEX K-30, K-90, XL-10, H <sub>2</sub> bisVP, amorphous H <sub>2</sub> bisVP-H <sub>2</sub> O <sub>2</sub> and crystalline H <sub>2</sub> bisVP·2H <sub>2</sub> O <sub>2</sub> . ....	119
Table 4.2: Table of all titration results including calculated weight percentage of hydrogen peroxide and calculated ratio of hydrogen peroxide to VP (assuming no water present in peroxydone). ....	124
Table 4.3: Table of the elemental analysis results for PEX K-30, K-90 and XL-10 including average result and calculated hydrogen peroxide content per monomer unit based on the elemental percentages for carbon (assuming no water is present). ....	124
Table 4.4: Table of the expected elemental analysis values with of PEX with three different ratios of PVP monomer to hydrogen peroxide molecule. ....	125
Table 5.1: Amino acids in bleached and non-bleached hair. <sup>20</sup> .....	141
Table 5.2: The potential excess enthalpy of mixing of the 3 components of the haircare solution with all the amino acids in hair calculated using COSMOquick. <sup>38</sup> .....	149
Table 5.3: The potential excess enthalpy of mixing of the 3 components of the haircare solution with the molecules that mimic the substituent groups of the amino acids calculated using COSMOquick. ....	151
Table 6.1: The results of the polymorph screen of <b>1</b> with a range of solvents at 2 wt%. G = gel, PG = partial gel, S = solution, ND = not dissolved, P = precipitate. ....	170
Table 6.2: Gel screen of <b>1</b> with a range of aniline and amine derivatives with varying wt%. G = gel, PG = partial gel, S = solution, ND = not dissolved, P = Precipitate, VL = viscous liquid. ....	174



Table 8.1: Crystallographic information for BisVP·1.7H <sub>2</sub> O <sub>2</sub> ·0.3H <sub>2</sub> O. ....	193
Table 8.2: Crystallographic information for BisVP·H <sub>2</sub> O <sub>2</sub> ·H <sub>2</sub> O. ....	194
Table 8.3: Crystallographic information for BisVP·2H <sub>2</sub> O <sub>2</sub> . ....	195
Table 8.4: Crystallographic information for hydroxypropyl- <i>L</i> -gluconamide ( <b>1</b> ) form I. ....	196
Table 8.5: Crystallographic information for hydroxypropyl- <i>D</i> -gluconamide ( <b>1</b> ).....	197
Table 8.6: Crystallographic information for hydroxypropyl- <i>L</i> -gluconamide ( <b>1</b> ) form II. ....	198
Table 8.7: Crystallographic information for 3-hydroxypropylammonium hydrogen sulfate. .....	199
Table 8.8: Crystallographic information for 3-hydroxypropylammonium sulfonate. ....	200
Table 8.9: Crystallographic information for 3-hydroxypropylammonium hydrogen oxalate. .....	201
Table 8.10: Crystallographic information for guanidine carbonate methanol solvate. ....	202
Table 8.11: Crystallographic information for <i>N,N'</i> -ethylene bis- <i>L</i> -gluconamide. ....	203
Table 8.12: Crystallographic information for <i>L</i> -cysteic acid dimethylsulfoxide solvate. ....	204
Table 8.13: Crystallographic information for 4,4'-biphenol·morpholine (1:2).....	205

## List of Schemes

Scheme 3.1. Chemical structure of bisVCap and the 13 APIs used in the COAM screen. ....	70
Scheme 6.1: Aniline, benzyl alcohol and the aniline and amine derivatives used for the second gel screen.....	173

# 1 Introduction

## 1.1 Crystallisation

### 1.1.1 Nucleation and Growth

Crystallisation is the formation of a solid material which has an ordered repeating arrangement of atoms or molecules in three dimensions.<sup>1</sup> The process of crystallisation requires a supersaturated solution, formed when the concentration of the solution exceeds the equilibrium solubility of the solute under a given set of conditions (e.g. temperature, pressure). To determine the point of supersaturation a solubility curve can be determined which shows the maximum solubility of a substance against a chosen parameter e.g. temperature (Figure 1.1). The solubility curve contains three zones: supersaturated, metastable, and under-saturated. In the supersaturated zone, the solution undergoes spontaneous nucleation causing molecules to aggregate and stabilise the solid-solution interface resulting in crystal nucleation. In the metastable zone, only heterogeneous nucleation can occur and in the undersaturated zone, the sample remains dissolved in solution. To determine the saturation line the clear point can be measured and for the supersaturation line, the cloud point can be measured.<sup>2</sup> The cloud point is the point at which the formation of crystals from a heated solution can be detected which varies with both temperature and concentration. The clear point is the point at which the solid suspended in the solution is fully dissolved when heated, turning the solution clear. The cloud and clear points can be determined using a variety of methods including visual observation, an optical probe, attenuated total reflectance Fourier transform infrared or focused beam reflectance measurement.<sup>3-5</sup> The supersaturation line can be reached by changing the temperature in a cooling crystallisation or increasing the concentration of the solution by evaporation or antisolvent crystallisation.<sup>6, 7</sup> The level of supersaturation can be described numerically using the supersaturation ratio which is defined as the concentration of the solution divided by the solubility of the solution in the current conditions.<sup>8</sup> A supersaturation ratio over 1 indicates the solution is supersaturated and crystals can grow.

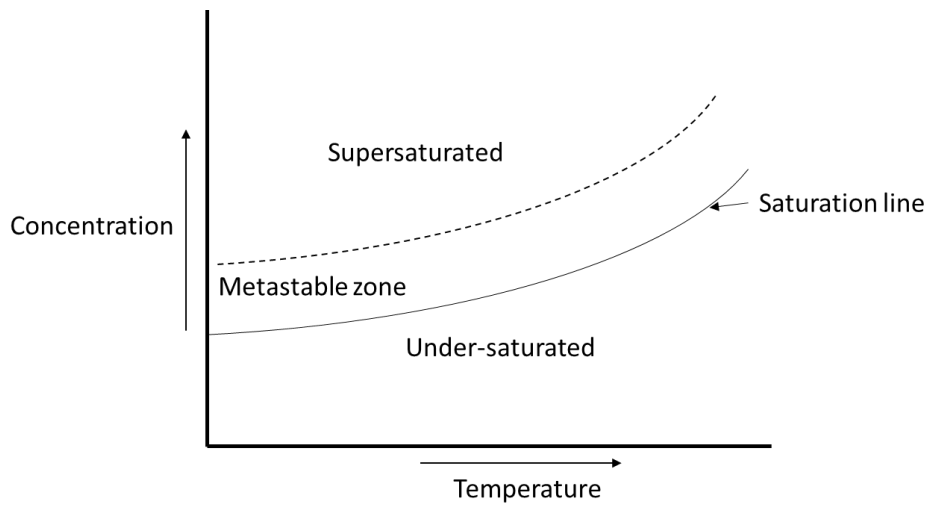


Figure 1.1: A solubility curve showing how the increase in temperature or concentration affects solubility.<sup>9</sup>

The two key theories for the process of nucleation are classical and non-classical nucleation theory. In classical nucleation theory, crystals are formed via nucleation and then undergo crystal growth. According to this theory, nucleation involves the formation of small clusters with the same properties as the bulk crystal phase, in a supersaturated solution. The bulk solid state is more stable compared to the surface solid state as the molecules in the bulk solid have more interactions compared to molecules at the surface of the cluster. Thus, it is more favourable to form crystals, however, the boundary formed between the solid and liquid boundary is unfavourable but is stabilised by supersaturation. This instability causes the crystal nucleus to form and re-dissolve dynamically until a nucleus is formed which is equal to or larger than the critical size required for spontaneous growth (Figure 1.2).<sup>1</sup> Classical nucleation theory makes the following assumptions: the clusters are spherical droplets having uniform interior densities, the structure of the nucleus matches the structure of the final crystal, the surface tension is neglected, the growing clusters do not move or rotate, the growth occurs by the addition of one unit at a time and the clusters cannot be compressed.<sup>10</sup> These assumptions work for large nuclei, however, for smaller critical nucleus sizes the assumptions are less valid. The assumptions fail for smaller nuclei because the small clusters do not have structures matching the final crystal, as the structure rearranges during formation.<sup>11</sup>

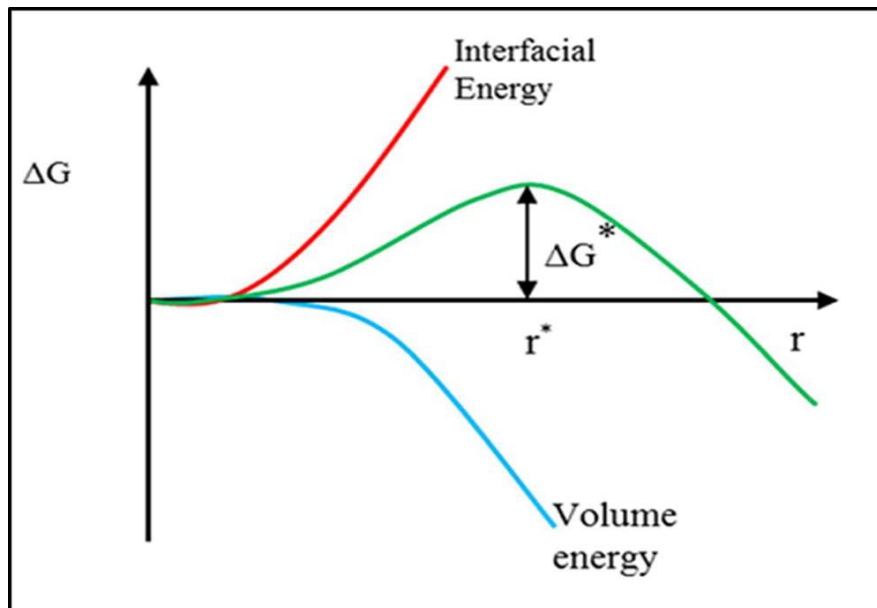


Figure 1.2: A graph of the Gibbs free energy of the system ( $\Delta G$ ) vs the radius of the nucleus ( $r$ ) showing how  $\Delta G$  increases until reaching the nucleation barrier ( $\Delta G^*$ ) where it starts to decrease. The  $\Delta G$  contribution from the interfacial energy is shown in red and the volume energy is shown in blue. Reproduced with permission from reference 12.

More recently non-classical nucleation theory (Figure 1.3) has been introduced.<sup>12</sup> Non-classical nucleation covers multiple nucleation methods to form crystal nuclei including two-step nucleation, barrier-free nucleation, non-equilibrium nucleus shape, and nuclei with variable and diffuse interfaces.<sup>13-17</sup> Two-step nucleation begins with the formation of a highly concentrated droplet in the solution defined as a disordered precursor, this is followed by the formation of crystal nuclei within the droplet.<sup>18-24</sup> The two-step nucleation mechanism was directly observed by atomic force microscopy (AFM) during the formation of olanzapine hydrate from olanzapine.<sup>25</sup> AFM showed the formation of small droplets which coalesced to form larger droplets, nucleation began to occur in the droplets leading to a fully developed crystal. Barrier-free nucleation is where the energy barrier to nucleation drops below the kinetic energy of the atom or molecules at a given temperature, allowing the formation of a nucleus of one or very few atoms or molecules.<sup>26-28</sup> Non-equilibrium nucleus shape involves the formation of nuclei with the correct crystal phase packing but a shape that does not maximise the volume to surface area ratio.<sup>14, 26, 29</sup> An example of non-equilibrium nuclei shape was shown during the crystallisation of apoferritin where AFM was used to observe that the apoferritin molecules arranged in one or two layers containing 5-

10 rods of up to 7 molecules, forming a planar structure with a high surface area.<sup>30</sup> The planar structure was shown to have the same packing arrangement as was found in apoferritin crystals. The dynamic diffuse interface is based around work by Zhou *et al.*<sup>31</sup> using atomic electron tomography, which found that the order parameter of a nucleus, which describes how closely atoms adopt the current crystal shape, is not uniform. The order parameter instead changes with the distance from the nucleus core, therefore the interface between the surrounding phase and nucleus is diffuse with the structure varying over time.

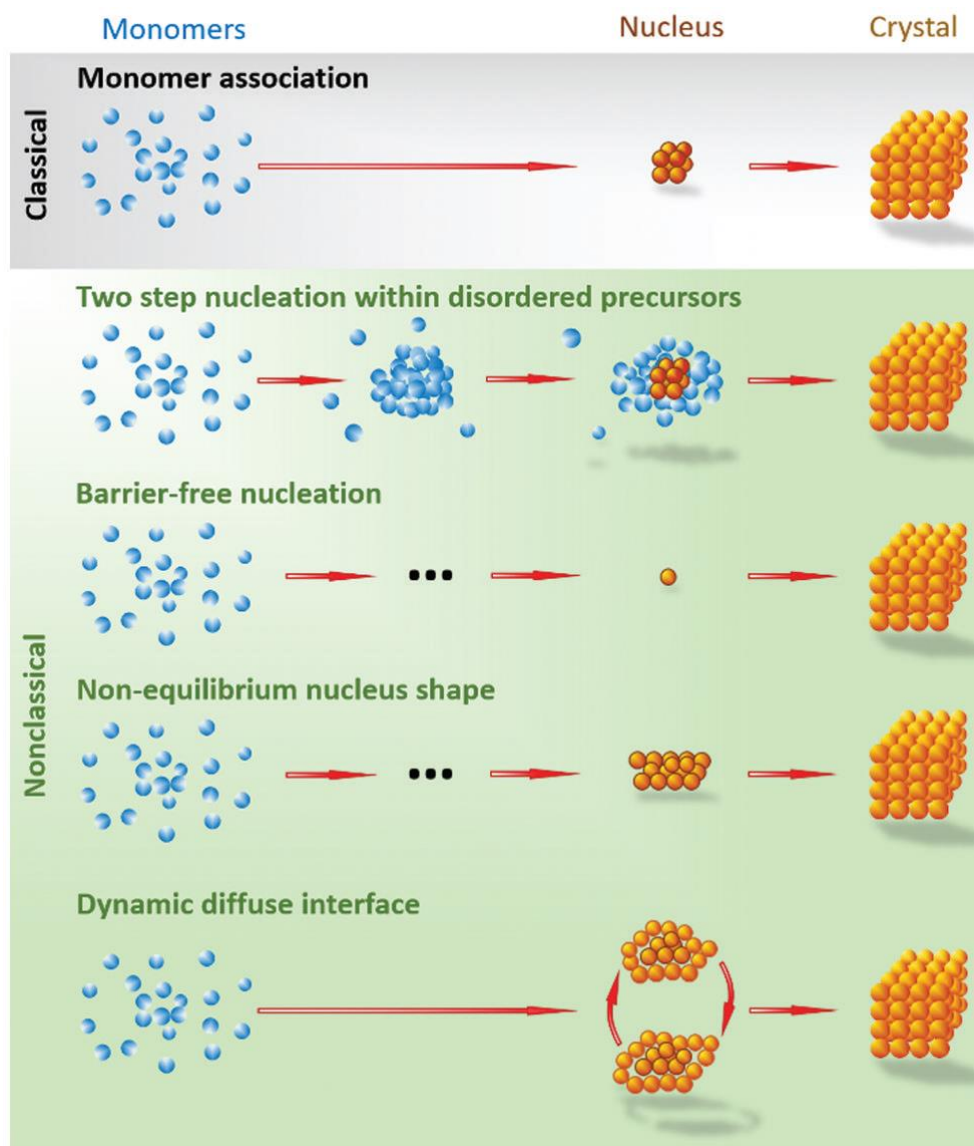


Figure 1.3: The different models of nucleation. Classical nucleation involves the formation of small crystal nuclei which grow into larger crystals. Two-step nucleation involves the formation of crystal nuclei within a disordered precursor. Barrier-free nucleation involves the

formation of a nucleus from one or very few molecules. Non-equilibrium nucleus shape involves the formation of nuclei with the correct crystal structure but with a non-equilibrium shape, the shape converts to the equilibrium shape during crystal growth. Dynamic diffuse interface involves the formation of crystal nuclei which varies in shape over time due to diffuse interfaces. Reproduced with permission from reference 14.

Another interesting step of crystallisation is oriented attachment which involves the crystal particles attaching onto specific faces.<sup>32</sup> Oriented attachment is driven by the reduction in surface energy caused by attaching crystal particles to the highest energy crystal face.<sup>33</sup>

An expansion of oriented attachment is known as Viedma ripening, where a single enantiomer crystal forms from a racemic mixture.<sup>34</sup> The Viedma ripening process can occur by stirring a suspension with small glass balls to grind the sample in a closed system with a constant temperature. Most of the currently proposed mechanism relies on four key factors.<sup>34</sup> The first is racemisation in solution, the process of one enantiomer changing to the other in solution. As one enantiomer is used to grow the crystal, the equilibrium effect caused by racemisation causes the other enantiomer to convert to the enantiomer which is more enriched in the solid phase. The second is Ostwald ripening which is where the larger crystals grow more compared to small crystals.<sup>35</sup> The Ostwald ripening occurs because one enantiomer grows larger crystals leading to the other enantiomer growing less causing deracemisation. The third is the incorporation of enantioselective clusters into larger crystals, leading to the amplification of the growth of one enantiomer. The fourth is attrition caused by the constant grinding, this maintains small crystal sizes which enhances Ostwald ripening and causes the deracemisation times to decrease.<sup>34</sup>

If the nucleation proceeds in a pure solution with no impurities or seed crystals it is classed as homogeneous nucleation and requires large supersaturations to occur. Heterogeneous nucleation is another method that requires impurities such as dust particles, interfaces, or vessel walls, and this requires a lower supersaturation. Small crystals of a defined crystal structure called seed crystals can be added to a supersaturated solution to induce crystal growth of the same crystal structure, this is a form of secondary nucleation.

After the crystal has been nucleated crystal growth occurs, crystal growth is when the number of units joining the surface exceeds the number of units leaving.<sup>1</sup> The rate of this

growth depends on the number of interactions and the strength of these interactions with the surface. This means that the crystal face with the largest number of interactions will grow fastest, therefore the slower growing faces will be larger in the final bulk crystal. The different growth sites are categorised according to the number of possible interaction points; kinked (K) when three interaction points are available, stepped (S) for two interaction points and flat (F) for one interaction point (Figure 1.4).

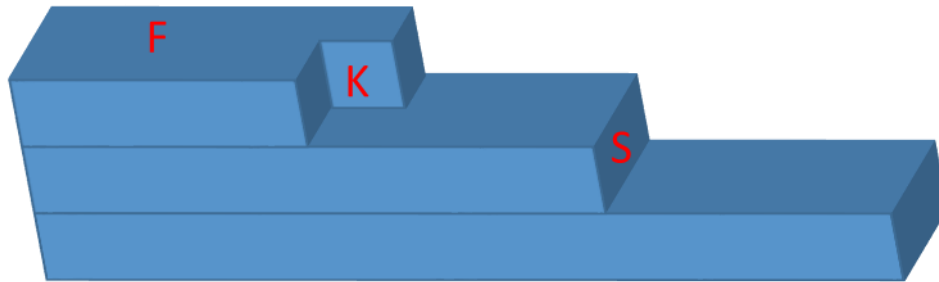


Figure 1.4: A three-dimensional crystal surface showing the three different types of crystal growth with F being the flat face, K the kinked face and S the step face.<sup>36</sup>

There are a few different variations on the mechanism of crystal growth (Figure 1.5) which rely on the  $\alpha$ -factor (Equation 1.1).<sup>37</sup> The  $\alpha$ -factor relies on  $\Delta E$  which is the energy change when a perfectly flat surface is roughened by removing one block to start a new layer and depends on  $k$  the Boltzmann constant and  $T$  the temperature. Thus, the  $\alpha$ -factor describes the ease with which a surface can form sites with multiple binding interactions.<sup>38</sup> Low  $\alpha$ -factor indicates that there is a low energy barrier for growth due to a rough crystal surface. When the  $\alpha$ -factor is below three the energy required to form a stepped surface is low. Therefore, many kinks and steps will form, and this is called continuous growth. When the  $\alpha$ -factor is between three and five the surface roughness decreases so not all units reaching the surface find growth sites. This causes surface nucleation as incoming growth units join other adsorbed growth units and form islands over the surface.<sup>39</sup> When the  $\alpha$ -factor is greater than five the surface is flat, and a spiral growth mechanism occurs. The growth in this process occurs around dislocations that are misaligned parts of the crystal lattice due to stresses occurring during crystal growth. This means a screw dislocation pattern forms on the crystal face.<sup>1</sup>

$$\alpha = \Delta E/kT \quad (1.1)$$

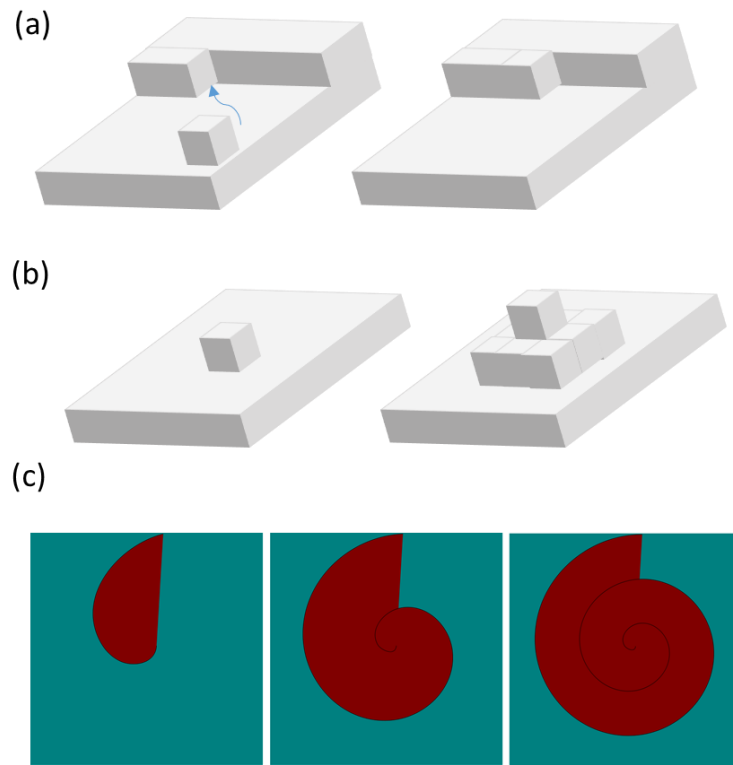


Figure 1.5: The three different layer growth mechanisms continuous growth (a) occurs on stepped or kinked faces when these surface sites are favourable for attachment. Surface nucleation (b) occurs when stepped growth occurs at high supersaturations causing the formation of layers. Spiral growth (c) is also a stepped growth mechanism occurring at low supersaturation.<sup>40</sup>

A very important part of crystallisation are the phases of the system.<sup>41</sup> Phases are formed of homogenous, physically distinct, and separate portions of a system. The phase rule (Equation 1.2) describes how different phases relate when in equilibrium.

$$P + F = C + 2 \quad (1.2)$$

The phase rule uses  $F$  as the number of degrees of freedom,  $P$  as the number of phases in equilibrium and  $C$  as the number of components. The degrees of freedom are the number of variables that affect the equilibrium state. The components are the number of different chemical compounds that are present in any phase. This allows the production of a phase diagram by changing the temperature and pressure and recording the state of the material (Figure 1.6). The phase diagrams can contain a critical point where only liquid and gaseous phases can coexist in equilibrium and a triple point when solid, liquid, and gaseous phases can coexist in equilibrium.



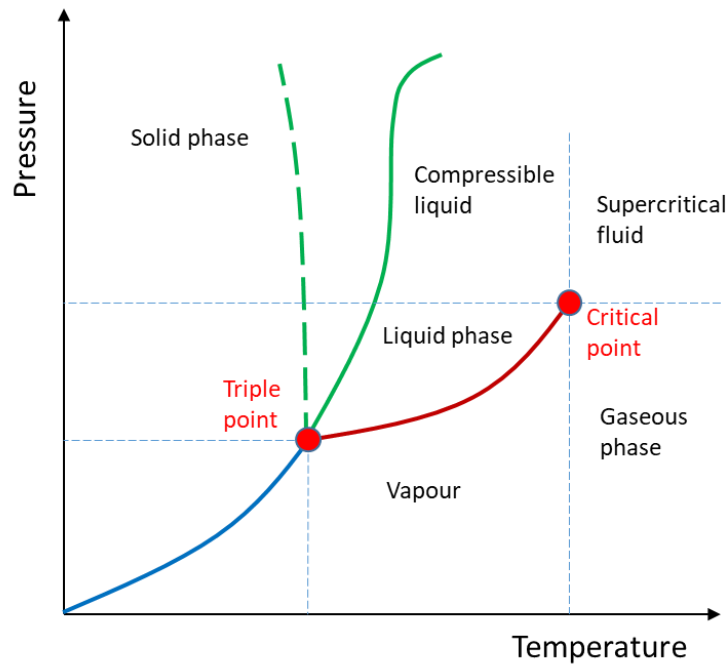


Figure 1.6: A general phase diagram to show how the temperature and pressure affect the state of a material. The blue line is the sublimation line, the red line is the vaporization line, and the green line is the fusion line. The dashed green line shows the behaviour of water.

Phase diagrams can also be determined for binary mixtures by mixing two components in different ratios and measuring their melting temperatures. A eutectic system forms when the mixture of the two components has a lower melting point compared to the separate components (Figure 1.7).<sup>42</sup> When there are two eutectic points a co-crystal is formed which has a higher melting point phase between the two eutectic points. When there are no eutectic points a solid solution forms which is where the melting point increases as the ratio of the higher melting point component increases.

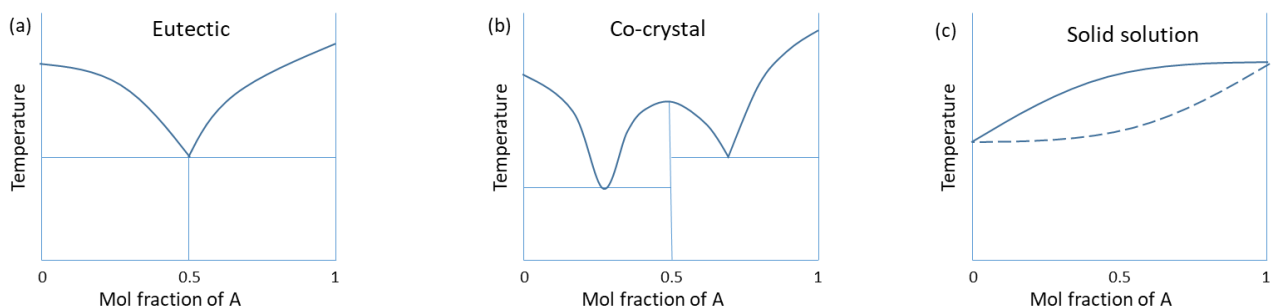


Figure 1.7: Binary phase diagrams. Eutectic (a) shows how mixing two components lowers their melting point. Co-crystals contain multiple eutectic points (b) with varying mole

fraction affecting the melting point. Solid solutions (c) show a gradual change in melting point related to the change in mole fraction of the components with the solid line showing the liquidus line and the dashed line showing the solidus line. Above the liquidus line the system is in a liquid state, below the solidus line the system is in a solid state and between the solidus and liquidus lines the system is a mix of solid and liquid.<sup>42</sup>

Phase diagrams can also be made for three-component mixtures and are called ternary phase diagrams. Ternary phase diagrams are displayed as a triangle and they show the composition at a constant parameter, *i.e.*, one temperature (Figure 1.8). Ternary phase diagrams indicate how varying the composition would change the phase. An example of a system that can form a ternary phase diagram is a co-crystal system of ethenzamide and saccharin formed in different solvents.<sup>43</sup> The different solvents tested include ethanol, isopropanol and ethyl acetate and it was found that with ethanol and isopropanol an asymmetric phase diagram was formed due to the different solubility of ethenzamide and saccharin. However, with ethyl acetate, the ethenzamide and saccharin have similar solubility resulting in a more symmetric phase diagram which is more preferable for co-crystal formulation because when the solvent is cooled the solubility of both components drop at a similar rate meaning the co-crystal formation should be more controlled.<sup>43</sup>

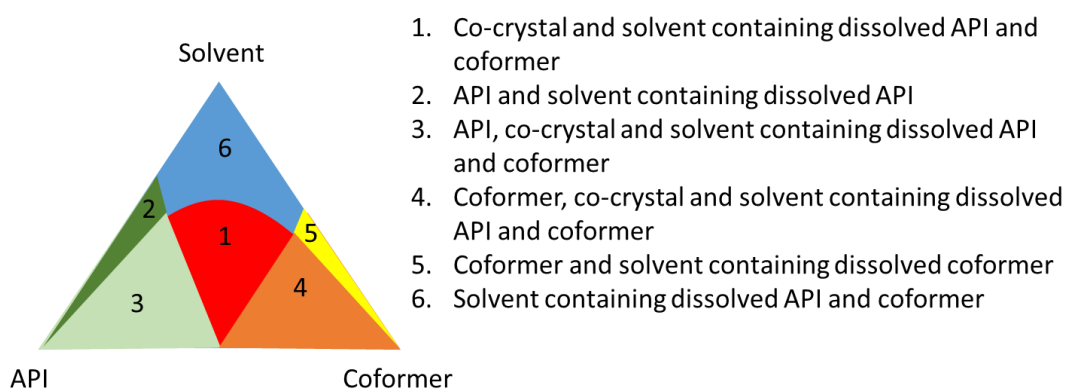


Figure 1.8: Example of a ternary phase diagram showing the changes of active pharmaceutical ingredient (API), co-former and solvent affect solubility. The axes are from 0-100%.<sup>42</sup>

### 1.1.2 Crystal Engineering

Crystal engineering is based on understanding and thus designing molecular solid-state structures based on their intermolecular interactions.<sup>44, 45</sup> Crystal engineering relies on an

understanding of both molecular properties and crystal packing tendencies.<sup>46</sup> This relationship was first discussed by W. H. Bragg where he stated that aromatic systems such as benzene and naphthalene adopt a structure with a definite size and form which remains constant even in different crystal structures.<sup>47</sup> The relationship helps define the key aims of crystal engineering which is to build up crystal structures from individual molecules in a rational or predictable way.

Intermolecular interactions are very important for crystal engineering. Sarma and Desiraju discussed the use of hydrogen and halogen bonds in crystal engineering in 1986.<sup>48</sup> M. C. Etter discussed the idea that hydrogen bonds are both directional and relatively strong, therefore very important in determining crystal structure.<sup>49</sup> A key problem in designing and predicting crystallization behaviour from a consideration of molecular structure is that crystallisation depends on all of the functional groups present in the molecule as well as properties such as molecular shape, size, and surface characteristics.<sup>46</sup> A simplified method to address the problem is the use of supramolecular synthons (Figure 1.9).<sup>50</sup> Supramolecular synthons are structural units that can be formed and/or assembled with intermolecular interactions.<sup>51</sup> The main supramolecular interaction for molecular recognition is hydrogen bonding as it provides directionality and strength, allowing greater reproducibility in the structures formed. This is supported by other weaker interactions including  $\pi$ - $\pi$  interactions, van der Waals interactions and halogen bonding. Supramolecular synthons help with the prediction of crystal structures as synthons with strong and directional interactions are formed in preference compared with weaker and less directional interactions.

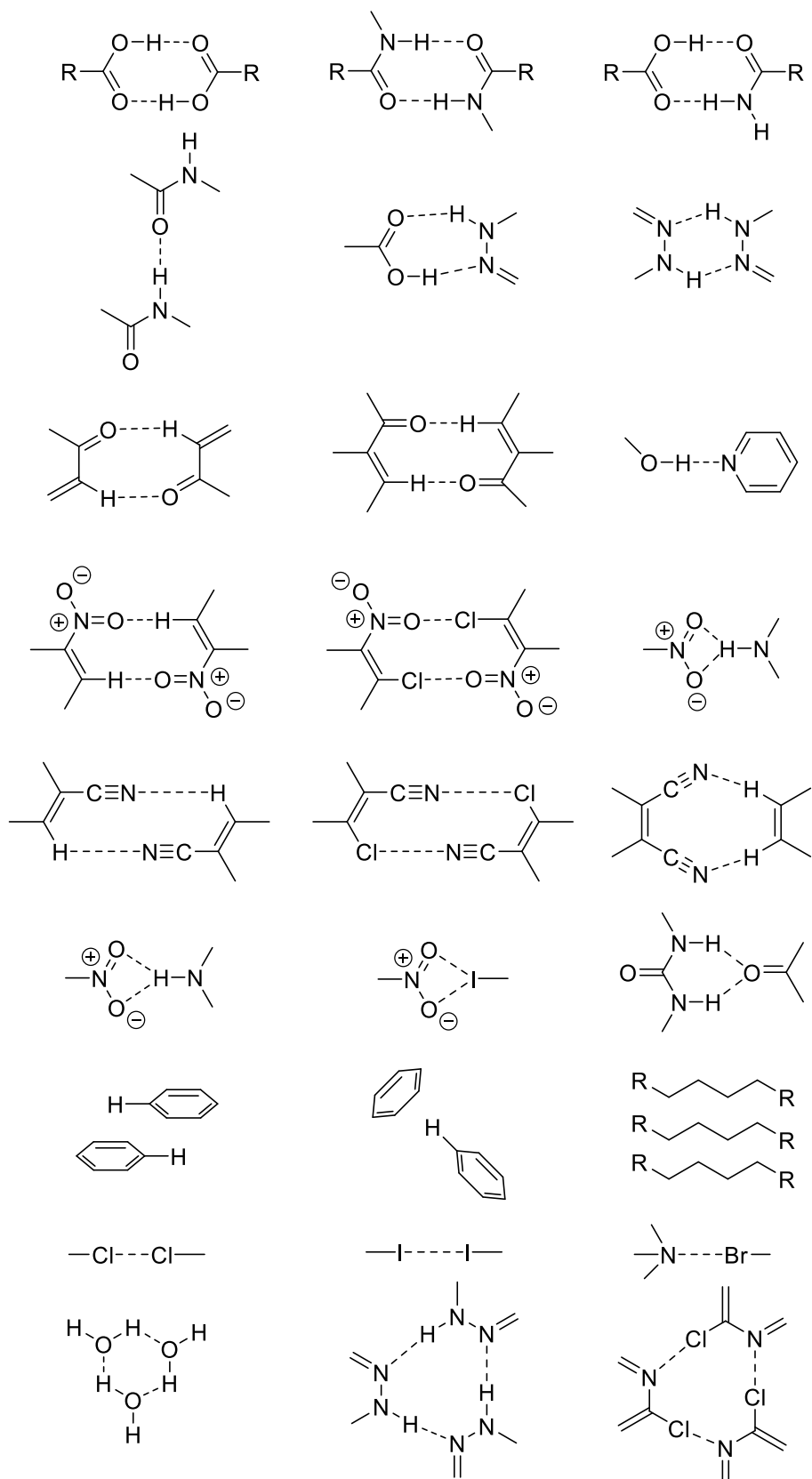


Figure 1.9: Examples of representative supramolecular synthons.

### 1.1.3 Cambridge Structural Database

Single crystal X-ray crystallography is a key technique as it provides both the structure of a molecule and its interactions with other molecules in a given crystal form. The information gathered is very important for areas including supramolecular chemistry, conformational analysis, drug design, crystal engineering, crystal growth, crystal structure prediction and polymorphism.<sup>52</sup> The importance of this information led to the compilation of all known crystal structures in the form of the Cambridge Structural Database (CSD) which began in 1965 with fewer than 1000 structures.<sup>52</sup> As of 2021 the CSD now contains over 1,150,000 crystal structures of small organic and metal-organic compounds, with a growth rate of around 50,000 structures added each year.<sup>53, 54</sup> The database records cell dimensions, space group, atomic coordinate data, bibliographic information and chemical information.

The CSD also has software tools to search through, visualize and analyse this structural information. *ConQuest* allows the searching of the CSD by either text, structural formula or numerical methods. *Mercury* is used to view the three-dimensional crystal structures; this includes displaying networks of intermolecular interactions. *Mogul* can perform substructure searches using fragments of molecules including the angles and acyclic torsions, which helps understand intramolecular interactions. *IsoStar* provides information on where the contact group tends to be positioned around the central group and the frequency of interactions between two groups, which helps understand intermolecular interactions.<sup>52</sup> All of this software provides a way of investigating and comparing different crystal structures and using the information gathered to design new potential structures.<sup>55</sup> Also, the large size of the database allows statistical analysis of trends in molecular and crystal structures. Furthermore, the CSD is a useful resource to find binding characteristics in crystal structures to inform predictions of crystal packing. The CSD can be used to compare measured unit cells against the reported value to check for novel crystal structures.<sup>56</sup> An example of a study that can be performed using the CSD was by Infantes *et al.*<sup>57</sup> where a database study was undertaken to find the trends in hydrate formation. Using the CSD, it was found that the ratio of hydrogen bond donor to acceptor groups does not affect the frequency of hydrate formation but an increase in the sum of donor and acceptor groups increases the frequency of hydrate formation.

#### 1.1.4 Polymorphism

The term polymorphism comes from the Greek word for “many forms”.<sup>58</sup> Polymorphism in terms of crystallization is the ability of a solid material to exist in more than one crystal form but decompose to identical liquid and vapour states.<sup>59</sup> These different polymorphs can have varying properties including solubility, dissolution rates, melting points, conductivity, chemical activity, tensile strength, optical activity, flowability, toxicity, tableting, bioavailability and spectroscopic properties.<sup>60</sup>

One type of polymorphism can be caused by different crystal packing which is called packing polymorphism. A second type is conformational polymorphism which arises from the rotation of a single bond causing a change in the molecular conformation and hence in the overall crystal structure.<sup>58</sup> When two or more different polymorphs form from the same solution and under the same conditions they are described as concomitant polymorphs.

Polymorphs can transform into different forms via temperature changes, pressure changes, solvent-mediated transformation, time, or mechanical shock. This is due to different polymorphs having different amounts of free energy. The form with the lowest free energy under a given set of conditions is called the thermodynamic form and the other forms are usually metastable forms with a local free energy minimum. If a system is monotropic one polymorph is always thermodynamically stable and the other is always metastable (Figure 1.10). If a system is enantiotropic the thermodynamically stable polymorph changes with one polymorph more stable below the transition temperature and another more stable above the transition temperature (Figure 1.10).<sup>61, 62</sup> The thermodynamically stable polymorph can vary in different solvents due to the different polymorph having varying solubilities, therefore to screen for new polymorph an extensive study using different solvents and crystallisation methods is required.<sup>63</sup> One method to screen for new polymorphs is high throughput crystallisation which involves setting up lots of small scale crystallisation with a variety of different conditions including solvents and crystallisation methods, to produce a large library of initial characterisation data.<sup>64</sup> Interestingly the supersaturation ratio is important for the formation of polymorphs, with a metastable form of carbamazepine forming when the supersaturation ratio is higher due to the lower interfacial energy of the metastable form.<sup>65</sup> At a lower supersaturation ratio

thermodynamics were more important, therefore the more thermodynamically stable form was obtained.

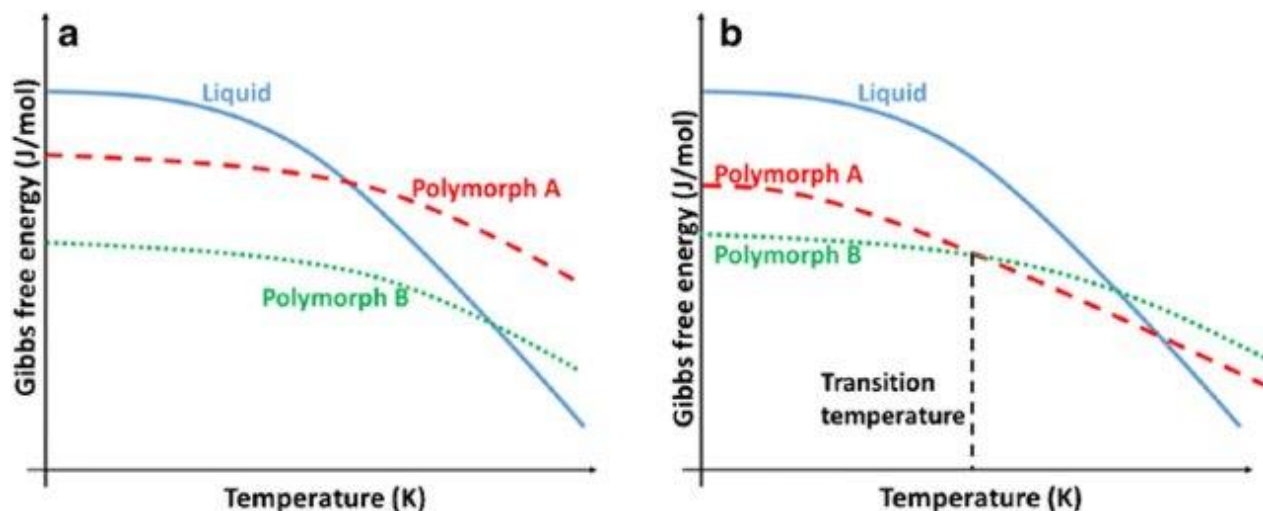


Figure 1.10: The Gibbs free energy diagrams for (a) monotropic and (b) enantiotropic conditions. For (a) polymorph B is the most stable across the temperature range. For (b) below the transition temperature polymorph B is the stable polymorph, however, above the transition temperature polymorph A is more stable. Reproduced with permission from reference 61.

The type of polymorph formed can be very important to the pharmaceutical industry. An example of changing the polymorphic form on its pharmaceutical importance is lornoxicam which has at least two polymorph forms with form II being more soluble than form I so the second form is more suitable for oral dosage forms.<sup>66</sup> Therefore it is key for pharmaceutical companies to aim to use the most beneficial form and try to prevent change as a polymorph change could reduce the solubility of the active pharmaceutical ingredient which could reduce or increase the absorption dosage giving a different therapeutic outcome.<sup>67</sup>

## 1.2 Multicomponent Solid Forms

### 1.2.1 Overview

Improving the properties of the solid form of a particular active pharmaceutical ingredient (API) without altering the API itself is very important in the pharmaceutical industry. In these cases, a second component can be mixed with the API which alters the formation of the solid form, changing the free energy of the system.<sup>42, 68-70</sup> The change in free energy of the system leads to different properties of the system such as different solubility, melting

point, stability, compressibility and many more properties important to the pharmaceutical application. The main multicomponent solid forms important for the pharmaceutical industry include co-crystals, hydrates, solvates, salts and amorphous solid dispersions (Figure 1.11, Figure 1.12).

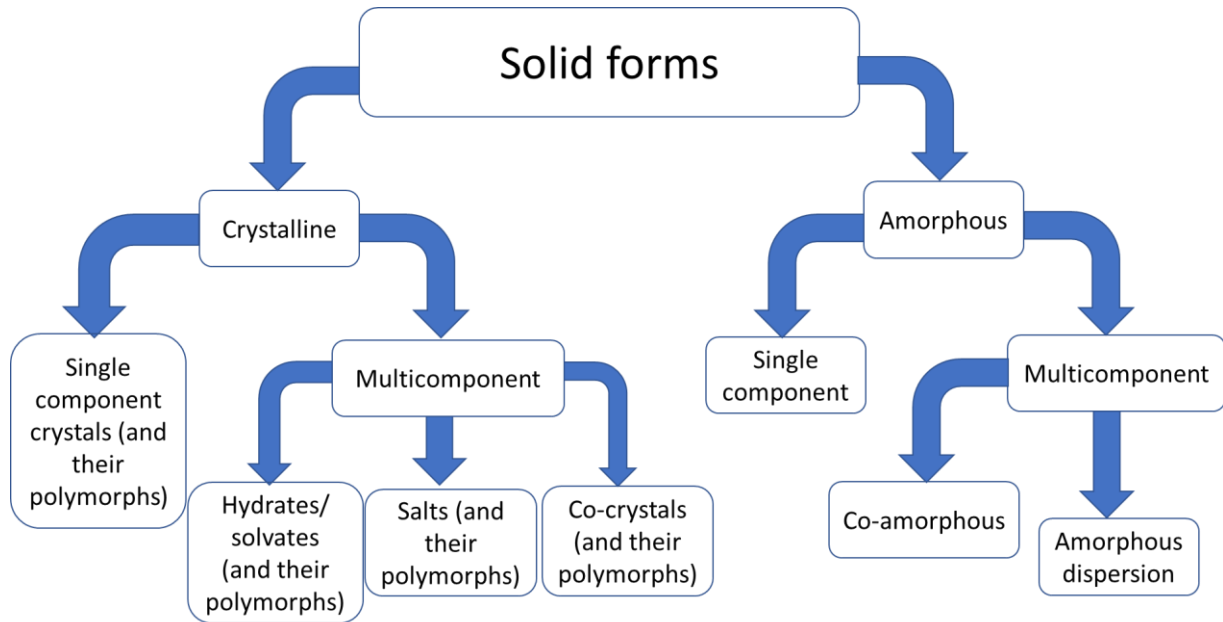


Figure 1.11: A scheme showing the division of solid forms. Modified from reference 69.



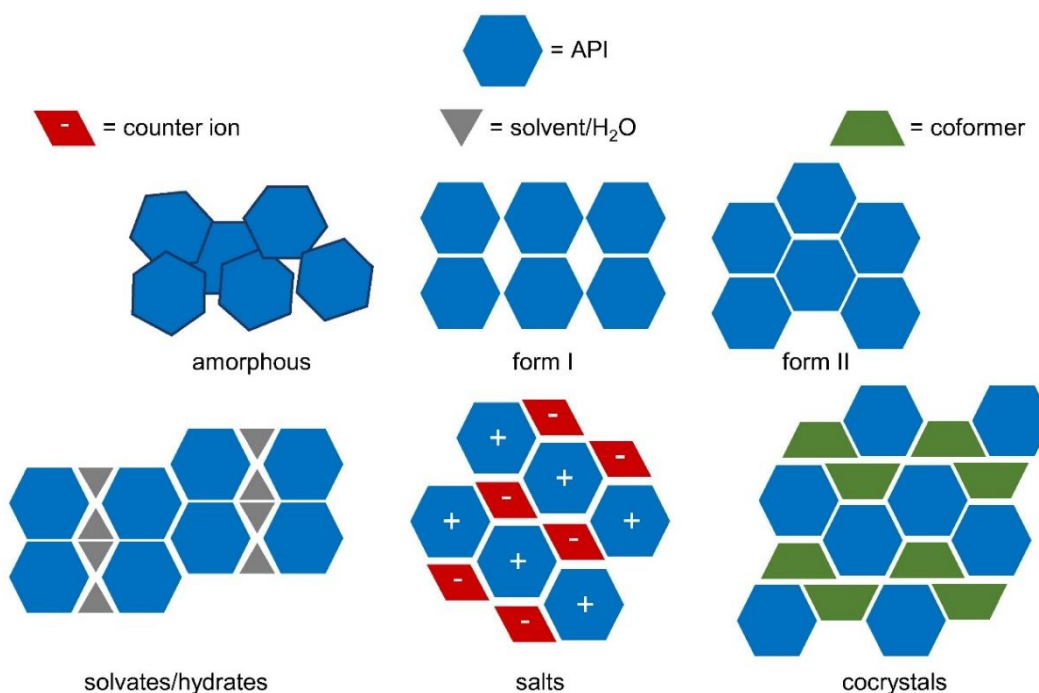


Figure 1.12: Simplified images of the different solid forms of APIs including an amorphous form, two different polymorphic forms, a solvate/hydrate, a salt, and a co-crystal.

Reproduced with permission from reference 70.

### 1.2.2 Co-crystals

A co-crystal (Figure 1.12) was defined by Grothe *et al.*<sup>71</sup> as “a crystal with a co-former molecule plus either another co-former or at least two ions”. This can be broken down into four key groups which are: true co-crystals which contain only co-formers, co-crystal solvates which contain one or more solvents and two or more co-formers but no ions, co-crystal salts which contain one or more co-formers and two or more ions but no solvents and co-crystal salt solvates which contain one or more solvents, two or more ions and one or more co-formers.<sup>42, 72</sup> It was believed that co-crystals could control polymorphism in APIs by locking the APIs in specific bonding structures, however it has been proven by Cruz-Cabeza *et al.* that polymorphism is just as likely in co-crystals as it is in single component systems.<sup>73-75</sup>

The formation of co-crystals is based on hydrogen bonding and other intermolecular interactions between the components. Co-crystals can have different properties compared to the components as the intermolecular interactions are different, causing a new crystal structure to form.<sup>76</sup> A co-crystal is usually formed from an API and co-former connected by

weak hydrogen bonds that can break easily and dissociate in a biological medium.<sup>77</sup> The co-former is usually the more water soluble component, therefore it is drawn out of the crystal lattice and dissolved, leaving behind the hydrophobic API. The hydrophobic API becomes supersaturated in the solution and forms an unstable metastable state which can precipitate lowering the dissolved API concentration. The rapid increase in API concentration is therefore followed by a rapid decrease in drug concentration which is known as the “spring” effect (Figure 1.13).<sup>78</sup> The high concentration can be maintained in the solution by the use of a co-former which inhibits the crystallisation of the system causing a “parachute” effect where the concentration of the drug in solution slowly drops after the “spring”.<sup>79</sup> The “spring and parachute” effect has been shown by a range of co-crystals with an imidazopyridazine antimalarial API.<sup>80</sup> The co-crystal formed with adipic acid underwent the “spring” effect suggesting adipic acid could not prevent the API from recrystallising, however when the co-former was changed to fumaric or glutaric acid the powder dissolution profiles showed that the systems underwent a “spring and parachute” effect, suggesting the glutaric and fumaric acid could stabilise the metastable API state.

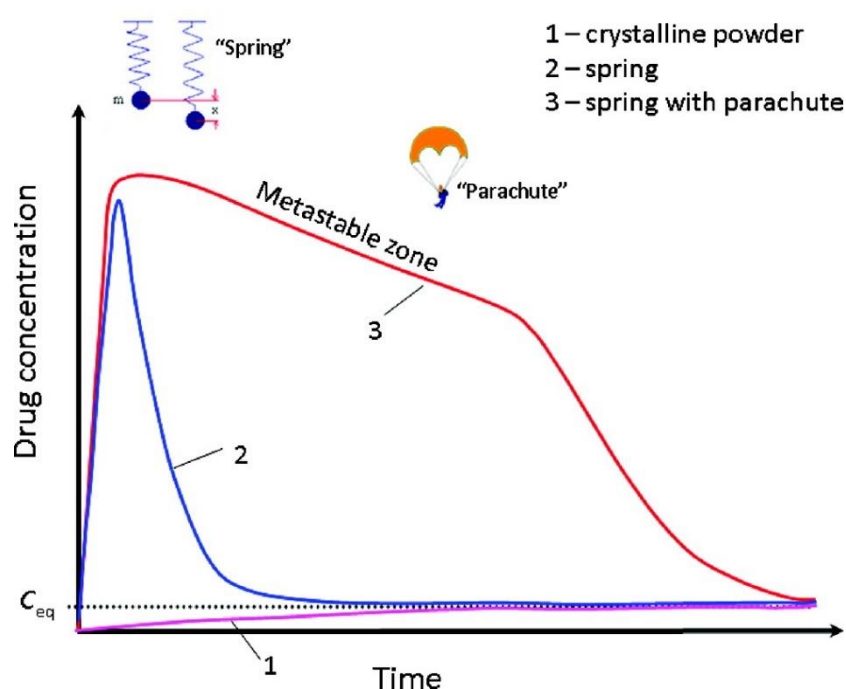


Figure 1.13: A graph of drug concentration against time showing the “spring” and “parachute” effects. (1) The crystalline powder is stable and has low solubility. (2) The “spring” effect shows a rapid increase in drug concentration which quickly drops to the equilibrium concentration ( $C_{eq}$ ). (3) The “spring” effect is followed by the “parachute” effect,

showing a rapid increase in drug concentration which gradually drops over a long time. Reproduced with permission from reference 79.

The key advantage of co-crystals is that they can have different properties to their constituent components. The co-crystals formed are intrinsically stable crystalline structures meaning they shouldn't change during storage; therefore, they are safer for consumption. Also, as the list of potential co-formers is very large many different co-crystals could potentially be designed to improve the chemical properties of active pharmaceutical ingredients (APIs) without affecting the pharmaceutical benefit. An example of a co-crystal with improved properties, when compared with the original API, is a carbamazepine-saccharin co-crystal. The resulting co-crystal has improved solubility and bioavailability showing the value of co-crystals to the pharmaceutical industry.<sup>81</sup> Other drug properties that can be altered include melting point, stability to relative humidity, mechanical properties, and different polymorphic forms can be produced.<sup>82</sup> Furthermore, certain co-crystals can be produced in an environmentally friendly process using non-solvent production methods and the co-crystals can be designed to use materials that are easily acquired and green to produce.<sup>83</sup>

### 1.2.3 Hydrates and Solvates

A hydrate (Figure 1.12) is a form of a co-crystal in which one of the components is water.<sup>84</sup> Hydrates can be split into stoichiometric or non-stoichiometric hydrates. Stoichiometric hydrates have crystal structures containing water in well-defined lattice sites and if the water is removed the crystal structures become unstable and collapse forming a new crystal phase or an amorphous phase. In non-stoichiometric hydrates, the water content can change without changing the crystal structure and the ratio of water to the host molecule is not always an integer.

Hydrates can be split further based on their structural aspects: isolated site hydrates, channel hydrates, ion-coordinated hydrates, and clathrate hydrates.<sup>85</sup> Isolated site hydrates are where the water molecule isn't in contact with another water molecule and only interacts with the host molecules or counterions. Channel hydrates contain channels of water running through the crystal structure and removal of the water may cause a crystal structure to collapse. Ion-coordinated hydrates contain water molecules loosely bonded to a

metal ion or crystallized with a metal complex and include salts of organic acids or purely inorganic hydrates. Clathrate hydrates are formed from cages of water molecules trapping a small polar or non-polar molecule. Some hydrates are capable of forming anhydrous complexes by releasing their water molecules. Common inorganic hydrates include copper sulfate which changes colour from blue in its hydrated form to grey-white in its anhydrous form and cobalt chloride which is purple when hydrated and sky blue when anhydrous. Some inorganic complexes can absorb water over time causing them to change colour.

Pharmaceutical hydrates and solvates are crystalline solids of an API and either water molecules for hydrates or solvent molecules for solvates, incorporated in the crystal structure.<sup>86</sup> The process of formation involves using water or organic solvents as the solvent for crystallisation. The change of properties is caused by the addition of the solvent molecules changing the unit cell dimension, shape and symmetry.<sup>87</sup> Hydrates are important in the pharmaceutical industry as the addition of water to the crystal structure can cause changes in properties such as bioavailability, solubility, dissolution and chemical and physical stability. An example of an API that forms a hydrate is carbamazepine which can be transformed into a dihydrate form when at 37 °C in the presence of water vapour. The anhydrous form of carbamazepine was found to have better solubility and bioavailability when compared with the dihydrate.<sup>88</sup> The carbamazepine example shows that hydrates don't always have more desirable properties and one of the aims could be to prevent the hydrate formation if undesirable.

#### 1.2.4 Salts

Salts are two component systems similar to co-crystals with the key difference being that in a salt a proton is transferred from a donor to an acceptor to create two charged species a cation and an anion, compared to a co-crystal where the hydrogen atom is involved in hydrogen bonding but is not transferred (Figure 1.12).<sup>89, 90</sup> Whether a multicomponent system forms as a co-crystal or salt can be predicted using the difference in  $pK_a$  between the two components, with a difference greater than 3 indicating salt formation is expected.<sup>91</sup> The majority of APIs are weak acids or bases, therefore salt formation can occur by mixing the API with a suitable counter ion.<sup>92</sup> Salts are very important in the pharmaceutical industry due to them increasing the solubility of a poorly soluble API.<sup>93</sup> The increased solubility of the salt in an aqueous solution is due to the strong interactions between the ionized molecules

and water molecules.<sup>94</sup> The formation of salts can also be useful when no known crystal forms of the pure API have been identified, with the salt expected to have greater stability compared to an amorphous state.

#### 1.2.5 Amorphous Forms

An amorphous form is defined as a non-crystalline system with no long-range order or repeating crystal lattice.<sup>95</sup> Amorphous forms have fewer and less optimal intermolecular interactions compared to the crystalline form, meaning the amorphous form will always have higher free energy, therefore amorphous materials will convert to crystalline solids if enough energy is provided to overcome the activation barrier. The higher free energy of the amorphous system changes the properties relative to the crystalline form, with the amorphous form having a higher solubility and lower stability. One of the key characteristics of an amorphous system is its glass transition temperature ( $T_g$ ), which is the temperature below which an amorphous system exists as a glassy solid and above as a supercooled liquid.<sup>96</sup> For a crystalline material the system has a melting temperature ( $T_m$ ) and upon gradually cooling a molten solution, the molecules rearrange into an orderly system reducing the free energy of the system. However, if the system is rapidly cooled below its  $T_m$  without crystallising it forms a supercooled liquid state and continued cooling leads to the  $T_g$  where the supercooled liquid is frozen (Figure 1.14). A  $T_g$  is necessary because if the system remains as a supercooled liquid below the  $T_g$  it will reach a temperature where the supercooled liquid would have lower entropy than the crystalline system, which means the entropy would eventually become negative before zero kelvin violating the third law of thermodynamics.<sup>97</sup> The amorphous system provides an initial increased solubility called a “spring” (Figure 1.13) as discussed for co-crystals however the amorphous system recrystallises in the process of devitrification which decreases the solubility.<sup>79</sup>

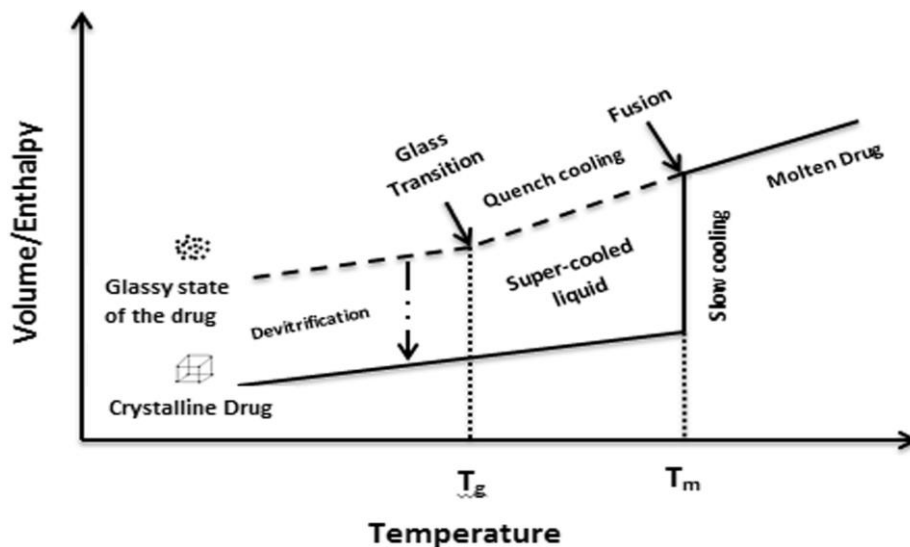


Figure 1.14: Enthalpy and volume of a drug in both a crystalline and amorphous state as a function of temperature. Reproduced with permission from reference 96.

Amorphous systems are usually avoided in the pharmaceutical industry due to the low stability of the system during storage.<sup>86, 98</sup> To increase the stability the API can be dispersed in a polymeric matrix forming a polymeric amorphous solid dispersion (PASD) (Figure 1.15).<sup>96</sup> Amorphous forms undergo crystallisation due to the free energy difference between the amorphous and crystalline states. PASDs prevents crystallisation by increasing the entropy of the system and through the formation of energetically favourable intermolecular interaction between the polymer and API.<sup>99</sup> The higher entropy and increased intermolecular interactions result in lower chemical potential of the PASD vs the pure amorphous system, which reduces the thermodynamic driving force.<sup>100-102</sup> The polymers also create a viscous matrix which increases the glass transition temperature reducing the molecular mobility delaying phases separation and crystallisation.<sup>103-105</sup> Common polymers used are polyvinylpyrrolidone, polyvinylpyrrolidone/vinyl acetate and hydroxypropyl methylcellulose.<sup>99</sup> The key issue with PASDs is that they require a high loading of polymer to be effective due to the low miscibility of the polymer and API.<sup>106, 107</sup> Also, if the polymer used in PASD is hygroscopic, meaning it absorbs water from the environment, then the absorbed water can act as a plasticizer increasing molecular movement in the PASD enhancing the phase separation and recrystallization process.<sup>108</sup>

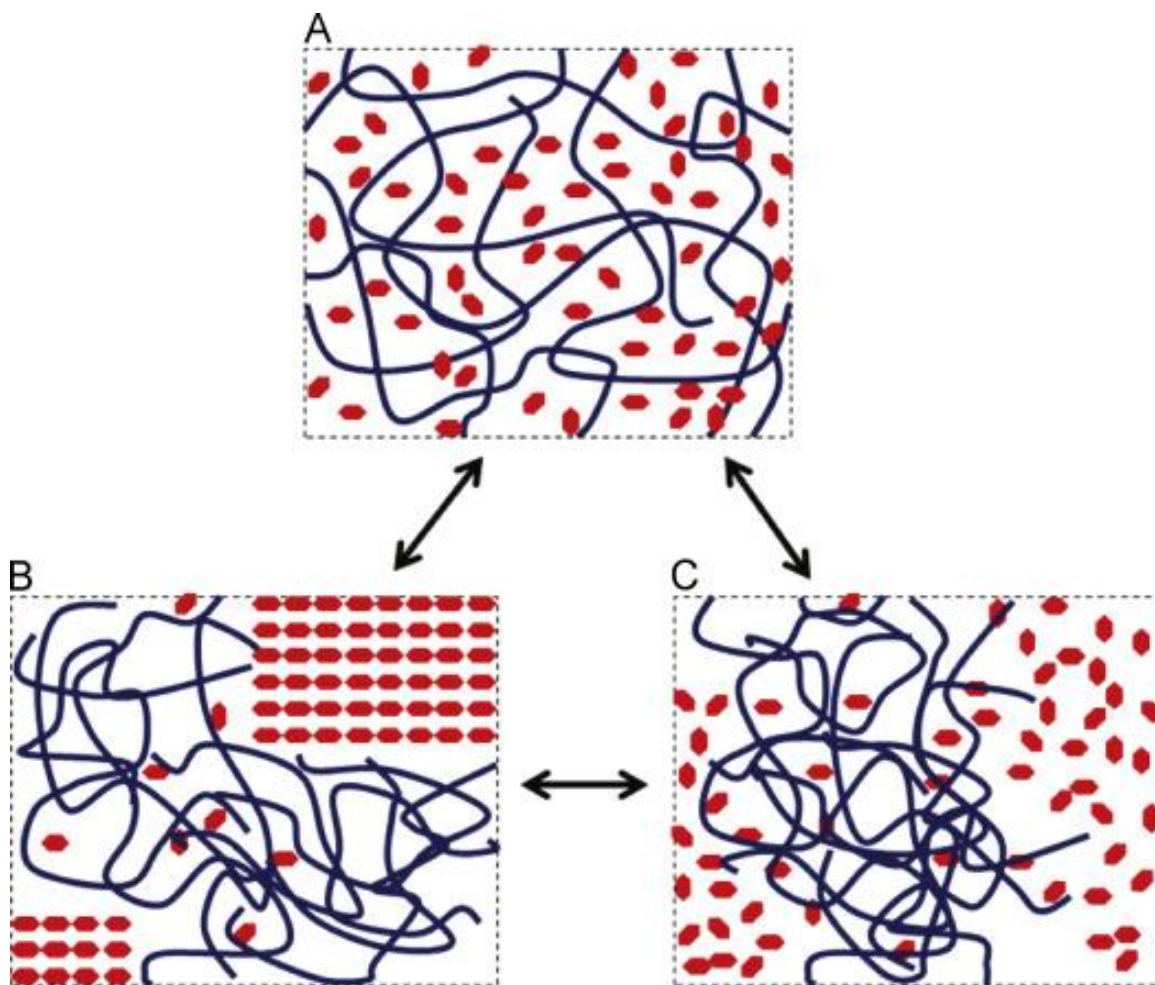


Figure 1.15: The structure of a PASD with the API represented as a red hexagonal and the polymer as curvy lines. Image (A) shows the ideal structure with the API molecularly dispersed in the polymer matrix, (B) shows the phase separation and crystallisation of the API, and (C) shows the phases separation into amorphous API rich domains. Reproduced with permission from reference 98.

### 1.2.6 Co-amorphous Phases

The first co-amorphous (COAM) system was introduced by Chieng *et al.* with a mixture of ranitidine hydrochloride and indomethacin and it was initially labelled as a “co-milled amorphous sample”.<sup>109</sup> A co-amorphous system is defined as a mixture of multiple low molecular weight components in a single-phase homogeneous amorphous system (Figure 1.16).<sup>110, 111</sup> The main research interest for co-amorphous systems is for pharmaceutical products, therefore at least one of the components is usually an API and the other is either an inactive co-former or another API.<sup>112</sup> Co-amorphous systems are of interest to the pharmaceutical industry due to the increased stability of co-amorphous systems compared

to the amorphous system. The co-amorphous systems also help overcome the key issues of PASDs including the hygroscopicity and large ratio of polymer required to stabilise the API.<sup>113</sup>

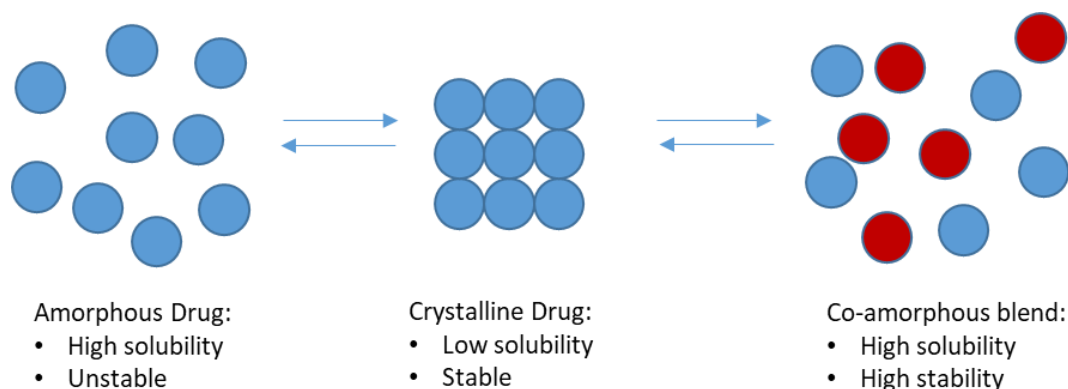


Figure 1.16: The advantages and structure of co-amorphous systems.<sup>114, 115</sup> Reproduced with permission from reference 115.

The stabilization mechanisms of co-amorphous systems include elevated  $T_g$  compared to the pure drug, molecular-level mixing and intermolecular interactions. Intermolecular interactions, including hydrogen bonding, salt formation and  $\pi$ - $\pi$  interactions, were identified by Fourier-transform infrared spectroscopy (FTIR) in a range of co-amorphous systems of carbamazepine and indomethacin with a range of amino acids.<sup>116</sup> A stable co-amorphous system of glipizide and simvastatin was analysed via FTIR and it was found that no intermolecular interactions formed between the two APIs. Therefore, the formation of the co-amorphous system was attributed to the molecular-level mixing of the two components with glipizide speculated to act as an anti-plasticizer.<sup>117</sup> The co-amorphous mixture of ritonavir and indomethacin displayed no intermolecular interactions when analysed by FTIR, therefore the stability of the system was attributed to the increased  $T_g$  compared to pure indomethacin.<sup>118</sup> The combination of valsartan and nicotinamide was shown to produce a co-amorphous system and FTIR was combined with the density functional theory, quantum theory of atoms in molecules and non-covalent interaction index calculations to visualize and reveal the presence of hydrogen bonding.<sup>119</sup>

Co-amorphous systems have been shown to be stable for long periods of time after preparation even at increased temperatures and humidities. A study by Liu *et al.* showed that pure amorphous carvedilol remained stable for 1 week when stored at 40 °C at 55%



relative humidity (RH), however, the co-amorphous mixture formed from a 1:1 molar ratio of carvedilol with *L*-aspartic acid remained amorphous for over 47 weeks.<sup>120</sup>

An interesting study was performed with a ternary amorphous solid dispersion containing two APIs and one polymer.<sup>121</sup> The co-amorphous mixture of flutamide and bicalutamide at a 15:1 ratio (corresponding to the daily doses) was analysed by differential scanning which showed a low  $T_g$  and recrystallisation above the  $T_g$ . Therefore, to stabilize the system a 30% (w/w) concentration of poly(vinylpyrrolidone) was added which increased the  $T_g$ , prevented recrystallization from the supercooled liquid state and the system remained stable at room temperature for at least 182 days.

Co-amorphous systems are known to increase the solubility of a crystalline API in a similar way to co-crystals with the “spring and parachute” effect (Figure 1.13).<sup>122</sup> However, in some cases the rise dissolution rate of the co-amorphous system can be too fast, causing the solution to become supersaturated which results in the API crystallising.<sup>123</sup> One such case involves the system of carvedilol with *L*-aspartic acid, however when it was prepared with 10% (w/w) of hydroxypropyl methylcellulose the initial dissolution rate was reduced but the supersaturation period was maintained for longer, due to the hydroxypropyl methylcellulose preventing recrystallisation.<sup>124</sup>

### 1.3 Characterisation of Solid Forms

The complete characterisation of crystals, co-crystals, polymorphs co-amorphous phases and salts requires a variety of methods including crystallographic, spectroscopic, and thermochemical analysis.

#### 1.3.1 Crystallographic Analysis

The two useful forms of crystallographic techniques for crystal characterisation are single-crystal X-ray diffraction (SXRD) and powder X-ray diffraction (XRPD). SXRD requires a single crystal and it provides chemical composition, geometric information including bond lengths, bond angles and torsion angles, interplanar distances, and geometries of intermolecular and intramolecular bonds.<sup>125</sup> X-ray diffraction involves the scattering of X-rays by the electron distribution of the crystal with atoms of greater electron density contributing more significantly to the diffraction pattern compared to lighter atoms. Amorphous systems cannot be analysed by SXRD due to them not containing a repeating crystalline unit cell.

XRPD requires a microcrystalline powder which makes samples simpler to prepare than the larger single crystals required for SXRD. For single component crystals, XRPD gives a pattern that can be regarded as a fingerprint of the crystal packing arrangement for a given substance.<sup>125</sup> This technique is very useful in assessing co-crystal, salt and polymorph formation by comparing the XRPD patterns of the components to the new structure.<sup>82</sup> The XRPD pattern is a plot of diffraction angle ( $2\theta$  - the angle between the source and detector) against the observed diffraction intensity. The different  $2\theta$  values are correlated with the  $d$  spacing which is the distance between planes of atoms that give rise to diffraction peaks. The technique detects changes between different polymorphs, solvates, salts, co-crystals and it can even be used to identify amorphous materials and co-amorphous phases which give an amorphous 'halo' of scattering rather than discrete Bragg diffraction peaks. XRPD data can be used to derive a structural model in many cases by applying a structure solution and Rietveld refinement method which uses a least squares approach to refine a theoretical line profile until it matches a measured profile.<sup>126</sup> XRPD works with bulk samples whereas SXRD works with a single crystal. Therefore, in SXRD as only one crystal is selected it may not be representative of the bulk sample. As a check on bulk purity, a powder X-ray pattern can be calculated from SXRD data and compared to the experimental XRPD pattern to confirm the single crystal is not an impurity or a different polymorph.

### 1.3.2 Spectroscopic Analysis

Spectroscopic techniques used for crystal structure identification can be split into two key categories vibrational spectroscopy and nuclear magnetic resonance (NMR). Vibrational spectroscopy includes the techniques mid-infrared spectroscopy, near-infrared spectroscopy and Raman spectroscopy. Mid-infrared (MIR) spectroscopy involves the bending and stretching region of infrared (IR) bands. The MIR region is from  $4000-400\text{ cm}^{-1}$  and like near-infrared (NIR) spectroscopy at  $14000-4000\text{ cm}^{-1}$  it is an absorption technique. NIR is comprised of combination and overtone bands with the strongest belonging to OH, CH, NH and SH groups.<sup>125</sup> Both NIR and MIR can be used to monitor changes in crystal structure and the formation of different solid forms including identifying intermolecular interactions formed in co-amorphous systems.<sup>116</sup> Raman spectroscopy involves using a laser light source to irradiate a sample that generates scattered light. The laser light can be scattered in an elastic or inelastic way.<sup>127</sup> Elastic scattering is called Rayleigh scattering and

is caused by the photon absorbed having the same frequency as the photon emitted. Inelastic scattering is called Raman scattering and is caused by the photon absorbed having a different frequency to the photon emitted. The difference is caused by a change in the vibrational energy level of the sample. This change causes Stokes lines which are caused by the incident radiation having a lower frequency compared to the frequency of scattered radiation and anti-Stokes lines are caused by an increase in frequency for the scattered radiation. Therefore, to observe these small differences in frequency, a monochromatic light source is required such as a laser because if a non-monochromatic light source is used the Stokes and Anti-stokes lines will be harder to identify. The Raman measurement can cover the range of 4000-40  $\text{cm}^{-1}$ . Raman analysis can be performed through glass and plastic packaging allowing monitoring of samples or reaction media in a non-destructive fashion.<sup>125</sup> Raman spectroscopy is very useful in analysing crystals as it can monitor phase transformations and crystallisations. It also helps in evaluating if a new solid form is present if the new form has characteristic Raman bands that are different to the individual components.<sup>82</sup>

In solution state NMR spectroscopy the spectra recorded are a series of sharp transitions due to the averaging of anisotropic NMR interactions by rapid random tumbling. With solid-state (SS) NMR the effects of anisotropic or orientation-dependent interactions are observed which cause broad lines in the spectra. To overcome this problem high-resolution NMR is used which requires a number of special techniques which minimize anisotropic NMR interactions between nuclei. The techniques are magic-angle spinning, dilution, multiple-pulse sequences and cross polarization. Magic-angle spinning involves rapidly spinning the sample at an angle of  $54.74^\circ$  with respect to the external magnetic field. The spinning causes the three interactions of dipolar coupling, chemical shift anisotropy and quadrupolar interaction to be averaged out.<sup>128</sup> Dilution is the decrease in the amount of NMR active isotopes which means using isotopes with naturally low abundance such as carbon 13, dilution helps prevent homonuclear dipolar interactions which stops the spectra from broadening. Certain magnetic nuclei can have an effect on other NMR active nuclei and this is called coupling. To reduce coupling a multiple-pulse sequence is used which decouples the interactions between heteronuclear nuclei. Cross polarization involves the transfer of polarization from abundant nuclei such as  $^1\text{H}$  to dilute spins such as carbon-13.<sup>129</sup>

SS NMR is useful for crystal characterisation as the peak positions and intensities can be used to find the composition of the molecule which forms the crystal. SS NMR provides information on the local environment of the molecule so it can be used for studying disorder, guest dynamics and amorphous systems which differs from long-range averaging observed by diffraction methods.<sup>130</sup> NMR crystallography is important as it is a method that uses NMR experimental data and quantum chemistry calculations for structure determination, refinement or selection.<sup>130</sup> It is mainly used as a replacement for SXRD if a suitable crystal can't be grown or if the SXRD doesn't appear to be representative of the bulk sample.<sup>130</sup>

### 1.3.3 Thermal Analysis

Thermal analysis includes techniques that monitor the physical or chemical changes of a sample against a change in temperature versus time. The three main thermal analysis techniques used for solid form analysis are differential scanning calorimetry (DSC), thermogravimetric analysis (TGA) and hot-stage microscopy (HSM). DSC involves recording the heat flow required to keep a sample and reference at the same temperature and plotting the heat flow against time or temperature. If the sample undergoes an exothermic process more heat needs to be supplied to the reference to maintain the same temperature and the opposite is true for an endothermic process. This allows the difference in heat flow to be recorded between the sample and reference during phase transitions. DSC can, therefore, be used to identify phase transitions such as glass transitions, melting and polymorph transformation also it can be used as a determination of crystallinity.<sup>125</sup> It can be used to identify co-crystal formation or the existence of eutectic mixing due to the reduced melting point. Co-amorphous material can be identified using DSC with a heating, cooling and heating process. The initial heating of two individual components displays a melting point of both components but if upon cooling no crystallisation process is detected, then a second heating cycle shows a single glass transition temperature and no melting point the final material is likely to be a co-amorphous phase.

TGA involves recording the mass change of a sample in a controlled atmosphere.<sup>125</sup> TGA can be used to monitor thermal stability by increasing or decreasing the temperature and monitoring the effect on the mass of the sample. The water absorbance or loss of hygroscopic materials or hydrates can also be monitored using TGA by keeping the

temperature constant and monitoring the mass change over time. TGA is useful for monitoring the stability of co-crystals as it can record decomposition temperatures. The retention of water molecules in hydrates can also be analysed.

HSM involves heating and cooling a few milligrams of material on a microscope slide and analysing it visually by using an attached microscope.<sup>125</sup> The heating is controlled by a metal element that heats the slide and water or liquid nitrogen-based cooling. The microscope allows visualizing of the melting point, melting ranges, crystal melt and growth.<sup>82</sup> This method allows analysis of co-amorphous phase formation when paired with a polarizer as it can show no crystallisation upon cooling a melted mixture of at least two materials that usually crystallize.

## 1.4 Production Methods for Solid Forms

### 1.4.1 Crystallisation Methods

New potential co-crystals and salts can be discovered in many ways including serendipitous discoveries or by matching complementary functional groups.<sup>131</sup> However, more advanced computational methods are becoming more important in co-crystal and salt discovery. The Cambridge Structural Database can be used to predict the success of co-crystal formation by calculating the hydrogen bond propensity between the reactants. The results are given in the form of an estimate of the chance of the co-crystallisation being successful.<sup>131</sup> The liquid phase thermodynamics theory COSMO-RS (Conductor-like Screening Model for Real Solvents) has also been shown to be useful for predicting the viability of different co-formers with a defined active ingredient.<sup>132</sup> COSMO-RS works by first calculating the polarization charges on the COSMO surface for the co-former and active ingredient.<sup>133</sup> The intermolecular interactions are then calculated by using the local contacts of the COSMO surfaces and quantified by the polarization charge densities  $\sigma$  and  $\sigma'$  of the two surfaces. The simulation then derives the macroscopic properties from an ensemble of the surface segments of the interacting molecules. The macroscopic properties provided are the free energy, chemical potential and all related physio-chemical properties of the mixed system. The COSMO-RS theory only takes into account the most important molecular interactions, electrostatics, hydrogen bonding and Van der Waals interactions.<sup>133</sup> To use this data to calculate co-crystal formation the mixing enthalpy is used which relies on the enthalpy of the co-crystal and the enthalpies of the individual components and their mole fraction. The

entropy of mixing is assumed to be close to zero which is usually a reasonable assumption for crystalline materials.<sup>133</sup> The number of rotatable bonds of the active ingredient and the co-former also affects the formation of co-crystals, therefore, it is taken into account to calculate a co-former ranking. The co-former ranking is just a numerical system ranking the chance of a co-crystal forming, with 1 being a high chance, relative to the other co-formers.

To physically prepare co-crystals and salts, there are a variety of different methods including solvent based and solid based methods. Solution crystallisation for co-crystal formation requires two components with similar solubility in a solvent otherwise one would precipitate out in preference. One method is cooling crystallisation, where the components are dissolved into a heated solution, the solution is then cooled in a controlled manner. The rate of cooling influences crystal size with larger crystals typically occurring with a slower cooling rate. The cooling rate can also affect which polymorphs grow if the crystal is capable of forming different polymorphs.<sup>72</sup> Larger crystals can be formed once the solution has cooled by slowly raising and lowering the temperature by a few degrees in a repeated cycle, this can be useful for generating crystals for SXRD.<sup>134</sup>

Co-crystals and salt can be formed by using a slurry technique. This technique involves slurries of physical mixtures of both components and requires high concentrations of each of them. The mixture will then start to form co-crystals or salts via a solution mediated phase transformation, this process continues until the activity of either component reaches its critical value.<sup>135</sup> An example of this technique is the formation of a co-crystal of caffeine and 2-hydroxy-1-naphthoic acid. The slurry method produced co-crystals where other methods failed.<sup>135</sup>

Evaporative crystallisation works by first dissolving the components into a solution that can be heated to help them dissolve. The solution is then left to slowly evaporate causing the concentration of the components to increase until they reach supersaturation and form a crystal.<sup>136</sup> However, this method may result in the formation of crystals of the pure components instead of co-crystals or salts if the two components have very different solubility in solution.<sup>137</sup>

Co-melting co-crystallisation can be performed using a hot stage microscope. One method of co-melting co-crystallisation is the contact method which involves melting the

component with the highest melting point then allowing it to recrystallize by cooling, the second component is then heated and added as molten material to the edge of the first component.<sup>138</sup> The addition causes the solubilisation of the contact area from the first component causing a mixing zone with a concentration gradient going from 100% of one material to 100% of the other material. The mixture is allowed to cool and then reheated. It can then be visualised whilst heating using a light microscope with crossed polar filters to view the number of eutectic melting points in the system. If there are two or more eutectic melting points it means a co-crystal phase should be present. The co-crystal region can be collected and used to seed the production of a co-crystal using a solution based crystallisation method.<sup>138</sup> This method can be scaled up by melting the two components together and cooling them, this should cause the formation of a co-crystal.

Mechanochemical grinding is a method that forms co-crystals or salts by using mechanical energy. In its simplest form the method involves grinding the components together by using manual grinding with a pestle and mortar or via automated methods such as ball milling. The key drawback with the process is there might not be enough energy to complete the crystallisation.<sup>139</sup> To overcome the lack of energy liquid assisted grinding (LAG) was conceived which involves using a small amount of solvent to facilitate the reaction. LAG also helps to control polymorphism with different solvents having a preference for different polymorphs.<sup>139</sup>

Interfacial crystallisation is based on the generation of a liquid-liquid interface between two immiscible solutions of co-crystal forming compounds.<sup>140</sup> The co-crystals precipitate at the solvent interfaces due to the interface being supersaturated.<sup>141</sup> Interfacial crystallisation can be used to produce a range of multicomponent crystal forms and it has the potential to be used to screen several potential co-former molecules in one reaction vessel.

Spray drying involves producing a dry powder from a liquid or slurry by rapidly drying. The spray nozzle helps to form controlled droplet sizes. The mechanism for the formation of co-crystals by spray drying isn't fully understood but it is assumed that the co-crystals nucleate and rapidly grow due to evaporating solvents causing more highly saturated regions.<sup>142</sup>

Antisolvent crystallisation involves adding a second liquid to a solution of the two components to induce the supersaturation process. This is due to the two-component

solution being miscible with the new solvent, but the co-crystals or salts are insoluble or barely soluble. The co-crystals or salts then precipitate out due to the supersaturation.<sup>143</sup>

Continuous crystallisation is very important in the pharmaceutical industry as it reduces the variability between batches.<sup>144-146</sup> In continuous crystallisation the mother liquid is continuously added, whilst the final slurry product is removed.

#### 1.4.2 Preparation of Co-amorphous Systems

Mechanochemistry has previously been discussed as a method to produce co-crystal but it can also be used to produce co-amorphous systems.<sup>117, 147</sup> However, the formation of an amorphous system during milling is more favourable when milled below the glass transition temperature, due to the temperature rise when milling inducing crystallisation.<sup>148, 149</sup>

Solvent evaporation methods such as spray drying can also be used to produce co-amorphous systems in a similar way to co-crystals.<sup>150-153</sup> Co-melting can also be used to form co-amorphous systems, which involves melting the components together and then quench cooling to reduce nucleation and prevent crystallisation.<sup>154, 155</sup>

### 1.5 Small Molecule Models

#### 1.5.1 Introduction

To investigate all the different interactions of small molecules with a polymer or protein, a smaller and more controlled system is required. A model is needed due to the large molecular weights and dispersity of the polymer making it hard to visualize and run computer simulations.<sup>156</sup> Furthermore it is harder to crystallise a polymer due to their usual preference of forming an amorphous structure whereas a smaller, more rigid molecule could crystallise and be analysed via diffraction methods. As a monomer is just a single unit of a polymer chain it can be used to model how each individual unit interacts, however as it is only one unit it cannot account for interactions between monomer subunits along the polymer backbone or the cooperation between the adjacent monomer units. To overcome the limits of a monomer a dimer or a larger section of the polymer chain can be used as it provides insight into the binding of the substrate by adjacent monomer units. The same logic can be applied to a protein chain with an amino acid acting as a small molecular model. Small molecule models of the poly(lactams) poly(vinylpyrrolidone) and poly(vinylcaprolactam), formed from two monomer units, have been used to help analyse



interactions in different areas of research including the oil and gas industry, and the pharmaceutical industry.<sup>157</sup> The small molecules have also found new uses related to their analogous polymers which includes new pharmaceutical co-amorphous phases.

### 1.5.2 Povidone-iodine

Povidone-iodine is a complex of poly(vinylpyrrolidone) (PVP) and iodine discovered in 1949<sup>158</sup> and is an essential medicine according to the World Health Organization's list.<sup>159</sup> Its antiseptic properties are caused by the slow release of free iodine from the complex, which goes on to kill eukaryotic and prokaryotic cells. The structure was originally thought to contain a proton which is hydrogen bonded to the two carbonyl groups and a triiodide anion that is bound to the proton (Figure 1.18).<sup>160</sup> This structure was refined by Goodwin *et al.*<sup>161</sup> based on the X-ray crystal structure of a dimeric model compound (H<sub>2</sub>bisVP) (Figure 1.17) which showed that the structure was better represented as involving intermolecular hydrogen bonding between separate polymer chains rather than an intramolecular hydrogen bond between adjacent monomer units (Figure 1.19). This paper was only published in 2017 suggesting there is still a lack of understanding of how lactams interact in complexes even with essential medicines. This example shows how the small molecule models can assist understanding of the interaction with lactam based polymers.

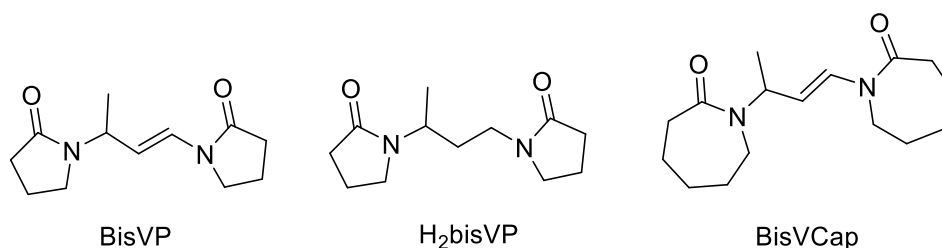


Figure 1.17: Chemical structures of bisVP, H<sub>2</sub>bisVP and bisVCap.

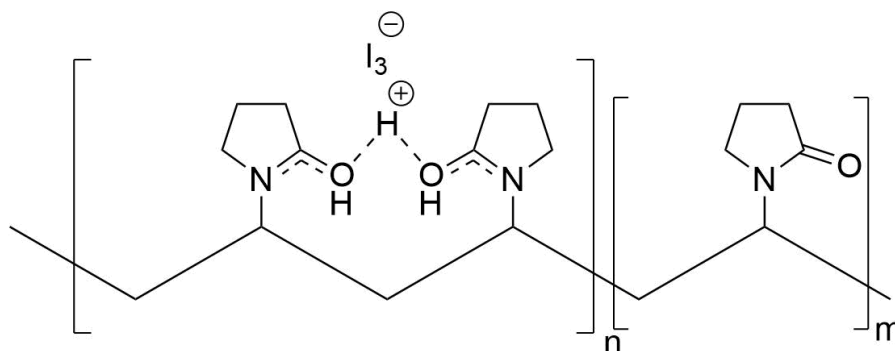


Figure 1.18: Originally proposed structure of povidone-iodine.<sup>161</sup>

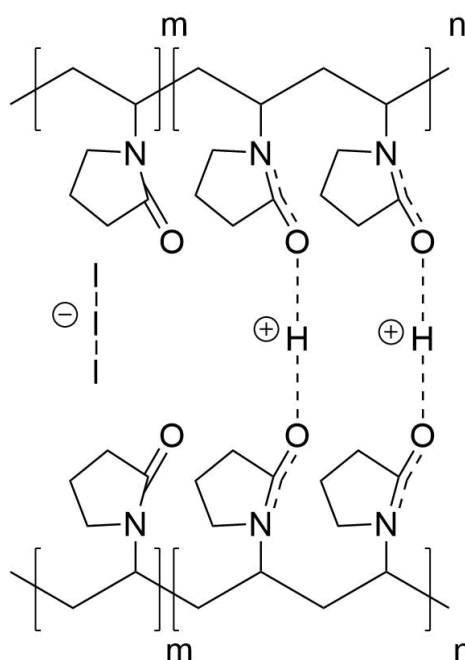


Figure 1.19: Revised structure of povidone-iodine showing bridging between two PVP chains.<sup>161</sup>

### 1.5.3 Co-amorphous Pharmaceutical Phases

As previously discussed in section 1.2.5 PVP is used in PASDs to stabilise amorphous forms. A co-amorphous screen was performed using bisVCap and the dimer of poly(vinylpyrrolidone) (bisVP) (Figure 1.17) with a range of APIs.<sup>154</sup> The screen involved melting the two components together in a 1:1 molar ratio on a glass slide, leaving them to cool overnight and then checking for crystallisation using a microscope (Figure 1.20). In some of the systems, bisVCap is shown to stabilise the API in an amorphous state as shown by the lack of recrystallisation. The samples showing no crystallisation were further analysed via DSC, XRPD and IR to leave the stable co-amorphous mixtures. Carbamazepine,

carisoprodol, isoniazid and 5-methyl-2-[(2-nitrophenyl)amino]-3-thiophenecarbonitrile (ROY) all proved to form stable co-amorphous materials.

Substance	No coformer	bisVCap	bisVP
Benzocaine			
Caffeine			
Carbamazepine			
Carisoprodol			
Dopamine			
Ethionamide			
Ibuprofen			
Isoniazid			
Metformin			
Mexiletine			
Tolfenamic Acid			
Valsartan			

Figure 1.20: Microscopy images of APIs and the co-formers, showing the stabilisation effects.<sup>154</sup> The bisVCap is shown to stabilise more APIs when compared with bisVP and no co-former. Reproduced with permission from reference 154.

## 1.6 Project Aims and Overview

The aims of this work are split into three key sections. Section one which is covered with Chapters 2 and 3, aims to design and test a method to predict the likelihood of an API and co-former forming a co-amorphous system. Chapter 2 is based on using statistical methods to build up a prediction model using the results from a large co-amorphous screen.<sup>162</sup> Chapter 3 involves testing the prediction model from Chapter 2 with bisVCap as the co-former using the results from a previous screen by Goodwin *et al.* and a new extensive co-amorphous screen.<sup>154</sup>

Section two is covered in Chapter 4 and is based on using H<sub>2</sub>bisVP as a model for PVP to identify the bonding structure present in a PVP hydrogen peroxide complex.<sup>163, 164</sup> To achieve this three different molecular weight pairs of PVP and PVP hydrogen peroxide complex will be analysed by Fourier transform Infrared spectroscopy (FTIR) and <sup>13</sup>C SS-NMR to understand the intermolecular interactions, and by elemental analysis and permanganate titrations to determine the amount of hydrogen peroxide present. Co-crystals of H<sub>2</sub>bisVP with hydrogen peroxide will be analysed by SXRD to determine the structure. The structure of the co-crystals will be used to give insight into the potential bonding structure present in the PVP hydrogen peroxide complex.

Section three, covered in Chapters 5 and 6, is based on the haircare mixture formed from a gluconamide and the corresponding gluconate salt, which strengthens hair fibres.<sup>165-167</sup> Chapter 5 is based on understanding how the haircare mixture interacts with the amino acids present in keratin protein by producing salts and co-crystals to speculate how the strengthening process occurs. Chapter 6 is based on understanding the formation of supramolecular gels with the gluconamide in a range of solvents.

## 1.7 References

1. R. Davey and J. Garside, *From molecules to crystallizers*, Oxford University Press, New York, USA, 1st edn., 2000.
2. A. R. Parsons, S. N. Black and R. Colling, *Chem. Eng. Res. Des.*, 2003, **81**, 700-704.
3. A. Jaiswal and D. Sarkar, *Cryst. Res. Technol.*, 2015, **50**, 347-353.
4. K. Hanaki and I. Hirasawa, *J. Chem. Eng. Japan*, 2009, **42**, 386-392.
5. M. Barrett, M. McNamara, H. Hao, P. Barrett and B. Glennon, *Chem. Eng. Res. Des.*, 2010, **88**, 1108-1119.
6. M. Nishimaru, S. Kudo and H. Takiyama, *J. Chem. Eng. Japan*, 2019, **52**, 579-585.

7. S. Kaneko, Y. Yamagami, H. Tochihara and I. Hirasawa, *J. Chem. Eng. Japan*, 2002, **35**, 1219-1223.
8. J. McGinty, N. Yazdanpanah, C. Price, J. H. ter Horst and J. Sefcik, *Chapter 1 Nucleation and Crystal Growth in Continuous Crystallization*, in *The Handbook of Continuous Crystallization*, The Royal Society of Chemistry, Croydon, UK, 1st edn., 2020, pp. 1-50.
9. M. Giuliatti, M. M. Seckler, S. Derenzo, M. I. Ré and E. Cekinski, *Braz. J. Chem. Eng.*, 2001, **18**, 423-440.
10. D. Erdemir, A. Y. Lee and A. S. Myerson, *Acc. Chem. Res.*, 2009, **42**, 621-629.
11. P. G. Vekilov, *Cryst. Growth Des.*, 2004, **4**, 671-685.
12. S. Karthika, T. K. Radhakrishnan and P. Kalaichelvi, *Cryst. Growth Des.*, 2016, **16**, 6663-6681.
13. H. Cölfen and M. Antonietti, *Mesocrystals and Nonclassical Crystallization*, John Wiley & Sons, Ltd, Chichester, UK, 1st edn., 2008.
14. P. G. Vekilov, *Nonclassical Nucleation*, in *Crystallization via Nonclassical Pathways Volume 1: Nucleation, Assembly, Observation & Application*, American Chemical Society, Washington, USA, 1st edn., 2020, vol. 1358, ch. 2, pp. 19-46.
15. M. A. Durán-Olivencia, P. Yatsyshin, S. Kalliadasis and J. F. Lutsko, *New J. Phys.*, 2018, **20**, 083019-083019.
16. B. Jin, Z. Liu and R. Tang, *Cryst. Eng. Comm.*, 2020, **22**, 4057-4073.
17. C. Li, Z. Liu, E. C. Goonetilleke and X. Huang, *Nat. Commun.*, 2021, **12**, 4954.
18. H. J. Schöpe, G. Bryant and W. van Megen, *Phys. Rev. Lett.*, 2006, **96**, 175701-175701.
19. P. G. Vekilov, *Nanoscale*, 2010, **2**, 2346-2346.
20. P. G. Vekilov and M. A. Vorontsova, *Acta Cryst. F*, 2014, **70**, 271-282.
21. D. Gebauer and H. Cölfen, *Nano Today*, 2011, **6**, 564-584.
22. J. Cookman, V. Hamilton, S. R. Hall and U. Bangert, *Sci. Rep.*, 2020, **10**, 19156.
23. J. C. Mergo III and J. Seto, *Front. Mater.*, 2020, **7**.
24. M. Bruno, *Cryst. Eng. Comm.*, 2019, **21**, 4918-4924.
25. M. Warzecha, R. Guo, R. M. Bhardwaj, S. M. Reutzel-Edens, S. L. Price, D. A. Lamprou and A. J. Florence, *Cryst. Growth Des.*, 2017, **17**, 6382-6393.
26. P. G. Vekilov, *Nature*, 2019, **570**, 450-452.
27. D. Kashchiev, *J. Chem. Phys.*, 2003, **118**, 1837-1851.
28. Y.-H. Lee, C.-K. Fang, S.-H. Chang, R. Kumar, K. Chatterjee and I.-S. Hwang, *Appl. Surf. Sci.*, 2020, **500**, 143986.
29. U. Gasser, R. Weeks Eric, A. Schofield, P. N. Pusey and D. A. Weitz, *Science*, 2001, **292**, 258-262.
30. S. T. Yau and P. G. Vekilov, *Nature*, 2000, **406**, 494-497.
31. J. Zhou, Y. Yang, Y. Yang, D. S. Kim, A. Yuan, X. Tian, C. Ophus, F. Sun, A. K. Schmid, M. Nathanson, H. Heinz, Q. An, H. Zeng, P. Ercius and J. Miao, *Nature*, 2019, **570**, 500-503.
32. C. Viedma, L. A. Cuccia, A. McTaggart, B. Kahr, A. T. Martin, J. M. McBride and P. Cintas, *Chem. Commun.*, 2016, **52**, 11673-11676.
33. L. Bahrig, S. G. Hickey and A. Eychmüller, *Cryst. Eng. Comm.*, 2014, **16**, 9408-9424.
34. L.-C. Sögütöglü, R. R. E. Steendam, H. Meekes, E. Vlieg and F. P. J. T. Rutjes, *Chem. Soc. Rev.*, 2015, **44**, 6723-6732.

35. T. Vetter, M. Iggländ, D. R. Ochsenbein, F. S. Hänseler and M. Mazzotti, *Cryst. Growth Des.*, 2013, **13**, 4890-4905.
36. A. K. El-Zhry El-Yafi and H. El-Zein, *Asian J. Pharm. Sci.*, 2014, **10**, 283-391.
37. P. Bennema, *J. Phys. D Appl. Phys.*, 1993, **26**, B1-B6.
38. K. A. Jackson, *J. Cryst. Growth*, 2004, **264**, 519-529.
39. D. P. Woodruff, *Philos. Trans. A Math. Phys. Eng. Sci.*, 2015, **373**, 20140230.
40. J. Li, C. J. Tilbury, S. H. Kim and M. F. Doherty, *Prog. Mater. Sci.*, 2016, **82**, 1-38.
41. G. Coquerel, *Chem. Soc. Rev.*, 2014, **43**, 2286-2300.
42. D. J. Berry and J. W. Steed, *Adv. Drug. Deliv. Rev.*, 2017, **117**, 3-24.
43. Y. Tong, Z. Wang, L. Dang and H. Wei, *Fluid Ph. Equilibria*, 2016, **419**, 24-30.
44. A. K. Nangia and G. R. Desiraju, *Angew. Chem. Int. Ed.*, 2019, **58**, 4100-4107.
45. B. Moulton and M. J. Zaworotko, *Chem. Rev.*, 2001, **101**, 1629-1658.
46. G. R. Desiraju, *J. Am. Chem. Soc.*, 2013, **135**, 9952-9967.
47. S. W. H. Bragg, *Proc. Phys. Soc. Lond.*, 1921, **34**, 33-50.
48. J. A. R. P. Sarma and G. R. Desiraju, *Acc. Chem. Res.*, 1986, **19**, 222-228.
49. M. C. Etter, *Acc. Chem. Res.*, 1990, **23**, 120-126.
50. J. W. Steed and J. L. Atwood, *Supramolecular Chemistry*, John Wiley & Sons, Ltd, Chichester, UK, 2nd edn., 2009.
51. G. R. Desiraju, *Angew. Chem. Int. Ed. Engl.*, 1995, **34**, 2311-2327.
52. F. H. Allen and R. Taylor, *Chem. Soc. Rev.*, 2004, **33**, 463-463.
53. personal communication.
54. CSD Statistics and Insights, <https://www.ccdc.cam.ac.uk/CCDCStats/>, (accessed 14th October 2021).
55. L. Fábíán, *Cryst. Growth Des.*, 2009, **9**, 1436-1443.
56. C. R. Groom, I. J. Bruno, M. P. Lightfoot and S. C. Ward, *Acta Crystallogr. B*, 2016, **72**, 171-179.
57. L. Infantes, L. Fábíán and W. D. S. Motherwell, *Cryst. Eng. Comm.*, 2007, **9**, 65-71.
58. J. P. Brog, C. L. Chanez, A. Crochet and K. M. Fromm, *RSC Adv.*, 2013, **3**, 16905-16931.
59. J. Bernstein, *Polymorphism In Molecular Crystals*, Oxford University Press, Oxford, UK, 1st edn., 2002.
60. K. Raza, P. Kumar, S. Ratan, R. Malik and S. Arora, *SOJ Pharm. Pharm. Sci.*, 2014, **1**, 1-10.
61. E. Hadjittofis, M. Isbell, V. Karde, S. Varghese, C. Ghoroi and J. Heng, *Pharm. Res.*, 2018, **35**.
62. E. H. Lee, *Asian J. Pharm. Sci.*, 2014, **9**, 163-175.
63. A. J. Alvarez, A. Singh and A. S. Myerson, *Cryst. Growth Des.*, 2009, **9**, 4181-4188.
64. S. L. Morissette, Ö. Almarsson, M. L. Peterson, J. F. Remenar, M. J. Read, A. V. Lemmo, S. Ellis, M. J. Cima and C. R. Gardner, *Adv. Drug Deliv. Rev.*, 2004, **56**, 275-300.
65. J. Ouyang, J. Chen, I. Rosbottom, W. Chen, M. Guo and J. Y. Y. Heng, *Cryst. Eng. Comm.*, 2021, **23**, 813-823.
66. J. Zhang, X. Tan, J. Gao, W. Fan, Y. Gao and S. Qian, *J. Pharm. Pharmacol.*, 2013, **65**, 44-52.
67. M. Saifee, N. Inamdar, D. L. Dhamecha and A. A. Rathi, *Int. J. Health Res.*, 2009, **2**, 291-306.
68. B. C. Rahul and R. S. Nalini, *J. Nanotoxicol. Nanomed.*, 2018, **3**, 23-48.

69. S. Aitipamula, R. Banerjee, A. K. Bansal, K. Biradha, M. L. Cheney, A. R. Choudhury, G. R. Desiraju, A. G. Dikundwar, R. Dubey, N. Duggirala, P. P. Ghogale, S. Ghosh, P. K. Goswami, N. R. Goud, R. R. K. R. Jetti, P. Karpinski, P. Kaushik, D. Kumar, V. Kumar, B. Moulton, A. Mukherjee, G. Mukherjee, A. S. Myerson, V. Puri, A. Ramanan, T. Rajamannar, C. M. Reddy, N. Rodriguez-Hornedo, R. D. Rogers, T. N. G. Row, P. Sanphui, N. Shan, G. Shete, A. Singh, C. C. Sun, J. A. Swift, R. Thaimattam, T. S. Thakur, R. Kumar Thaper, S. P. Thomas, S. Tothadi, V. R. Vangala, N. Variankaval, P. Vishweshwar, D. R. Weyna and M. J. Zaworotko, *Cryst. Growth Des.*, 2012, **12**, 2147-2152.
70. P. Cerreia Vioglio, M. R. Chierotti and R. Gobetto, *Adv. Drug Deliv. Rev.*, 2017, **117**, 86-110.
71. E. Grothe, H. Meekes, E. Vlieg, J. H. Ter Horst and R. De Gelder, *Cryst. Growth Des.*, 2016, **16**, 3237-3243.
72. A. V. Yadav, A. S. Shete, A. P. Dabke, P. V. Kulkarni and S. S. Sakhare, *Indian J. Pharm. Sci.*, 2009, **71**, 359-359.
73. L. S. Reddy, N. J. Babu and A. Nangia, *Chem. Commun.*, 2006, 1369-1371.
74. A. J. Cruz-Cabeza, S. M. Reutzel-Edens and J. Bernstein, *Chem. Soc. Rev.*, 2015, **44**, 8619-8635.
75. P. Vishweshwar, J. A. McMahon, M. L. Peterson, M. B. Hickey, T. R. Shattock and M. J. Zaworotko, *Chem. Commun.*, 2005, 4601-4603.
76. N. Qiao, M. Li, W. Schlindwein, N. Malek, A. Davies and G. Trappitt, *Int. J. Pharm.*, 2011, **419**, 1-11.
77. T. Friščić and W. Jones, *J. Pharm. Pharmacol.*, 2010, **62**, 1547-1559.
78. D. D. Bavishi and C. H. Borkhataria, *Prog. Cryst. Growth Charact. Mater.*, 2016, **62**, 1-8.
79. N. J. Babu and A. Nangia, *Cryst. Growth Des.*, 2011, **11**, 2662-2679.
80. T. J. Noonan, K. Chibale, P. M. Cheuka, S. A. Bourne and M. R. Caira, *J. Pharm. Sci.*, 2019, **108**, 2349-2357.
81. M. B. Hickey, M. L. Peterson, L. A. Scoppettuolo, S. L. Morrisette, A. Vetter, H. Guzmán, J. F. Remenar, Z. Zhang, M. D. Tawa, S. Haley, M. J. Zaworotko and Ö. Almarsson, *Eur. J. Pharm. Biopharm.*, 2007, **67**, 112-119.
82. A. Karagianni, M. Malamataris and K. Kachrimanis, *Pharmaceutics*, 2018, **10**, 18-18.
83. S. Cherukuvada, R. Kaur and T. N. Guru Row, *Cryst. Eng. Comm.*, 2016, **18**, 8528-8555.
84. M. E. Aulton and K. Taylor, *Aulton's pharmaceuticals : the design and manufacture of medicines*, Churchill Livingstone/Elsevier, London, UK, 4th edn., 2013.
85. A. L. Gillon, N. Feeder, R. J. Davey and R. Storey, *Cryst. Growth Des.*, 2003, **3**, 663-673.
86. A. M. Healy, Z. A. Worku, D. Kumar and A. M. Madi, *Adv. Drug Deliv. Rev.*, 2017, **117**, 25-46.
87. R. K. Khankari and D. J. W. Grant, *Thermochim. Acta*, 1995, **248**, 61-79.
88. Y. Kobayashi, S. Ito, S. Itai and K. Yamamoto, *Int. J. Pharm.*, 2000, **193**, 137-146.
89. G. R. Desiraju, *Chapter 1 Pharmaceutical Salts and Co-crystals: Retrospect and Prospects*, in *Pharmaceutical Salts and Co-crystals*, The Royal Society of Chemistry, Cambridge, UK, 1st edn., 2012, pp. 1-8.
90. A. T. M. Serajuddin, *Adv. Drug Deliv. Rev.*, 2007, **59**, 603-616.



91. A. Fernández Casares, W. M. Nap, G. Ten Figás, P. Huizenga, R. Groot and M. Hoffmann, *J. Pharm. Pharmacol.*, 2015, **67**, 812-822.
92. P. C. Acharya, S. Marwein, B. Mishra, R. Ghosh, A. Vora and R. K. Tekade, *Chapter 13 - Role of Salt Selection in Drug Discovery and Development*, in *Dosage Form Design Considerations*, ed. R. K. Tekade, Academic Press, London, UK, 1st edn., 2018, pp. 435-472.
93. T. S. Wiedmann and A. Naqwi, *Asian J. Pharm. Sci.*, 2016, **11**, 722-734.
94. J. Cassens, A. Prudic, F. Ruether and G. Sadowski, *Ind. Eng. Chem. Res.*, 2013, **52**, 2721-2731.
95. E. Vranić, *Bosn. J. Basic Med. Sci.*, 2004, **4**, 35-39.
96. S. Baghel, H. Cathcart and N. J. O'Reilly, *J. Pharm. Sci.*, 2016, **105**, 2527-2544.
97. K. J. Crowley and G. Zografi, *Thermochim. Acta*, 2001, **380**, 79-93.
98. Y. Huang and W.-G. Dai, *Acta Pharm. Sin. B*, 2014, **4**, 18-25.
99. S. V. Bhujbal, B. Mitra, U. Jain, Y. Gong, A. Agrawal, S. Karki, L. S. Taylor, S. Kumar and Q. Zhou, *Acta Pharm. Sin. B*, 2021, **11**, 2505-2536.
100. L. S. Taylor and G. Zografi, *Pharm. Res.*, 1997, **14**, 1691-1698.
101. K. Khougaz and S. D. Clas, *J. Pharm. Sci.*, 2000, **89**, 1325-1334.
102. P. J. Marsac, S. L. Shamblin and L. S. Taylor, *Pharm. Res.*, 2006, **23**, 2417.
103. Y. Aso and S. Yoshioka, *J. Pharm. Sci.*, 2006, **95**, 318-325.
104. B. C. Hancock and G. Zografi, *J. Pharm. Sci.*, 1997, **86**, 1-12.
105. G. Van den Mooter, M. Wuyts, N. Bleton, R. Busson, P. Grobet, P. Augustijns and R. Kinget, *Eur. J. Pharm. Sci.*, 2001, **12**, 261-269.
106. Y. Tian, D. S. Jones and G. P. Andrews, *Mol. Pharm.*, 2015, **12**, 1180-1192.
107. A. Karagianni, K. Kachrimanis and I. Nikolakakis, *Pharmaceutics*, 2018, **10**, 98.
108. A. C. Rumondor and L. S. Taylor, *Mol. Pharm.*, 2010, **7**, 477-490.
109. N. Chieng, J. Aaltonen, D. Saville and T. Rades, *Eur. J. Pharm. Biopharm.*, 2009, **71**, 47-54.
110. D. Kim, Y. Kim, Y.-Y. Tin, M.-T.-P. Soe, B. Ko, S. Park and J. Lee, *Pharmaceutics*, 2021, **13**.
111. J. Liu, H. Grohgan, K. Löbmann, T. Rades and N.-J. Hempel, *Pharmaceutics*, 2021, **13**.
112. D. L. Yarlagadda, V. Sai Krishna Anand, A. R. Nair, K. S. Navya Sree, S. J. Dengale and K. Bhat, *Int. J. Pharm.*, 2021, **602**, 120649.
113. F. Qian, J. Huang and M. A. Hussain, *J. Pharm. Sci.*, 2010, **99**, 2941-2947.
114. S. J. Dengale, H. Grohgan, T. Rades and K. Löbmann, *Adv. Drug Deliv. Rev.*, 2016, **100**, 116-125.
115. A. V. Hall, L. I. Chambers, O. M. Musa and J. W. Steed, *Cocrystals, Coamorphous Phases and Coordination Complexes of  $\gamma$ - and  $\epsilon$ -Lactams*, in *Handbook of Pyrrolidone and Caprolactam Based Materials*, New Jersey, USA, 1st edn., 2021, pp. 1171-1237.
116. K. Löbmann, R. Laitinen, C. Strachan, T. Rades and H. Grohgan, *Eur. J. Pharm. Biopharm.*, 2013, **85**, 882-888.
117. K. Löbmann, C. Strachan, H. Grohgan, T. Rades, O. Korhonen and R. Laitinen, *Eur. J. Pharm. Biopharm.*, 2012, **81**, 159-169.
118. S. J. Dengale, O. P. Ranjan, S. S. Hussen, B. S. M. Krishna, P. B. Musmade, G. Gautham Shenoy and K. Bhat, *Eur. J. Pharm. Sci.*, 2014, **62**.
119. M. Turek, E. Różycka-Sokołowska, M. Koprowski, B. Marciniak and P. Bałczewski, *Mol. Pharm.*, 2021, **18**, 1970-1984.
120. J. Liu, T. Rades and H. Grohgan, *Int. J. Pharm.*, 2021, **605**, 120802.

121. J. Pacutt, M. Rams-Baron, K. Chmiel, K. Jurkiewicz, A. Antosik, J. Szafraniec, M. Kurek, R. Jachowicz and M. Paluch, *Eur. J. Pharm. Sci.*, 2021, **159**, 105697.
122. J. Han, Y. Wei, Y. Lu, R. Wang, J. Zhang, Y. Gao and S. Qian, *Expert Opin. Drug Deliv.*, 2020, **17**, 1411-1435.
123. W. Wu, K. Löbmann, J. Schnitzkewitz, A. Knuhtsen, D. S. Pedersen, T. Rades and H. Grohgan, *Eur. J. Pharm. Biopharm.*, 2019, **134**, 68-76.
124. J. Liu, H. Grohgan and T. Rades, *Int. J. Pharm.*, 2020, **588**, 119768.
125. E. Pindelska, A. Sokal and W. Kolodziejski, *Adv. Drug Deliv. Rev.*, 2017, **117**, 111-146.
126. L. B. McCusker, R. B. Von Dreele, D. E. Cox, D. Louër and P. Scardi, *J. Appl. Crystallogr.*, 1999, **32**, 36-50.
127. G. S. Bumbrah and R. M. Sharma, *Egypt. J. Forensic Sci.*, 2016, **6**, 209-215.
128. T. Polenova, R. Gupta and A. Goldbourt, *Anal. Chem.*, 2015, **87**, 5458-5469.
129. W. Kolodziejski and J. Klinowski, *Chem. Rev.*, 2002, **102**, 613-628.
130. D. L. Bryce, *IUCrJ.*, 2017, **4**, 350-359.
131. A. Delori, P. T. A. Galek, E. Pidcock, M. Patni and W. Jones, *Cryst. Eng. Comm.*, 2013, **15**, 2916-2916.
132. A. Klamt, *Wires Comput. Mol. Sci.*, 2018, **8**, e1338.
133. C. Loschen and A. Klamt, *J. Pharm. Pharmacol.*, 2015, **67**, 803-811.
134. M. D. Eddleston, N. Madusanka and W. Jones, *J. Pharm. Sci.*, 2014, **103**, 2865-2870.
135. D.-K. Bučar, R. F. Henry, R. W. Duerst, X. Lou, L. R. MacGillivray and G. G. Z. Zhang, *J. Chem. Crystallogr.*, 2010, **40**, 933-939.
136. S. Basavoju, D. Boström and S. P. Velaga, *Pharm. Res.*, 2008, **25**, 530-541.
137. K. Fucke, S. A. Myz, T. P. Shakhtshneider, E. V. Boldyreva and U. J. Griesser, *New J. Chem.*, 2012, **36**, 1969-1969.
138. D. J. Berry, C. C. Seaton, W. Clegg, R. W. Harrington, S. J. Coles, P. N. Horton, M. B. Hursthouse, R. Storey, W. Jones, T. Frišćić and N. Blagden, *Cryst. Growth Des.*, 2008, **8**, 1697-1712.
139. D. Douroumis, S. A. Ross and A. Nokhodchi, *Adv. Drug Deliv. Rev.*, 2017, **117**, 178-195.
140. S. J. Diez, M. D. Eddleston, M. Arhangeliskis, M. Milbled, M. J. Müller, A. D. Bond, D. K. Bučar and W. Jones, *Cryst. Growth Des.*, 2018, **18**, 3263-3268.
141. K. Kadota, Y. Shirakawa, I. Matsumoto, A. Shimozaka and J. Hidaka, *Adv. Powder Technol.*, 2007, **18**, 775-785.
142. D. Walsh, D. R. Serrano, Z. A. Worku, B. A. Norris and A. M. Healy, *Int. J. Pharm.*, 2018, **536**, 467-477.
143. I. C. Wang, M. J. Lee, S. J. Sim, W. S. Kim, N. H. Chun and G. J. Choi, *Int. J. Pharm.*, 2013, **450**, 311-322.
144. M. Jiang and R. D. Braatz, *Cryst. Eng. Comm.*, 2019, **21**, 3534-3551.
145. Y. Ma, S. Wu, E. G. J. Macaringue, T. Zhang, J. Gong and J. Wang, *Org. Process Res. Dev.*, 2020, **24**, 1785-1801.
146. D. Zhang, S. Xu, S. Du, J. Wang and J. Gong, *Engineering*, 2017, **3**, 354-364.
147. M. Allesø, N. Chieng, S. Rehder, J. Rantanen, T. Rades and J. Aaltonen, *J. Control. Release*, 2009, **136**, 45-53.
148. M. Descamps, J. F. Willart, E. Dudognon and V. Caron, *J. Pharm. Sci.*, 2007, **96**, 1398-1407.
149. J. F. Willart and M. Descamps, *Mol. Pharm.*, 2008, **5**, 905-920.

150. K. T. Jensen, L. I. Blaabjerg, E. Lenz, A. Bohr, H. Grohgan, P. Kleinebudde, T. Rades and K. Löbmann, *J. Pharm. Pharmacol.*, 2016, **68**, 615-624.
151. W. Lu, T. Rades, J. Rantanen and M. Yang, *Int. J. Pharm.*, 2019, **565**, 1-8.
152. R. Ojarinta, L. Lermiaux and R. Laitinen, *Int. J. Pharm.*, 2017, **532**, 289-298.
153. A. Shayanfar and A. Jouyban, *J. Pharm. Innov.*, 2013, **8**, 218-228.
154. M. J. Goodwin, O. M. Musa, D. J. Berry and J. W. Steed, *Cryst. Growth Des.*, 2018, **18**, 701-709.
155. K. Löbmann, R. Laitinen, H. Grohgan, K. C. Gordon, C. Strachan and T. Rades, *Mol. Pharm.*, 2011, **8**, 1919-1928.
156. J. R. Davenport, O. M. Musa, M. J. Paterson, M.-O. M. Piepenbrock, K. Fucke and J. W. Steed, *Chem. Commun.*, 2011, **47**, 9891-9893.
157. A. Perrin, M. J. Goodwin, O. M. Musa, D. J. Berry, P. Corner, K. Edkins, D. S. Yufit and J. W. Steed, *Cryst. Growth Des.*, 2017, **17**, 3236-3249.
158. H. Beller and H. W. Austin, Process for the Preparation of Iodine-Polyvinylpyrrolidone by Dry Mixing, U.S. Patent 2,706,701A, 1955.
159. WHO Model List of Essential Medicines, World Health Organization, 2017
160. H.-U. Schenck, P. Simak and E. Haedicke, *J. Pharm. Sci.*, 1979, **68**, 1505-1509.
161. M. J. Goodwin, B. W. Steed, D. S. Yufit, O. M. Musa, D. J. Berry and J. W. Steed, *Cryst. Growth Des.*, 2017, **17**, 5552-5558.
162. G. Kasten, H. Grohgan, T. Rades and K. Lobmann, *Eur. J. Pharm. Sci.*, 2016, **95**, 28-35.
163. D. A. Shiraeff, Solid stabilized hydrogen peroxide compositions, U.S. Patent 3,376,110A, 1968.
164. D. A. Shiraeff, Solid stabilized hydrogen peroxide compositions, U.S. Patent 3,480,557, 1969.
165. R. V. Moorsel-Murerikaite, T. D. T. Tran and G. Kroon, Method of strengthening non-keratinous fibers, and uses thereof, WO2020150384A1, 2020.
166. E. P. J. M. Everaert, G. Kroon and X. Zhang, Method of strengthening hair fibers and protecting dyed hair color from fading or wash-out, US20170007518A1, 2017.
167. E. P. J. M. Everaert, G. Kroon and T. D. T. Tran, Method for coloring or bleaching hair fibers, US20180193242A1, 2018.

## 2 Predictive Identification of Co-formers in Co-amorphous Systems

### 2.1 Introduction

A large proportion of newly discovered active pharmaceutical ingredients (APIs) display poor solubility in gastrointestinal fluids, which is likely to decrease their bioavailability.<sup>1-4</sup> To improve the aqueous solubility of APIs, different formulation methods have been designed including amorphous forms, which have no long-range crystallographic order and higher internal energy compared with their respective crystalline forms.<sup>5-8</sup> However, pure amorphous APIs are often physically unstable and can crystallise as a result of increased molecular mobility, especially when stored above their glass transition temperature or in humid environments.<sup>9-11</sup> Methods to improve the stability of amorphous APIs include the formation of amorphous solid dispersions and co-amorphous (COAM) materials.<sup>12-15</sup>

Amorphous solid dispersions are formed by (molecularly) dispersing an API in a (usually amorphous) polymer such as poly(vinylpyrrolidone) and cellulose based polymers, which act as an inactive stabilizer.<sup>16-18</sup> Stabilization (even above the solubility limit of the API in the polymer) is caused by the polymer increasing the glass transition temperature and forming intermolecular interactions, which in turn result in reduced molecular mobility.<sup>19-21</sup> The main challenges with using amorphous solid dispersions are their often high hygroscopicity (causing increased molecular mobility of the API), and the usually large mass ratios of polymer to API (causing downstream formulation problems when high API dosages are required).<sup>22-24</sup>

COAM systems are formed by mixing an API with a low molecular weight compound called a co-former, which is usually inactive but could also be another API.<sup>25-28</sup> The ratio of API to co-former can be relatively high which helps in the formation of high API dosage tablets.<sup>29, 30</sup>

COAM systems are similar to co-crystals with them both containing two components, usually with one API and one co-former.<sup>31</sup> The difference between co-crystals and COAM systems is that co-crystals are based on a repeating three dimensional crystal lattice whereas COAM systems have no repeating units and an amorphous structure.<sup>26</sup> The physical stability of COAM systems is usually higher than that of pure amorphous materials and COAM systems often have improved dissolution characteristics compared to pure amorphous APIs.<sup>32, 33</sup> COAM systems are stabilised, for example, by the formation of

hydrogen bonds,  $\pi$ - $\pi$  stacking and ionic bonds between the two compounds, as shown by infrared spectroscopy.<sup>34, 35</sup> Methods to produce COAM systems include co-melting, solvent evaporation and mechanochemistry.<sup>36</sup> Co-melting involves melting the components followed by rapid cooling to avoid nucleation and recrystallization.<sup>37-39</sup> A key challenge in co-melting is that some of the APIs or co-formers may thermally degrade if kept at high temperatures for too long.<sup>40, 41</sup> Solvent evaporation involves dissolving the two components into a solvent or solvent mixture followed by rapidly evaporating the solvent to prevent nucleation and recrystallization.<sup>42, 43</sup> However, finding a solvent or solvent mixture which can dissolve both the co-former and the API without one component crystallising prematurely is a challenge.<sup>44</sup> Mechanochemistry involves using mechanical stress to reduce crystallinity and induce intimate mixing.<sup>45, 46</sup> The conventional method used for mechanochemistry is milling. A low temperature is preferred during milling to promote the formation of an amorphous material by keeping the mixture below the glass transition temperature of the amorphous system.<sup>47</sup>

The possible co-formers used to form COAM systems are numerous but there is no clear method of predicting whether a certain co-former will generate a COAM system with a specific API. Mizoguchi *et al.*<sup>48</sup> linked the formation of COAM systems to the mixing enthalpy and the difference in lipophilicity ( $\Delta \log P$ ). This work used COSMOquick, a computational program which uses the Conductor like Screening Model for Real Solvents (COSMO-RS) method to derive charge density surfaces which describe each molecule and can be used to calculate interaction energies with other components.<sup>49</sup> COSMOquick can be used to screen for potential co-crystals and provides values for the Gibbs energy of mixing ( $\Delta G_{mix}$ ), which determines whether mixing between potential co-crystal formers at constant temperature and pressure is spontaneous, as well as the excess enthalpy of mixing, which is the enthalpy released or absorbed upon mixing.<sup>50</sup> Ueda *et al.*<sup>51</sup> performed a multivariate analysis of physiochemical variables of co-formers and concluded that a range of these variables (crystallisation tendency, glass transition temperature and molecular flexibility) contributed to COAM formation; however, this study only used one API (naproxen) and a small number of co-formers (felbinac, flufenamic acid, loxoprofen, ketoprofen, indomethacin, aceclofenac, indoprofen).

Mend-Lund *et al.*<sup>52</sup> used a range of molecular descriptors to produce a partial least squares-discriminant analysis (PLS-DA) model to predict the likelihood of success of co-amorphisation between amino acids and an API. The model used a dataset formed from 6 APIs and 20 amino acids from Kasten *et al.*<sup>53</sup> The variables used include physical properties, Hückel theory descriptors, subdivided surface areas, atom counts, bond counts, pharmacophore feature descriptors, partial charge descriptors, surface area, volume and shape descriptors. To test the model, one of the six APIs (mebendazole) was left out of the model and used as a validation set. Out of the 20 systems in the validation set, 19 were correctly assigned. The model showed that polar amino acids were less likely to form COAM systems and non-polar side chains were more likely to form COAM systems. However, this model only investigated amino acid co-formers.

The current study aims to develop a method to improve the selection of co-formers to formulate COAM systems. The previously reported COAM screen by Kasten *et al.*<sup>53</sup> was used to understand which variables affect the formation of COAM systems. Variables used to describe the systems were obtained using COSMOquick to calculate properties that describe the two-component systems and Pubchem to source physico-chemical variables to describe the co-formers. The 36 variables from COSMOquick and Pubchem were used to develop a PLS-DA prediction method to identify which co-formers are likely to form COAM systems.

## 2.2 Results and Discussion

### 2.2.1 Correlation of $\Delta H_{mix}$ and $\Delta \log P$ with Co-amorphisation

The COAM systems used in this screen were experimentally identified by Kasten *et al.*<sup>53</sup> and the responses listed in Table 2.1 indicate which systems formed COAM materials after 60 min of ball milling. The APIs used were carvedilol (CAR), furosemide (FUR), indomethacin (IND) simvastatin (SIM), carbamazepine (CBZ) and mebendazole (MEB). Previous research on theoretical descriptors for the prediction of the formation of a COAM system identified two indicators ( $\Delta H_{mix}$  and  $\Delta \log P$ ) using a combination of APIs with other APIs or sugars to screen for COAM systems using differential scanning calorimetry.<sup>48</sup> The  $\Delta H_{mix}$  was calculated using COSMOquick and the  $\Delta \log P$  was sourced from Pubchem; it was found that COAM systems form with a  $\Delta \log P$  below 6 and a negative  $\Delta H_{mix}$  and a clear divide between the COAM systems and the crystalline systems was observed. When the  $\Delta H_{mix}$  and  $\Delta \log P$  for the API/amino acids systems tested by Kasten *et al.*<sup>53</sup> were plotted against each other the same

clear divide was not evident (Figure 2.1). The data indicates that COAM materials tend to form in systems with a lower value of  $\Delta \log P$  and a negative  $\Delta H_{mix}$ . However, many combinations break these trends; a few COAM systems form with a  $\Delta \log P$  above 6 and many systems with a  $\Delta \log P$  below 6 remain crystalline. Furthermore, COAM systems form with positive values of  $\Delta H_{mix}$ .

To further assess the predictive ability of COAM formation using the two variables a range of 29 different co-formers (Table 2.2) were paired with mebendazole and analysed. The 29 different co-formers were then ball milled with mebendazole to determine whether they formed COAM mixtures (Figure 2.2) and the results were compared with the predicted trends. Figure 2.3 shows that all the systems including COAM and not COAM have a  $\Delta \log P$  below 6 suggesting  $\Delta \log P$  is not a good predictor of COAM material formation. Figure 2.3 also shows that the majority of the 29 systems have negative values of  $\Delta H_{mix}$  but not all the systems are COAM and there is no clear divide between COAM and not COAM systems. Using these two variables to predict the formation of co-amorphous API-co-former systems was poor predictively suggesting that more variables were required to predict the propensity to form COAM systems.

Table 2.1: Results of experimental COAM screening using ball milling by Kasten et al.<sup>53</sup> N indicates the system is not COAM including crystalline salts or crystalline starting material and Y indicates COAM formation including COAM salts.

Amino acid	API					
	CAR	MEB	CBZ	SIM	FUR	IND
ASP	N	N	N	N	N	N
GLU	N	N	N	N	N	N
ARG	N	N	N	N	Y	Y
HIS	N	N	N	N	Y	N
LYS	N	Y	N	Y	Y	Y
ASN	N	N	N	N	N	N
CYS	N	N	N	N	Y	N

GLN	N	N	N	N	N	N
SER	N	N	N	N	N	N
THR	N	N	N	N	N	N
TYR	N	N	N	N	N	N
ALA	N	N	N	N	N	N
GLY	N	N	N	N	N	N
ILE	Y	Y	N	N	Y	Y
LEU	Y	Y	N	N	Y	Y
MET	Y	Y	N	N	Y	Y
PHE	Y	Y	N	Y	Y	Y
PRO	N	N	N	N	Y	Y
TRP	Y	Y	Y	Y	Y	Y
VAL	Y	N	N	N	Y	Y

---



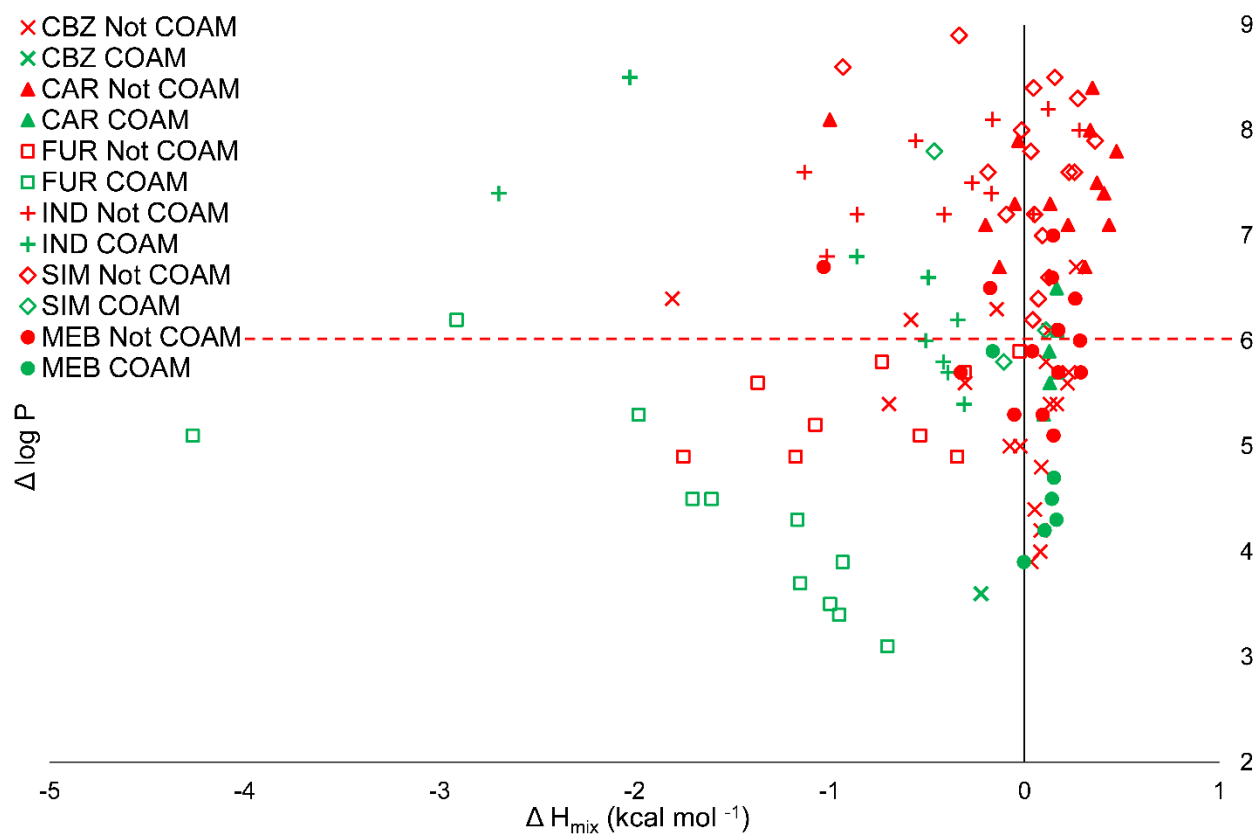


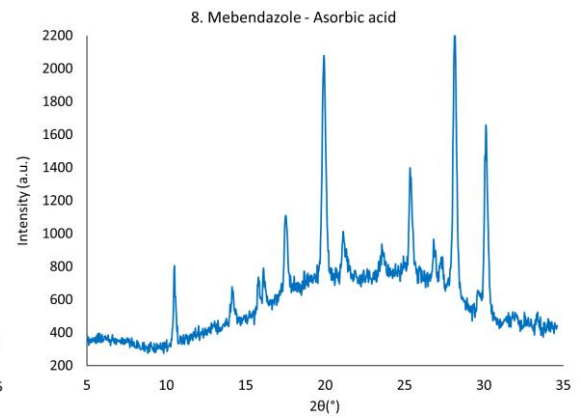
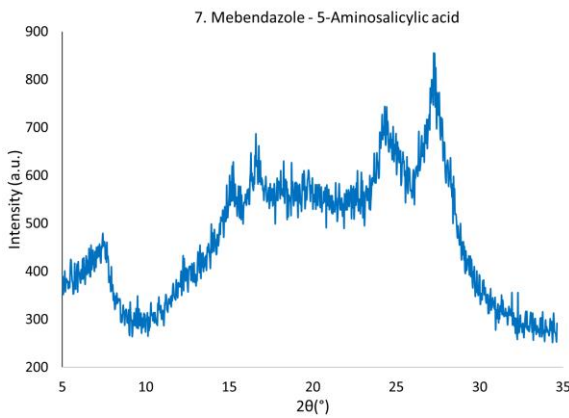
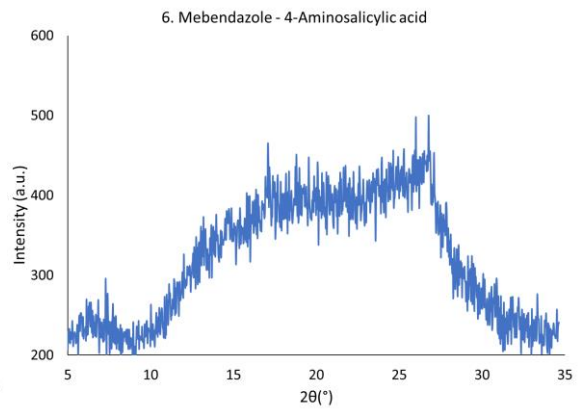
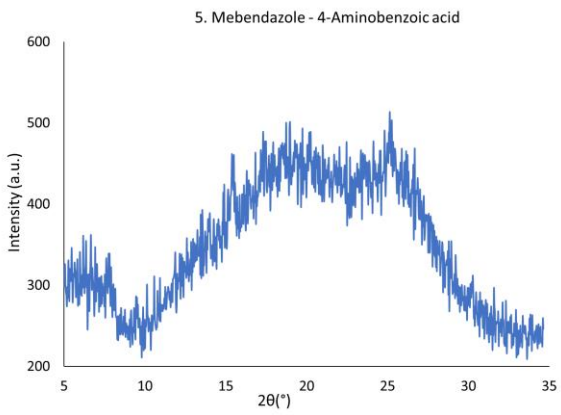
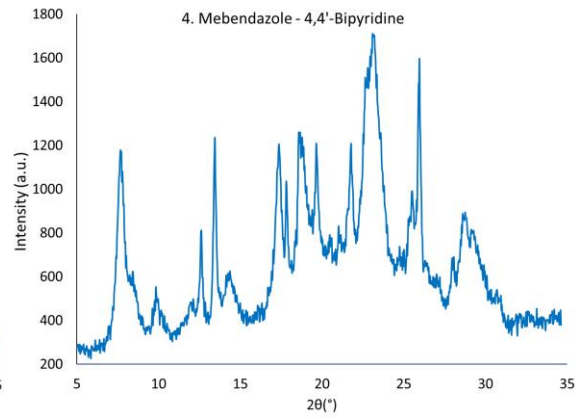
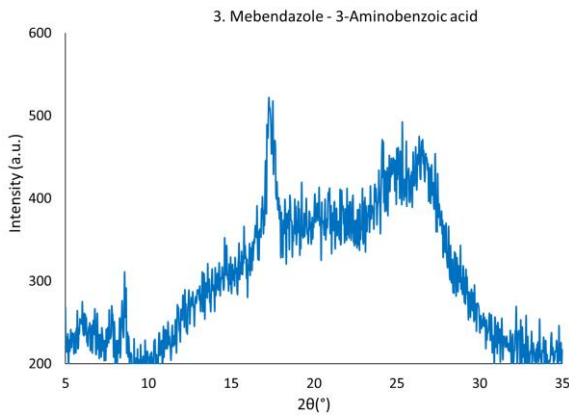
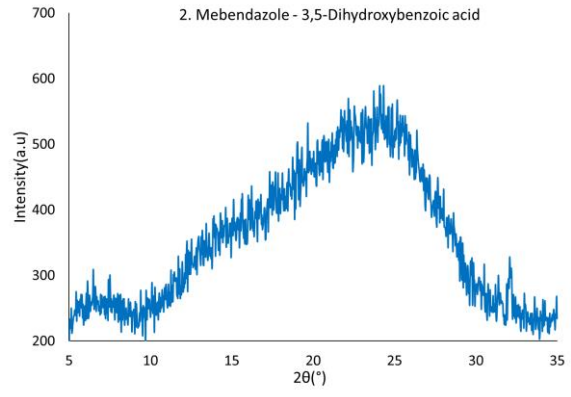
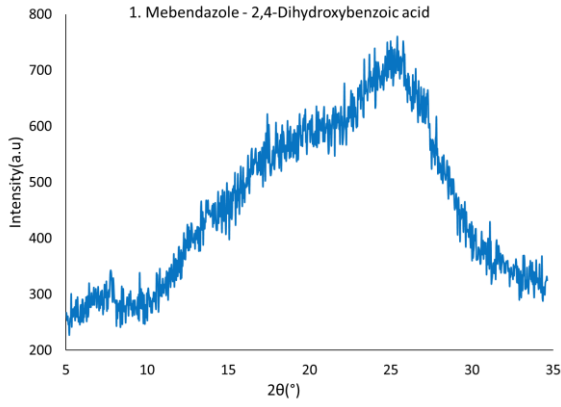
Figure 2.1. Relationship between the formation of COAM systems from Kasten et al.<sup>53</sup>,  $\Delta H_{\text{mix}}$  and  $\Delta \log P$ . Green markers indicate COAM systems were formed and red markers indicate not COAM systems. The red dotted line is the expected boundary line between COAM and not COAM systems<sup>48</sup>.

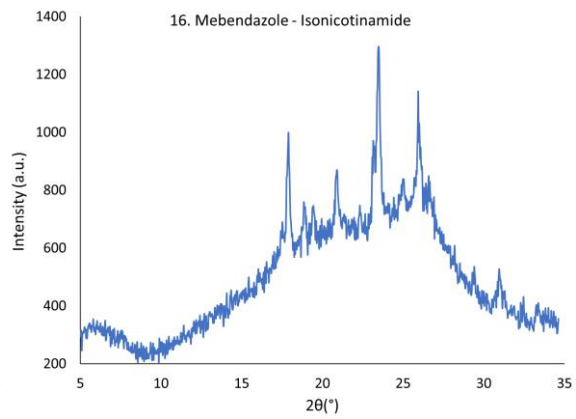
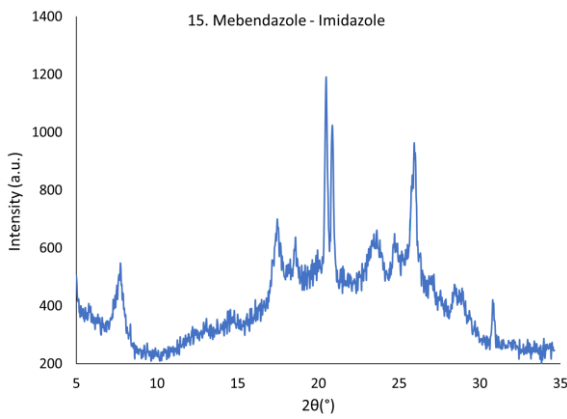
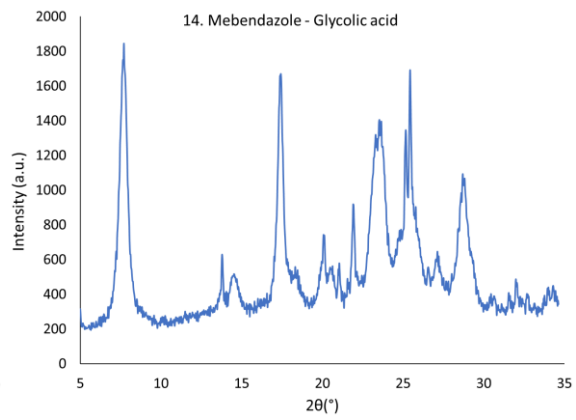
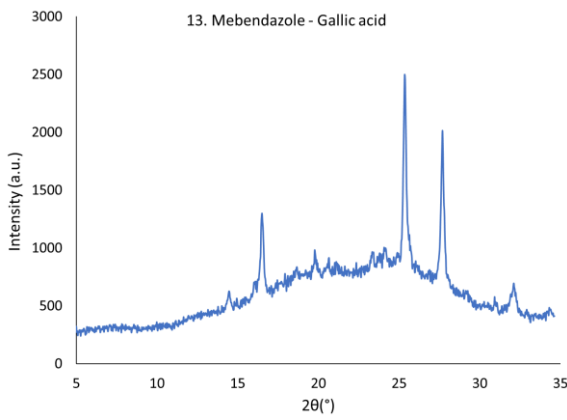
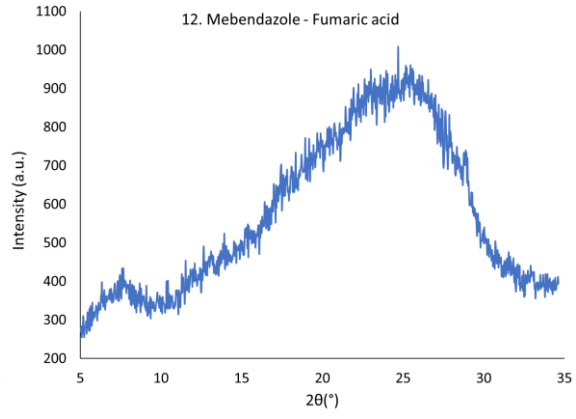
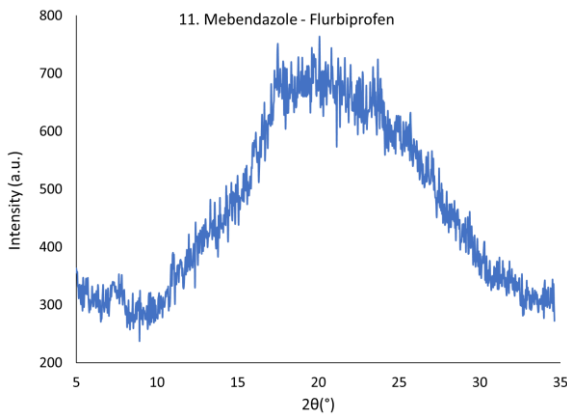
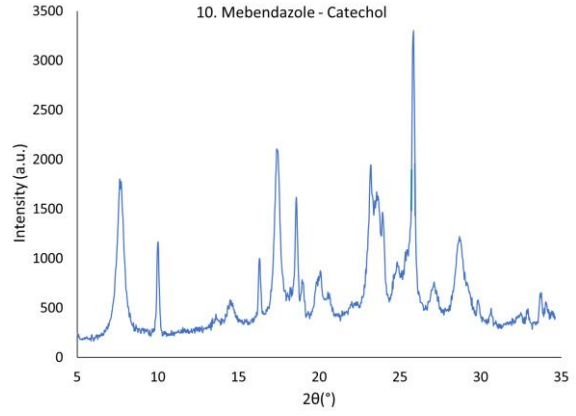
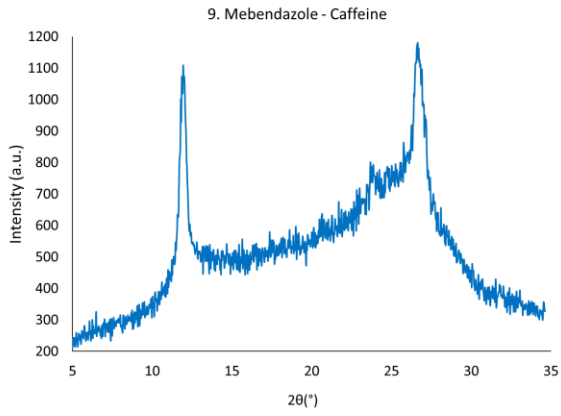
Table 2.2: Results of COAM screening by ball milling with mebendazole.

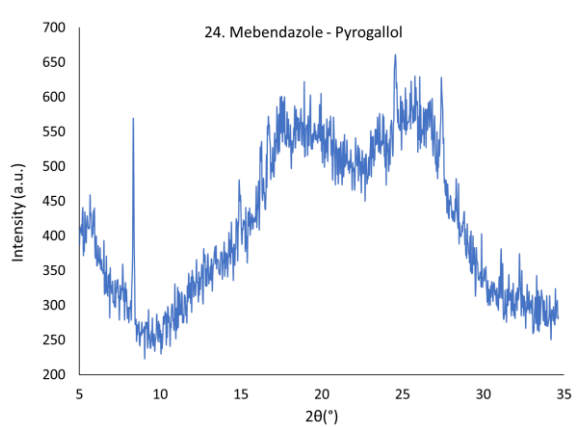
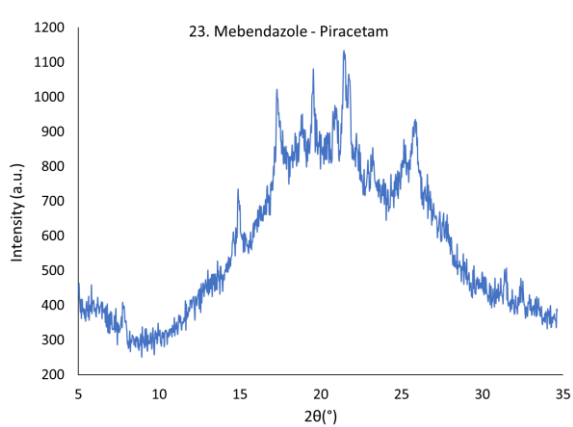
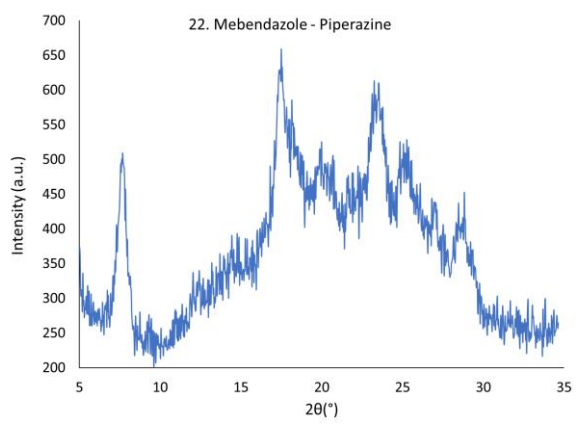
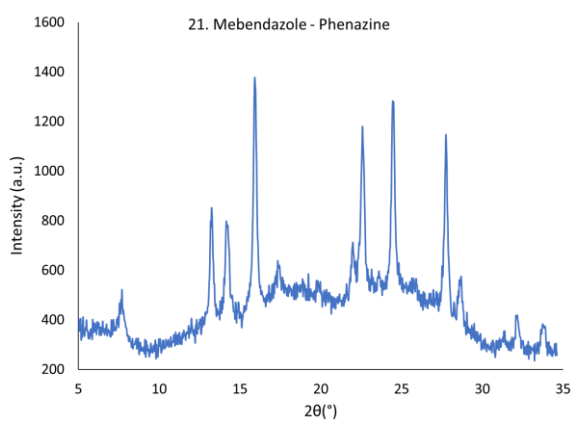
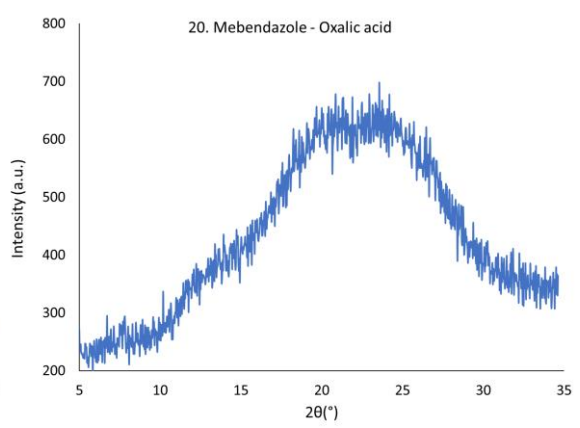
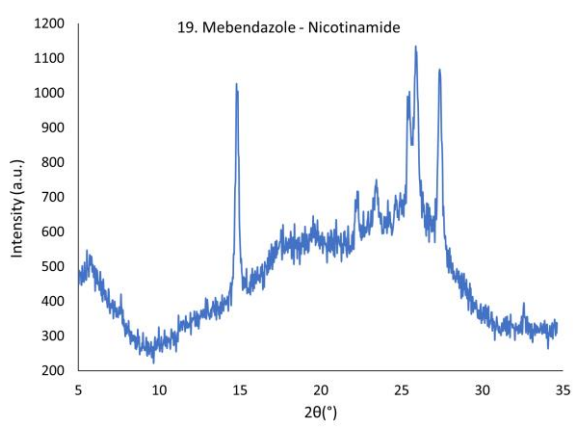
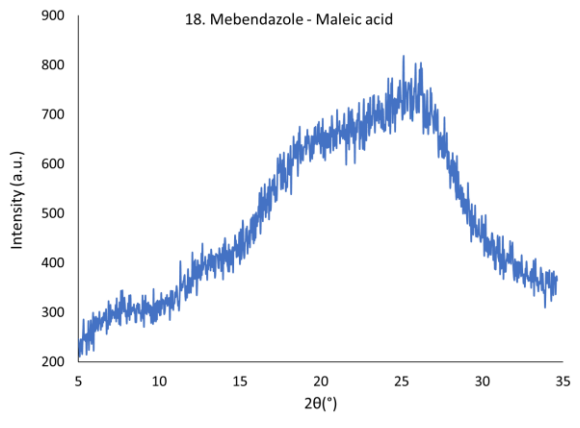
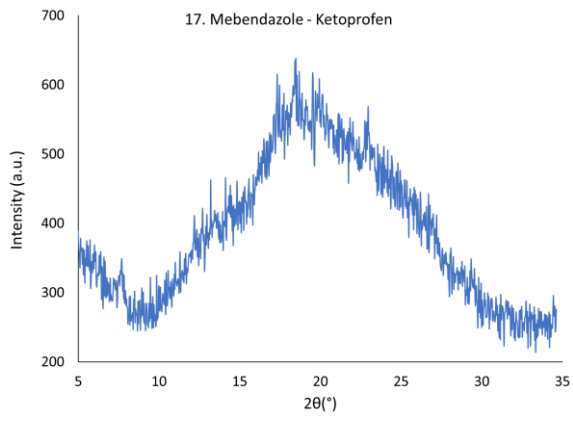
Co-former	Identifier	COAM
2,4-dihydroxybenzoic acid	2,4-DHBA	Y
3,5-dihydroxybenzoic acid	3,5-DHBA	Y
3-aminobenzoic acid	3-ABA	N
4,4'-bipyridine	BIPY	N
4-aminobenzoic acid	4-ABA	Y
4-aminosalicylic acid	4-AS	Y
5-aminosalicylic acid	5-AS	N
ascorbic acid	ASCA	N

caffeine	CAF	N
catechol	CATEC	N
flurbiprofen	FLURB	Y
fumaric acid	FUMA	Y
gallic acid	GALA	N
glycolic acid	GLYA	N
imidazole	IMID	N
isonicotinamide	INICO	N
ketoprofen	KETO	Y
maleic acid	MALA	Y
nicotinamide	NICO	N
oxalic acid	OXA	Y
phenazine	PHENA	N
piperazine	PIP	N
piracetam	PIRA	N
pyrogallol	PYROG	Y
salicylic acid	SALCA	Y
succinic acid	SUCA	N
tartaric acid	TARTA	N
theophylline	THEO	Y
urea	UREA	N

---







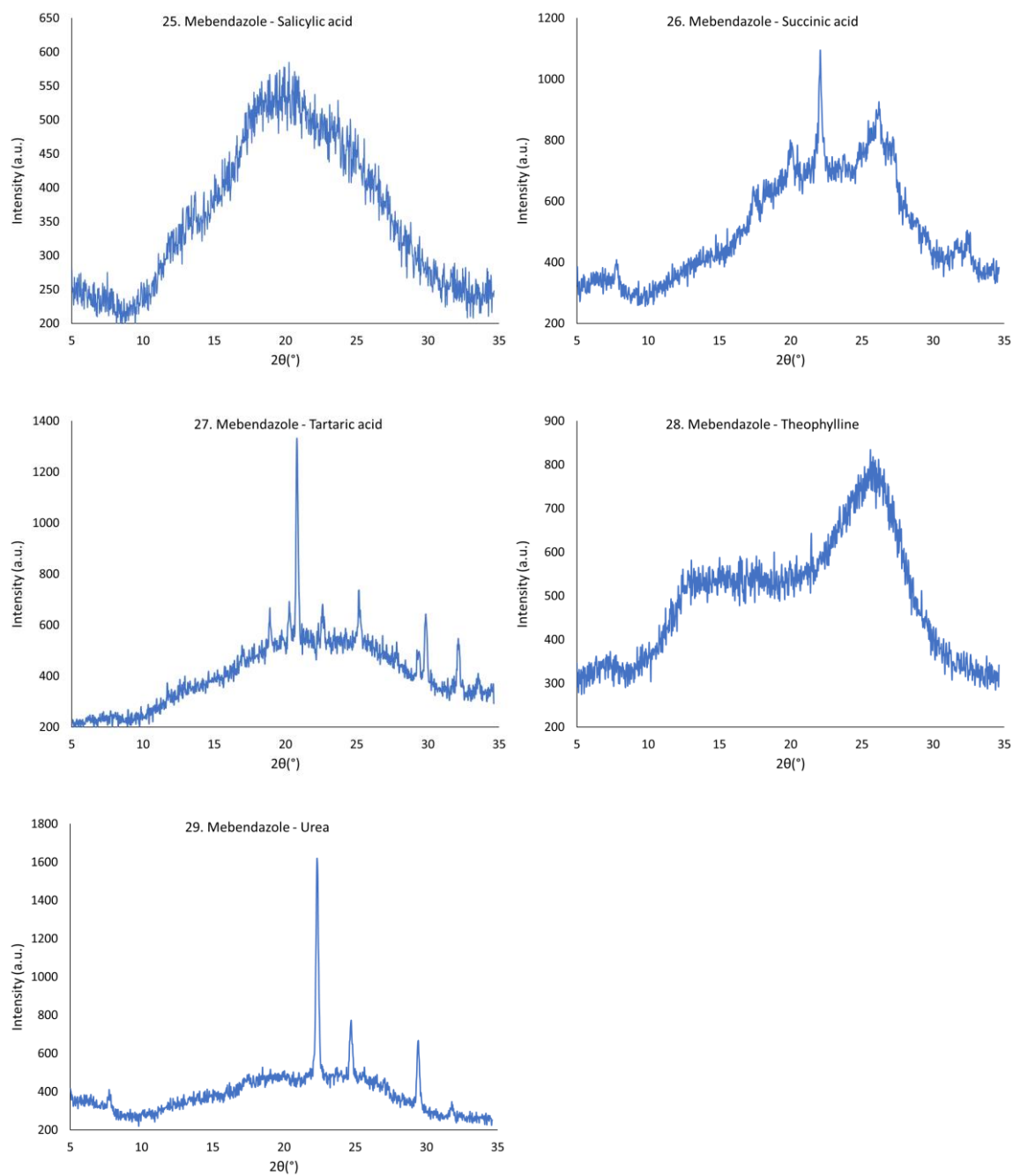


Figure 2.2: XRPD results of equimolar mixtures of mebendazole and 29 different coformers after ball milling.

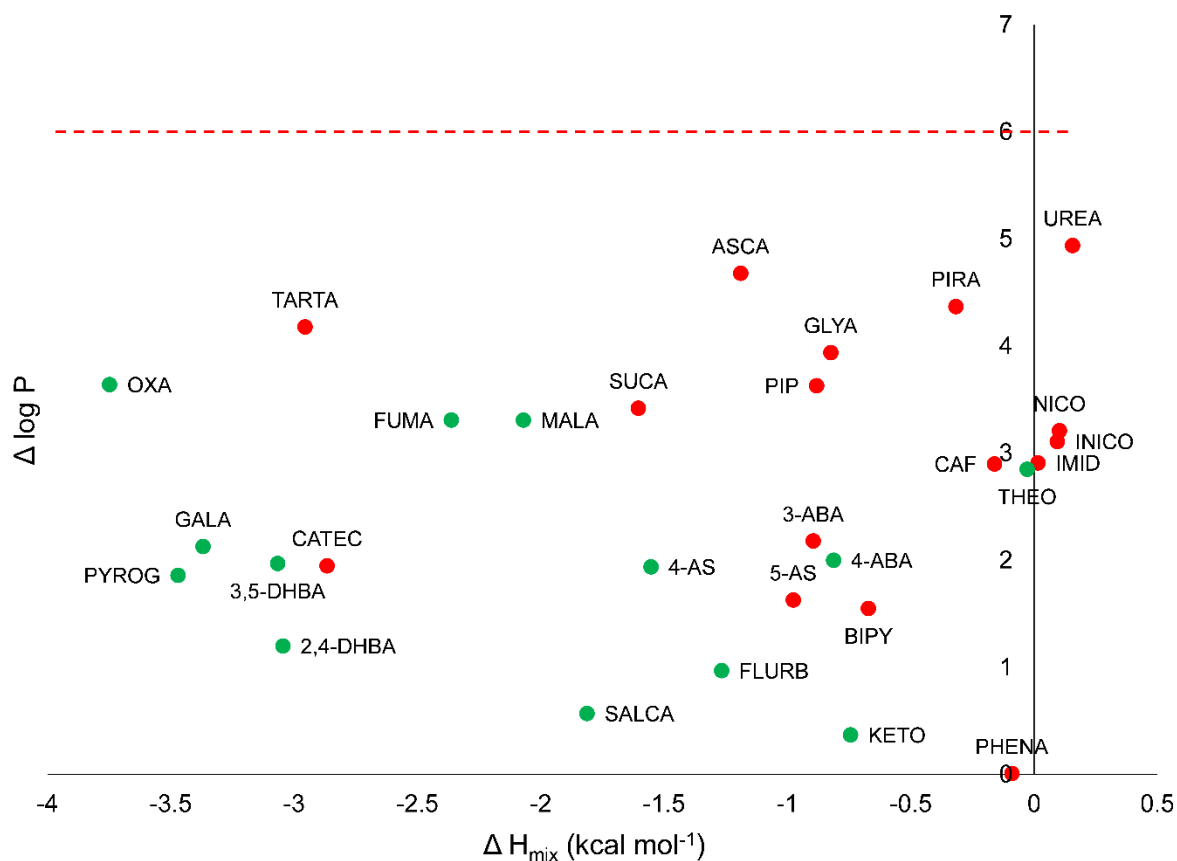


Figure 2.3. Relationship between the formation of COAM systems of mebendazole with 29 co-formers,  $\Delta H_{mix}$  and  $\Delta \log P$ . Green markers indicate COAM systems were formed and red markers indicate not COAM systems were formed. The red dotted line is the expected boundary line between COAM and not COAM systems based on previous research by Mizoguchi et al.<sup>48</sup> Abbreviations of the cofomers are shown in Table 2.2.

### 2.2.2 PLS-DA

To improve the prediction accuracy of the COAM systems, 34 additional variables were selected to describe the properties and interactions of the two components and combined with  $\Delta H_{mix}$  and  $\Delta \log P$ . These 36 variables (Table 2.3) were used to produce a PLS-DA model to understand which variables affect COAM system formation. Variable selection was then used to reduce the initial 36 variables to seven key variables. Variable selection was performed by removing variables one after the other and checking the effect on the prediction ability of the model for the API amino acid data set; if the variable had no effect it was removed and if the prediction ability was reduced it was retained. The variables selected describe differences between the API and co-former allowing the model to be applied to systems where the API and co-former cannot be easily defined, such as systems

formed from two APIs. The final PLS-DA model includes the seven descriptors (Table 2.3):  $\Delta H_{hb}$ ,  $\Delta H_{mix}$ ,  $\Sigma HBC_{self}$ , *AV. MW*,  $\Delta TPSA$ ,  $\Delta\mu$  and  $\Delta(\delta h)$ . The goodness of fit is  $R^2Y = 33.0\%$ ,  $R^2X = 47.8\%$  and the goodness of prediction is  $Q^2 = 29.0\%$  based on two latent variables. Latent variables are variables which cannot be measured and are inferred from mathematical models.

Table 2.3: The definitions of all the variables used to find the PLS-DA model. The key parameters identified are in bold.

Variable	Definition
$\Delta G_{mix}$	Gibbs energy of mixing.
<b><math>\Delta H_{hb}</math></b>	Excess enthalpy of hydrogen bonding.
<b><math>\Delta H_{mix}</math></b>	Excess enthalpy of mixing.
$\Delta \log P$	The difference between the log of the octanol/water partition coefficient of the API and the co-former
<i>AV. log P</i>	The average value of the log of the octanol/water partition coefficient of the API and the co-former
<b><math>\Sigma HBC_{self}</math></b>	The sum of the difference of hydrogen bond donors to hydrogen bond acceptors for the individual components, for both the API and co-former. To represent the hydrogen bonding present in the individual components.
$\Sigma HBC_{API-COF}$	The sum of the difference of hydrogen bond donors to hydrogen bond acceptors for the mixed components, for both the API and co-former. To represent the hydrogen bonding between the two components.
<i>AV. TM</i>	The average melting point of the two components.
$\Delta TM$	The difference of the melting point of the co-former and the API.
<b><i>AV. MW</i></b>	The average molecular weight of the API and the co-former.
$\Delta MW$	The difference of the molecular weights of the API and the co-former.
<i>AV. TPSA</i>	The average topological polar surface area of the API and the co-former.
<b><math>\Delta TPSA</math></b>	The difference between the topological polar surface area of the API and the co-former.
<i><math>\Delta rotatable bonds</math></i>	The difference between the number of rotatable bonds of the co-former and the API.
<i><math>\Delta rotbsdmod</math></i>	The difference between the general molecular flexibility parameter of the co-former and the API.
$\Delta M2$	The difference between the second order sigma moments of the co-former and the API.
$\Delta M3$	The difference between the third order sigma moments of the co-former and the API.
$\Delta M4$	The difference between the fourth order sigma moments of the co-former and the API.
$\Delta M5$	The difference between the fifth order sigma moments of the co-former and the API.
$\Delta M6$	The difference between the sixth order sigma moments of the co-former and the API.



$\Delta$ Dielectric energy	The difference between the dielectric energy of the co-former and the API.
$\Delta$ volume	The difference between the COSMO volume of the co-former and the API.
$\Delta$ Macc1	The difference between the first order sigma acceptor moments of the co-former and the API.
$\Delta$ Macc2	The difference between the second order sigma acceptor moments of the co-former and the API.
$\Delta$ Macc3	The difference between the third order sigma acceptor moments of the co-former and the API.
$\Delta$ Macc4	The difference between the fourth order sigma acceptor moments of the co-former and the API.
$\Delta$ Mdon1	The difference between the first order sigma donor moments of the co-former and the API.
$\Delta$ Mdon2	The difference between the second order sigma donor moments of the co-former and the API.
$\Delta$ Mdon3	The difference between the third order sigma donor moments of the co-former and the API.
$\Delta$ Mdon4	The difference between the fourth order sigma donor moments of the co-former and the API.
$\Delta$ avratio	The difference between the surface-volume ratio based on COSMO of the co-former and the API.
$\Delta$ ovality	The difference between co-former and the API of the ratio of the molecular COSMO area to the area of a sphere with the same volume as the molecule.
$\Delta\mu$	The difference between the pseudo chemical potential of the pure solute of the API and the co-former.
$\Delta(\delta d)$	The difference between the Hansen parameter for dispersion in MPa <sup>0.5</sup> of the API and the co-former.
$\Delta(\delta p)$	The difference between the Hansen parameter for permanent dipole-dipole interactions in MPa <sup>0.5</sup> of the API and the co-former.
$\Delta(\delta h)$	The difference between the Hansen parameter for hydrogen bonding in MPa <sup>0.5</sup> of the API and the co-former.

### 2.2.3 Model

The score scatter plot of the PLS-DA model for the API amino acid systems (Figure 2.4) shows a division between COAM and not COAM systems with COAM systems appearing more in the top right quadrant. The dotted line in Figure 2.4 shows the predicted separation for visualization purposes between the COAM and not COAM systems. The not COAM systems occur on the left of the plot and mainly in the bottom left quadrant. Equation 2.1 shows the relationship of each variable to the overall prediction.

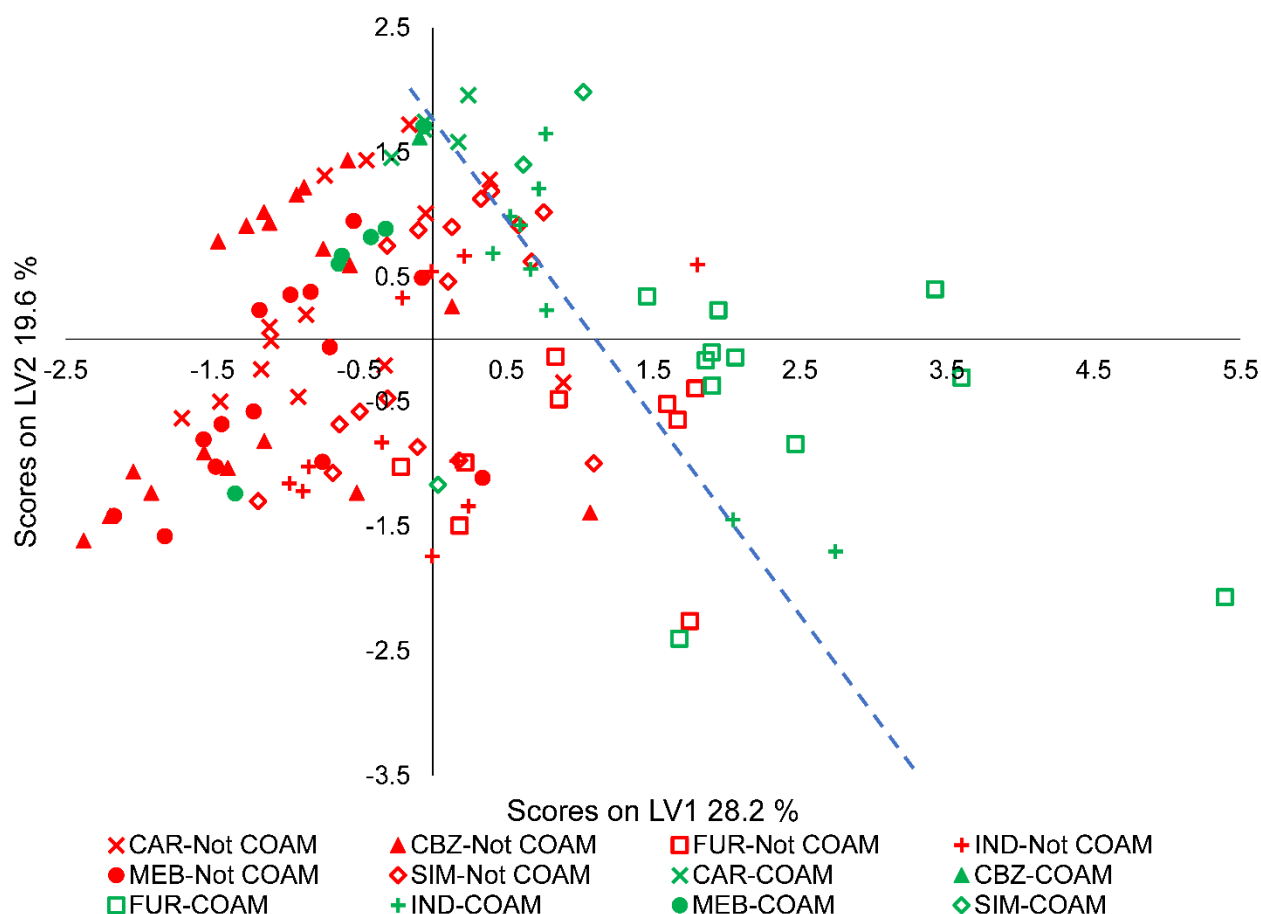


Figure 2.4. PLS-DA score scatter plot of latent variables (LV) 1 and 2. The red markers indicate not COAM systems and the green markers show COAM systems. The APIs are displayed with different markers with carvedilol (CAR) displayed as an X, carbamazepine (CBZ) as a triangle, furosemide (FUR) as a hollow square, indomethacin (IND) as a cross, mebendazole (MEB) as a circle and simvastatin (SIM) as a hollow diamond. The dashed blue line shows the predicted separation between COAM and Not COAM systems for visualization purposes.

Predicted COAM value

$$\begin{aligned}
 &= (-0.123 \times \Delta H_{hb}) + (-0.136 \times \Delta H_{mix}) + (-0.00350 \times \Sigma HBC_{self}) \\
 &+ (0.00297 \times AV.MW) + (-0.00176 \times \Delta TPSA) + (0.0105 \times \Delta \mu) \\
 &+ (-0.0441 \times \Delta(\delta h)) + (-0.204)
 \end{aligned}$$

Equation 2.1: The equation to describe the relation of the seven key variables to the predicted COAM value. All numbers have been rounded to 3 significant figures. A value closer to one indicates the system should be COAM and a value closer to zero indicates it should not be COAM.

The loading plot (Figure 2.5) shows how each variable is related to COAM formation. The variables closest to the COAM response are linked to COAM formation and the variables closest to the not COAM response are linked to not COAM formation. The three variables  $\Sigma HBC_{self}$ ,  $\Delta TPSA$  and  $\Delta\mu$  are located roughly in the middle between the COAM and not COAM point and therefore, do not appear to influence the COAM formation to a strong degree, however, when they are removed the prediction ability of the model is reduced. The variables related to COAM formation, therefore, appear to be a relatively large value of  $AV.MW$  and a relatively small or negative value of  $\Delta H_{mix}$ ,  $\Delta H_{hb}$ , and  $\Delta(\delta h)$ . A large  $AV.MW$  seems to correlate with COAM formation possibly due to slower diffusion which would inhibit recrystallization. A negative value of  $\Delta H_{mix}$  favours COAM formation, as expected since negative values indicate that the mixed system has a lower free energy state due to stronger attractive forces between the mixed molecules compared to the individual component interaction. A negative value of  $\Delta H_{hb}$  also favours COAM formation which is due to stronger hydrogen bonding between the mixed molecules when compared with the individual components. A small  $\Delta(\delta h)$  value seems to favour COAM formation suggesting molecules with similar hydrogen-bonding potential are more likely to interact and stabilise a COAM system.

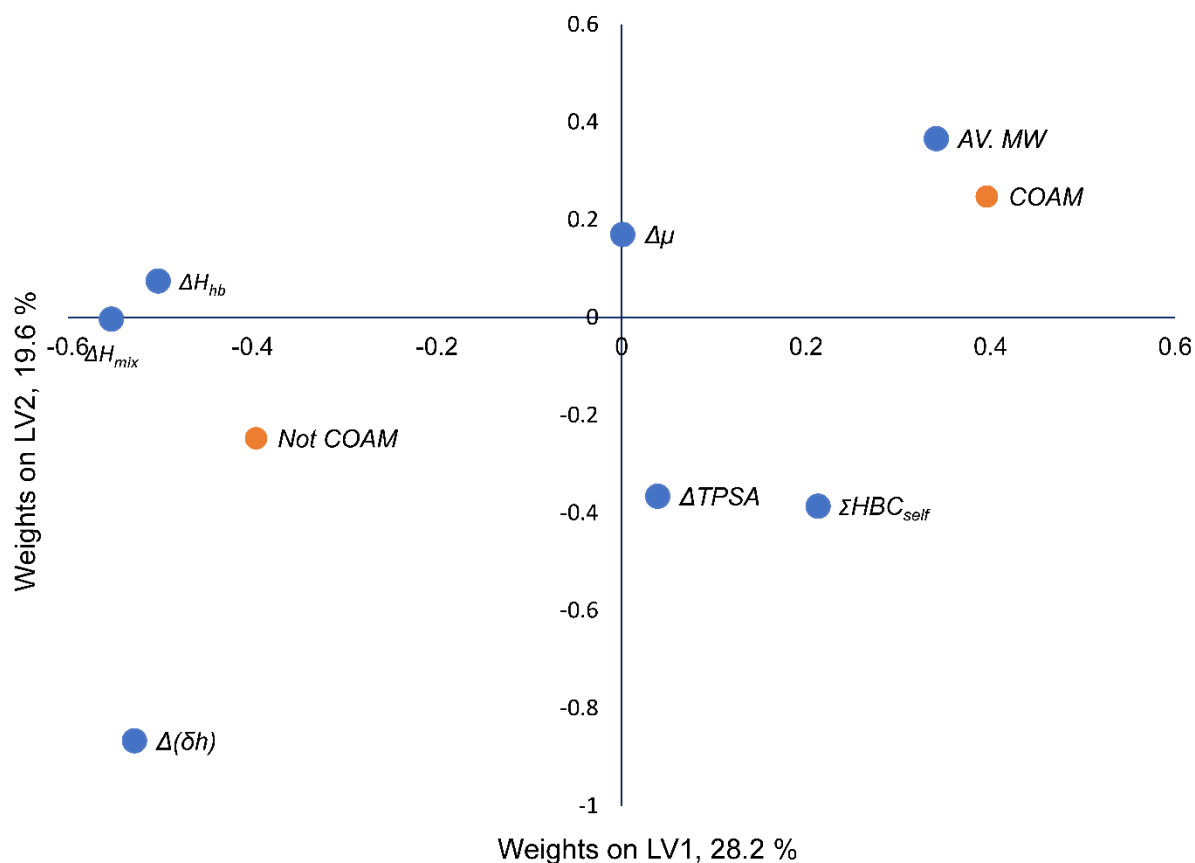


Figure 2.5. PLS-DA loading weights scatter plot of the latent variables (LV) 1 and 2. The responses are shown with orange circles and the variables with blue circles. The responses show how the two groups are related to the variables.

The score plot (Figure 2.4) shows the two clusters of COAM and not COAM samples overlap to some degree. Overall, the misclassification table (which shows if the prediction matches the experimental result) (Table 2.4) of the 120 API – amino acid dataset shows that 81% of the data points are correctly placed, suggesting the PLS-DA model is successful at modelling the amino acid data. Out of the 23 misplaced systems, 18 are close to the separation line and five are very far from the separation line, these five systems are MEB with LYS, LEU and ILE, SIM with LYS, and IND with HIS. The MEB with LYS, LEU and ILE and SIM with LYS systems were shown by Kasten *et al.*<sup>54</sup> to have a low stability and underwent crystallisation within a few weeks suggesting the model helps identify stable COAM systems. The fifth system furthest from the separation line was IND with HIS which was not COAM by milling, however a study by Jensen *et al.*<sup>55</sup> showed IND with HIS system was co-amorphous when spray dried, this suggest the model could be valid for other co-amorphous production methods.

Table 2.4. Misclassification table showing the percentage of correctly assigned observations of the 120 API-amino acid combinations. Fisher's probability of  $4.7 \times 10^{-8}$ .

Model	Members	Correct	Not COAM	COAM
Not COAM	84	90.48%	76	8
COAM	36	58.33%	15	21
Total	120	80.83%	91	29

#### 2.2.4 Prediction of Co-amorphous Formation by Mebendazole with 29 Co-formers

To test the applicability of the PLS-DA model (Figure 2.4, Figure 2.5) to other non-amino acid systems, a new dataset of 29 different co-formers with mebendazole was used (Table 2.2, Figure 2.2). Mebendazole was selected due to it forming a range of both of COAM and not COAM systems with the amino acids; therefore, it was expected to form a range of both COAM and not COAM systems with other co-formers. The 29 co-formers were selected on the basis of being small molecules capable of forming a range of different hydrogen-bonding motifs. The model was applied to predict the classification of the mebendazole co-former mixtures and the prediction was compared to experimental data. The misclassification table (Table 2.5) shows that overall, 86% of the samples were predicted correctly and only four of 29 mixtures were predicted incorrectly. The score plot of the predicted scores (Figure 2.6) shows a clear divide between systems that were COAM and systems that were not COAM, with only a slight overlap of the two clusters.

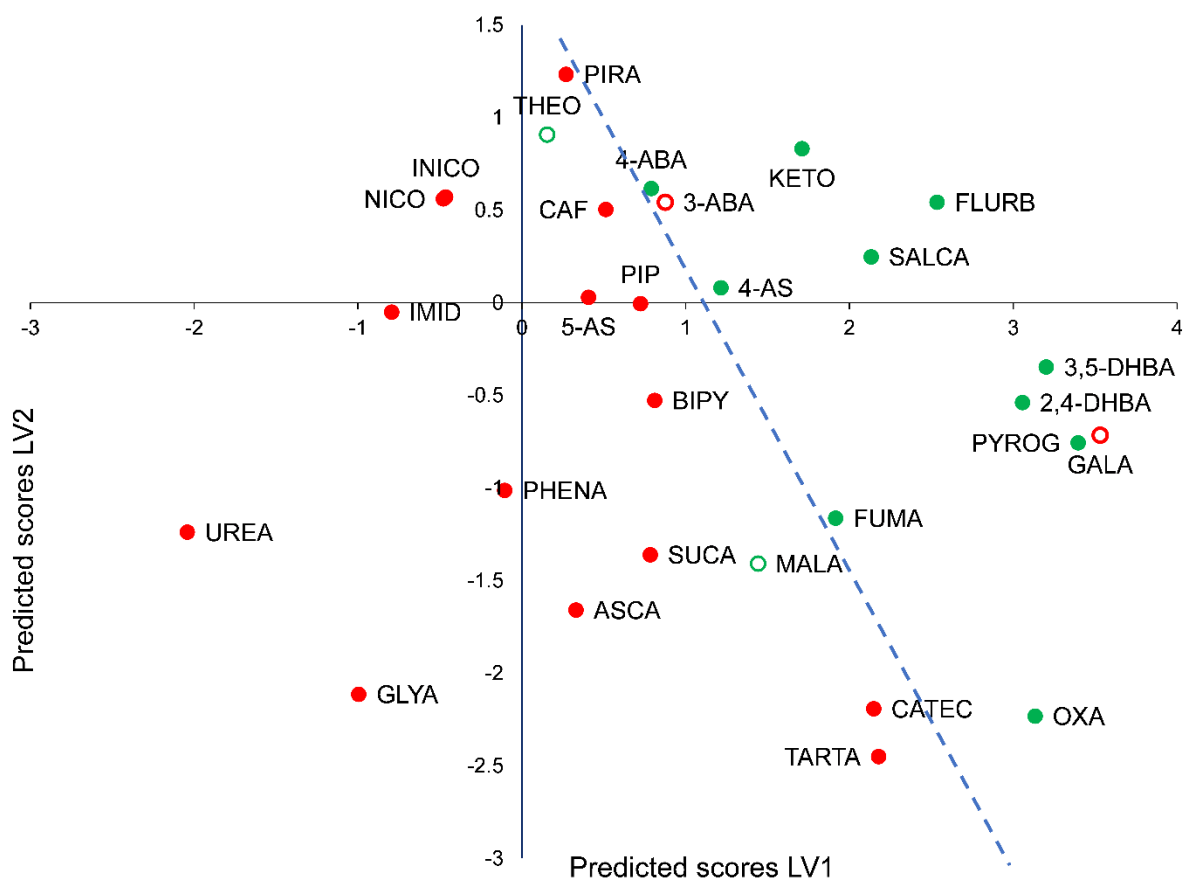


Figure 2.6. Score scatter plot of the predicted scores for the mebendazole-co-former combinations. COAM samples are shown in green, not COAM samples are shown in red. The hollow circles indicate samples which have been predicted incorrectly. The blue dashed line shows the predicted separation line for visualization purposes.

Table 2.5. Misclassification table showing the percentage of correctly assigned observation of the 29 MEB-co-former combinations. Fisher's probability of  $1.8 \times 10^{-4}$ .

Model	Members	Correct	Not COAM	COAM
Not COAM	17	88.24%	15	2
COAM	12	83.33%	2	10
Total	29	86.21%	17	12

The four samples that were predicted incorrectly were MEB combinations with theophylline, 3-aminobenzoic acid, maleic acid and gallic acid, with predicted COAM values of 0.43, 0.52, 0.40 and 0.86, respectively. The COAM values indicate how close the prediction is to assigning the system as COAM or not COAM with a value above 0.5 indicating COAM and a value below 0.5 indicating not COAM. Three of the samples had COAM values close to the cross over point at 0.5, suggesting they were close to being predicted correctly and may have been misplaced by one or two variables having extreme values. Theophylline appears to be incorrectly predicted due to the system having a relatively high value of  $\Delta H_{mix}$  and  $\Delta H_{hb}$  compared to the other systems. 3-aminobenzoic acid was misplaced due to a relatively small/negative  $\Delta H_{mix}$  and  $\Delta H_{hb}$  and a small  $\Delta(\delta h)$ . Maleic acid is misplaced due to a small molecular weight. The gallic acid system is the furthest away from the crossover line between COAM and not COAM systems, suggesting it should be COAM. The mebendazole gallic acid system was investigated using film casting (Figure 2.7) which resulted in a COAM system, this suggests the model is not limited to system produced by only ball milling. Film casting was selected because it involves a thermodynamic pathway with the initial solution containing no crystalline material compared to ball milling which is a kinetic pathway involving the disruption of the crystal lattice.<sup>15</sup> Therefore, film casting is likely to help the formation of a co-amorphous system if the initial crystalline material is too stable to be broken down by ball milling. With the mebendazole gallic acid system now being classed as COAM the misclassification table improves and the correct prediction percentage is now 90 % (Table 2.6). The model now shows an even clearer divide between the two clusters with only a few outliers which are close to the cross over line. Film casting was not used to test other systems due to other co-amorphous formation methods usually producing a similar result.<sup>56, 57</sup>

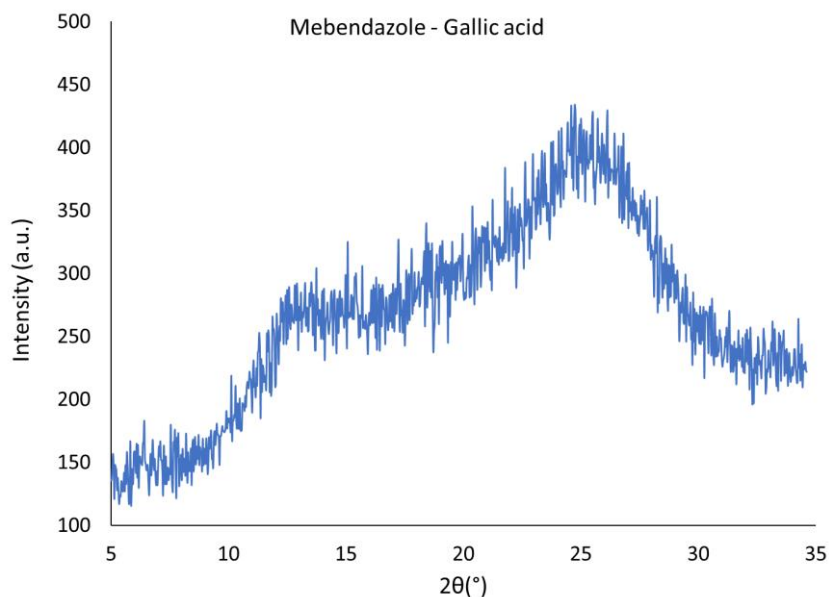


Figure 2.7: XRPD results of an equimolar mixture of mebendazole and gallic acid after film casting.

Table 2.6: Misclassification table showing the percentage of correctly assigned observations of the 29 MEB-co-former combinations after gallic acid was confirmed as being COAM by film casting. Fisher's probability of  $2.4 \times 10^{-5}$ .

Model	Members	Correct	Not COAM	COAM
Not COAM	16	93.75%	15	1
COAM	13	84.62%	2	11
Total	29	89.66%	17	12

### 2.3 Conclusion

Known COAM systems formed with APIs and amino acid co-formers were analysed to identify properties of the co-former that correlate with COAM material formation.<sup>53</sup> A range of 36 variables were used to describe the properties of the API-amino acid systems and a multivariate PLS-DA was used to create a prediction model. The initial 36 variables were reduced to seven variables including  $\Delta H_{hb}$ ,  $\Delta H_{mix}$ ,  $\Sigma HBC_{self}$ ,  $AV$ ,  $MW$ ,  $\Delta TPSA$ ,  $\Delta \mu$  and  $\Delta(\delta h)$ . The model predicts 81% of the API-amino acid systems correctly. The model was tested using a dataset of mebendazole with 29 different co-formers and 90% of the systems were correctly predicted. Overall, the model can predict the potential COAM formation of a range



of co-formers significantly expanding its applicability beyond the relatively limited set of amino acid co-formers.

## 2.4 Experimental

### 2.4.1 Materials

Succinic acid was purchased from Avocado Research Chemicals (Heysham, UK). Glycine (GLY) was purchased from BDH Chemicals Limited (Hull, UK). Carvedilol (CAR) was obtained from Cilpa Ltd. (Mumbai, India). *L*-Alanine (ALA), flurbiprofen, furosemide (FUR), *L*-isoleucine (ILE), *L*-leucine (LEU), *L*-lysine (LYS), mebendazole (MEB) and *L*-tyrosine (TYR) were purchased from Flourochem (Hadfield, UK). Indomethacin (IND) was purchased from Hawkins Pharmaceutical group (Minnesota, USA). Urea was purchased from Lancaster Synthesis (Lancaster, UK). Maleic acid was purchased from M&B Chemicals (London, UK). 3-aminobenzoic acid, 4-aminobenzoic acid, 4-aminosalicylic acid, 5-aminosalicylic acid, *L*-arginine (ARG), ascorbic acid, *L*-asparagine (ASN), *L*-aspartic acid (ASP), 4,4'-bipyridine, caffeine, catechol, *L*-cysteine (CYS), 2,4 dihydroxybenzoic acid, 3,5-dihydroxybenzoic acid, fumaric acid, gallic acid, *L*-glutamine (GLN), *L*-glutamic acid (GLU), glycolic acid, *L*-histidine (HIS), imidazole, isonicotinamide, ketoprofen, *L*-methionine (MET), nicotinamide, oxalic acid, *L*-phenylalanine (PHE), phenazine, piperazine, piracetam, *L*-proline (PRO), pyrogallol, salicylic acid, *L*-serine (SER), tartaric acid, theophylline, *L*-threonine (THR), *L*-tryptophan (TRP) and *L*-valine (VAL) were purchased from Sigma Aldrich (Missouri, USA).

### 2.4.2 X-ray Powder Diffraction (XRPD)

XRPD measurements were performed using a Bruker D8 X-ray diffractometer (Billerica, Massachusetts) with CuK $\alpha$  radiation (1.54187 Å), and acceleration voltage and current of 40 kV and 40 mA, respectively. The samples were scanned in reflectance mode between 2° and 35° 2 $\theta$  with a scan rate of 0.067335° 2 $\theta$ /s and a step size of 0.026°.

### 2.4.3 Mebendazole Co-former Screening

Ball milling was used to screen for potential COAM systems. A 1:1 molar ratio of API and co-former (total 100 mg), was placed into a 5 mL milling jar and premixed at a frequency of 30 Hz for 5 minutes without a mixing ball to homogenize the material. A stainless-steel ball with a diameter of 5 mm was added and the mixture was milled at 30 Hz for 60 min. The milling time of 60 min was selected due to it matching the original study the model was

produced from.<sup>53</sup> Milling was performed using a Mixer mill MM200, vibrational ball mill, from Retsch GmbH & Co. (Haan, Germany). The mixtures were analysed by XRPD to assess crystallinity (see below).

#### 2.4.4 Film Casting Mebendazole – Gallic acid

A 1:1 molar ratio of mebendazole to gallic acid (63.5 mg: 36.5 mg), was dissolved in a minimum amount of formic acid (approx. 10 mL). The solution was cast onto a petri dish and the formic acid was left to evaporate. Once the mixture was dry, it was analysed by XRPD.

#### 2.4.5 COSMOquick Calculations

COSMOquick version 1.7 (COSMOlogic GmbH & Co. KG, Leverkusen, Germany) was used to calculate the Gibbs energy of mixing ( $\Delta G_{mix}$ ), excess enthalpy of mixing ( $\Delta H_{mix}$ ) and excess enthalpy of hydrogen bonding ( $\Delta H_{hb}$ ), of the two-component system. For each component the following variables were calculated and are displayed in Table 2.3: the number of *Rotatable bonds*; *rotbsdmod*, a general molecular flexibility parameter; *M2*, *M3*, *M4*, *M5* and *M6*, the different order sigma moments; the dielectric energy; the molecular COSMO volume; *Macc1*, *Macc2*, *Macc3* and *Macc4*, the different order sigma acceptor moments; *Mdon1*, *Mdon2*, *Mdon3* and *Mdon4*, the different order sigma donor moments; *avratio*, the surface-volume ratio based on COSMO; *ovality*, the ratio of the molecular COSMO area to the area of a sphere with the same volume as the molecule;  $\mu$ , the pseudo chemical potential of the pure solute;  $\delta d$ , the Hansen parameter for dispersion;  $\delta p$ , the Hansen parameter for permanent dipole-dipole interaction;  $\delta h$ , the Hansen parameter for hydrogen bonding. The difference between the API and co-former values were calculated and used as the variables in the PLS-DA.

#### 2.4.6 Partial Least Squares – Discriminant Analysis

Partial least squares – discriminant analysis (PLS-DA) was performed using SIMCA V.16 (Umetrics, Umeå, Sweden) to plot 36 variables for each combination of API and co-former.<sup>58</sup>

<sup>59</sup> The 36 different variables plotted were  $\Delta G_{mix}$ ,  $\Delta H_{mix}$ ,  $\Delta H_{hb}$ ,  $\Delta \log P$ ,  $AV.\log P$ ,  $\Sigma HBC_{self}$ ,  $\Sigma HBC_{API-COF}$ ,  $AV.TM$ ,  $\Delta TM$ ,  $AV.MW$ ,  $\Delta MW$ ,  $AV.TPSA$ ,  $\Delta TPSA$ ,  $\Delta Rotatable\ bonds$ ,  $\Delta rotbsdmod$ ,  $\Delta M2$ ,  $\Delta M3$ ,  $\Delta M4$ ,  $\Delta M5$ ,  $\Delta M6$ ,  $\Delta Dielectric\ energy$ ,  $\Delta volume$ ,  $\Delta Macc1$ ,  $\Delta Macc2$ ,  $\Delta Macc3$ ,  $\Delta Macc4$ ,  $\Delta Mdon1$ ,  $\Delta Mdon2$ ,  $\Delta Mdon3$ ,  $\Delta Mdon4$ ,  $\Delta avratio$ ,  $\Delta ovality$ ,  $\Delta \mu$ ,  $\Delta(\delta d)$ ,  $\Delta(\delta p)$  and  $\Delta(\delta h)$  (Table 2.3). The data was scaled using unit variance. Each system was assigned as

either COAM or not COAM (any crystalline material present) as determined by Kasten *et al.*<sup>53</sup> based on analysing the mixture by XRPD after ball milling for 60 minutes. The PLS-DA was fitted using two latent variables and all 36 variables. The quality of the model was assessed using an internal cross-validation procedure which involved leaving one out using seven cross-validation groups.

The prediction ability of the model was assessed by checking the predicted values of COAM formation of the 120 API-amino acid dataset and comparing the values with the experimental results. The prediction gives a predicted numerical value with a value closer to one being COAM and a value closer to zero being not COAM. The prediction of the model was also assessed by using a dataset of 29 co-formers paired with mebendazole. The predicted values for the mebendazole-co-former dataset were compared with the experimental values to determine the prediction ability.

Variable selection was used to reduce the number of variables from 36 to 7 based on optimising the number of correctly predicted samples for the API-amino acid dataset. The final model was produced in JMP Pro 15 to view the equation used to assign the COAM value (Equation 2.1).<sup>60</sup>

## 2.5 References

1. L. Di, P. V. Fish and T. Mano, *Drug. Discov. Today*, 2012, **17**, 486-495.
2. K. T. Savjani, A. K. Gajjar and J. K. Savjani, *ISRN Pharm.*, 2012, **2012**, 195727-195727.
3. S. Kalepu and V. Nekkanti, *Acta Pharm. Sin. B.*, 2015, **5**, 442-453.
4. P. Khadka, J. Ro, H. Kim, I. Kim, J. T. Kim, H. Kim, J. M. Cho, G. Yun and J. Lee, *Asian J. Pharm. Sci.*, 2014, **9**, 304-316.
5. H. D. Williams, N. L. Trevaskis, S. A. Charman, R. M. Shanker, W. N. Charman, C. W. Pouton and C. J. Porter, *Pharmacol. Rev.*, 2013, **65**, 315-499.
6. D. J. Berry and J. W. Steed, *Adv. Drug. Deliv. Rev.*, 2017, **117**, 3-24.
7. S. Khodadadi and G. M. H. Meesters, *Amorphous APIs: Improved Release, Preparation, Characterization*, in *Particles and Nanoparticles in Pharmaceutical Products: Design, Manufacturing, Behavior and Performance*, Springer International Publishing, Cham, Switzerland, 1st edn., 2018, pp. 329-346.
8. A. M. Healy, Z. A. Worku, D. Kumar and A. M. Madi, *Adv. Drug Deliv. Rev.*, 2017, **117**, 25-46.
9. E. O. Kissi, H. Grohgan, K. Lobmann, M. T. Ruggiero, J. A. Zeitler and T. Rades, *J. Phys. Chem. B*, 2018, **122**, 2803-2808.
10. M. Rams-Baron, R. Jachowicz, E. Boldyreva, D. Zhou, W. Jamroz and M. Paluch, *Physical Instability: A Key Problem of Amorphous Drugs*, in *Amorphous Drugs: Benefits and Challenges*, Springer International Publishing, Cham, Switzerland, 1st edn., 2018, pp. 107-157.

11. Y. Sun, L. Zhu, T. Wu, T. Cai, E. M. Gunn and L. Yu, *AAPS J.*, 2012, **14**, 380-388.
12. G. Van Den Mooter, *Drug Discov. Today Technol.*, 2012, **9**, e71-e174.
13. W. Wu, K. Lobmann, J. Schnitzkewitz, A. Knuhtsen, D. S. Pedersen, H. Grohganz and T. Rades, *Int. J. Pharm.*, 2018, **549**, 380-387.
14. X. Ma and R. O. Williams, *J. Drug Deliv. Sci. Tec.*, 2019, **50**, 113-124.
15. A. Karagianni, K. Kachrimanis and I. Nikolakakis, *Pharmaceutics*, 2018, **10**, 98.
16. T. Vasconcelos, S. Marques, J. das Neves and B. Sarmento, *Adv. Drug Deliv. Rev.*, 2016, **100**, 85-101.
17. L. H. Nielsen, T. Rades and A. Müllertz, *Int. J. Pharm.*, 2015, **490**, 334-340.
18. R. B. Chavan, S. Rathi, V. G. S. S. Jyothi and N. R. Shastri, *Asian J. Pharm. Sci.*, 2019, **14**, 248-264.
19. S. Baghel, H. Cathcart and N. J. O'Reilly, *J. Pharm. Sci.*, 2016, **105**, 2527-2544.
20. D. S. Frank and A. J. Matzger, *Mol. Pharm.*, 2018, **15**, 2714-2720.
21. D. Medarević, J. Djuriš, P. Barmpalexis, K. Kachrimanis and S. Ibrić, *Pharmaceutics*, 2019, **11**, 372.
22. P. J. Marsac, H. Konno, A. C. Rumondor and L. S. Taylor, *Pharm. Res.*, 2008, **25**, 647-656.
23. A. C. Rumondor, P. J. Marsac, L. A. Stanford and L. S. Taylor, *Mol. Pharm.*, 2009, **6**, 1492-1505.
24. Y. Tian, D. S. Jones and G. P. Andrews, *Mol. Pharm.*, 2015, **12**, 1180-1192.
25. Q. Shi, S. M. Moinuddin and T. Cai, *Acta. Pharm. Sin. B*, 2019, **9**, 19-35.
26. A. Newman, S. M. Reutzel-Edens and G. Zografi, *J. Pharm. Sci.*, 2018, **107**, 5-17.
27. A. Shayanfar and A. Jouyban, *J. Pharm. Innov.*, 2013, **8**, 218-228.
28. Y. Gao, J. Liao, X. Qi and J. Zhang, *Int. J. Pharm.*, 2013, **450**, 290-295.
29. Z. Wang, M. Sun, T. Liu, Z. Gao, Q. Ye, X. Tan, Y. Hou, J. Sun, D. Wang and Z. He, *Asian J. Pharm. Sci.*, 2019, **14**, 95-103.
30. K. T. Jensen, F. H. Larsen, K. Lobmann, T. Rades and H. Grohganz, *Eur. J. Pharm. Biopharm.*, 2016, **107**, 32-39.
31. M. Karimi-Jafari, L. Padrela, G. M. Walker and D. M. Croker, *Cryst. Growth Des.*, 2018, **18**, 6370-6387.
32. K. Löbmann, H. Grohganz, R. Laitinen, C. Strachan and T. Rades, *Eur. J. Pharm. Biopharm.*, 2013, **85**, 873-881.
33. K. Löbmann, C. Strachan, H. Grohganz, T. Rades, O. Korhonen and R. Laitinen, *Eur. J. Pharm. Biopharm.*, 2012, **81**, 159-169.
34. K. Löbmann, R. Laitinen, C. Strachan, T. Rades and H. Grohganz, *Eur. J. Pharm. Biopharm.*, 2013, **85**, 882-888.
35. K. Löbmann, R. Laitinen, H. Grohganz, C. Strachan, T. Rades and K. Gordon, *Int. J. Pharm.*, 2012, **453**, 80-87.
36. R. B. Chavan, R. Thipparaboina, D. Kumar and N. R. Shastri, *Int. J. Pharm.*, 2016, **515**, 403-415.
37. P. Hoppu, S. Hietala, S. Schantz and A. M. Juppo, *Eur. J. Pharm. Biopharm.*, 2009, **71**, 55-63.
38. J. Knapik, Z. Wojnarowska, K. Grzybowska, K. Jurkiewicz, L. Tajber and M. Paluch, *Mol. Pharmaceutics*, 2015, **12**, 3610-3619.
39. A. Teja, P. B. Musmade, A. B. Khade and S. J. Dengale, *Eur. J. Pharm. Sci.*, 2015, **78**, 234-244.

40. M. J. Goodwin, O. M. Musa, D. J. Berry and J. W. Steed, *Cryst. Growth Des.* , 2018, **18**, 701-709.
41. W. Fan, W. Zhu, X. Zhang, Y. Xu and L. Di, *RSC Adv.*, 2019, **9**, 22263-22273.
42. S. Yamamura, H. Gotoh, Y. Sakamoto and Y. Momose, *Int. J. Pharm.*, 2002, **241**, 213-221.
43. A. Ahmed Mahmoud Abdelhaleem, A. Adel Ahmed and M. Ibrahim Abdullah, *Acta Pharm.*, 2015, **65**, 133-146.
44. J. Mishra, T. Rades, K. Lobmann and H. Grohgan, *Pharmaceutics*, 2018, **10**, 47.
45. Y. Hu, K. Gniado, A. Erxleben and P. McArdle, *Cryst. Growth Des.* , 2014, **14**, 803-813.
46. N. Chieng, J. Aaltonen, D. Saville and T. Rades, *Eur. J. Pharm. Biopharm.*, 2009, **71**, 47-54.
47. L. I. Blaabjerg, E. Lindenberg, T. Rades, H. Grohgan and K. Lobmann, *Int. J. Pharm.*, 2017, **521**, 232-238.
48. R. Mizoguchi, H. Waraya and Y. Hirakura, *Mol. Pharm.*, 2019, **16**, 2142-2152.
49. A. Klamt, *Wiley Interdiscip. Rev. Comput. Mol. Sci.*, 2018, **8**, e1338.
50. C. Loschen and A. Klamt, *J. Pharm. Pharmacol.*, 2015, **67**, 803-811.
51. H. Ueda, N. Muranushi, S. Sakuma, Y. Ida, T. Endoh, K. Kadota and Y. Tozuka, *Pharm. Res.*, 2016, **33**, 1018-1029.
52. H. Meng-Lund, G. Kasten, K. T. Jensen, A. Poso, T. Pantsar, T. Rades, J. Rantanen and H. Grohgan, *Eur. J. Pharm. Sci.*, 2018, **119**, 31-38.
53. G. Kasten, H. Grohgan, T. Rades and K. Lobmann, *Eur. J. Pharm. Sci.*, 2016, **95**, 28-35.
54. G. Kasten, K. Lobmann, H. Grohgan and T. Rades, *Int. J. Pharm.*, 2019, **557**, 366-373.
55. K. T. Jensen, L. I. Blaabjerg, E. Lenz, A. Bohr, H. Grohgan, P. Kleinebudde, T. Rades and K. Löbmann, *J. Pharm. Pharmacol.*, 2016, **68**, 615-624.
56. A. W. Lim, K. Löbmann, H. Grohgan, T. Rades and N. Chieng, *J. Pharm. Pharmacol.*, 2016, **68**, 36-45.
57. P. Karmwar, K. Graeser, K. C. Gordon, C. J. Strachan and T. Rades, *Int. J. Pharm.*, 2011, **417**, 94-100.
58. R. G. Brereton and G. R. Lloyd, *J. Chemom.*, 2014, **28**, 213-225.
59. H. Sadeghi-Bazargani, A. Banani and S. Mohammadi, *2010 World Automation Congress*, 2010, 1-9.
60. JMP, Version Pro 15, SAS Institute Inc., Cary, NC, 1989-2020

## 3 Prediction and Preparation of Co-amorphous Phases of a Bislactam

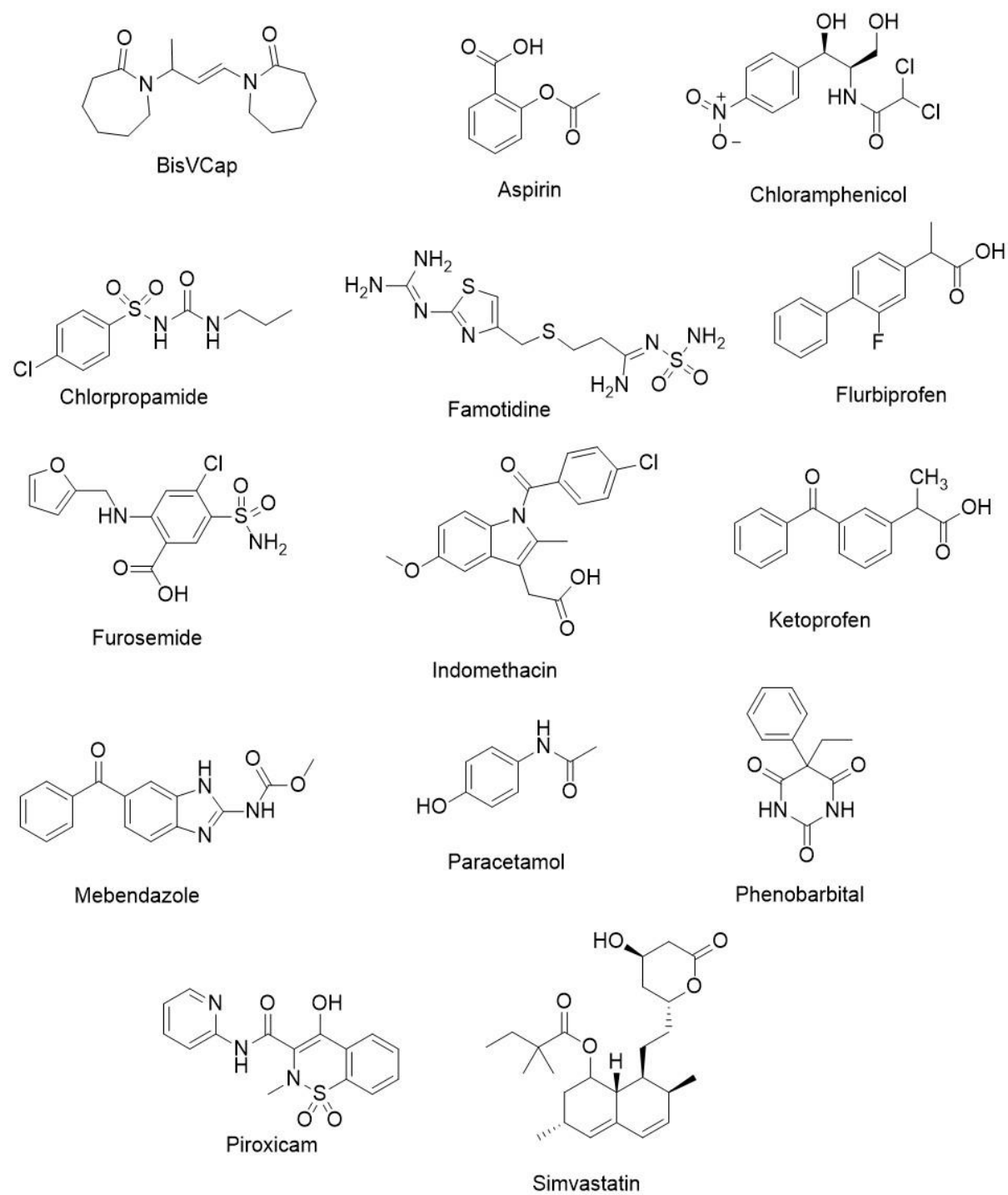
### 3.1 Introduction

Current trends in the discovery of active pharmaceutical ingredients (APIs) are towards an increase in the number of APIs which are part of the classes II or IV in the biopharmaceutical classification system meaning they are poorly soluble in aqueous solutions.<sup>1-5</sup> One reason for the lower solubility, in some cases, is that the APIs form a highly ordered crystalline state which is thermodynamically stable and difficult to break down.<sup>6, 7</sup> One method to increase the solubility of the APIs involves stabilising them in an amorphous form with a small molecule co-former as a co-amorphous (COAM) system.<sup>8-18</sup> COAM systems have been discussed in detail in Chapter 1 and Chapter 2.

Having designed a partial least squares – discriminant analysis (PLS-DA) model using a dataset of amino acids with six APIs to predict COAM formation in Chapter 2, in this Chapter this model will be applied to a new dataset not containing amino acids.<sup>19, 20</sup> To achieve this bisvinylcaprolactam (BisVCap) was selected as co-former and screened with a range of APIs. BisVCap has previously been shown by Goodwin *et al.* to stabilise a range of APIs in the COAM state.<sup>21</sup>

BisVCap (Scheme 3.1) is the unsaturated dimer of vinylcaprolactam and contains two highly polar lactam carbonyl groups which act as hydrogen bond acceptor sites.<sup>21-24</sup> BisVCap is structurally similar to the polymer polyvinylpyrrolidone (PVP) which contains a five-membered ring as opposed to bisVCap's seven-membered rings. One use of PVP is in the formation of polymeric amorphous solid dispersion (PASD) where it stabilises a range of APIs in an amorphous state.<sup>25-29</sup> PASDs involve mixing an API with a polymer which acts as a stabiliser and prevents the API from crystallising by producing a kinetic energy cost to movement.<sup>30</sup> The main disadvantages of PASDs are that they are usually hygroscopic and require a large ratio of polymer to API for the system to remain stable, this causes larger tablets required for a particular dosage which reduces patient compliance.<sup>31, 32</sup> BisVCap is shown to be significantly less hygroscopic compared to PVP with dynamic vapour sorption (DVS) study showing amorphous bisVCap displays a mass increase of 1.2 % when at 90% relative humidity compared to a 40% mass increase of PVP at 80% relative humidity.<sup>21</sup>

Scheme 3.1. Chemical structure of bisVCap and the 13 APIs used in the COAM screen.



In this Chapter, the reliability of the prediction model from Chapter 2 is tested with bisVCap by applying the model to the COAM screen performed by Goodwin *et al.* and a new COAM screen involving combining bisVCap with a further 13 APIs by both co-melting (CM) and rapid solvent evaporation (RSE).<sup>19, 21</sup> COAM formation was confirmed by XRPD, DSC and HSM. FTIR was used to analyse the potential interactions formed between bisVCap and each API to understand the nature of the stabilisation. A stability study of three of the resulting co-amorphous systems was performed at two different temperatures to determine if the location in the prediction space correlates with the stability of the system. The COAM system formed from bisVCap furosemide was studied further with an increased ratio of furosemide to see if the system remains stable and a study at a variety of humidities to determine long term storage stability.

## 3.2 Results and Discussion

### 3.2.1 Testing Model with Literature Co-amorphous Screen

The results of the COAM screen of bisVCap (Scheme 3.1) with a range of APIs previously published by Goodwin *et al.*<sup>21</sup> were analysed using a co-amorphous PLS-DA prediction model introduced in Chapter 2 to investigate the effectiveness of the model with bisVCap systems.<sup>19</sup> The model from Chapter 2 was created using a dataset containing amino acid co-formers with six APIs, however, it was shown to work well at predicting systems containing mebendazole with a small molecule co-former, therefore it is expected to work well with the bisVCap systems. The COAM screen involved 12 bisVCap API systems made by co-melting the two components and then cooling to room temperature. Three of the APIs used (ibuprofen, tolfenamic acid and ethionamide) decompose after their melting point, therefore the systems were removed from this study. Mexiletine and metformin were also removed from the study because they are hydrochloride salts, and the prediction model has not been designed to consider ionic compounds. From the remaining seven systems, the experimental results showed that three form COAM systems whilst the other four do not (Table 3.1).



Table 3.1: Results of an experimental co-amorphous screen from Goodwin *et al.*<sup>21</sup> compared to the predicted result using the prediction model from Chambers *et al.*<sup>19</sup>

API	Label	Experimental COAM	Predicted COAM	Correctly predicted
Benzocaine	BENZ	N	N	Y
Caffeine	CAFF	N	N	Y
Carbamazepine	CARB	Y	N	N
Carisoprodol	CARI	Y	N	N
Dopamine	DOPA	N	N	Y
Isoniazid	ISON	N	N	Y
Valsartan	VALS	Y	Y	Y

The prediction model produced a score plot which was used to visually represent how close each system was to the predicted crossover line between COAM and non-COAM systems (Figure 3.1). The model correctly predicts 71% of this sample set with a Fisher's probability of 0.43. The two systems incorrectly predicted are carbamazepine and carisoprodol which were experimentally COAM but are predicted not to be COAM. The Fourier-transform infrared spectra (FTIR) of the co-amorphous systems of bisVCap with carbamazepine and carisoprodol reported by Goodwin *et al.* displays the original hydrogen bonding structure breaking due to the API carbonyl peaks shifting to a higher wavenumber, but the bisVCap carbonyl peaks just broaden and do not shift to a lower wavenumber indicating the bisVCap carbonyls are not forming new hydrogen bonds with the API.<sup>21</sup> The incorrect prediction of carbamazepine and carisoprodol could therefore indicate the model is based around the potential formation of stabilising intermolecular bonds between the two components.

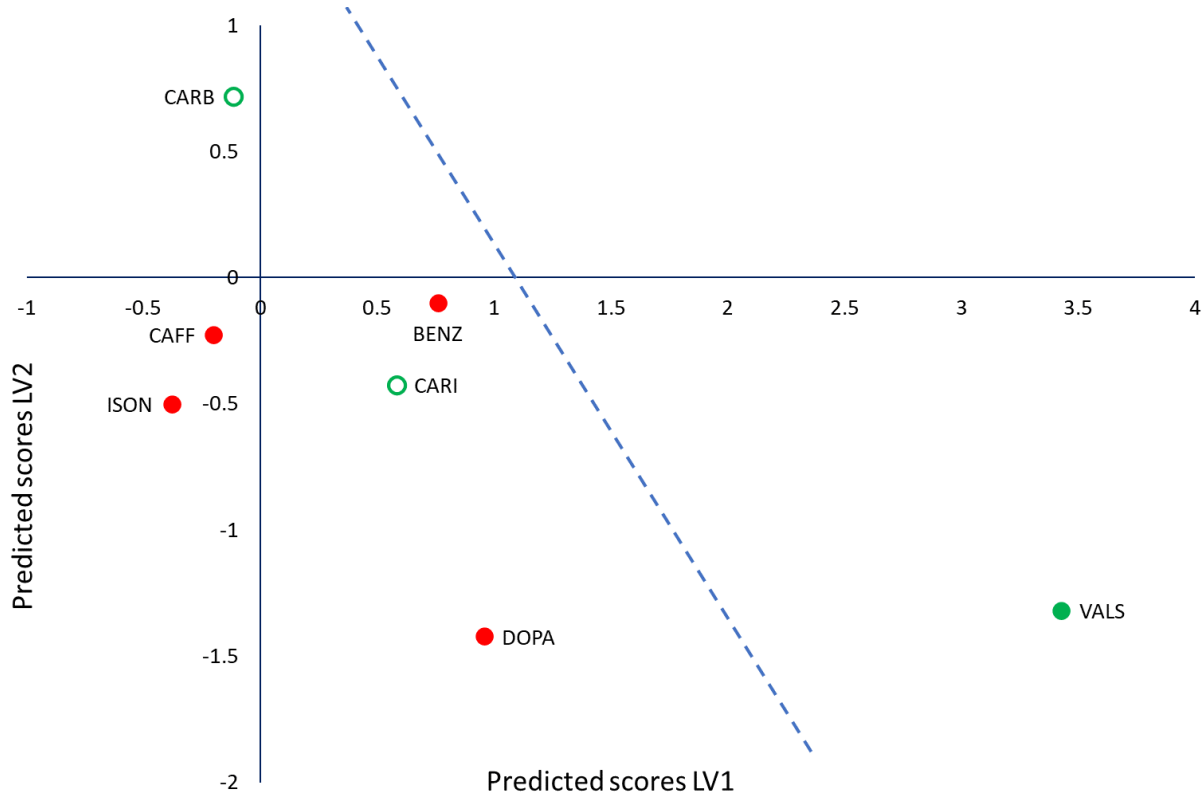


Figure 3.1: PLS-DA score scatter plot of latent variables (LV) 1 and 2. The colour of the markers displays the results of the experimental screen by Goodwin *et al.*<sup>21</sup> with red markers indicating not COAM systems and green markers indicating COAM systems. Samples incorrectly predicted by the prediction model are shown as hollow circles.<sup>19</sup> The blue dashed line shows the predicted separation line between COAM and not COAM systems for visualization purposes.

### 3.2.2 Testing Model with the New BisVCap Co-amorphous Screen

To determine the applicability of the model a chemically different range of 13 different APIs (Scheme 3.1) were selected and paired with BisVCap. The systems were initially analysed using the prediction model which predicted ten out of thirteen should be COAM (Table 3.2). To confirm these predictions bisVCap was mixed in a 1:1 molar ratio with each API and melted using hot-stage microscopy (HSM), after the sample had completely melted it was flash cooled using a freezer block and then stored at room temperature. The mixture was monitored for signs of recrystallisation after 24 hours using an optical microscope (Table 3.3). The HSM screen showed that bisVCap by itself recrystallises however when mixed with any of the APIs no recrystallisation occurs, showing the APIs used stabilise bisVCap in an amorphous state. Pure famotidine, furosemide, mebendazole and piroxicam all undergo

decomposition when heated to near their melting point as shown by the orange decolouration and bubbling. Similar decomposition occurred for bisVCap with famotidine, mebendazole and piroxicam, however, furosemide with bisVCap appears to remain amorphous and minimal decomposition appears to occur on melting. Pure aspirin, chlorpropamide, flurbiprofen, paracetamol and phenobarbital begin to recrystallise after 24 hours showing the amorphous state is unstable, however, the mixes with bisVCap remain amorphous, suggesting bisVCap can stabilise the systems in an amorphous state. Pure chloramphenicol, indomethacin, ketoprofen and simvastatin remain amorphous after 24 hours, and mixtures of these APIs with bisVCap are also amorphous suggesting the interactions between API and bisVCap are preventing the bisVCap from recrystallising.

The combination of bisVCap and the 13 APIs was repeated on a larger scale using both CM and RSE to allow further analysis by XRPD and FTIR (Figure 3.4, Figure 3.5). The two methods CM and RSE were selected to help cover a larger prediction space and to remove any issues caused by the decomposition of samples during CM or difficulty dissolving the samples in some solvents for RSE. Ball milling was not used because bisVCap has a low glass transition temperature ( $T_g$ ) and milling above the  $T_g$  usually leads to polymorphic transformation instead of amorphization, which makes ball milling unsuitable to form COAM systems with bisVCap.<sup>33, 34</sup> The XRPD traces (Figure 3.4) show the same results as observed in the HSM screen with the ten systems that did not decompose producing COAM systems using both CM and RSE. The three systems that decomposed via HSM (famotidine, mebendazole and piroxicam) did not produce a COAM system by RSE.

The ten systems found to be amorphous by HSM and XRPD were analysed by DSC to determine the  $T_g$  and check for decomposition (Figure 3.3). The API was physically mixed with bisVCap and then heated initially during the first DSC heating cycle to form the co-amorphous material. The sample then underwent a cooling ramp to observe if recrystallization occurs. The samples were then subjected to a second heating cycle which is used to identify the  $T_g$ . All of the DSC traces display the API and bisVCap melting in the first heating cycle, no recrystallisation during the cooling cycle and a clear glass transition in the second heating cycle. Each of the ten systems only display a single  $T_g$  confirming the samples as COAM and not a mix of two amorphous materials. The results of the experimental COAM screen are summarised in Table 3.2. Comparing these experimental

results with the predictions of the model shows that 11 of the 13 samples were correctly predicted (Table 3.2). The overall prediction success is therefore 85% suggesting the model is good at predicting bisVCap co-amorphous systems, which is surprising due to the training data set containing only amino acids as the co-former. The PLS-DA score scatter plot shows that the two incorrectly predicted systems paracetamol and mebendazole are close to the prediction separation line (Figure 3.2). It is possible that alternative preparation methods may result in the predicted COAM phase for mebendazole. The mebendazole decomposes during co-melting and is poorly soluble in acetone during RSE.

Table 3.2: The results of the COAM screen including the predicted and experimental results. The prediction includes the predicted COAM value. The experimental COAM screen includes the results from an initial HSM screen, the  $T_g$  from DSC, and the XRPD analysis of both CM and RSE samples. Y indicates the samples were COAM, N indicates the samples were not COAM and D indicates the samples decomposed. The predicted result was also compared with the experimental results to determine if the prediction was correct.

API	Label	Prediction (COAM value)	HSM	DSC ( $T_g/^\circ\text{C}$ )	CM XRPD	RSE XRPD	Correctly predicted
Aspirin	ASPR	Y (0.864)	Y	Y (-19)	Y	Y	Y
Chloramphenicol	CHPL	Y (0.682)	Y	Y (31)	Y	Y	Y
Chlorpropamide	CHPD	Y (0.500)	Y	Y (-4)	Y	Y	Y
Famotidine	FAMO	N (0.463)	D	D	D	N	Y
Flurbiprofen	FLURB	Y (1.096)	Y	Y (-5)	Y	Y	Y
Furosemide	FUR	Y (1.091)	Y	Y (35)	Y	Y	Y
Indomethacin	INDO	Y (1.142)	Y	Y (16)	Y	Y	Y
Ketoprofen	KETO	Y (0.833)	Y	Y (-5)	Y	Y	Y
Mebendazole	MEB	Y (0.556)	D	D	D	N	N
Paracetamol	PARA	N (0.450)	Y	Y (19)	Y	Y	N
Phenobarbital	PHB	Y (0.588)	Y	Y (28)	Y	Y	Y
Piroxicam	PIRO	N (0.443)	D	D	D	N	Y
Simvastatin	SIM	Y (0.751)	Y	Y (12.5)	Y	Y	Y

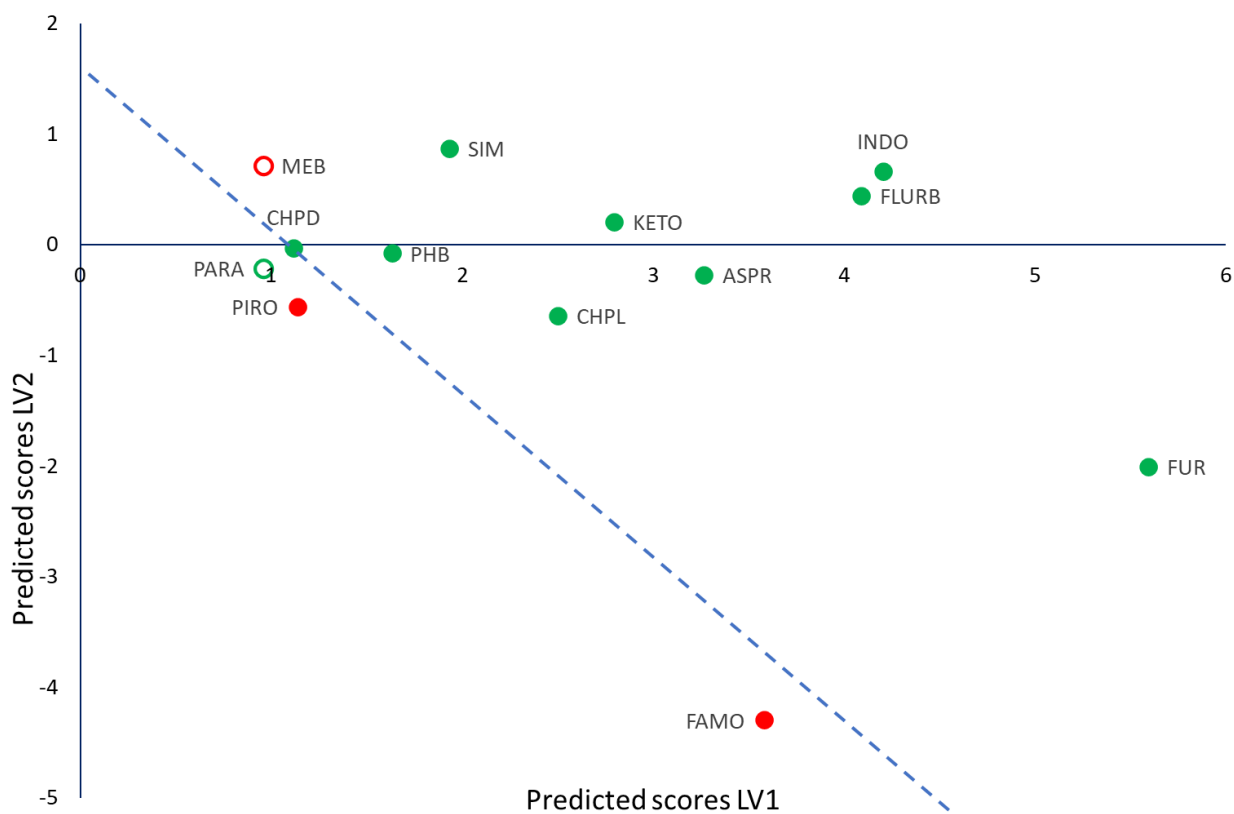


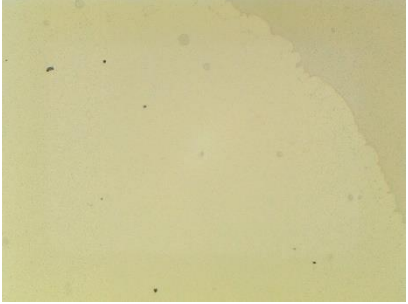
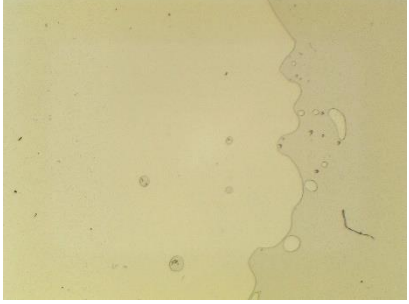
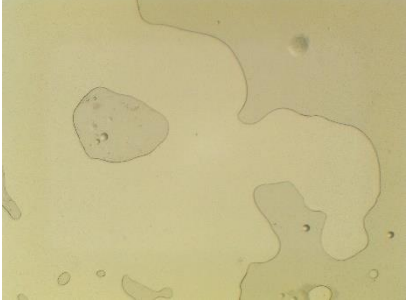
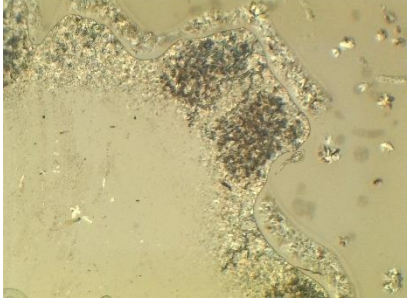
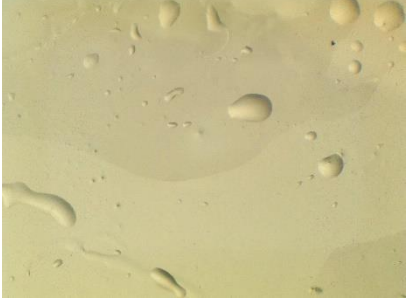
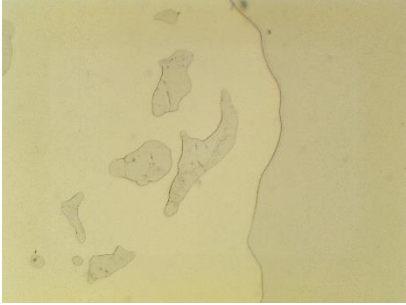
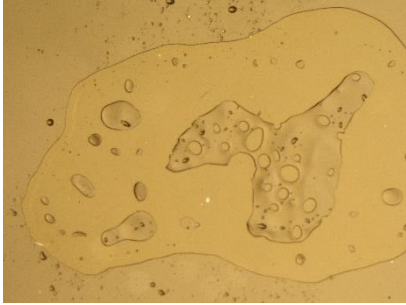


Figure 3.2: PLS-DA score scatter plot of latent variables (LV) 1 and 2. The colour of the markers displays the results of the experimental screen with red markers indicating not COAM systems and green markers indicating COAM systems. Samples incorrectly predicted by the prediction model are shown as hollow circles.<sup>19</sup> The blue dashed line shows the predicted separation line for visualization purposes.

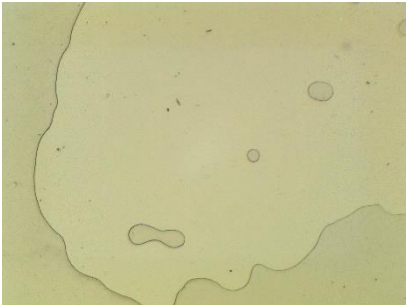
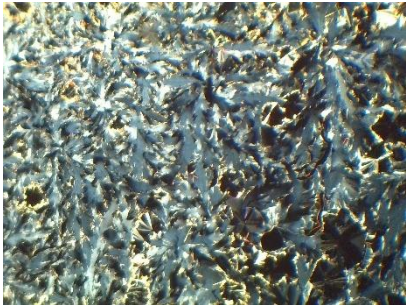
Table 3.3: Optical micrographs of samples melted using an HSM after 24 hours. The first column shows the pure APIs, and the second column shows the APIs in a 1:1 molar ratio with bisVCap.

API	Pure API	API with bisVCap
BisVCap		n/a
Aspirin		
Chloramphenicol		
Chlorpropamide		

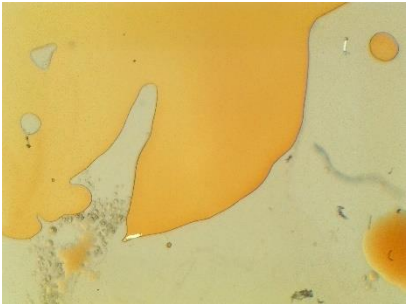
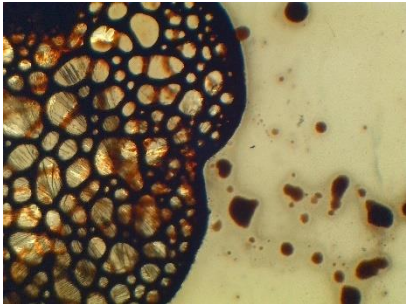
Famotidine



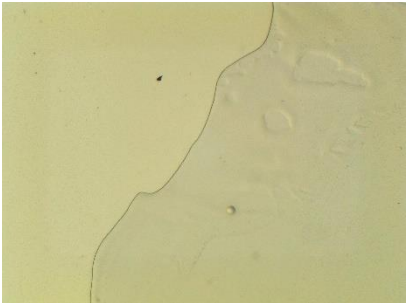
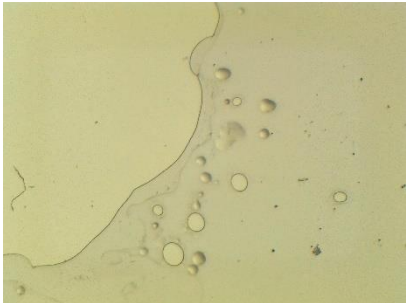
Flurbiprofen



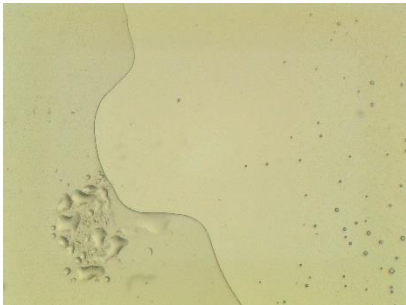
Furosemide



Indomethacin

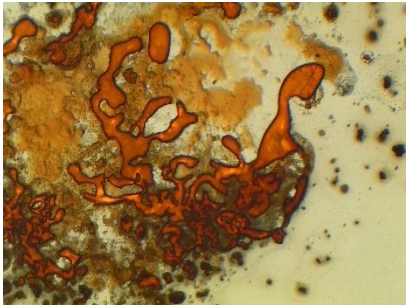


Ketoprofen

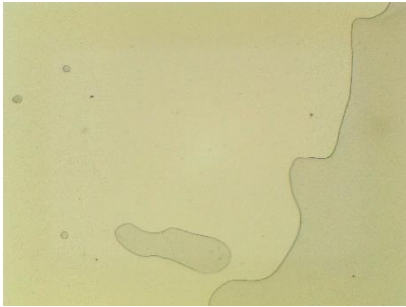
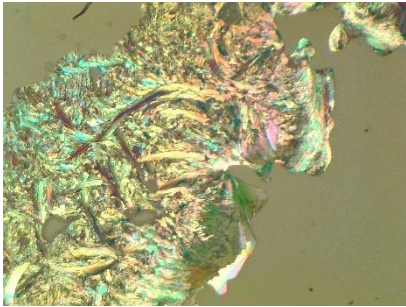




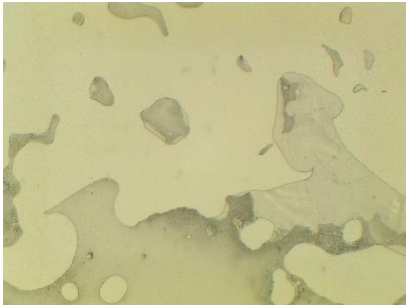
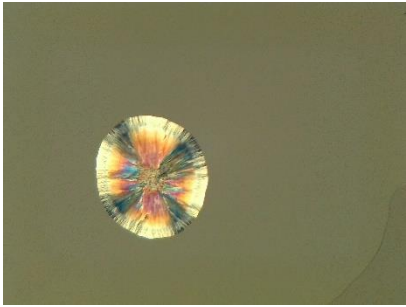
Mebendazole



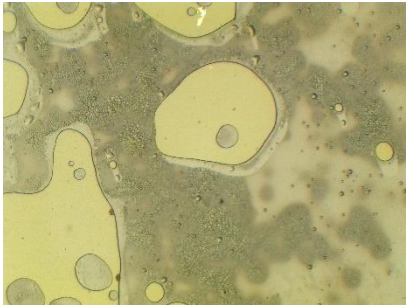
Paracetamol



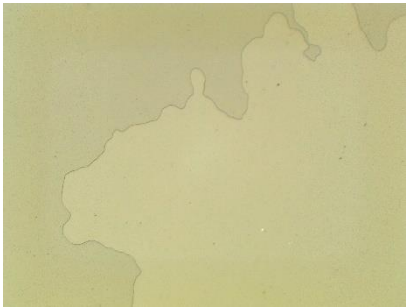
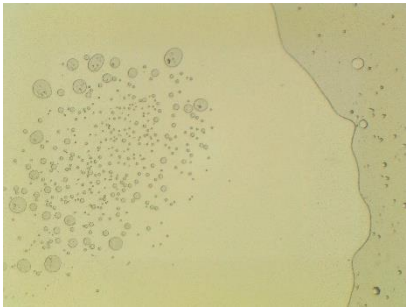
Phenobarbital



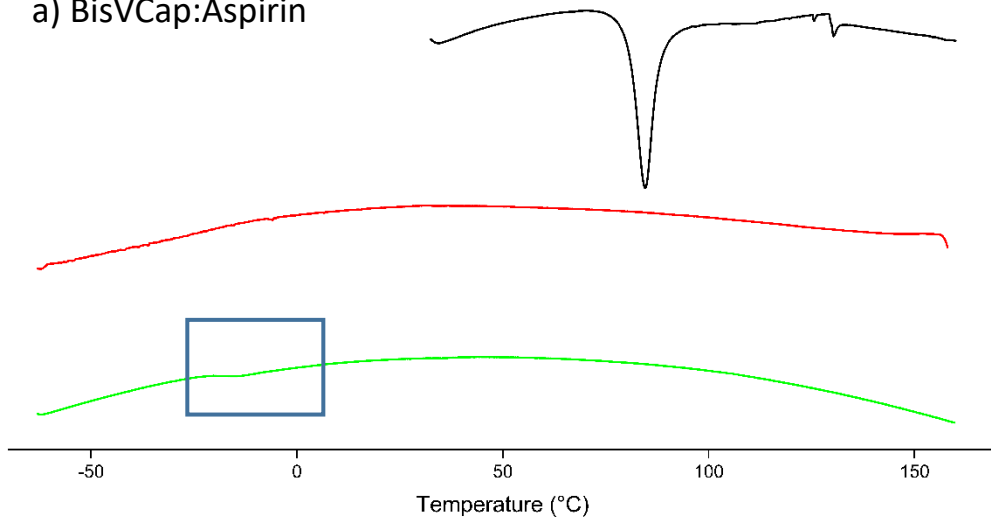
Piroxicam



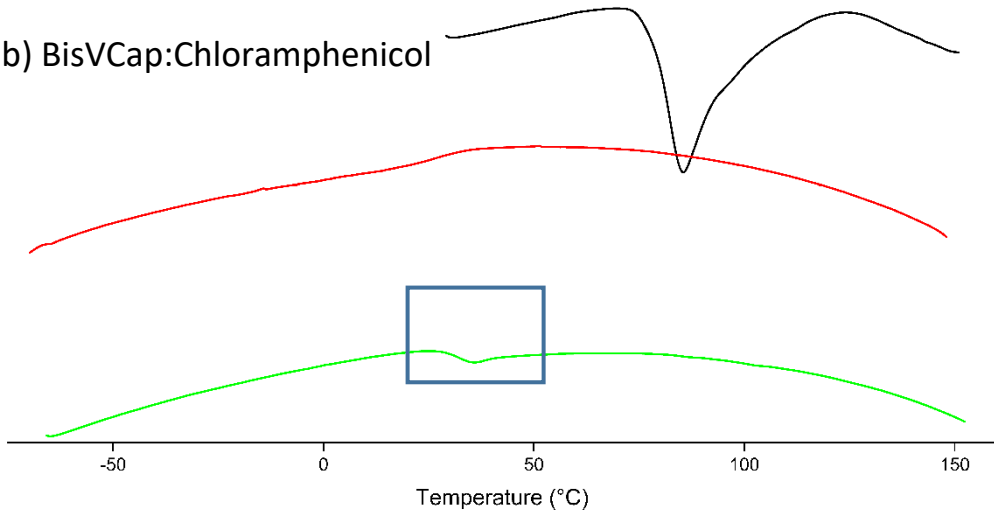
Simvastatin



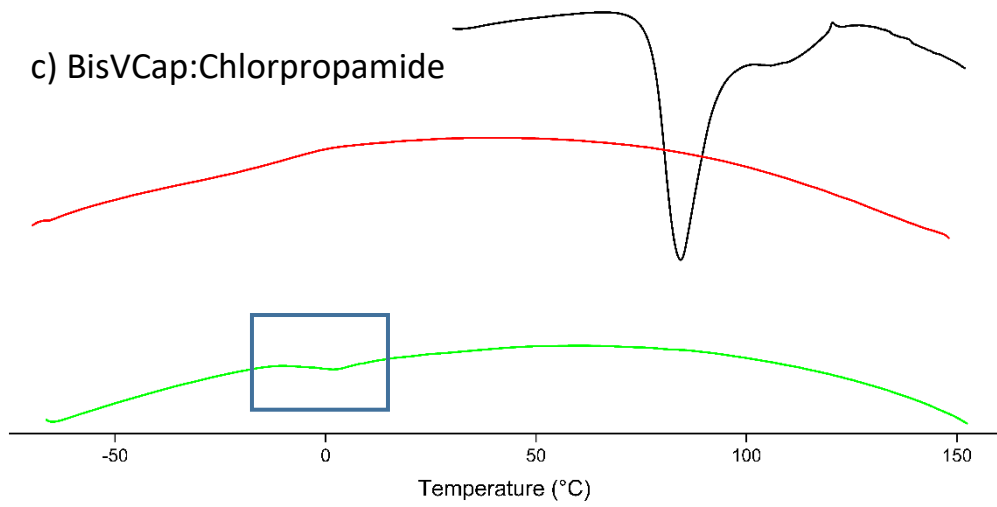
a) BisVCap:Aspirin



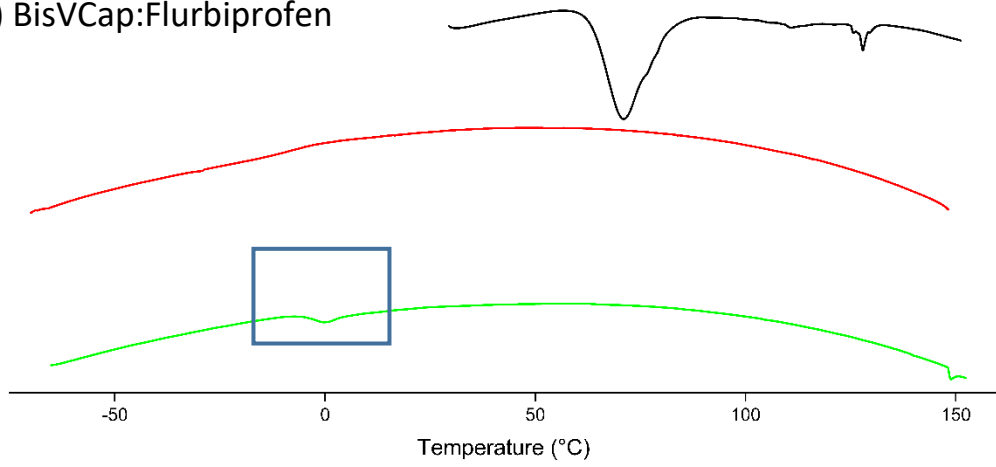
b) BisVCap:Chloramphenicol



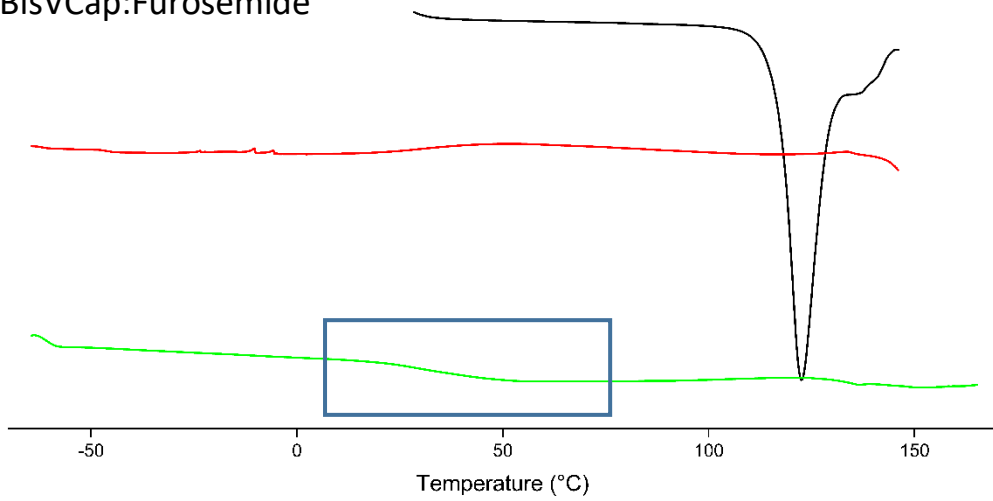
c) BisVCap:Chlorpropamide



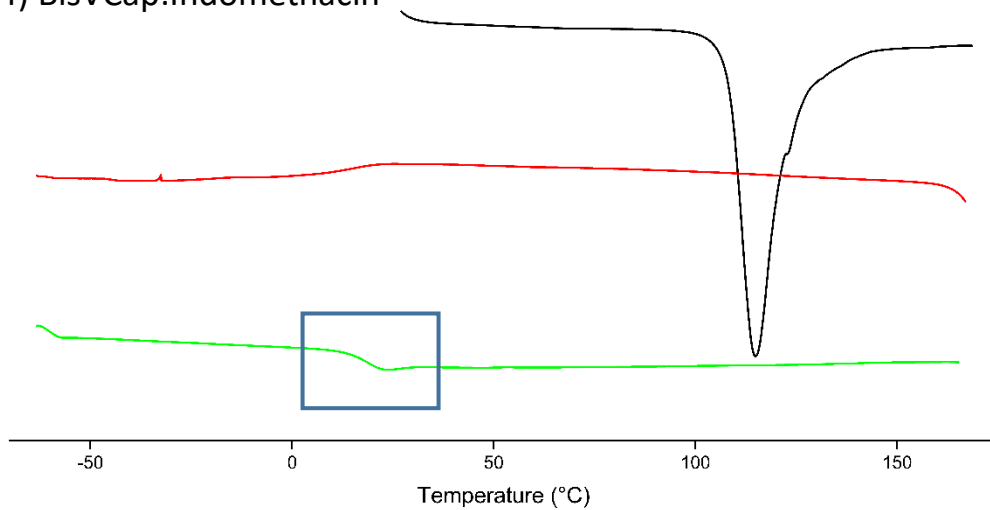
d) BisVCap:Flurbiprofen



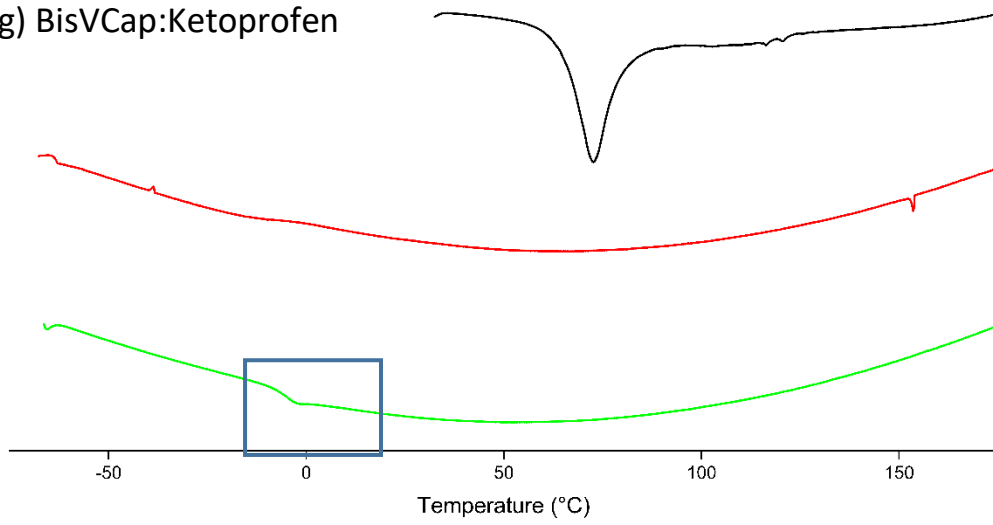
e) BisVCap:Furosemide



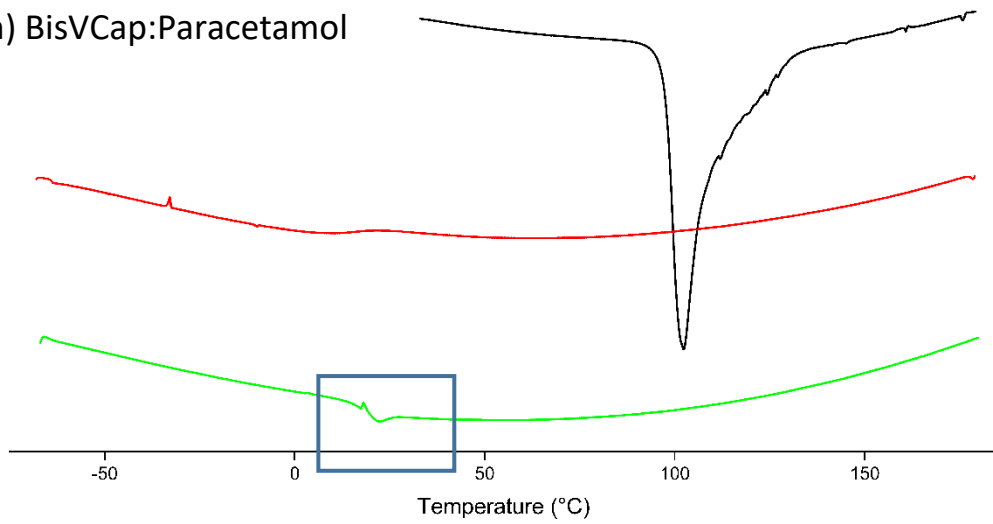
f) BisVCap:Indomethacin



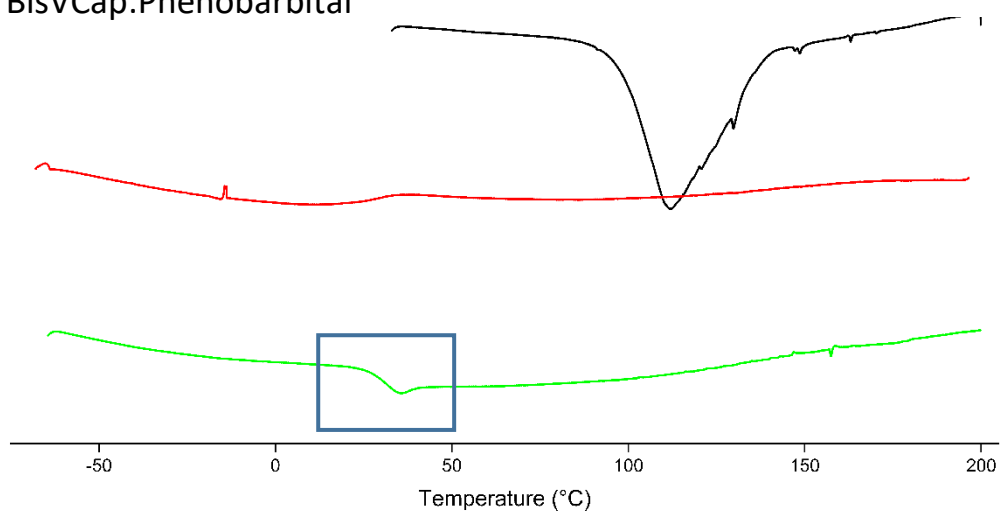
g) BisVCap:Ketoprofen



h) BisVCap:Paracetamol



i) BisVCap:Phenobarbital



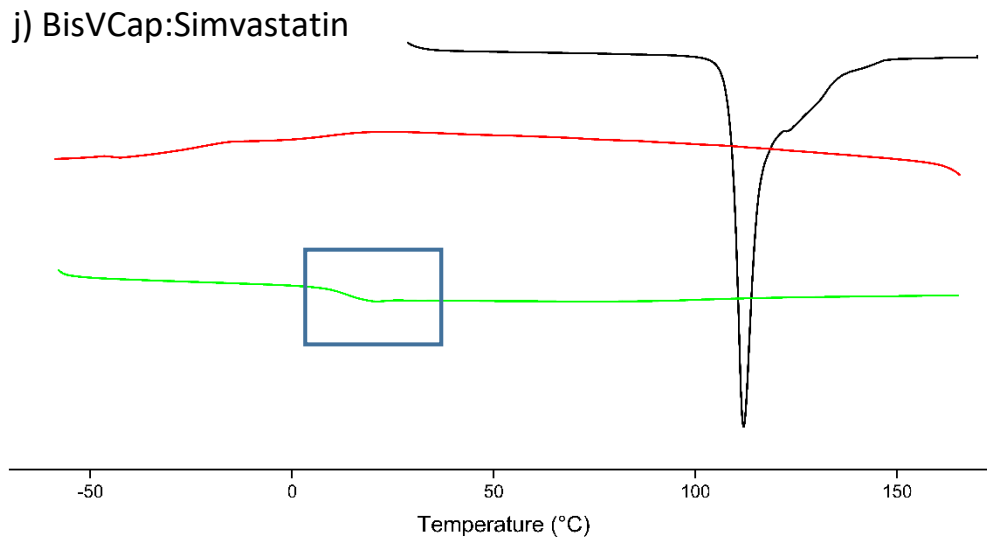
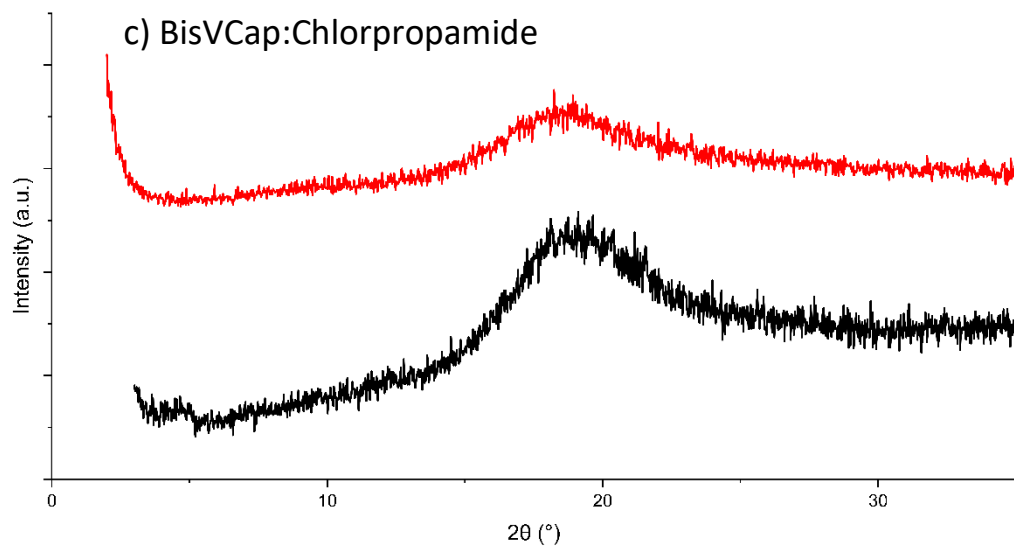
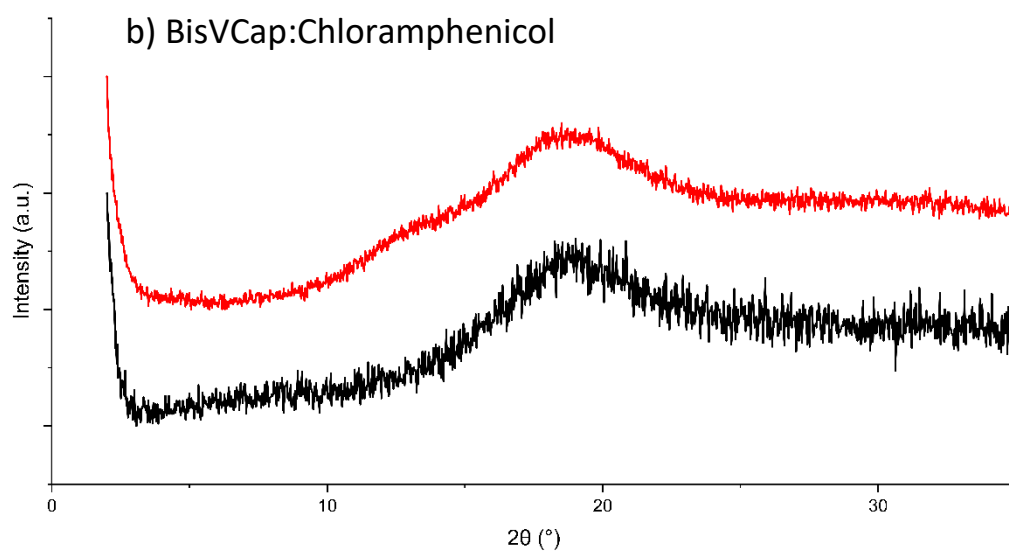
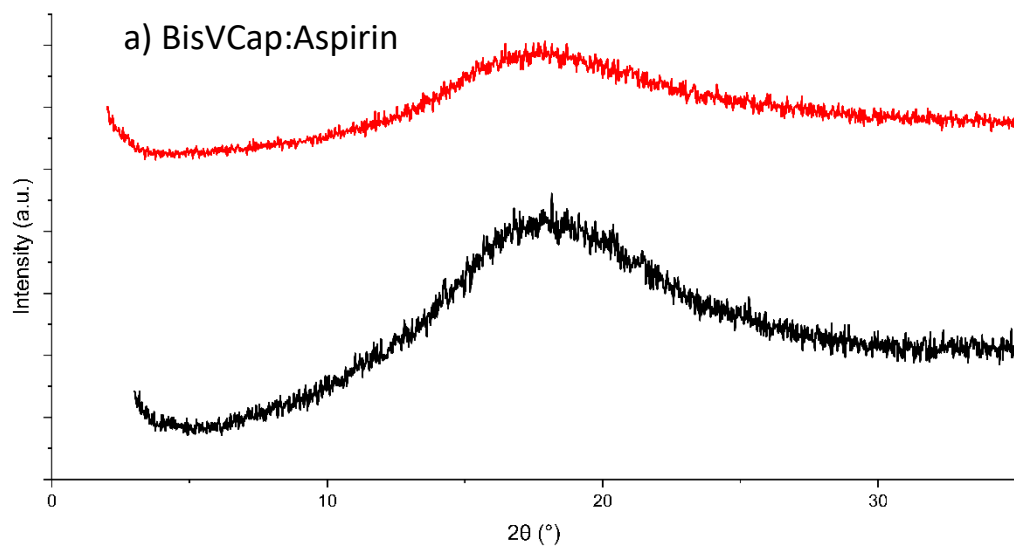
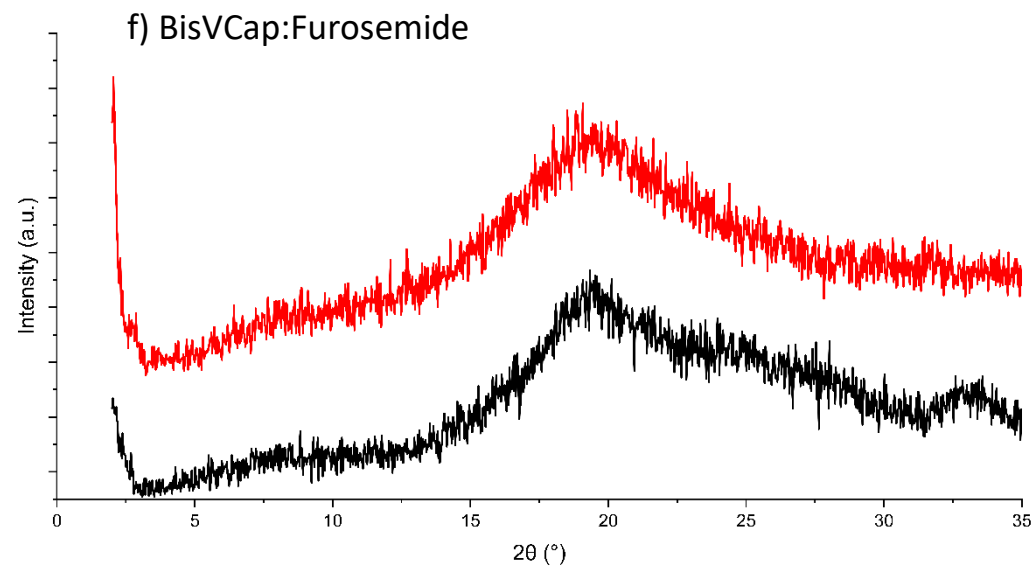
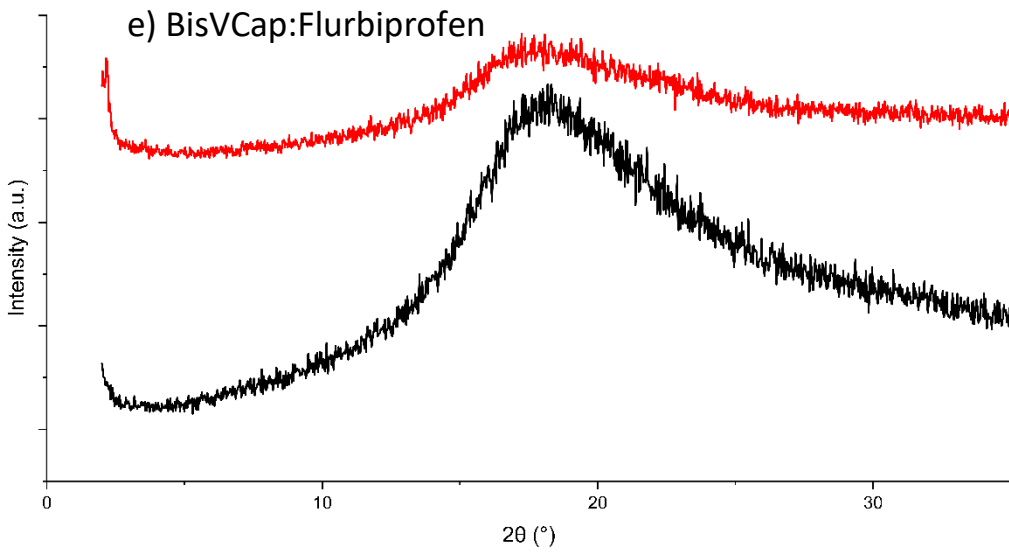
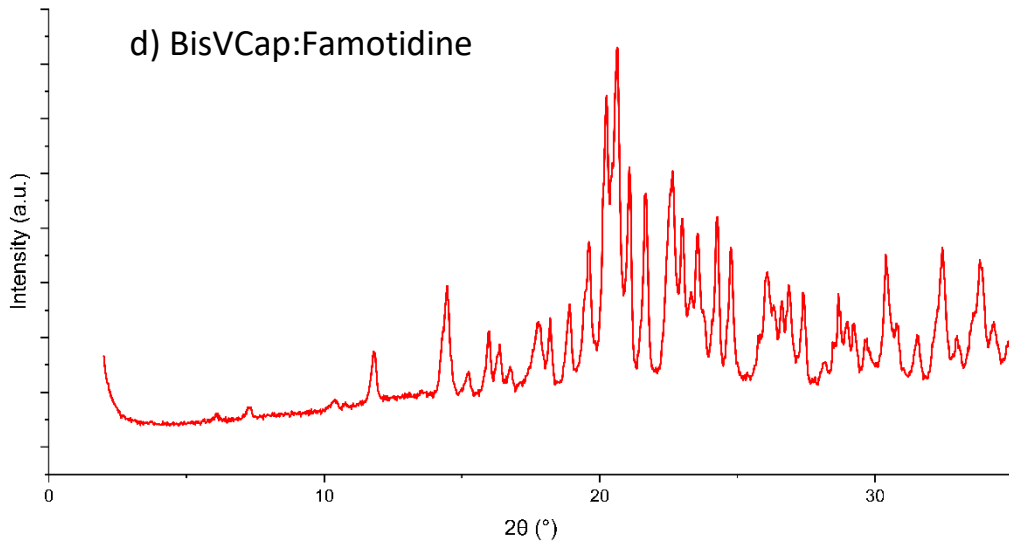
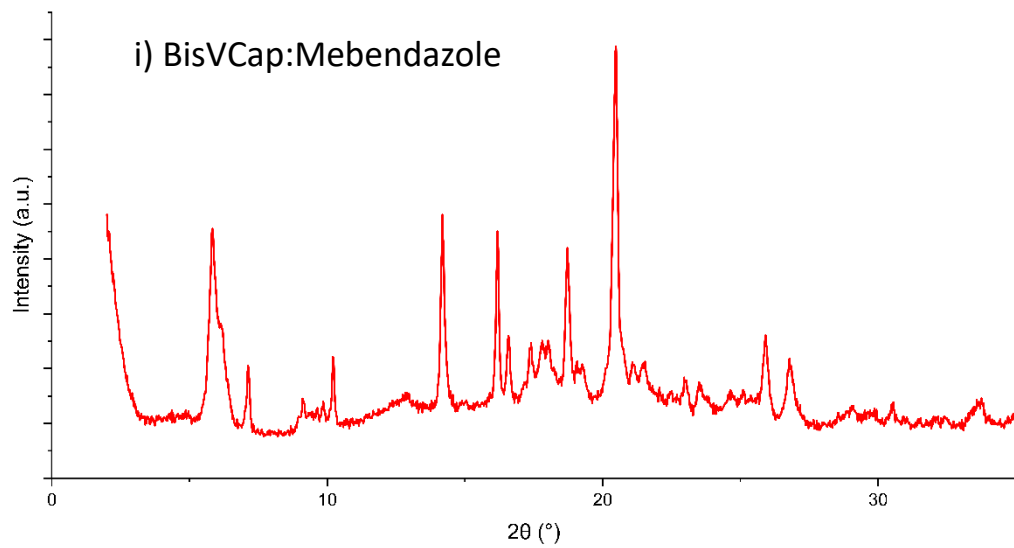
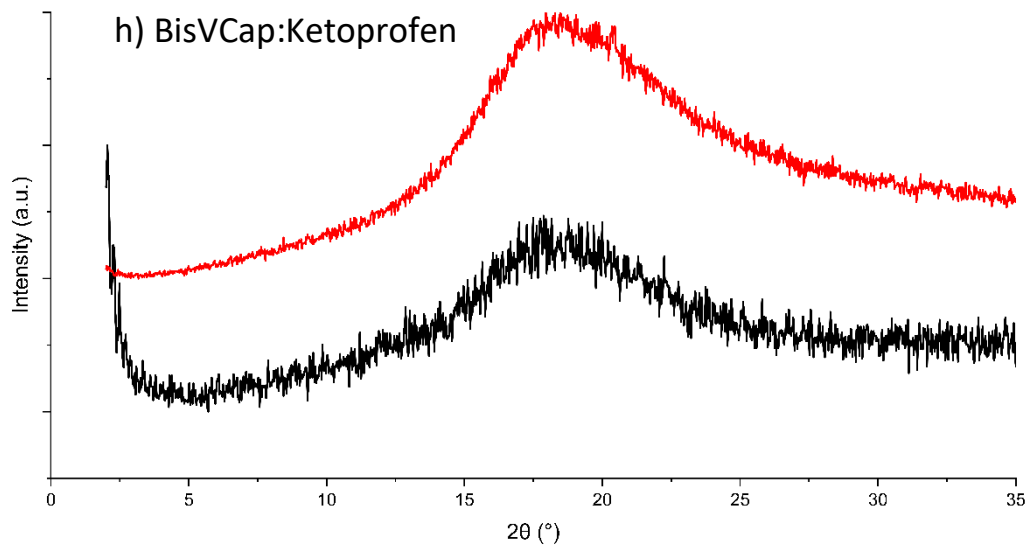
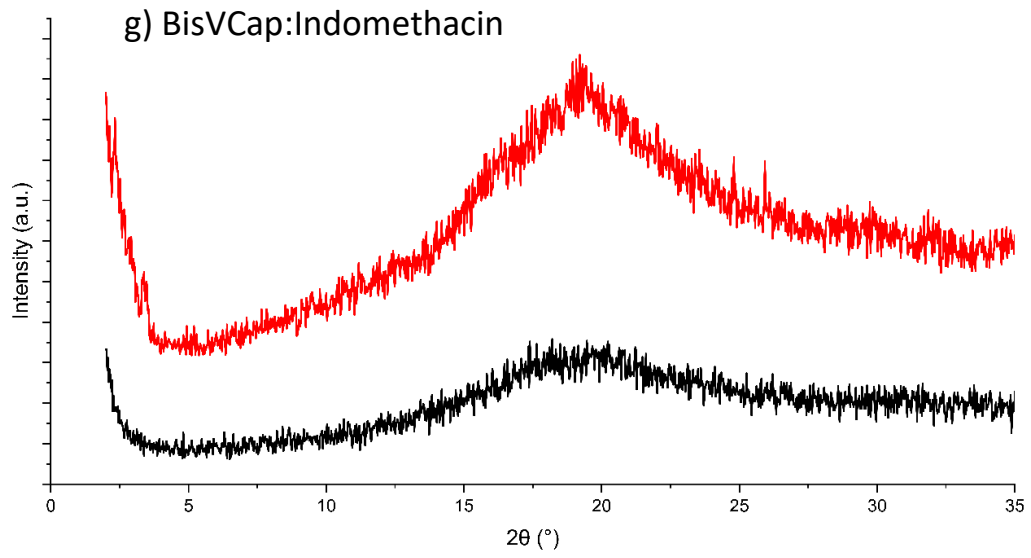


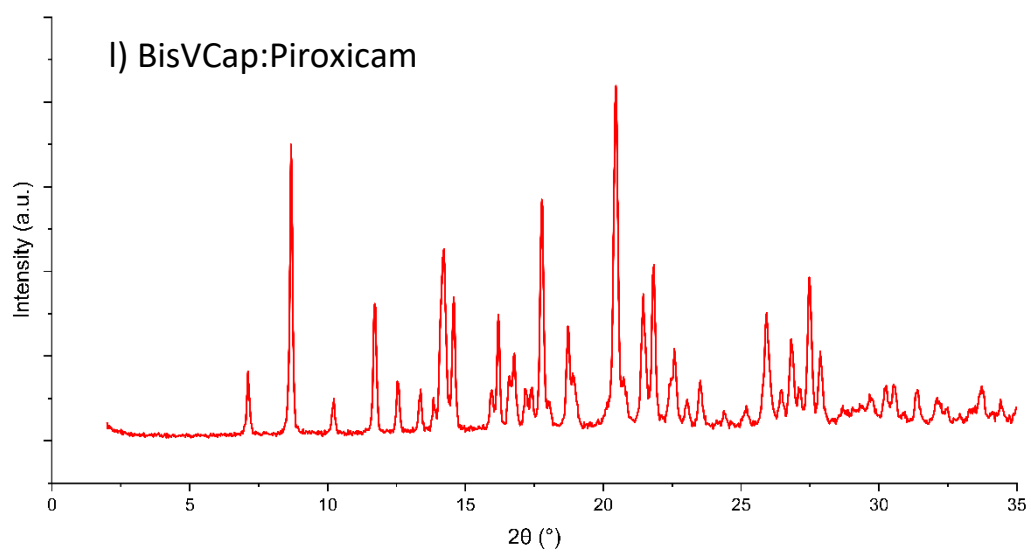
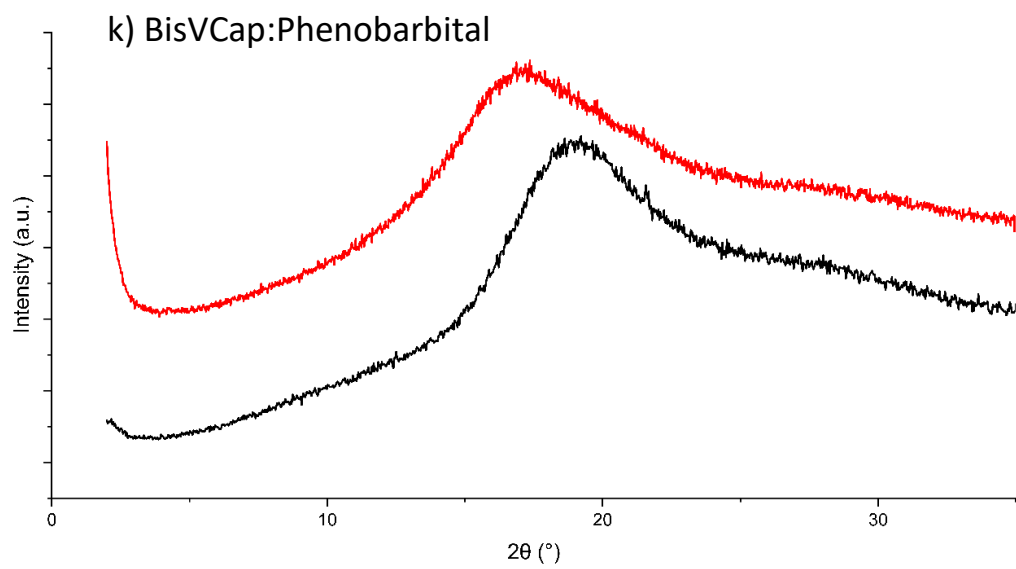
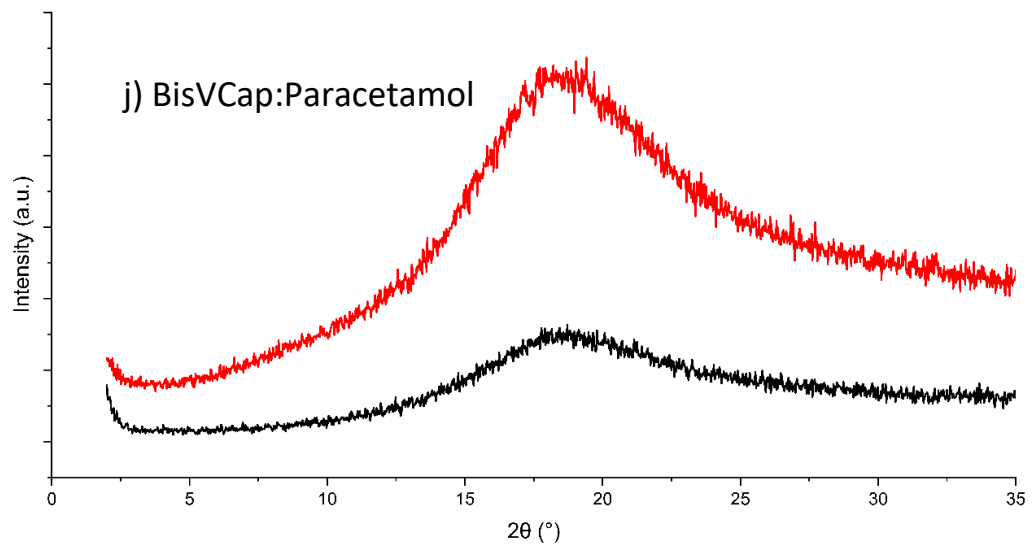
Figure 3.3: The heat/cool/heat DSC thermograms of 1:1 mixtures of the APIs with bisVCap with exotherms up. The different APIs are a) aspirin, b) chloramphenicol, c) chlorpropamide, d) flurbiprofen, e) furosemide, f) indomethacin, g) ketoprofen, h) paracetamol, i) phenobarbital and j) simvastatin. The black trace displays the initial heat cycle, followed by the cooling cycle in red and the second heat cycle in green. The  $T_g$  is highlighted with a blue box on each thermogram.











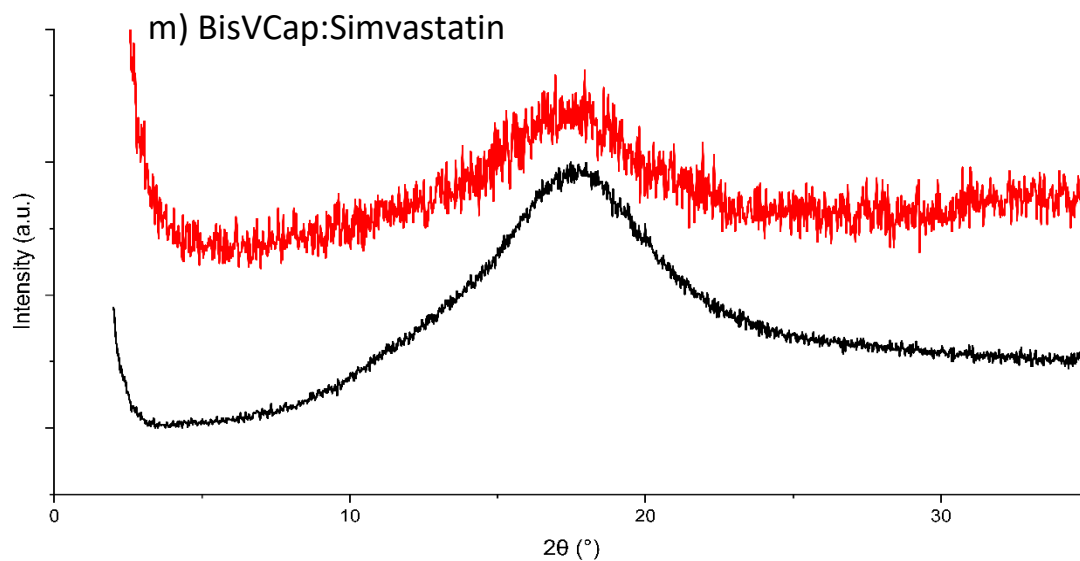


Figure 3.4: The XRPD diffractograms for the COAM screen (Table 3.2) of bisVCap with 13 APIs. The CM samples are shown in black and the RSE samples are in red. The different APIs are a) aspirin, b) chloramphenicol, c) chlorpropamide, d) famotidine, e) flurbiprofen, f) furosemide, g) indomethacin, h) ketoprofen, i) mebendazole, j) paracetamol, k) phenobarbital, l) piroxicam, and m) simvastatin. Famotidine, mebendazole and piroxicam only have an RSE trace due to the system decomposing when undergoing CM.

### 3.2.3 Analysing the Stabilising Interactions in COAM Systems

FTIR was used to understand the bonding interactions taking place in the COAM systems (Figure 3.5). The carbonyl peaks for solid bisVCap occur at 1622 and 1640  $\text{cm}^{-1}$  and in the crystal structure of bisVCap, the carbonyl groups can not form any strong hydrogen bonding interactions.<sup>24</sup> In all the non COAM systems (Table 3.2) the bisVCap carbonyl peaks are unchanged suggesting no new interactions are occurring, however, in all the COAM systems the bisVCap carbonyl peaks shift to a lower wavenumber and broaden. The shift to a lower wavenumber indicates the bisVCap carbonyl groups are forming hydrogen bonds causing the weakening of the C=O bond. The broadening of the peaks is indicative of amorphous systems due to the short-range order, the possibility of a range of molecular conformations, and altered molecular arrangement.<sup>9, 35, 36</sup>

Aspirin, flurbiprofen, furosemide, indomethacin and ketoprofen all contain a carboxylic acid group which usually forms a carboxylic acid dimer by hydrogen bonding.<sup>37-41</sup> However, in all five APIs the peak corresponding to the carbonyl bond shifts to a higher wavenumber upon

forming the COAM material, indicating the breaking of the carboxylic acid dimers (Figure 3.5a, e, f, g and i). The disruption of the carboxylic acid dimer along with the shift in the bisVCap carbonyl region, suggests the bisVCap interacts with the OH group from the carboxylic acid preventing the dimer from forming.

The crystal structure of pure chloramphenicol shows the formation of hydrogen bonds between the carbonyl and one of the alcohol groups.<sup>42</sup> However, the carbonyl peak shifts from 1682 to 1700  $\text{cm}^{-1}$  upon forming the co-amorphous material indicating the carbonyl is stronger and forms fewer hydrogen bonds. The alcohol and amine peaks in the 3200 – 3500  $\text{cm}^{-1}$  which are clearly defined in the pure chloramphenicol sample, broaden and form a single broad region indicating the formation of an amorphous material (Figure 3.5b). Therefore, it is speculated bisVCap disrupts the bonding by forming hydrogen bonds with the alcohol groups in chloramphenicol preventing the alcohol groups from forming hydrogen bonds with other chloramphenicol molecules.

Pure chlorpropamide forms a repeating chain of urea groups linked together by hydrogen bonds between the C=O and N-H. In the FTIR spectra of the COAM system, the carbonyl group of chlorpropamide is shifted from 1710 to 1715  $\text{cm}^{-1}$  and the peaks assigned to the NH groups at 3200 – 3500  $\text{cm}^{-1}$  broaden (Figure 3.5c).<sup>43</sup> The changes in the COAM system along with the bisVCap carbonyl peaks shifting to a lower wavenumber, indicates that bisVCap forms hydrogen bonds with the NH groups stabilising the COAM system and disrupting the original chain of urea groups.

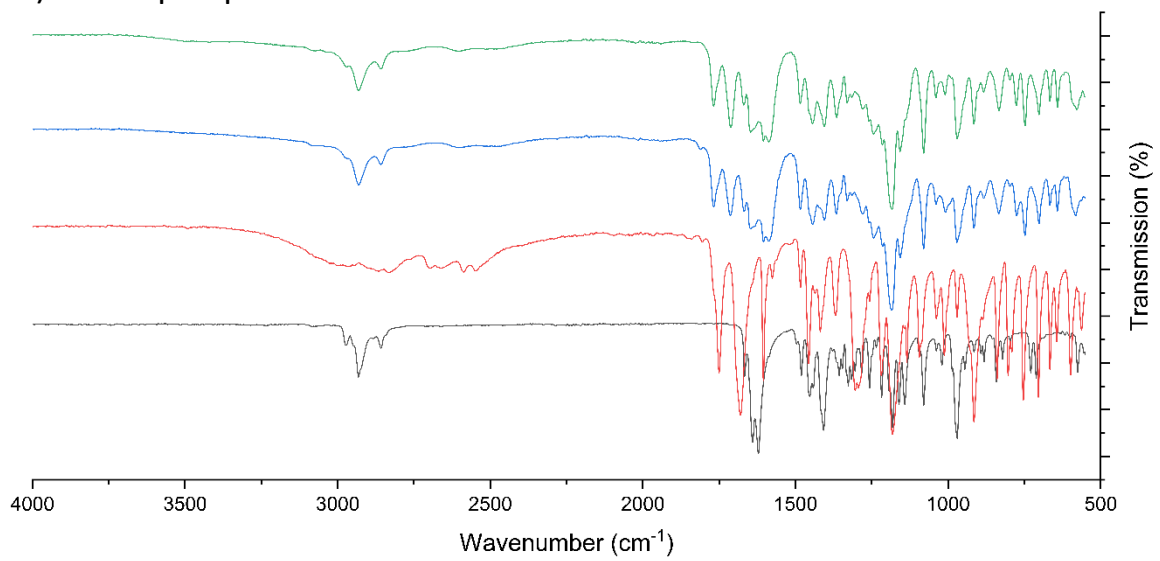
The crystal structure of pure paracetamol shows a repeating chain with the amide from one paracetamol hydrogen bonding with the alcohol group on another.<sup>44</sup> However, in the COAM system the carbonyl peak at 1651 shifts to 1670  $\text{cm}^{-1}$  indicating less hydrogen bonding which suggests the repeating amide phenol chain is broken (Figure 3.5j). The OH peak also broadens suggesting an amorphous system has formed. Therefore, it is likely the bisVCap is forming hydrogen bonds with the phenol on paracetamol preventing the amide alcohol chain from forming.

Pure phenobarbital is linked together by hydrogen bonds formed between the amide groups on the barbiturate ring.<sup>45</sup> The carbonyl peaks corresponding to the amide are shown to broaden and shift slightly to a higher wavenumber indicating disruption of the amide chain

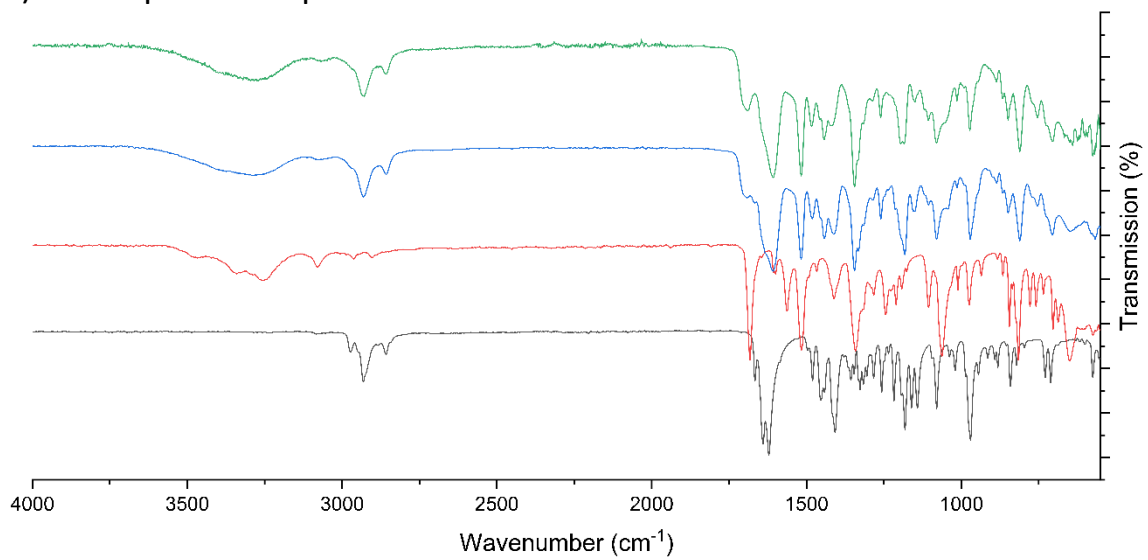
(Figure 3.5k). The peaks corresponding to the NH broaden indicating less regular hydrogen bonding suggesting an amorphous structure is present. The changes in the FTIR suggests the carbonyl groups on bisVCap are forming hydrogen bonds with the N-H groups of the barbiturate ring.

The crystal structure of simvastatin is usually formed with hydrogen bonds from the ester carbonyl to the alcohol group on the lactone ring.<sup>46</sup> However the FTIR peak assigned to the ester carbonyl at 1695 shifts to 1715  $\text{cm}^{-1}$  in the co-amorphous system indicating it is less involved in hydrogen bonding (Figure 3.5m). The alcohol region of the FTIR spectra also broadens indicating less regular bonding. The changes in the FTIR spectra along with the bisVCap carbonyl peaks shifting to a lower wavenumber, indicates the bisVCap carbonyl are forming new hydrogen bonds with the alcohol group on simvastatin.

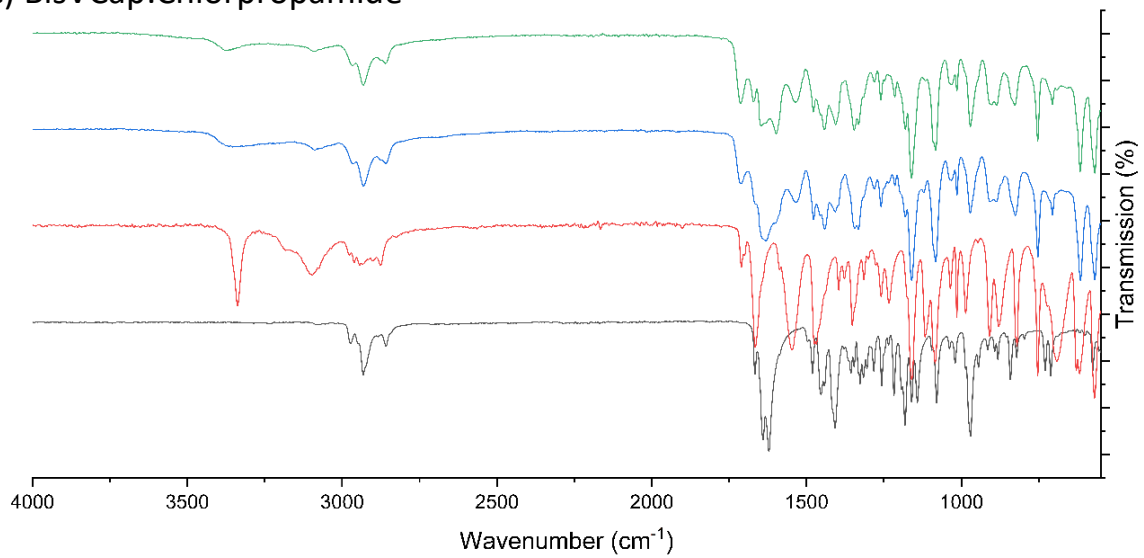
a) BisVCap:Aspirin



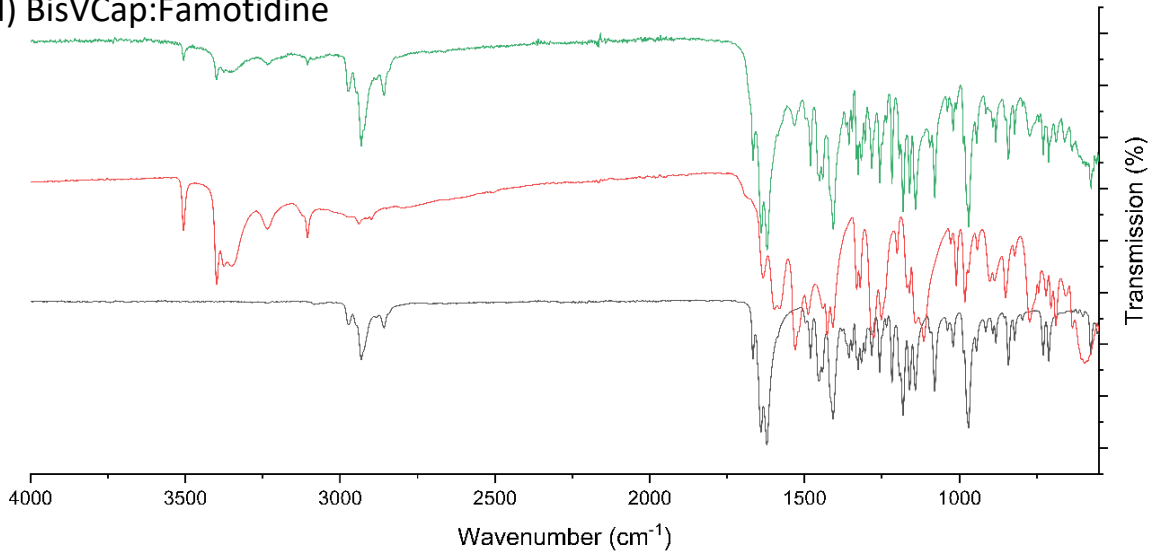
b) BisVCap:Chloramphenicol



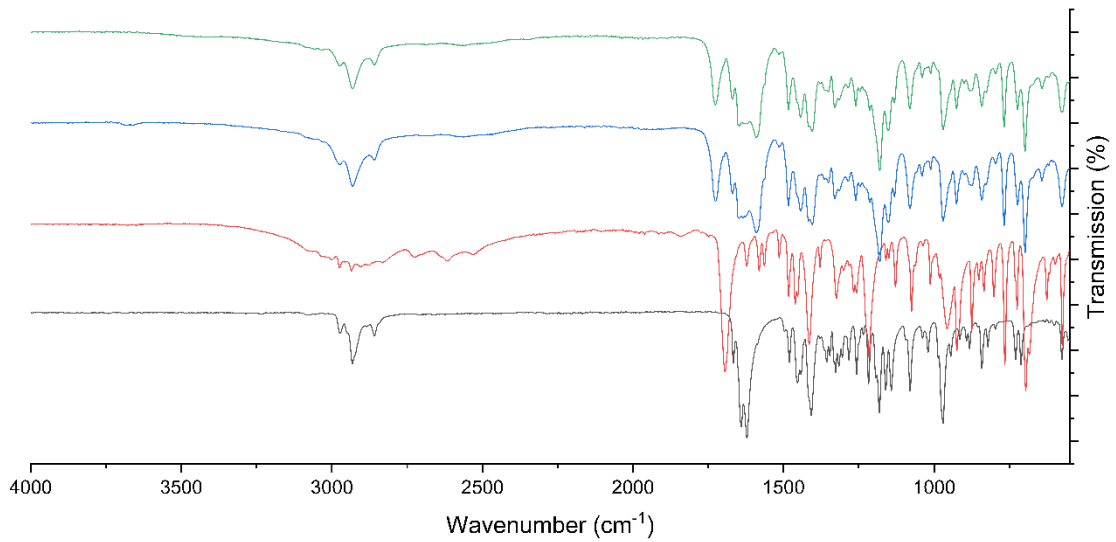
c) BisVCap:Chlorpropamide



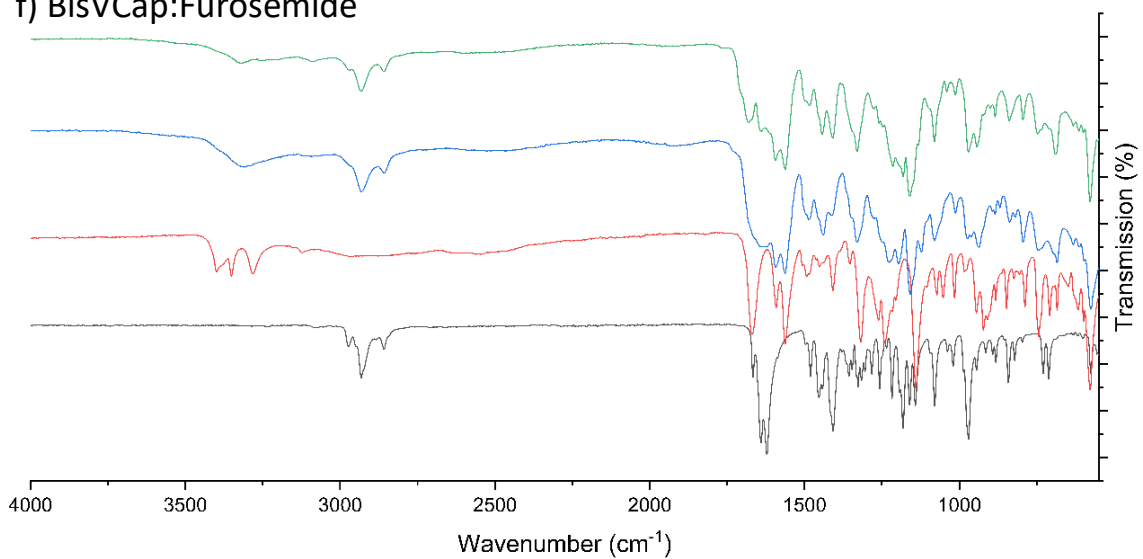
d) BisVCap:Famotidine



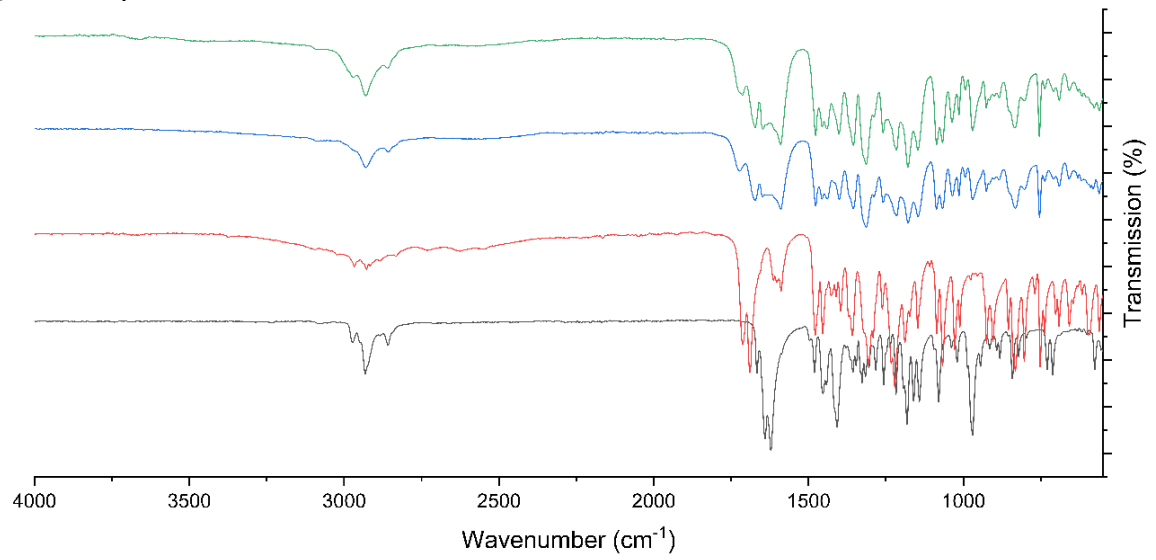
e) BisVCap:Flurbiprofen



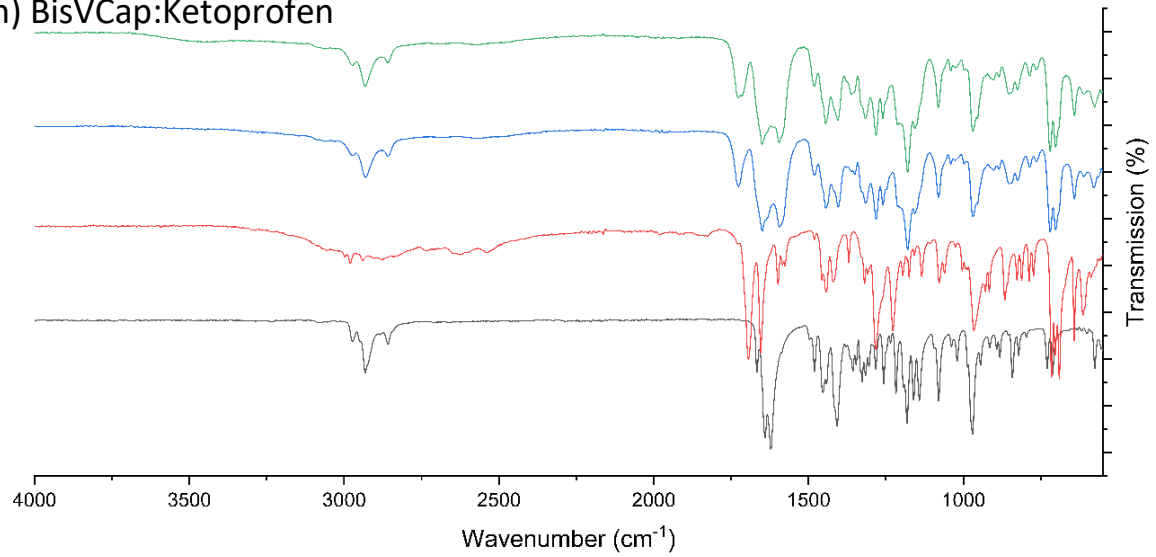
f) BisVCap:Furosemide



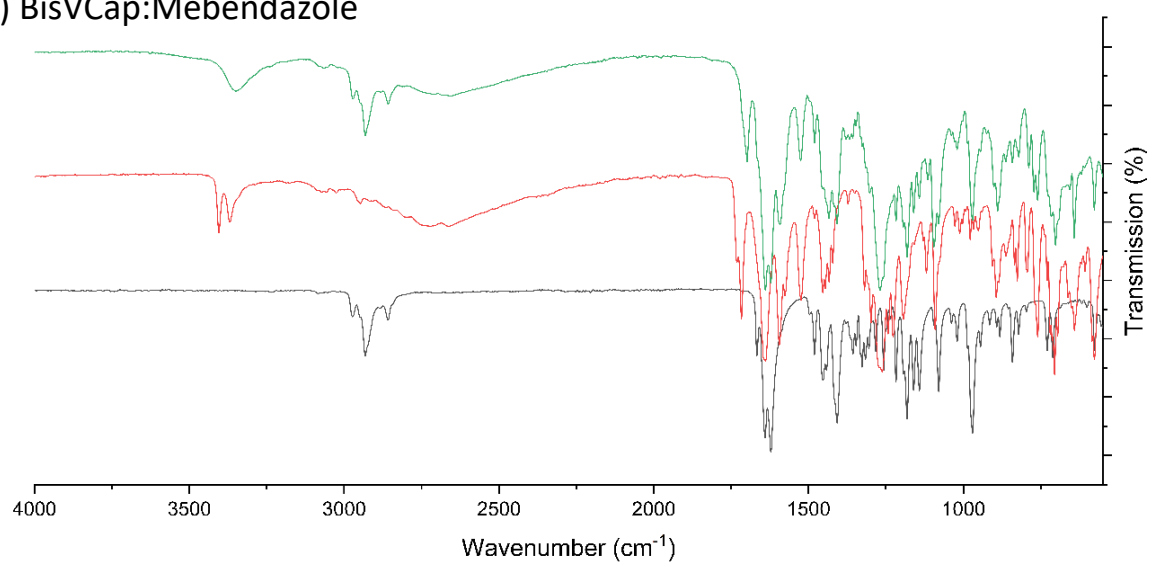
g) BisVCap:Indomethacin



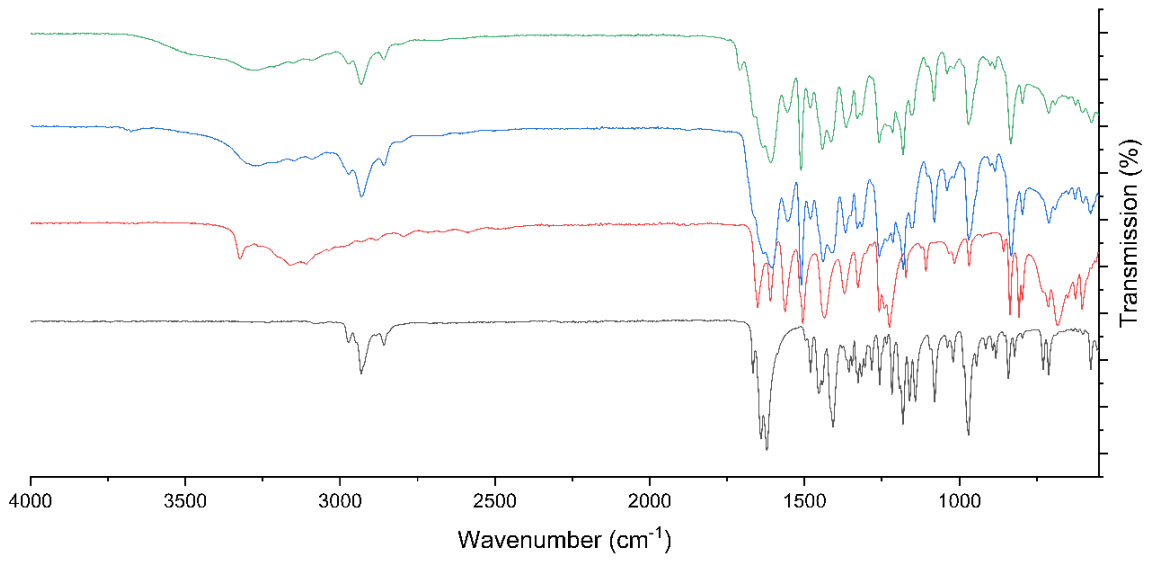
h) BisVCap:Ketoprofen



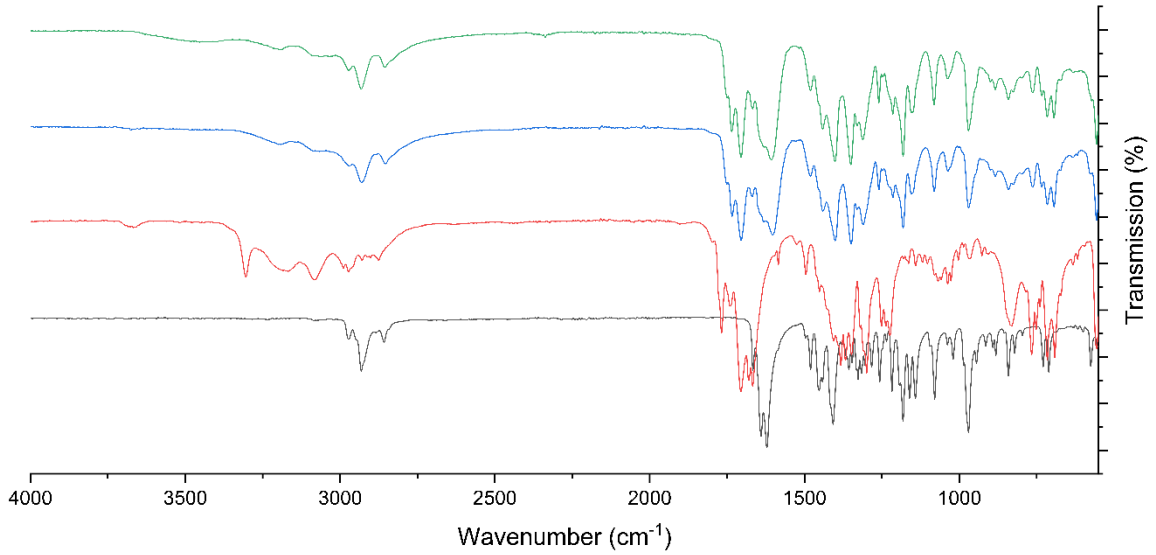
i) BisVCap:Mebendazole



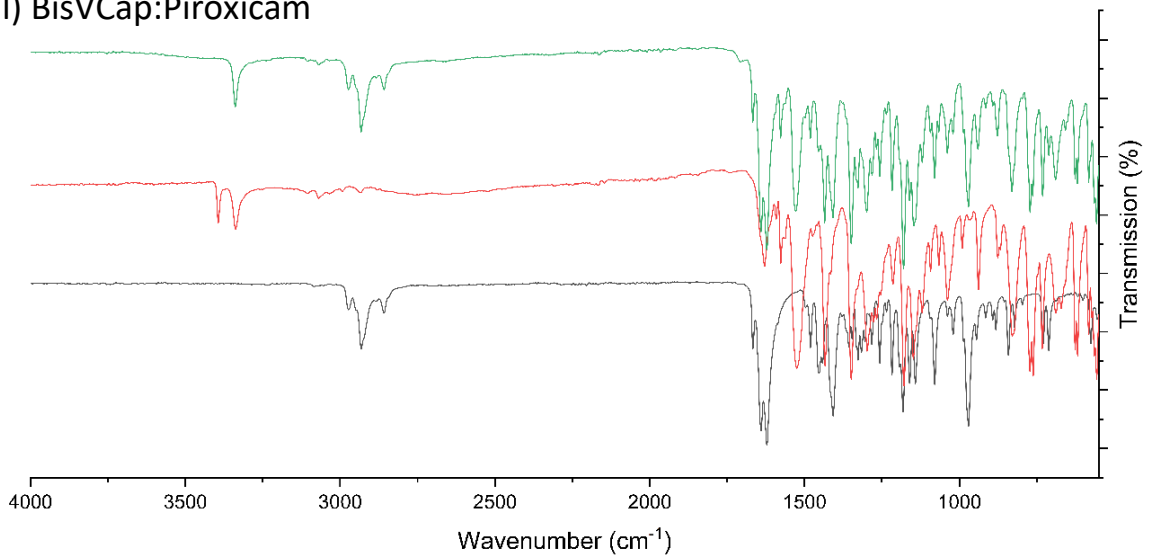
j) BisVCap:Paracetamol



k) BisVCap:Phenobarbital



l) BisVCap:Piroxicam





### m) BisVCap:Simvastatin

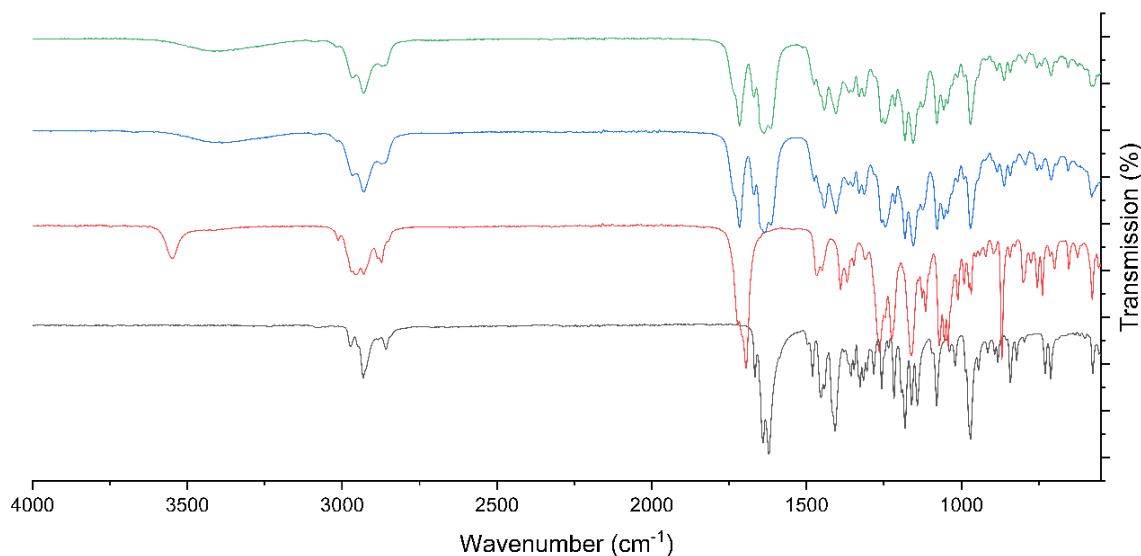


Figure 3.5: The FTIR spectra for the COAM screen Table 3.2 of bisVCap with 13 APIs. BisVCap is shown in black, the pure API in red, the CM sample in blue and the RSE sample in green. The different APIs are a) aspirin, b) chloramphenicol, c) chlorpropamide, d) famotidine, e) flurbiprofen, f) furosemide, g) indomethacin, h) ketoprofen, i) mebendazole, j) paracetamol, k) phenobarbital, l) piroxicam, and m) simvastatin. The famotidine, mebendazole and piroxicam spectra only display an RSE sample due to the system decomposing when undergoing CM.

#### 3.2.4 Stability Study at Different Temperatures

The stability of three of the experimentally generated COAM systems (Table 3.2) was tested to determine if the predicted COAM value correlates with the stability of the COAM product. The three systems selected were bisVCap with paracetamol, simvastatin, and indomethacin, with corresponding COAM values of 0.450, 0.751 and 1.142. Therefore, if the COAM value is an indication of stability, it would be expected that the system with indomethacin would be the most stable and paracetamol the least stable. These COAM materials were initially produced by RSE and stored in a desiccator at ~20 °C and analysed after two weeks by XRPD and FTIR to identify whether the samples remained COAM. The XRPD (Figure 3.6) and FTIR (Figure 3.7) data shows that indomethacin remains COAM after two weeks, however, both simvastatin and paracetamol have recrystallised. The XRPD pattern of the recrystallized co-amorphous simvastatin bisVCap system after two weeks at

both temperatures (Figure 3.6b) showed the crystallisation of bisVCap and the formation of the form I polymorph of simvastatin, which is the thermodynamically stable polymorph above 0 °C.<sup>46, 47</sup> The same is observed for the paracetamol bisVCap system (Figure 3.6c) with the system separately recrystallising into pure bisVCap and the form I polymorph of paracetamol, which is the thermodynamically stable form at the tested conditions.<sup>48, 49</sup> The formation of the thermodynamically stable polymorph of the simvastatin and paracetamol suggests bisVCap only slows the crystallization rate but does not affect the crystallisation process. The apparent greater stability of the indomethacin COAM phase correlates with the higher COAM value from the prediction model. Interestingly, the  $T_g$  values (Table 3.2) of all three systems are below the ~20 °C used for the stability study with simvastatin having the lowest  $T_g$  of 12.5 °C. Therefore, the stability study was repeated but the samples were stored at 3 °C to try and decrease the mobility of the systems by storing them below their  $T_g$ .

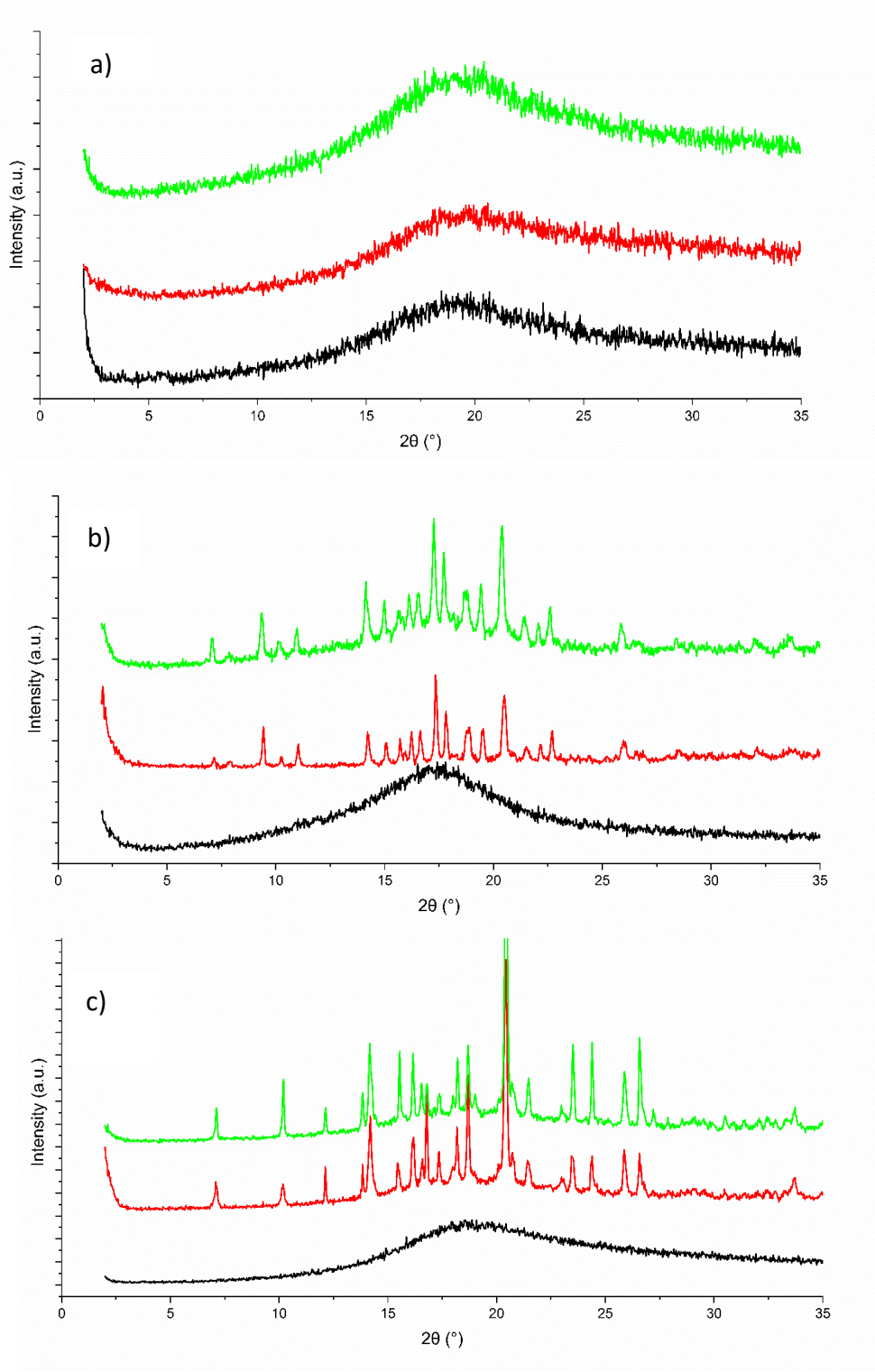


Figure 3.6: The XRPD traces of COAM samples of bisVCap with a) indomethacin, b) simvastatin and c) paracetamol. The initial COAM sample made by RSE is shown in black. The XRPD traces are shown after two weeks when stored at ~20 °C (red) and 3 °C (green).

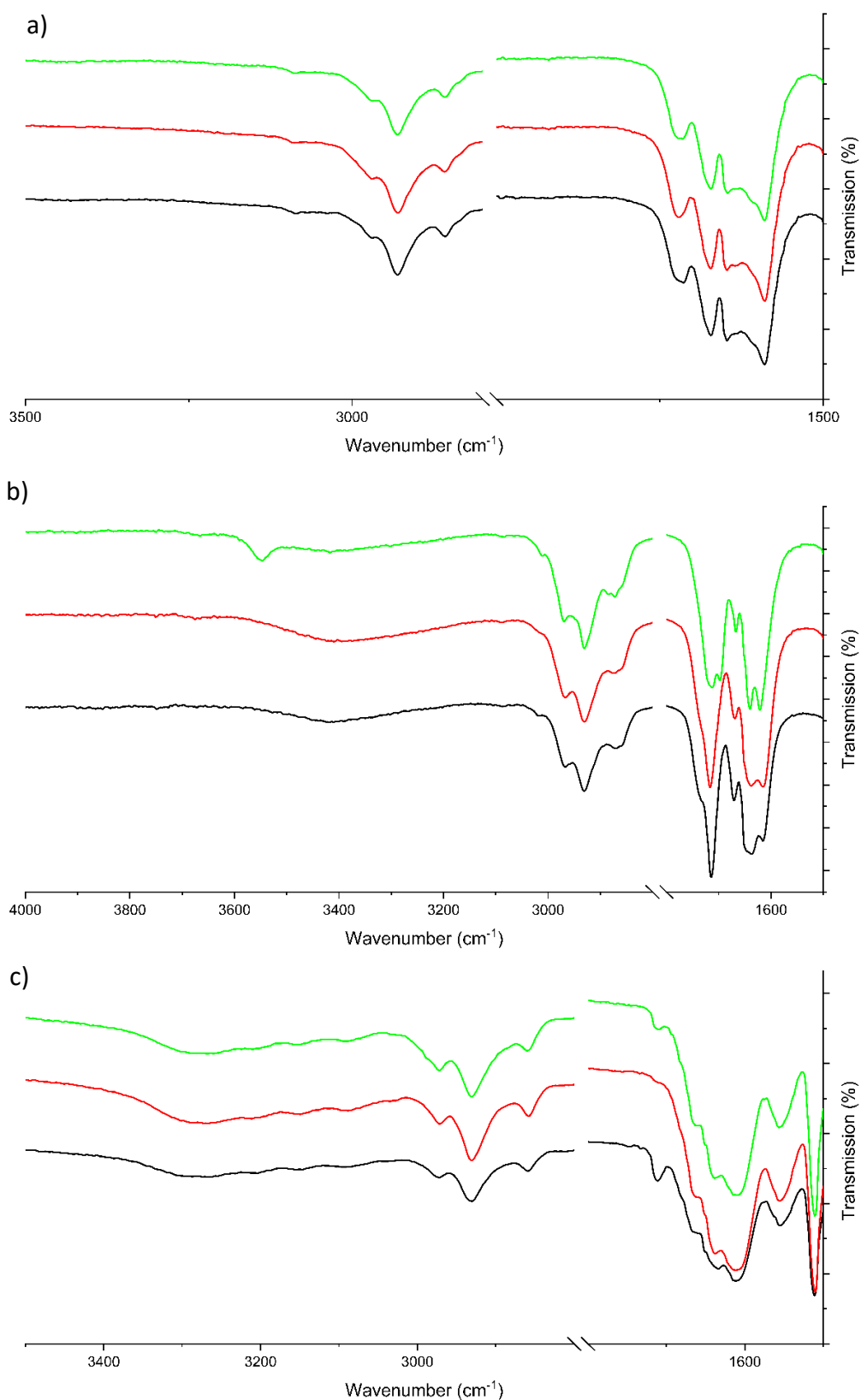


Figure 3.7: The FTIR spectra of COAM samples of bisVCap with a) indomethacin, b) simvastatin and c) paracetamol. The initial COAM sample made by RSE is shown in black. The FTIR spectra are shown after two weeks when stored at ~20 °C (red) and 3 °C (green).

The XRPD (Figure 3.6) and FTIR (Figure 3.7) results of the lower temperature study shows indomethacin remains amorphous which matches the results observed previously. However, the XRPD results show both simvastatin and paracetamol have recrystallised. Therefore, a stability experiment with a shorter timescale was carried out with just bisVCap with simvastatin and paracetamol. The two systems were produced by RSE and samples were stored for 1 week in both a desiccator at ~20 °C and 3°C. The samples were analysed via XRPD (Figure 3.8) and FTIR (Figure 3.9) after 1 week. The XRPD pattern shows the sample with simvastatin at ~20 °C crystallises into bisVCap and the form I polymorph of simvastatin, however, at 3 °C, only bisVCap recrystallises suggesting the simvastatin struggles to stabilise the bisVCap in a COAM state. In the system with paracetamol, no recrystallisation had occurred after 1 week stored at 3 °C and only slight recrystallisation had occurred when stored at ~20 °C. The paracetamol COAM system is therefore assumed to be more stable than the simvastatin COAM system, which is the opposite of the prediction based on the COAM values, indicating the model has limited use in predicting stability.

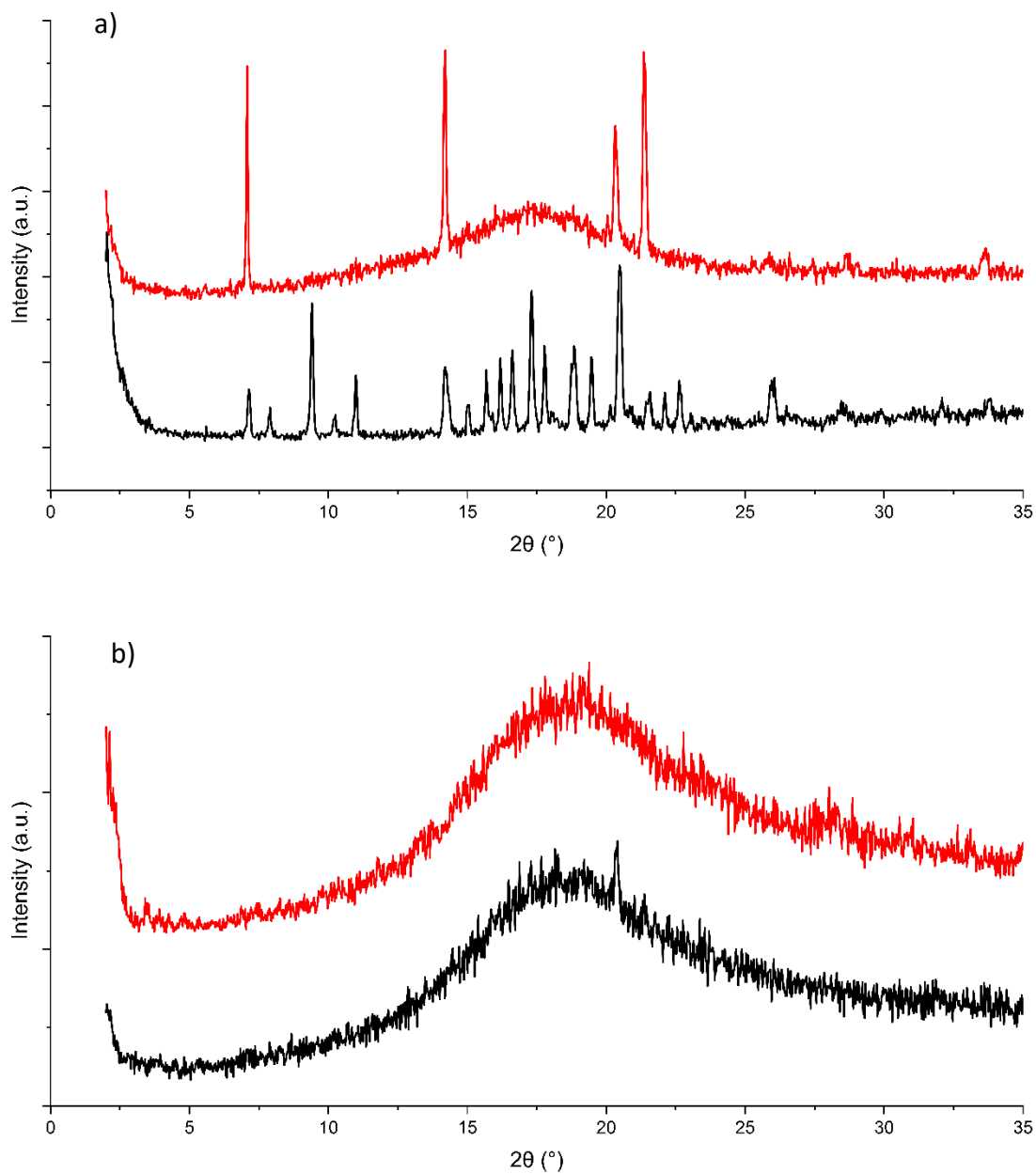


Figure 3.8: The XRPD traces of COAM samples of bisVCap with a) simvastatin and b) paracetamol. The XRPD traces are shown after one week when stored at  $\sim 20^\circ\text{C}$  (black) and  $3^\circ\text{C}$  (red).

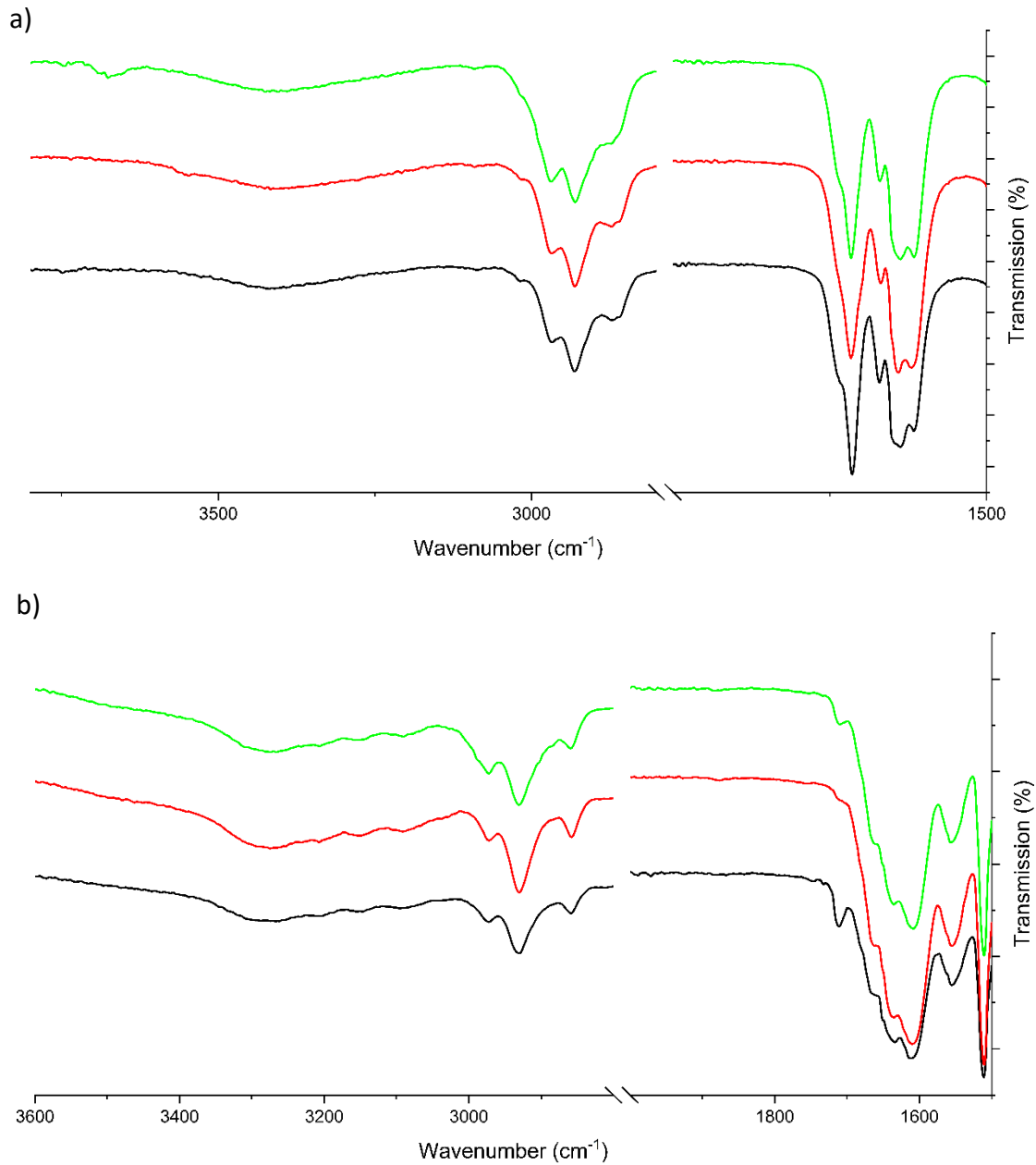


Figure 3.9: The FTIR spectra of COAM samples of bisVCap with a) simvastatin and b) paracetamol. The initial FTIR spectra after RSE is shown in black. The FTIR spectra are shown after one week when stored at  $\sim 20$  °C (red) and 3 °C (green).

### 3.2.5 Increasing the Ratio of Furosemide to BisVCap

The COAM system formed from furosemide and bisVCap has the highest  $T_g$  (Table 3.2) and exists as a light-yellow powder whereas the other systems were in the form of a thick sticky pastes. Therefore, bisVCap furosemide was chosen for further study. The initial COAM system was formed in a 1:1 molar ratio of bisVCap to furosemide. However, COAM systems have been shown to form with increased ratios of API to coformer.<sup>50</sup> Therefore, the preparation of the co-amorphous phase using RSE was repeated using 1:2, 1:3 and 1:4 ratio of bisVCap to furosemide. The RSE process was also repeated with a pure sample of furosemide to determine if the bisVCap is necessary to make the system amorphous. The systems were analysed by XRPD and FTIR to determine the crystallinity and solid form of the resulting products. The XRPD data (Figure 3.10) shows the bisVCap furosemide systems prepared via RSE remain amorphous up to a 1:2 ratio. The higher ratio samples undergo recrystallisation into the form II polymorph of furosemide which was expected as form II is usually formed from the evaporation under reduced pressure of a furosemide acetone solution.<sup>51</sup> The pure sample of furosemide undergoes recrystallisation indicating that bisVCap is required to stabilise the system in an amorphous state. The FTIR spectra (Figure 3.11) of all ratios, shows the bisVCap does not recrystallise as the carbonyl peaks do not return to the original position, also the peaks appearing in the XRPD diffractogram of the 1:4 ratio sample all match with the pure furosemide sample. Therefore, the 1:2 ratio seems to be the limit before crystallization begins. This may be because bisVCap contains only two carbonyl groups limiting the number of furosemide molecules bisVCap can form hydrogen bonds with. Also, the 1:3 system still displays a large amorphous hump suggesting co-amorphous interactions are present with the bisVCap interacting with two out of three furosemide molecules.



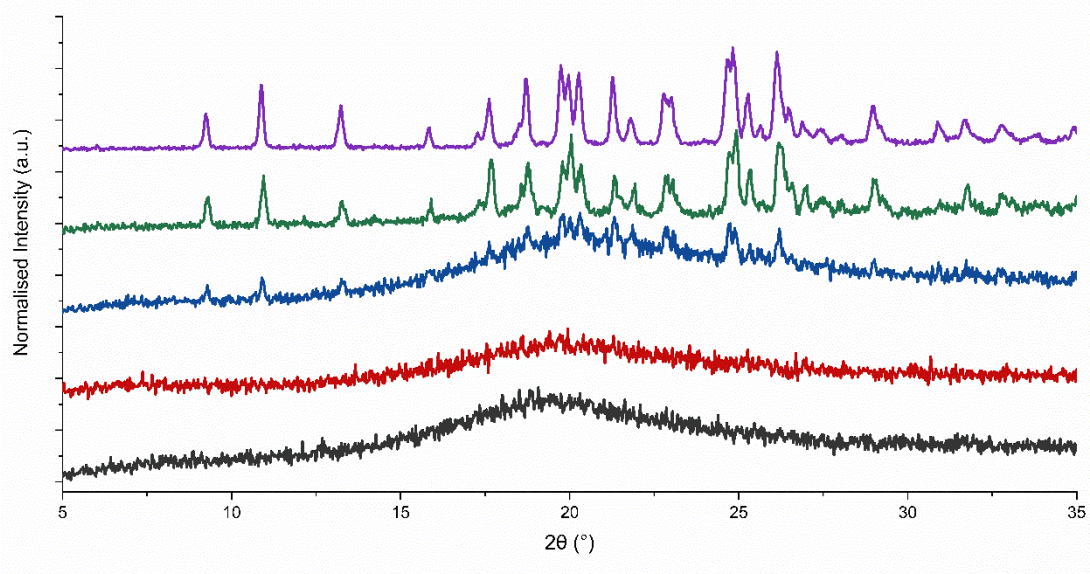


Figure 3.10: XRPD traces of bisVCap with furosemide after RSE in a 1:1 (black), 1:2 (red), 1:3 (blue) and 1:4 ratio (green). Pure furosemide after RSE is shown in purple.

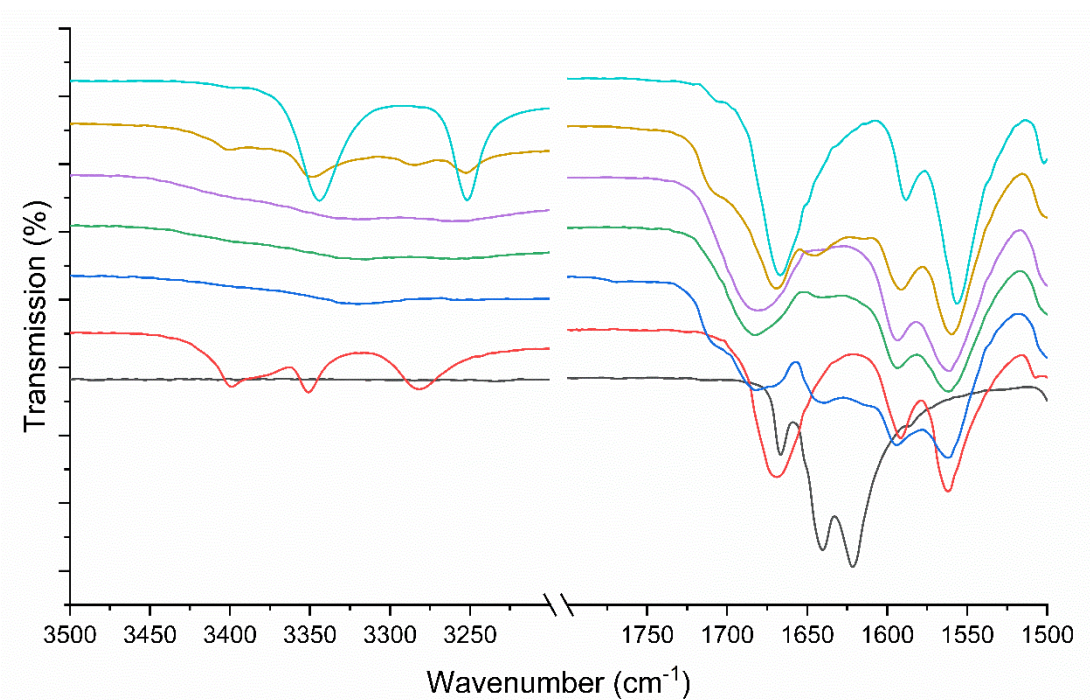


Figure 3.11: FTIR spectra for the increased ratio study of bisVCap and furosemide showing the carbonyl and alcohol region. The spectra display pure bisVCap (black) and pure furosemide (red). The bisVCap furosemide systems were made via RSE at different ratios with 1:1 in blue, 1:2 in green, 1:3 in purple and 1:4 in light brown. The furosemide systems which underwent RSE is also shown in cyan.

### 3.2.6 Stability Study on BisVCap and Furosemide at Different Humidities

To understand the effect of humidity on the bisVCap COAM systems a 1:1 mixture of bisVCap and furosemide was prepared by RSE and stored in five different humidity environments. The samples were periodically monitored by XRPD and FTIR. The bisVCap furosemide system was selected because it forms a free-flowing powder and has the highest  $T_g$  suggesting it is the most stable system. The five different relative humidity (RH) environments selected were 0%, 11%, 33%, 75% and 100% all maintained at room temperature. The system at 0% RH was stored in a desiccator under a static vacuum which was assumed to be free of any moisture. The system at 100% RH was produced by storing a vial containing the bisVCap furosemide COAM system inside a vial containing pure water. The other RHs were produced by forming multiple saturated salt solutions and storing vials of bisVCap furosemide inside the vials of saturated salt solution. The saturated salt solutions used were lithium chloride for 11% RH, magnesium chloride for 33% RH and sodium chloride for 75% RH.<sup>52</sup> The systems were analysed after seven days and 28 days to see the effect of the different humidity environments. The initial XRPD data (Figure 3.12) shows the system is amorphous with the characteristic featureless hump with no clear peaks. After seven days the material stored at 0%, 11% and 33% RH remained unchanged by XRPD (Figure 3.12) and FTIR (Figure 3.13) and retained the appearance of a free flowing powder. The material stored at 75% RH appears to remain amorphous by both FTIR (Figure 3.13) and XRPD (Figure 3.12), however, the material changed from a powder to a glass-like film. No recrystallisation was observed by polarised optical microscopy indicating the system remains stable even after absorption of water. The material stored at 100% RH turned into a thick paste and started to recrystallise as shown by XRPD with small Bragg peaks observed corresponding to the form I polymorph of furosemide which is the thermodynamically stable polymorph, however, the FTIR has remained unchanged suggesting only a small amount of the sample has recrystallised.<sup>53</sup>

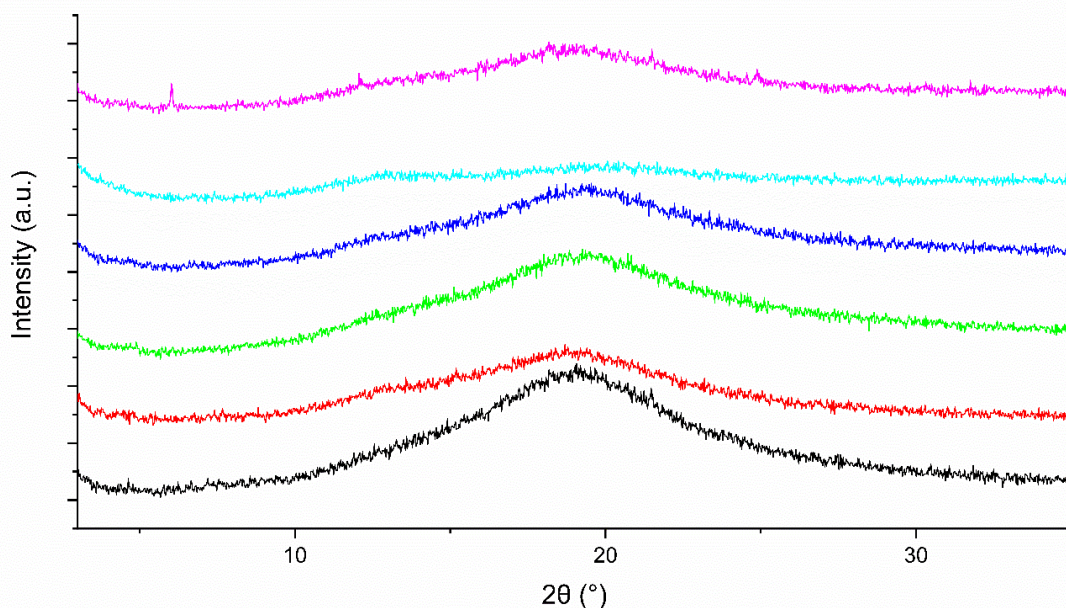


Figure 3.12: The XRPD traces of a COAM bisVCap furosemide system made via RSE. The initial system is shown in black. The system was stored for seven days at 0% RH (red), 11% RH (green), 33% RH (blue), 75% RH (cyan) and 100% RH (pink).

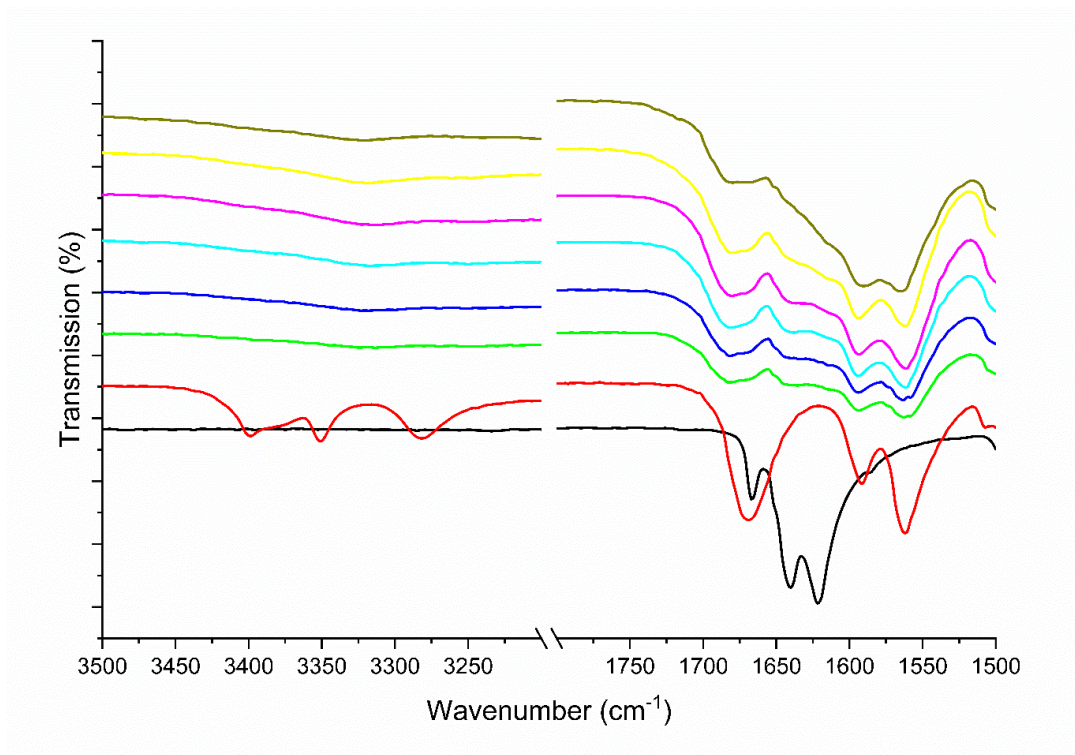


Figure 3.13: The FTIR spectra of a COAM bisVCap furosemide system made via RSE. Pure bisVCap is shown in black, pure furosemide in red and the initial bisVCap furosemide COAM system in green. The system was stored for seven days at 0% RH (blue), 11% RH (cyan), 33% RH (pink), 75% RH (yellow) and 100% RH (brown).

After storage for 28 days in the five different humidity environments, the materials stored at 0% to 75% RH remained unchanged with no indications of recrystallisation by FTIR (Figure 3.15) or XRPD (Figure 3.14). The material stored at 100% RH was the only system that changed with it undergoing crystallisation as observed by FTIR with the appearance of sharper peaks in the 3200-3500  $\text{cm}^{-1}$  region corresponding to the N-H stretching bands and XRPD displaying Bragg peaks matching the form I polymorph.<sup>53</sup> However, the system retains a lot of amorphous character with the amorphous halo still present. Overall, it appears the 1:1 bisVCap furosemide system remains stable up to 33% RH. Useful future work would involve studying the moisture sensitivity of this system using dynamic vapour sorption (DVS).

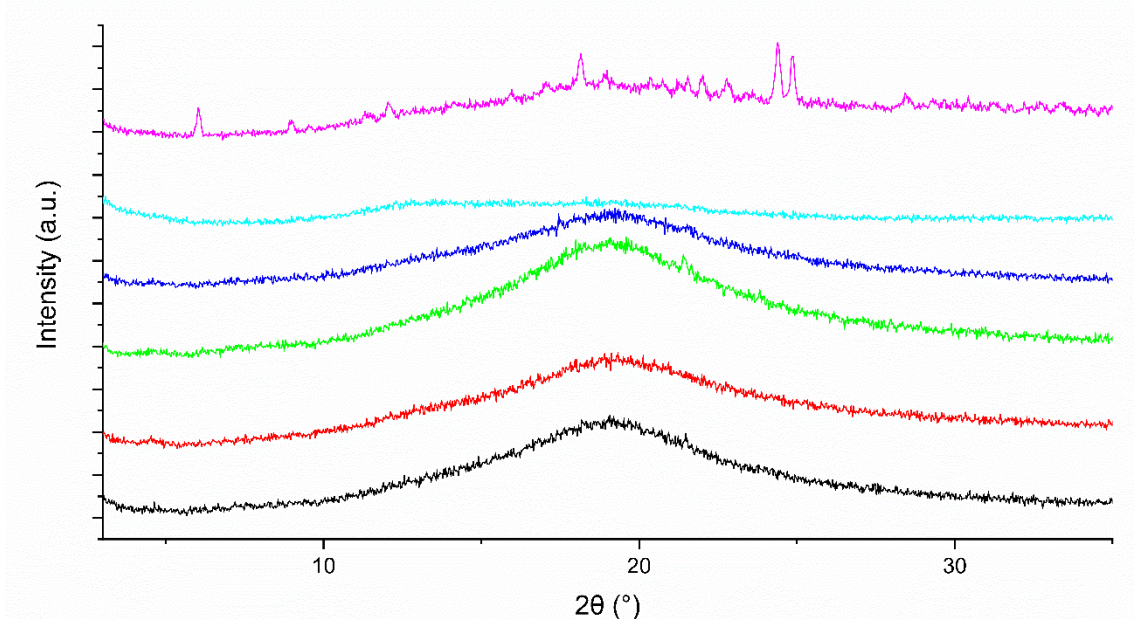


Figure 3.14: The XRPD traces of a COAM bisVCap furosemide system made via RSE. The initial system is shown in black. The system was stored for 28 days at 0% RH (red), 11% RH (green), 33% RH (blue), 75% RH (cyan) and 100% RH (pink).

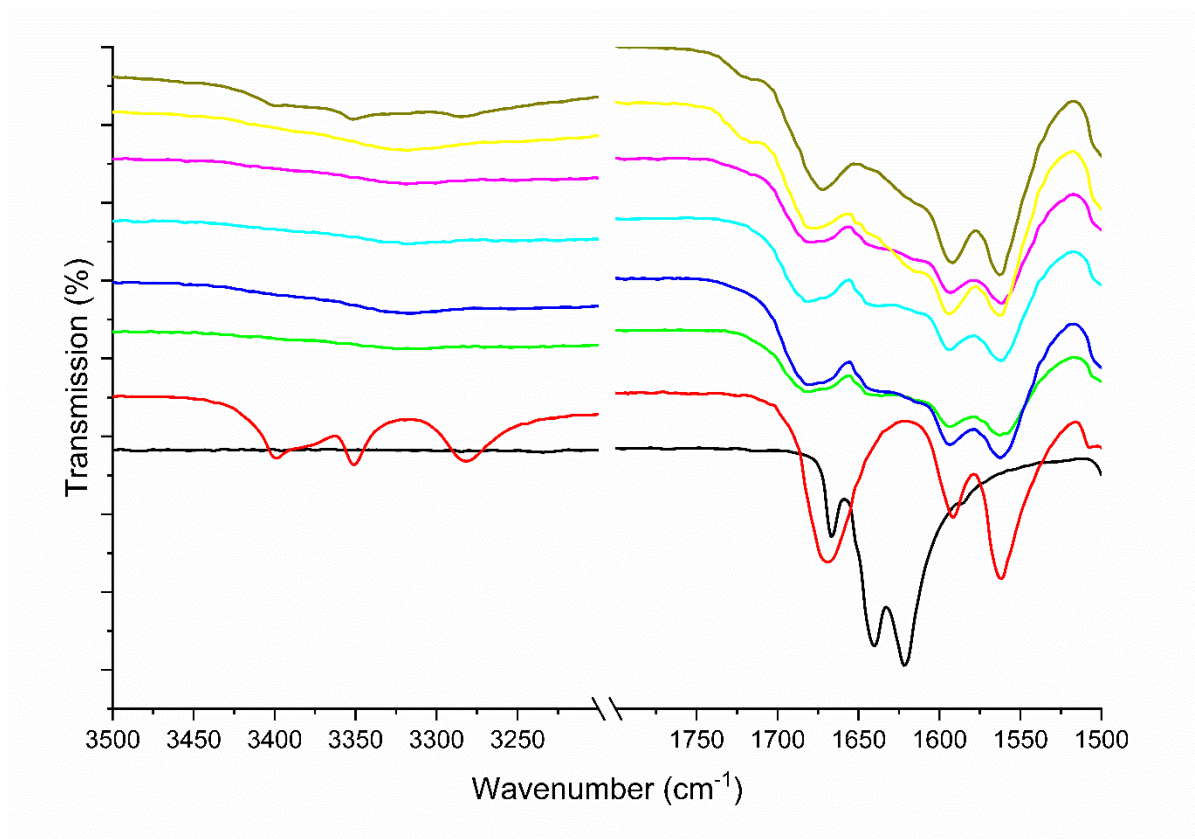


Figure 3.15: The FTIR spectra of a COAM bisVCap furosemide system made via RSE. Pure bisVCap is shown in black, pure furosemide in red and the initial bisVCap furosemide

COAM system in green. The system was stored for 28 days at 0% RH (blue), 11% RH (cyan), 33% RH (pink), 75% RH (yellow) and 100% RH (brown).

### 3.3 Conclusion

In conclusion, the PLS-DA prediction model produced in Chapter 2 was tested against the results of a previous co-amorphous screen of bisVCap with a range of APIs. The prediction model successfully predicted five out of seven systems. The bisVCap was then screened using the prediction model with 13 further APIs which were predicted to form both COAM and not COAM systems. Each of the mixtures were prepared by co-melting and rapid solvent evaporation and analysed via XRPD, FTIR, optical microscopy and DSC to determine if the systems were co-amorphous and to evaluate the success of the prediction model. It was found that the prediction model successfully predicted 11 of the 13 systems. The success of the prediction model suggests it can be used to predict the formation of a range of co-amorphous systems with co-formers and APIs not directly related to the original training set.

The FTIR data indicates that bisVCap stabilises the COAM systems by the formation of hydrogen bonds with the two carbonyl groups disrupting the intermolecular hydrogen bonding in the pure API. The FTIR data suggests bisVCap is a good co-amorphous co-former when paired with APIs containing hydrogen bond donor groups.

The stability of the three COAM systems of bisVCap with indomethacin, paracetamol and simvastatin was analysed at two different storage temperatures to determine if the prediction model COAM score correlates with the stability of the co-amorphous phases. The stability assessment showed indomethacin was the most stable agreeing with the prediction model, however, paracetamol was more stable than simvastatin suggesting the prediction model is not very good at predicting stability. The co-amorphous bisVCap systems with indomethacin and simvastatin that underwent crystallisation formed the thermodynamically stable polymorphic form at the storage conditions, suggesting bisVCap only affects the crystallisation rate and not the crystallisation process. The XRPD patterns also show bisVCap recrystallised from the COAM systems with indomethacin and simvastatin, suggesting the APIs are not capable of stabilising the bisVCap in an amorphous form.

The COAM system of bisVCap with furosemide made by RSE was selected for further experiments because it is a free flowing powder at room temperature with a high  $T_g$ . The stability of the COAM system as a function of the API to bisVCap ratio was studied using bisVCap furosemide at ratios of 1:2, 1:3 and 1:4. The 1:3 and 1:4 systems crystallised during the solvent evaporation into the form II polymorph, which is the usual polymorph that forms from the evaporation of acetone under reduced pressure, again suggesting bisVCap does not affect the crystallisation process. The system is stable up to a ratio of 1:2 and FTIR data indicates that bisVCap is limited to stabilising two molecules of furosemide, potentially because it contains only two carbonyl groups, as shown by the presence of amorphous material by XRPD in the 1:3 and 1:4 systems. A humidity study was also performed on the 1:1 bisVCap furosemide system with the system remaining stable for 28 days when stored at 33% RH. The bisVCap furosemide system that was stored at 100% RH underwent recrystallization into the form I polymorph of furosemide which is the thermodynamically stable form.

### 3.4 Experimental

#### 3.4.1 Materials

Piroxicam was purchased from Alfa Aesar (Massachusetts, USA). Aspirin, chloramphenicol, chlorpropamide, indomethacin, ketoprofen, n-vinyl caprolactam, paracetamol, phenobarbital and trifluoroacetic acid were purchased from Merck (Massachusetts, USA). Hexane and acetone were purchased from Thermo Fisher Scientific (Massachusetts, USA). Famotidine was purchased from Tokyo Chemical Industry (Tokyo, Japan). Flurbiprofen, furosemide, mebendazole and simvastatin were purchased from Fluorochem (Derbyshire, UK). All chemicals were used without further purification.

#### 3.4.2 Analytical Methods

IR spectra were measured with a Perkin-Elmer 100 FT-IR Spectrometer with an  $\mu$ ATR attachment. Data was recorded at a resolution of  $4\text{ cm}^{-1}$  for 8 scans over a range of  $4000\text{ cm}^{-1}$  to  $550\text{ cm}^{-1}$ .

XRPD measurements were performed using an X'Pert PANalytical PRO X-ray diffractometer (PANalytical, Almelo, The Netherlands) or a Bruker D8 with  $\text{CuK}\alpha$  radiation ( $1.54187\text{ \AA}$ ), acceleration voltage and current of 45 kV and 40 mA, respectively. The samples were

scanned in reflectance mode between 2° and 35° 2 $\theta$  with a scan rate of 0.067335° 2 $\theta$ /s and a step size of 0.0262606°. The data was collected and analysed using the software X'Pert Data Collector (PANalytical, Almelo, The Netherlands).

$^1\text{H}$  and  $\{^1\text{H}\}^{13}\text{C}$  solution NMR spectra were recorded using a Varian Mercury-400 spectrometer, operating at 400 MHz for  $^1\text{H}$  and 100 MHz for  $^{13}\text{C}$ , chemical shifts are reported in ppm ( $\delta$ ) and referenced to residual protic solvent.

Elemental analysis was performed by the University of Durham service using an Exeter CE-440 Elemental Analyser.

Electrospray mass spectrometry was recorded using a TQD mass spectrometer and an Acquity ultra-performance liquid chromatography. The Acquity photodiode array detector provides absorbance data from 210 nm to 400 nm. The sample is dissolved in methanol at 1 mg/mL.

Hot stage microscopy was performed using an Olympus XC50 microscope with a Linkam LTS420 heating stage. Samples were placed onto a glass microscope slide and covered with a thin glass cover slide.

Differential scanning calorimetry thermograms were recorded using a PerkinElmer 8500 calorimeter or a PerkinElmer DSC 4000 analyser, calibrated using an indium standard, with samples accurately weighed ( $\pm 0.5$  mg) into standard aluminium pans. The heating rate was 10 °C min $^{-1}$ .

#### 3.4.3 COSMOquick Calculations

COSMOquick version 1.7 (COSMOlogic GmbH & Co. KG, Leverkusen, Germany) was used to calculate the excess enthalpy of mixing ( $\Delta H_{mix}$ ) and excess enthalpy of hydrogen bonding ( $\Delta H_{hb}$ ), of the two-component system. For each component, the following variables were calculated  $\mu$ , the pseudo chemical potential of the pure solute and  $\delta h$ , the Hansen parameter for hydrogen bonding. The difference between the API and co-former values were calculated and used as the variables in the PLS-DA.

#### 3.4.4 Synthesis of BisVCap

N-vinyl caprolactam (30.0 g, 216 mmol) was added to hexane (150 cm $^3$ ) in a two-neck flask with a reflux condenser under nitrogen. The sample was heated to 50 °C to dissolve the N-



vinyl caprolactam. Trifluoroacetic acid (0.75 cm<sup>3</sup>) was added and the reaction mixture was heated to 60 °C for 2 hours. A white precipitate appeared during the reaction. The solid was removed via vacuum filtration and washed with hexane (3 x 20 mL). The white precipitate was recrystallized twice from acetone to give a white powder.

Yield 10.05 g, 36.1 mmol, 33%

Elemental analysis expected for C<sub>16</sub>H<sub>26</sub>N<sub>2</sub>O<sub>2</sub>: C, 69.03; H, 9.41; N, 10.06. Found: C, 69.10; H, 9.39; N, 9.99.

The analysis is in agreement with published work.<sup>24</sup> <sup>1</sup>H NMR (400 MHz, CDCl<sub>3</sub>) δ 7.26 (dd, *J* = 14.9, 1.7 Hz, 1H, vinyl NCH), 5.43 (qdd, *J* = 6.9, 5.0, 1.7 Hz, 1H, NCH), 5.01 (dd, *J* = 14.9, 5.0 Hz, 1H, vinyl CH), 3.60-3.54 (m, 2H, CH<sub>2</sub>), 3.32-3.12 (m, 2H, CH<sub>2</sub>), 2.68-2.62 (m, 2H, CH<sub>2</sub>), 2.59-2.48 (m, 2H, CH<sub>2</sub>), 1.84-1.47 (m, 12H, CH<sub>2</sub>), 1.27 (d, *J* = 6.9 Hz, 3H, CH<sub>3</sub>). <sup>13</sup>C NMR (101 MHz, CDCl<sub>3</sub>) δ 175.60, 174.33, 128.13, 110.28, 48.65, 45.32, 43.21, 37.51, 37.17, 30.52, 30.02, 29.54, 29.40, 27.25, 23.41, 16.78. <sup>13</sup>C{<sup>1</sup>H} SS NMR (101 MHz) δ 174.4, 129.2, 110.1, 50.6, 42.5, 36.4, 31.8, 30.0, 28.3, 25.6, 25.0, 22.3. IR ν = 1667 (C=C), 1641 (C=O), 1622 (C=O) cm<sup>-1</sup>. MS (ESI) *m/z*: 278 (M<sup>+</sup>).

#### 3.4.5 HSM Method for Co-amorphous Systems

BisVCap and each API were individually heated at 20 °C min<sup>-1</sup>. After the sample was fully melted it was removed from the HSM and placed on a freezer block to flash cool the sample and prevent crystallisation on cooling. The samples were monitored after 24 hours using an optical microscope with a polariser to determine if crystallisation had occurred. The same process was repeated using a 1:1 molar ratio of bisVCap and API.

#### 3.4.6 Co-melting for Co-amorphous Systems

A 1:1 molar ratio of bisVCap and API was heated in a vial to a few degrees above the highest melting point out of the API or bisVCap. The mixture was held at this temperature for ten minutes and then it was rapidly cooled by submerging the vial into dry ice and acetone. The mixtures were then analysed via powder X-ray diffraction and FTIR to check if the sample was amorphous.

#### 3.4.7 RSE for Co-amorphous Systems

The chosen ratio of bisVCap and API was dissolved in the minimum amount of acetone. The solvent was rapidly removed under reduced pressure on a water bath at 60 °C. The mixtures were then analysed via XRPD and FTIR to check if the sample was amorphous.

#### 3.4.8 Stability Test at Different Temperatures

Co-amorphous samples of bisVCap with indomethacin, paracetamol and simvastatin in a 1:1 molar ratio were produced by RSE. The samples were either stored in a desiccator at ~20 °C or 3 °C. The samples were characterised by powder X-ray diffraction and FTIR after 1 and 2 weeks.

#### 3.4.9 Varying Humidity Stability Test

A co-amorphous sample of bisVCap and furosemide in a 1:1 molar ratio was produced via RSE. Five 50 mg samples were placed in a vial and stored in five different humidity environments. Number one was sealed and placed in a vacuum desiccator under a static vacuum which is effectively classed as 0% RH. Number two was placed inside a vial containing a saturated lithium chloride solution and sealed which is effectively classed as 11% RH. Number three was placed inside a vial containing a saturated magnesium chloride solution and sealed which is effectively classed as 33% RH. Number four was placed inside a vial containing a saturated sodium chloride solution and sealed which is effectively classed as 75% RH. Number five was placed inside a vial containing distilled water and sealed which is effectively classed as 100% RH. The samples were analysed by powder X-ray diffraction and FTIR after seven days and 28 days.

### 3.5 References

1. M. Ku, *AAPS J.*, 2008, **10**, 208-212.
2. B. C. Hancock and G. Zografi, *J. Pharm. Sci.*, 1997, **86**, 1-12.
3. C. L.-N. Vo, C. Park and B.-J. Lee, *Eur. J. Pharm. Biopharm.*, 2013, **85**, 799-813.
4. J. A. Baird and L. S. Taylor, *Adv. Drug Deliv. Rev.*, 2012, **64**, 396-421.
5. C. A. Lipinski, F. Lombardo, B. W. Dominy and P. J. Feeney, *Adv. Drug Deliv. Rev.*, 1997, **23**, 3-25.
6. G. Van Den Mooter, *Drug Discov. Today Technol.*, 2012, **9**, e71-e174.
7. H. Grohganz, P. A. Priemel, K. Löbmann, L. H. Nielsen, R. Laitinen, A. Mullertz, G. Van den Mooter and T. Rades, *Expert Opin. Drug Deliv.*, 2014, **11**, 977-989.
8. K. Löbmann, H. Grohganz, R. Laitinen, C. Strachan and T. Rades, *Eur. J. Pharm. Biopharm.*, 2013, **85**, 873-881.

9. K. Löbmann, R. Laitinen, C. Strachan, T. Rades and H. Grohgan, *Eur. J. Pharm. Biopharm.*, 2013, **85**, 882-888.
10. H. Grohgan, K. Löbmann, P. Priemel, K. Tarp Jensen, K. Graeser, C. Strachan and T. Rades, *J. Drug Deliv. Sci. Technol.*, 2013, **23**, 403-408.
11. R. Mizoguchi, H. Waraya and Y. Hirakura, *Mol. Pharm.*, 2019, **16**, 2142-2152.
12. W. Wu, K. Lobmann, J. Schnitzkewitz, A. Knuhtsen, D. S. Pedersen, H. Grohgan and T. Rades, *Int. J. Pharm.*, 2018, **549**, 380-387.
13. R. B. Chavan, R. Thipparaboina, D. Kumar and N. R. Shastri, *Int. J. Pharm.*, 2016, **515**, 403-415.
14. J. Liu, H. Grohgan, K. Löbmann, T. Rades and N.-J. Hempel, *Pharmaceutics*, 2021, **13**.
15. A. Karagianni, K. Kachrimanis and I. Nikolakakis, *Pharmaceutics*, 2018, **10**, 98.
16. G. Kasten, H. Grohgan, T. Rades and K. Lobmann, *Eur. J. Pharm. Sci.*, 2016, **95**, 28-35.
17. S. J. Dengale, H. Grohgan, T. Rades and K. Löbmann, *Adv. Drug Deliv. Rev.*, 2016, **100**, 116-125.
18. P. A. Corner, J. J. Harburn, J. W. Steed, J. F. McCabe and D. J. Berry, *Chem. Commun.*, 2016, **52**, 6537-6540.
19. L. I. Chambers, H. Grohgan, H. Palmelund, K. Löbmann, T. Rades, O. M. Musa and J. W. Steed, *Eur. J. Pharm. Sci.*, 2021, **157**, 105636.
20. G. Kasten, K. Lobmann, H. Grohgan and T. Rades, *Int. J. Pharm.*, 2019, **557**, 366-373.
21. M. J. Goodwin, O. M. Musa, D. J. Berry and J. W. Steed, *Cryst. Growth Des.*, 2018, **18**, 701-709.
22. A. Perrin, M. J. Goodwin, O. M. Musa, D. J. Berry, P. Corner, K. Edkins, D. S. Yufit and J. W. Steed, *Cryst. Growth Des.*, 2017, **17**, 3236-3249.
23. A. Perrin, M. J. Goodwin, O. M. Musa, D. S. Yufit and J. W. Steed, *Cryst. Eng. Comm.*, 2017, **19**, 7125-7131.
24. J. R. Davenport, O. M. Musa, M. J. Paterson, M.-O. M. Piepenbrock, K. Fucke and J. W. Steed, *Chem. Commun.*, 2011, **47**, 9891-9893.
25. S. Baghel, H. Cathcart and N. J. O'Reilly, *J. Pharm. Sci.*, 2016, **105**, 2527-2544.
26. M. Mitrabhanu, S. S. Apte, A. Pavani and V. S. Appadwedula, *Indo Am. J. Pharm.*, 2018, **5**, 5494-5507.
27. A. C. F. Rumondor, I. Ivanisevic, S. Bates, D. E. Alonzo and L. S. Taylor, *Pharm. Res.*, 2009, **26**, 2523-2534.
28. A. C. Rumondor, P. J. Marsac, L. A. Stanford and L. S. Taylor, *Mol. Pharm.*, 2009, **6**, 1492-1505.
29. S. Sethia and E. Squillante, *Int. J. Pharm.*, 2004, **272**, 1-10.
30. A. Newman, K. Nagapudi and R. Wenslow, *Ther. Deliv.*, 2015, **6**, 247-261.
31. T. Vasconcelos, B. Sarmiento and P. Costa, *Drug Discov. Today*, 2007, **12**, 1068-1075.
32. A. T. M. Serajuddin, *J. Pharm. Sci.*, 1999, **88**, 1058-1066.
33. J. F. Willart and M. Descamps, *Mol. Pharm.*, 2008, **5**, 905-920.
34. M. Descamps, J. F. Willart, E. Dudognon and V. Caron, *J. Pharm. Sci.*, 2007, **96**, 1398-1407.
35. A. Heinz, K. C. Gordon, C. M. McGoverin, T. Rades and C. J. Strachan, *Eur. J. Pharm. Biopharm.*, 2009, **71**, 100-108.
36. A. Heinz, C. J. Strachan, K. C. Gordon and T. Rades, *J. Pharm. Pharmacol.*, 2009, **61**, 971-988.
37. P. J. Wheatley, *J. Chem. Soc.*, 1964, 6036-6048.

38. J. L. Flippen and R. D. Gilardi, *Acta Crystallogr. B*, 1975, **31**, 926-928.
39. J. Lamotte, H. Campsteyn, L. Dupont and M. Vermeire, *Acta Crystallogr. B*, 1978, **34**, 1657-1661.
40. T. J. Kistenmacher and R. E. Marsh, *J. Am. Chem. Soc.*, 1972, **94**, 1340-1345.
41. P. Briard and J. C. Rossi, *Acta Crystallogr. C*, 1990, **46**, 1036-1038.
42. C. Chatterjee, J. K. Dattagupta, N. N. Saha, W. Saenger and K. Müller, *J. Cryst. Mol. Struct.*, 1979, **9**, 295-304.
43. C. H. Koo, S. I. Cho and Y. H. Yeon, *Arch. Pharmacol Res.*, 1980, **3**, 37-49.
44. M. Haisa, S. Kashino and H. Maeda, *Acta Crystallogr. B*, 1974, **30**, 2510-2512.
45. P. Williams, *Acta Crystallogr. B*, 1974, **30**, 12-17.
46. J. Cejka, B. Kratochvil, I. Cisarova and A. Jegorov, *Acta Crystallogr. C*, 2003, **59**, o428-o430.
47. N. Y. Tan and J. A. Zeitler, *Mol. Pharmaceutics*, 2015, **12**, 810-815.
48. P. Espeau, R. Céolin, J. L. Tamarit, M. A. Perrin, J. P. Gauchi and F. Leveiller, *J. Pharm. Sci*, 2005, **94**, 524-539.
49. M. Haisa, S. Kashino, R. Kawai and H. Maeda, *Acta Crystallogr. B*, 1976, **32**, 1283-1285.
50. W. Wu, H. Ueda, K. Löbmann, T. Rades and H. Grohgan, *Eur. J. Pharm. Biopharm.*, 2018, **131**, 25-32.
51. C. Garnero, A. K. Chattah and M. Longhi, *Carbohydr. Polym.*, 2013, **94**, 292-300.
52. L. Greenspan, *J. Res. NBS. A Phys. Ch.*, 1977, **81A**, 89-96.
53. N. J. Babu, S. Cherukuvada, R. Thakuria and A. Nangia, *Cryst. Growth Des.*, 2010, **10**, 1979-1989.

## 4 Structure of the Poly(vinylpyrrolidone)-Hydrogen Peroxide Complex

### 4.1 Introduction

Hydrogen peroxide is a strong oxidizing agent, bleaching agent, and antiseptic used in a range of commercial applications including teeth whitening formulations.<sup>1-3</sup> It oxidises the aromatic amino acids present in dentin phosphoprotein, decreasing the fluorescent intensity and lightening the colour of teeth.<sup>4,5</sup> Hydrogen peroxide can be applied to the teeth in a variety of ways including bleaching trays, a bleaching gel or strips placed onto the teeth.<sup>6-9</sup> Pure hydrogen peroxide is unstable and easily decomposes in the presence of light or oxidizable compounds.<sup>10,11</sup> This instability can be partially overcome with adducts such as urea-hydrogen peroxide, a relatively stable complex in the form of a white crystalline solid.<sup>12,13</sup> Urea-hydrogen peroxide releases free hydrogen peroxide when dissolved in water, providing a more controlled application.<sup>14</sup> However, the urea-hydrogen peroxide complex is unstable at 40 °C and decomposes on storage.<sup>15-17</sup> Poly(vinylpyrrolidone) (PVP) forms a more stable complex with hydrogen peroxide called Peroxydone (PEX).<sup>18,19</sup> PEX is a stable powder that releases hydrogen peroxide on contact with water or saliva.<sup>15,20</sup> PEX was first described in 1967 when D. A. Shiraeff filed for a patent with GAF Chemicals Corp.<sup>21</sup> PEX can be prepared using a variety of methods including dissolving the PVP with hydrogen peroxide and evaporating the solvent,<sup>22</sup> spray drying<sup>22</sup> and spraying an aqueous solution of hydrogen peroxide onto a fluidised bed of PVP.<sup>23,24</sup> One of the main uses of PEX is in modern teeth whitening formulations.<sup>25-27</sup>

In a patent by Nacharaju *et al.* the material PEX is speculated to form in one of two structures (Figure 4.1) with either a 1:1 or 1:2 ratio of hydrogen peroxide to PVP monomer.<sup>28</sup> Infrared (IR) spectroscopy and *ab initio* calculations were used by Panarin *et al.* to investigate the complexation of hydrogen peroxide by PVP.<sup>18</sup> The calculations show that the interaction energy of the model monomer 1-ethyl-2-pyrrolidone with hydrogen peroxide is stronger than with water, which means the hydrogen peroxide stays associated with 1-ethyl-2-pyrrolidone even when in water. The calculations also reveal strong self-association between adjacent hydrogen peroxide units, which suggests the formation of extended ribbon structures in PEX.

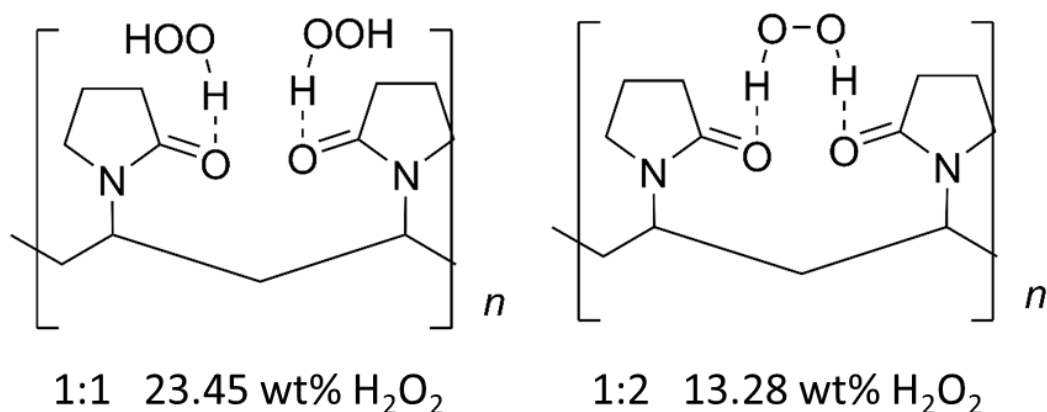


Figure 4.1: Suggested models of the bonding between hydrogen peroxide and PVP.<sup>28</sup>

The structure and interactions of polymers can be complex to study due to the large molecular weights and polydispersity making analytical data difficult to interpret.<sup>29</sup> To overcome this complexity, small molecule analogues of PVP can be used.<sup>29</sup> For example the X-ray crystal structure of a two monomer PVP model compound (H<sub>2</sub>bisVP) (Figure 4.2) showed that the structure of the WHO essential medicine povidone-iodine is better represented as involving intermolecular hydrogen bonding between separate polymer chains rather than an intramolecular hydrogen bond between adjacent units.<sup>30</sup> Small molecule analogues of PVP and poly(vinylcaprolactam) (PVCap) have also been used to help understand the interactions between polymeric amorphous solid dispersants and active pharmaceutical ingredients,<sup>31</sup> and to understand the role of PVP and PVCap as clathrate hydrate inhibitors in the petrochemical industry.<sup>32</sup> The present work aims to improve the understanding of the interactions between PVP and hydrogen peroxide and the effects of hydration using IR spectroscopy, solid-state (SS) NMR spectroscopy, density functional theory (DFT) calculations and structure elucidation of H<sub>2</sub>bisVP-H<sub>2</sub>O<sub>2</sub> model systems using single crystal X-ray diffraction.<sup>33, 34</sup>

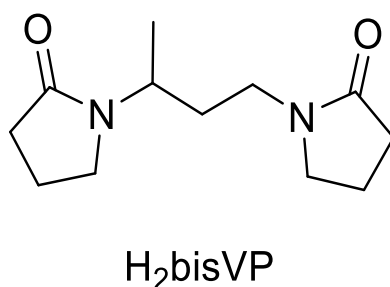


Figure 4.2: The chemical structure of H<sub>2</sub>bisVP.

## 4.2 Results and Discussion

### 4.2.1 Polymer Analysis

PEX K-30 and free PVP K-25 (the Fikentscher K-value<sup>35</sup> is derived from the viscosity of a 1 wt % solution of polymer, increasing K-value is correlated with increased molecular weight) of similar molecular weight were characterised by FTIR spectroscopy (Figure 4.3) the  $\nu$ OH stretching band from the hydrogen peroxide occurs at  $3226\text{ cm}^{-1}$  in PEX (Table 4.1). PVP is hygroscopic and also exhibits a  $\nu$ OH stretching band of lower intensity at  $3458\text{ cm}^{-1}$  which is assigned to trace quantities of water.<sup>36</sup> The  $\nu$ CO stretching band shifts from  $1667\text{ cm}^{-1}$  for PVP to  $1638\text{ cm}^{-1}$  for PEX, indicating that the C=O bond is weaker for PEX as a result of hydrogen bonding interactions between the C=O of PVP and the OH groups of the hydrogen peroxide.<sup>37</sup> Two other PVP and PEX pairs with different molecular weights were also characterised; a K-90 analogue and crosslinked XL-10 (Table 4.1, Figure 4.4, Figure 4.5). Both the K-90 and XL-10 samples show similar changes in the FTIR spectra upon hydrogen peroxide complexation indicating hydrogen bonding interactions, which are most pronounced for the XL-10 sample. The K-90 polymer has a significantly higher molecular weight than the K-25 and XL-10 polymer which may result in less accessible carbonyl groups.<sup>38</sup>

Table 4.1: FTIR  $\nu$ OH and  $\nu$ CO stretching bands for PVP K-25, K-90, XL-10, PEX K-30, K-90, XL-10, H<sub>2</sub>bisVP, amorphous H<sub>2</sub>bisVP-H<sub>2</sub>O<sub>2</sub> and crystalline H<sub>2</sub>bisVP·2H<sub>2</sub>O<sub>2</sub>.

Sample	Stretching band (cm <sup>-1</sup> )	
	$\nu$ OH	$\nu$ CO
PVP K-25	3458	1667
PEX K-30	3226	1638
PVP K-90	3460	1659
PEX K-90	3238	1642
PVP XL-10	3460	1663
PEX XL-10	3206	1637
H <sub>2</sub> bisVP	3448	1668
H <sub>2</sub> bisVP-H <sub>2</sub> O <sub>2</sub> amorphous	3309	1623
H <sub>2</sub> bisVP·H <sub>2</sub> O <sub>2</sub> ·H <sub>2</sub> O	3241	1639
H <sub>2</sub> bisVP·1.7H <sub>2</sub> O <sub>2</sub> ·0.3H <sub>2</sub> O	3247	1627
H <sub>2</sub> bisVP·2H <sub>2</sub> O <sub>2</sub>	3253	1625



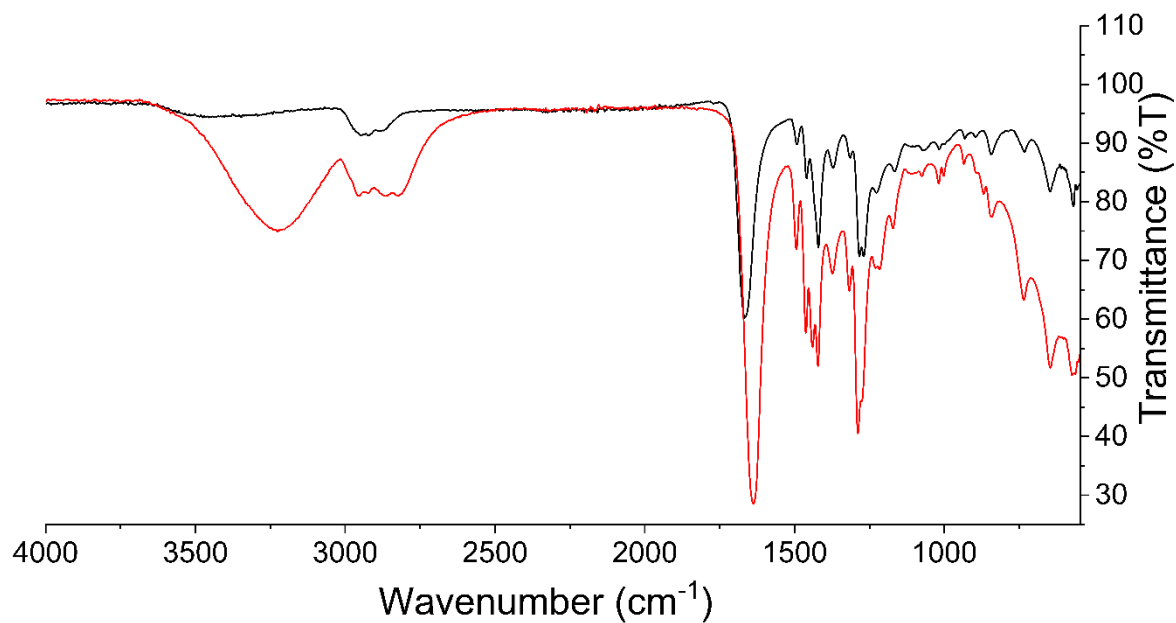


Figure 4.3: The FTIR spectra of PVP K-25 (black) and PEX K-30 (red).

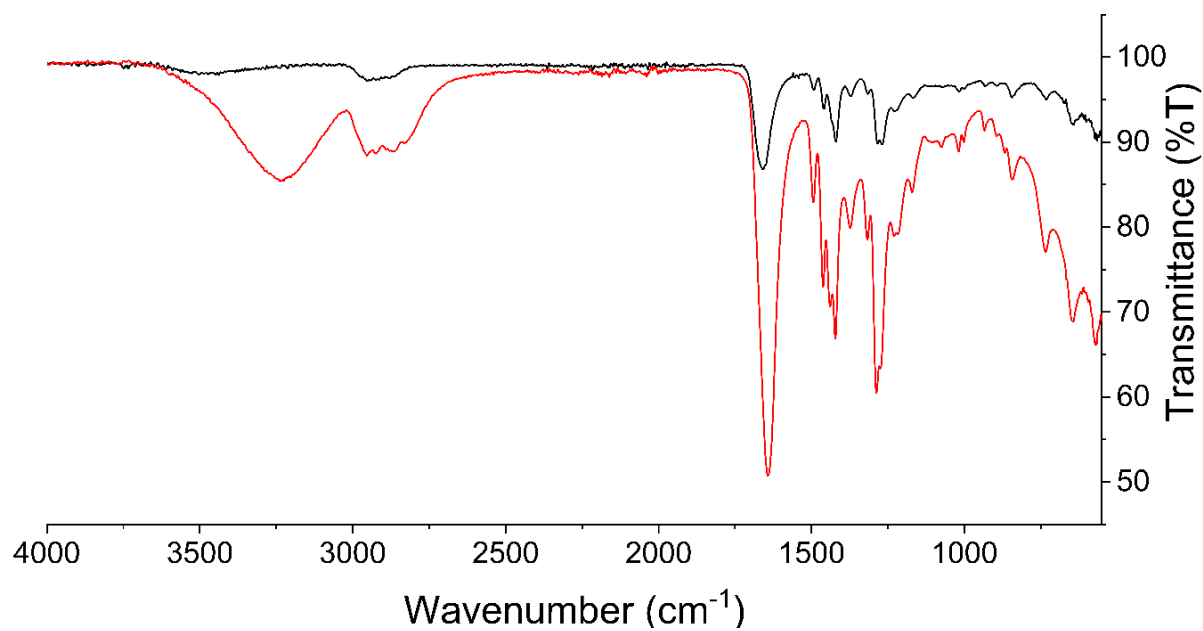


Figure 4.4: The FTIR spectra of PVP K-90 (black) and PEX K-90 (red).

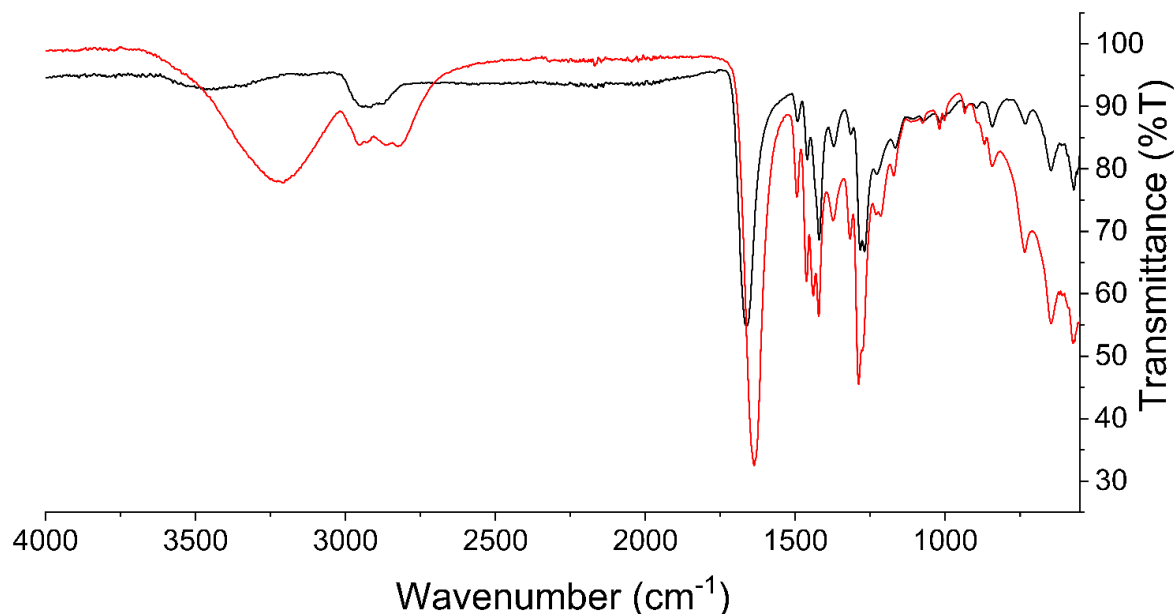


Figure 4.5: The FTIR spectra of PVP XL-10 (black) and PEX XL-10 (red).

The PVP K-25 and PEX K-30 samples were also characterised by solid-state MAS  $^{13}\text{C}$  NMR spectroscopy (Figure 4.6). The peak for the carbonyl carbon atom C1 shifts from 175.7 ppm for PVP to 177.8 ppm for PEX, consistent with the formation of hydrogen bonds between the carbonyl group and the hydrogen peroxide. The SS NMR spectra of PVP K-90 and PVP XL-10 (Figure 4.7, Figure 4.8) are similar indicating the three polymers interact with hydrogen peroxide in the same way. The occurrence of a single peak for the carbonyl carbon atom indicates the majority of PVP carbonyl groups form the same number of hydrogen bonds with hydrogen peroxide molecules.

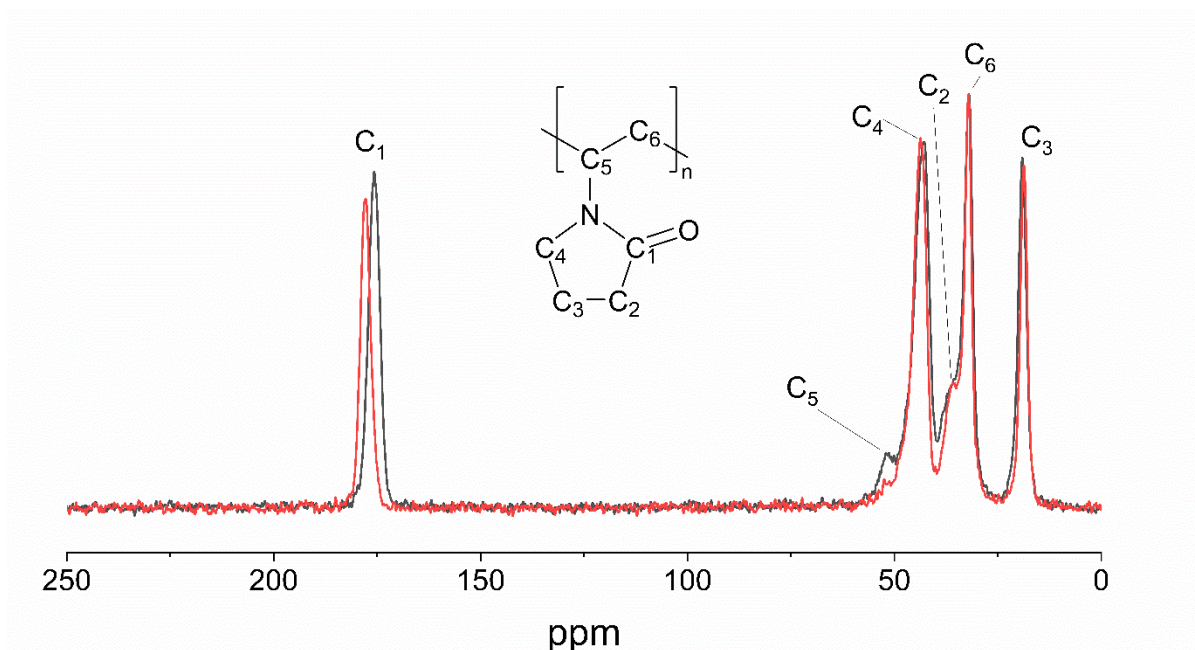


Figure 4.6: The MAS solid state NMR spectra of PVP K-25 (black) and PEX K-30 (red).

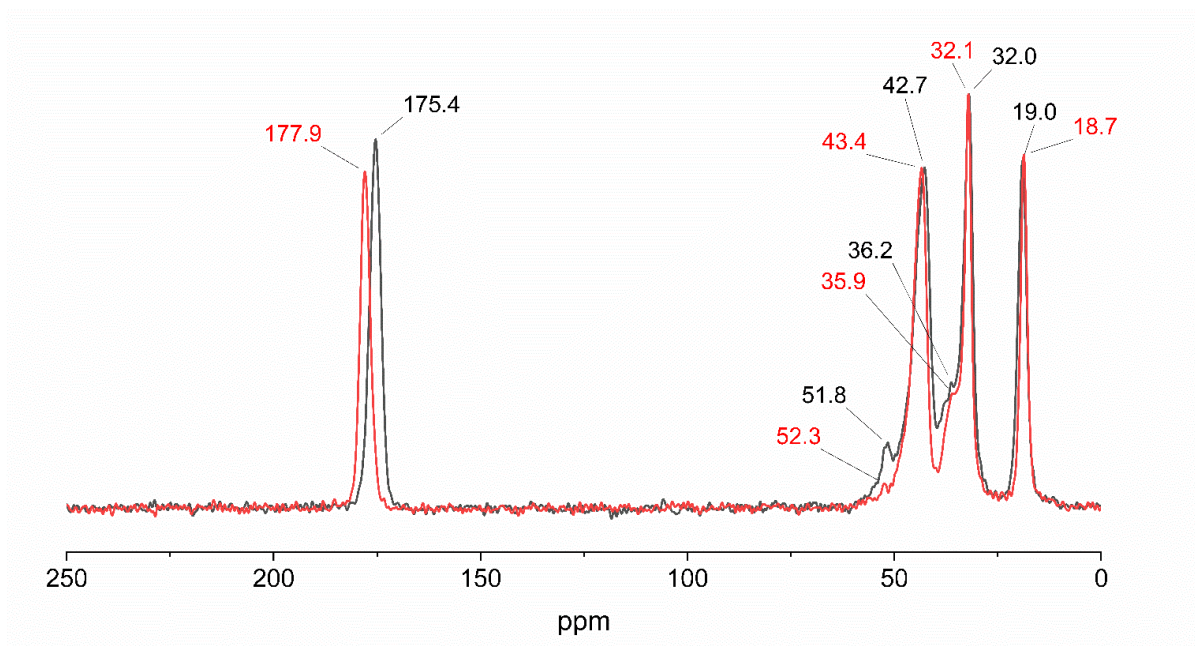


Figure 4.7: The MAS solid state NMR spectra of PVP K-90 (black) and PEX K-90 (red).

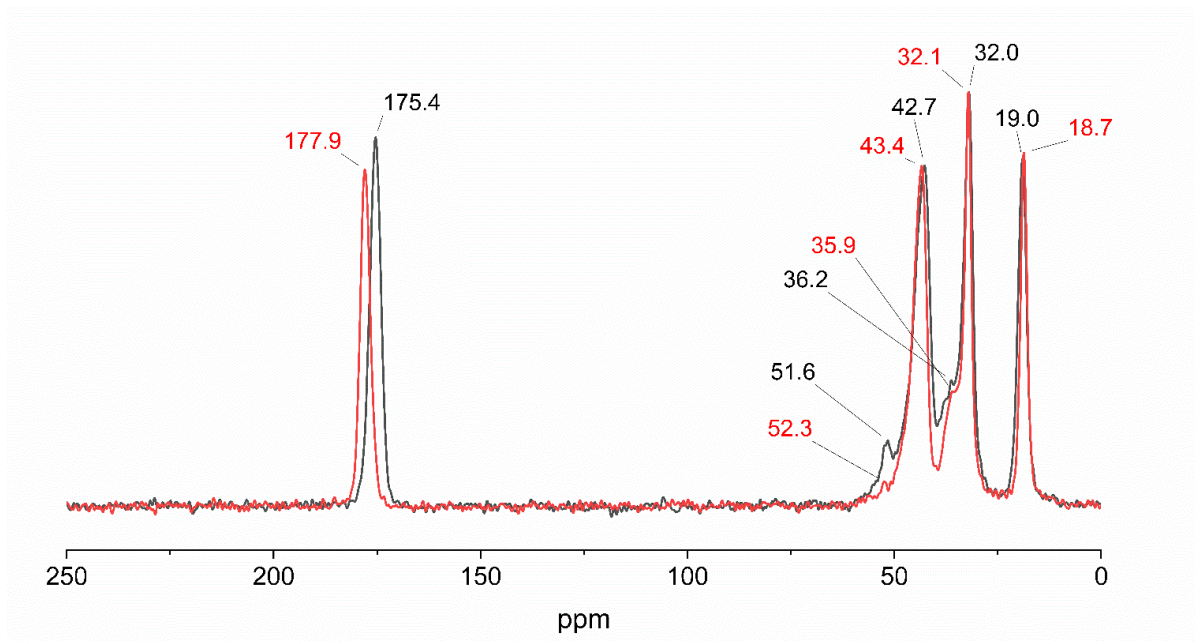


Figure 4.8: The MAS solid state NMR spectra of PVP XL-10 (black) and PEX XL-10 (red).

Potassium permanganate titration analysis (three repetitions) indicates ratios of hydrogen peroxide to pyrrolidone monomer unit of  $0.86(\pm 0.04):1$  for PEX K30,  $0.68(\pm 0.03):1$  for PEX K90 and  $0.76(\pm 0.04):1$  for PEX XL-10 (Table 4.2). Elemental analysis indicates ratios of hydrogen peroxide to pyrrolidone monomer unit of  $0.89:1$  for PEX K30,  $0.77:1$  for PEX K90 and  $0.92:1$  for PEX XL-10 (Table 4.3). These ratios of under 1:1 (Table 4.4) suggest that some PVP monomer units are either not associated with hydrogen peroxide or that a single hydrogen peroxide molecule can bridge between two pyrrolidone monomers. The presence of adventitious moisture is also likely, and some carbonyl sites may interact with water instead of hydrogen peroxide.

Table 4.2: Table of all titration results including calculated weight percentage of hydrogen peroxide and calculated ratio of hydrogen peroxide to VP (assuming no water present in peroxydone).

Sample	Mass of sample/ g	Volume/mL	Conc. of potassium permanganate /mol mL <sup>-1</sup>	wt% H <sub>2</sub> O <sub>2</sub>	Ratio of H <sub>2</sub> O <sub>2</sub> (x) to VP (1)
PEX K-30	0.0515	4.4	2.58E-05	18.73	0.75
PEX K-30	0.0510	5.2	2.58E-05	22.35	0.94
PEX K-30	0.0497	4.8	2.58E-05	21.17	0.88
			average	20.75	0.86
PEX K-90	0.0509	4	2.58E-05	17.22	0.68
PEX K-90	0.0512	4	2.58E-05	17.12	0.68
PEX K-90	0.0505	4	2.58E-05	17.36	0.69
			average	17.24	0.68
PEX XL-10	0.0514	4.6	2.58E-05	19.61	0.80
PEX XL-10	0.0504	4.2	2.58E-05	18.26	0.73
PEX XL-10	0.0511	4.4	2.58E-05	18.87	0.76
			average	18.92	0.76

Table 4.3: Table of the elemental analysis results for PEX K-30, K-90 and XL-10 including average result and calculated hydrogen peroxide content per monomer unit based on the elemental percentages for carbon (assuming no water is present).

Sample	Sample no.	Elemental percentage			Calculated H <sub>2</sub> O <sub>2</sub> content
		%C	%H	%N	
PEX K30	1	51.76	7.81	9.63	0.83
	2	50.73	7.43	9.88	0.91
	3	50.30	7.30	9.80	0.94
	Av	50.93	7.51	9.77	0.89
PEX K90	1	52.39	7.92	9.87	0.78
	2	52.41	7.43	10.19	0.77
	3	52.44	7.41	10.19	0.77
	Av	52.41	7.59	10.08	0.77
PEX XL10	1	50.54	7.77	9.45	0.92
	2	50.69	7.34	9.80	0.91
	3	50.69	7.33	9.79	0.91
	Av	50.64	7.48	9.68	0.92

Table 4.4: Table of the expected elemental analysis values with of PEX with three different ratios of PVP monomer to hydrogen peroxide molecule.

Sample	Ratio (H <sub>2</sub> O <sub>2</sub> to C=O)	Expected		
		%C	%H	%N
PEX (1 H <sub>2</sub> O <sub>2</sub> )	(1:1)	49.64	7.64	9.65
PEX (0.5 H <sub>2</sub> O <sub>2</sub> )	(1:2)	56.23	7.87	10.93
PEX (0.75 H <sub>2</sub> O <sub>2</sub> )	(3:4)	52.73	7.75	10.25

#### 4.2.2 Small Molecule Model

The small molecule model H<sub>2</sub>bisVP (Figure 4.2) was used for comparison with the polymer system and to obtain direct structural information. H<sub>2</sub>bisVP has been previously shown to form a good model to understand the bonding in PVP complexes.<sup>30-32</sup> H<sub>2</sub>bisVP was dissolved in ethyl acetate and aqueous hydrogen peroxide (80 wt%) was added, and the solvent was removed to leave an amorphous material. The FTIR spectrum of this amorphous material is similar to that of PEX K30 with both the νOH band and νCO bands shifting to lower wavenumber compared to PVP, suggesting that the H<sub>2</sub>bisVP behaves similarly to the polymer system. The lower wavenumbers observed for the H<sub>2</sub>bisVP model system (Table 4.1) compared to the polymer suggests the carbonyl group is more accessible for hydrogen bond formation in H<sub>2</sub>bisVP.

Cooling solutions of H<sub>2</sub>bisVP with varying amounts of hydrogen peroxide at -28 °C for one week resulted in the formation of three different crystalline samples. These materials are unstable and melt slowly at room temperature. The FTIR spectra of the crystalline materials (before melting) show considerably sharper peaks compared to the amorphous product (Figure 4.9). The νOH and νCO stretching bands are shifted to a lower wavenumber compared to the amorphous material which indicates stronger hydrogen bonding is present. The νCO stretching bands of the crystalline solid shift to a lower wavenumber when a higher ratio of hydrogen peroxide is used indicating increasing hydrogen bonding strength with increasing hydrogen peroxide content.

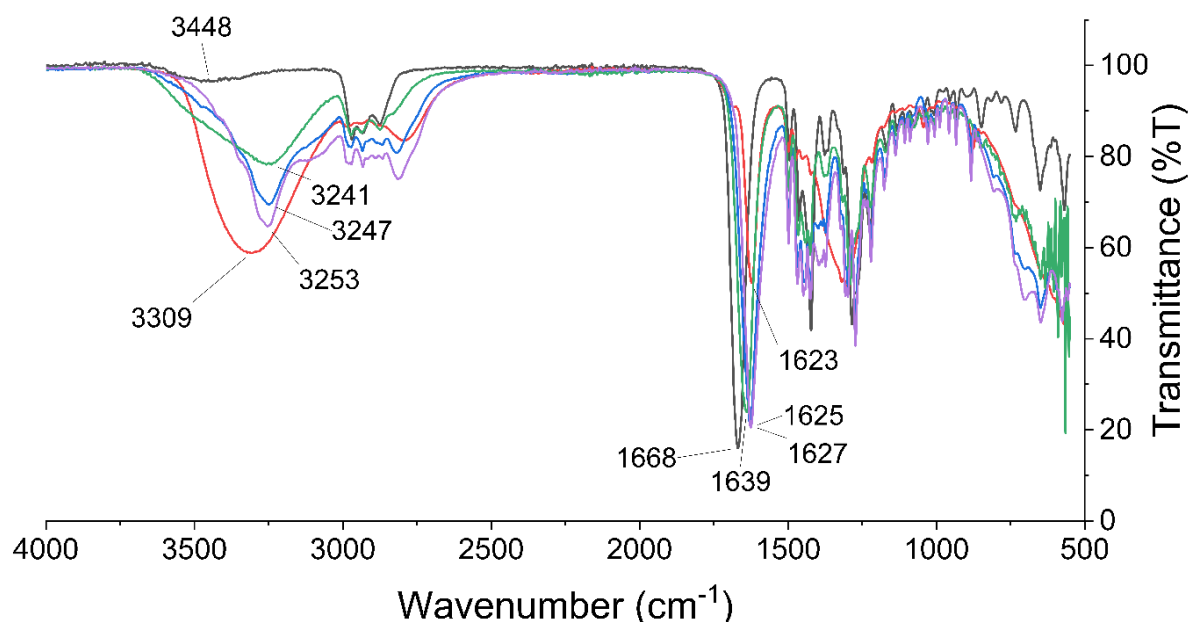


Figure 4.9: FTIR spectrum of H<sub>2</sub>bisVP (black), amorphous H<sub>2</sub>bisVP hydrogen peroxide complex (red), H<sub>2</sub>bisVP·H<sub>2</sub>O<sub>2</sub>·H<sub>2</sub>O (green), H<sub>2</sub>bisVP·1.7H<sub>2</sub>O<sub>2</sub>·0.3H<sub>2</sub>O (purple) and H<sub>2</sub>bisVP·2H<sub>2</sub>O<sub>2</sub> complex (blue).

These microcrystalline H<sub>2</sub>bisVP-H<sub>2</sub>O<sub>2</sub> adducts were added as seeds to H<sub>2</sub>bisVP solutions with different amounts of peroxide in ethanol and stored at -28 °C which resulted in the growth of single-crystal X-ray diffraction (SXRD) quality crystals for general formula H<sub>2</sub>bisVP·*n*H<sub>2</sub>O<sub>2</sub>·*m*H<sub>2</sub>O. A monohydrate-monohydrogenperoxide H<sub>2</sub>bisVP·H<sub>2</sub>O<sub>2</sub>·H<sub>2</sub>O was obtained from a peroxide deficient solution (H<sub>2</sub>bisVP to peroxide ratio 1:0.7). Increasing the amount of peroxide to 1:1.4 gave a mixed material of formula H<sub>2</sub>bisVP·1.7H<sub>2</sub>O<sub>2</sub>·0.3H<sub>2</sub>O while excess peroxide (ratio 1:3) gave a bis(hydrogenperoxide) complex, H<sub>2</sub>bisVP·2H<sub>2</sub>O<sub>2</sub>. All three materials were characterised by SXRD (Figure 4.10, Figure 4.11, Figure 4.12). The three structures are isomorphous. The two hydrogen peroxide molecules in H<sub>2</sub>bisVP·2H<sub>2</sub>O<sub>2</sub> have very different supramolecular environments and different conformations. One of the hydrogen peroxide molecules (A) has a torsion angle HOOH of 83(3)° while the other molecule (B) has a torsion angle of 119(3)°. Both torsion angles represent a skew geometry.<sup>39</sup> Molecule A is hydrogen bonded to one of the H<sub>2</sub>bisVP carbonyl groups with a relatively short O···O distance of 2.749(2) Å suggesting a strong hydrogen bond.<sup>39</sup> Importantly, this molecule is also hydrogen bonded to one of the oxygen atoms of another hydrogen peroxide molecule B connecting the two hydrogen peroxide units. This hydrogen

bond has a similar O...O distance of 2.759(2) Å. Hydrogen peroxide molecule B is hydrogen bonded to carbonyl groups of two different H<sub>2</sub>bisVP molecules resulting in a bridging interaction between two H<sub>2</sub>bisVP molecules (Figure 4.10). The O...O distances in these hydrogen bonds are remarkably short at 2.622(2) and 2.708(2) Å, suggesting they are considerably stronger than those formed by peroxide molecule A. The covalent O-O bond distance for hydrogen peroxide molecules A and B are 1.464(2) Å and 1.451(2) Å, respectively, both are close to the bond length in crystalline hydrogen peroxide (1.461(3) Å).<sup>40</sup> The crystal structure also shows that the hydrogen peroxide units form discrete dimers linked by hydrogen bonds to the H<sub>2</sub>bisVP carbonyl oxygen atoms in this two-monomer model rather than the chain of peroxides suggested by Panarin *et al.*<sup>18</sup>

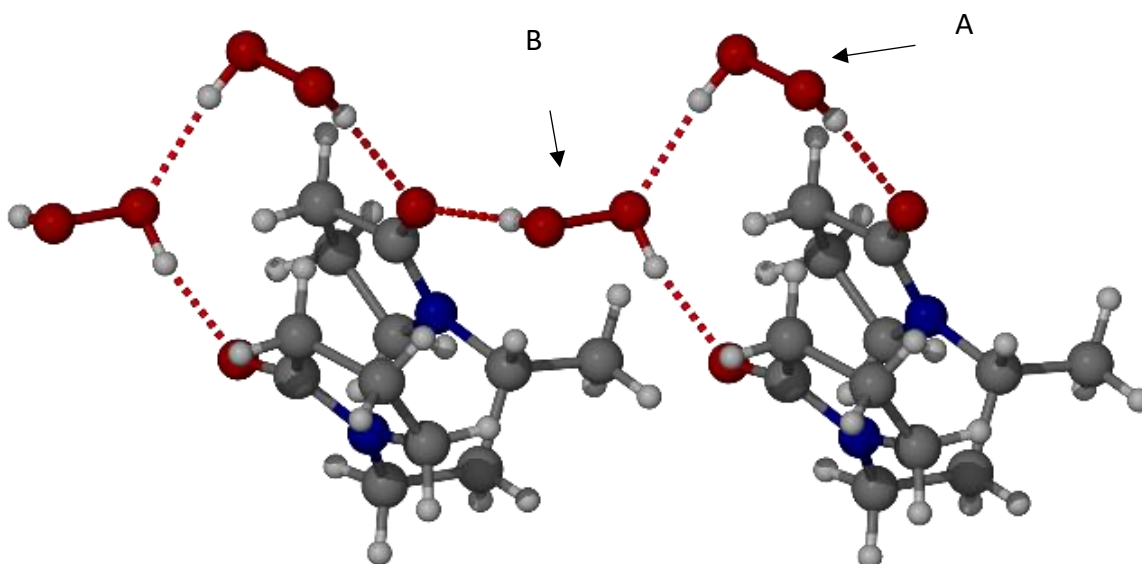


Figure 4.10: The X-ray structure of H<sub>2</sub>bisVP·2H<sub>2</sub>O<sub>2</sub> with the two crystallographically independent peroxide sites labelled A and B.



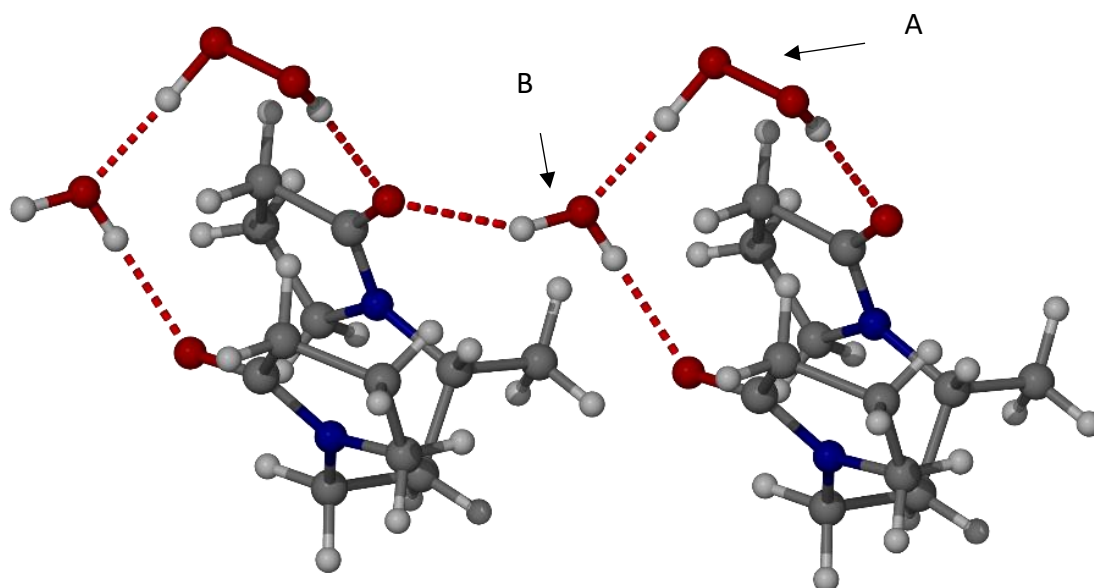


Figure 4.11: The X-ray structure of  $\text{H}_2\text{bisVP}\cdot\text{H}_2\text{O}_2\cdot\text{H}_2\text{O}$  showing the localisation of the water molecule at site B.

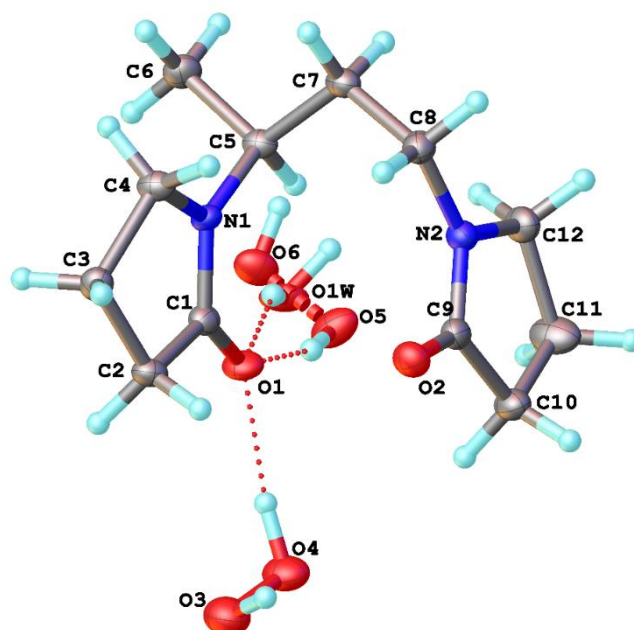


Figure 4.12: The X-ray structure of  $\text{H}_2\text{bisVP}\cdot 1.7\text{H}_2\text{O}_2\cdot 0.3\text{H}_2\text{O}$  showing the disorder in one of the hydrogen peroxide molecules.

The partial hydrate structures are very similar to the bis(hydrogenperoxide) adduct except that just one of the two hydrogen peroxide sites, molecule B, is either partially or completely occupied by water. The potential for water molecules to selectively replace

hydrogen peroxide is likely to be related to the sub-stoichiometric hydrogen peroxide content of PEX found by elemental analysis and manganate titration. The intramolecular distance between the two carbonyl oxygen atoms in the H<sub>2</sub>bisVP molecule varies across the three structures with H<sub>2</sub>bisVP·H<sub>2</sub>O<sub>2</sub>·H<sub>2</sub>O having a distance of 3.512(3) Å, H<sub>2</sub>bisVP·1.7H<sub>2</sub>O<sub>2</sub>·0.3H<sub>2</sub>O 3.436(3) Å, and H<sub>2</sub>bisVP·2H<sub>2</sub>O<sub>2</sub> 3.399(2) Å. Hence the binding site is somewhat flexible and exhibits its optimum geometry with H<sub>2</sub>O<sub>2</sub> explaining the preference for hydrogen peroxide uptake over water in the 1:1.4 ratio solution.

#### 4.2.3 DFT Calculated Models

DFT calculations were performed on multimolecular models of H<sub>2</sub>bisVP and PVP molecules and their H<sub>2</sub>O<sub>2</sub> and H<sub>2</sub>O complexes to investigate the preferred binding modes for water and H<sub>2</sub>O<sub>2</sub> in both H<sub>2</sub>bisVP and oligomer segments of PEX. Calculations using an array of 6 H<sub>2</sub>bisVP and 12 H<sub>2</sub>O<sub>2</sub> molecules derived from the crystal structure of H<sub>2</sub>bisVP·2H<sub>2</sub>O<sub>2</sub> as the starting geometry retained the overall packing arrangement after full optimisation. The simulated IR spectrum from a frequency calculation on this optimised geometry revealed peaks at 3312-3175 and 1636 cm<sup>-1</sup> corresponding to νOH and νCO stretching bands, respectively. The agreement with the corresponding observed values of 3253 and 1625 cm<sup>-1</sup> gives confidence in the accuracy of the multimolecular model at the B3LYP/6-31G(d)/GD3BJ level used here.

Replacement of the hydrogen peroxide with water molecules in this same starting geometry showed that water can replace both types of hydrogen peroxide in this structure with simulated νOH and νCO stretching bands of 3441 and 1643 cm<sup>-1</sup>, respectively. These values are consistent with the experimental values observed for 'wet' H<sub>2</sub>bisVP of 3448 cm<sup>-1</sup> and 1668 cm<sup>-1</sup>, although the experimental values are highly dependent on water content.

The crystal structure of H<sub>2</sub>bisVP·H<sub>2</sub>O<sub>2</sub>·H<sub>2</sub>O reveals a clear preference for water molecules to occupy the B positions rather than the A positions. Geometry optimisations of the AB hydrogen bonding structures containing 6H<sub>2</sub>bisVP, 6H<sub>2</sub>O<sub>2</sub> and 6H<sub>2</sub>O molecules at the A and B positions confirm this strong preference for the water molecules to localise at the B positions with a lower Gibbs free energy of 10.0 kcal mol<sup>-1</sup> (298.15K, 1 atm).

In order to extend the H<sub>2</sub>bisVP model to longer PVP fragments, geometry optimisations of four and six monomer fragments of PVP were examined. Starting geometries of PVP tetramers were generated from the H<sub>2</sub>bisVP geometries. These initial models were

optimised to establish whether AB and all-A motifs are possible in PVP materials with hydrogen peroxide and/or water molecules present. All motifs proved to be feasible and the DFT study does not rule out either the AB or all-A hydrogen bonding motifs in PEX materials. Frequency calculations reveal similar IR values for the H<sub>2</sub>bisVP complexes and hence lend weight to the argument that H<sub>2</sub>bisVP is a suitable model for PVP. The DFT optimised structure of three VP tetramers binding 12H<sub>2</sub>O<sub>2</sub> molecules in an AB cross-linked fashion is shown in Figure 4.13 and represents one possible idealised model for PEX. This geometry does not seem to tolerate water substitution while retaining an ordered cross-linked structure.

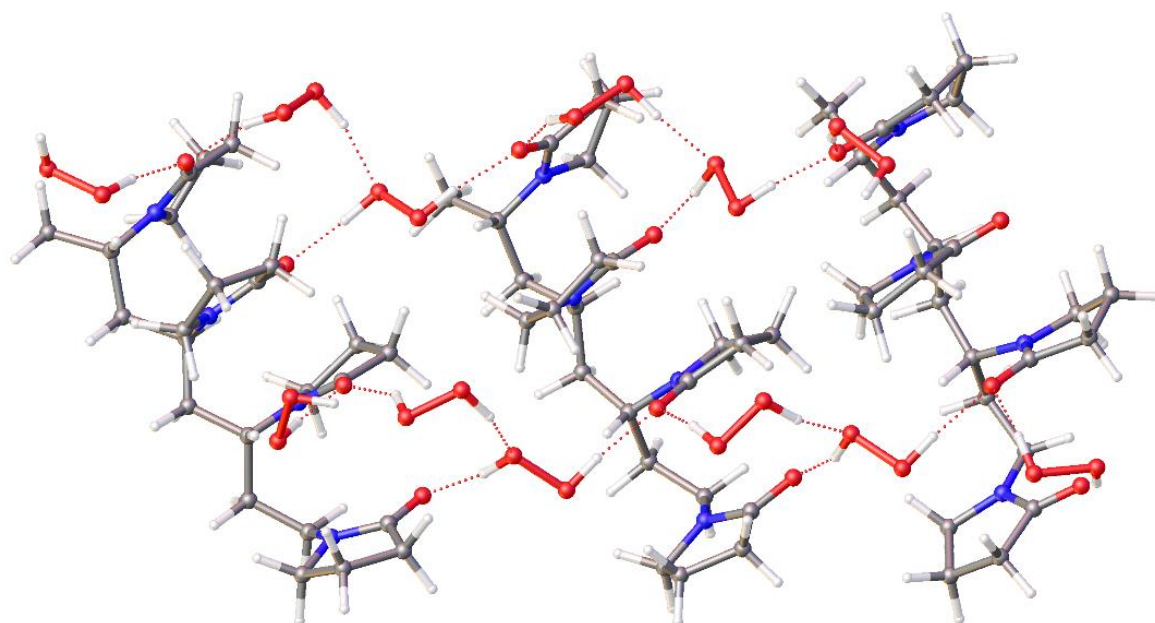


Figure 4.13: The DFT calculated structure of three tetramer models of PVP and twelve molecules of hydrogen peroxide in an alternating A and B hydrogen bonding form.

Optimisation of a longer six-monomer fragment starting with a chain of alternating A and B hydrogen peroxide molecules results in a regular geometry with only one type of hydrogen bonding motif resembling the A-type found in the single crystal structure (Figure 4.14). This implies that the distances between carbonyl groups along the PVP chain tolerate an extended chain of H<sub>2</sub>O<sub>2</sub> molecules of type A but are not appropriate for H<sub>2</sub>O<sub>2</sub> AB type motifs. If AB type motifs are present in PEX then they would result in cross-linking across PVP chains instead of hydrogen bonding along a single polymer chain.

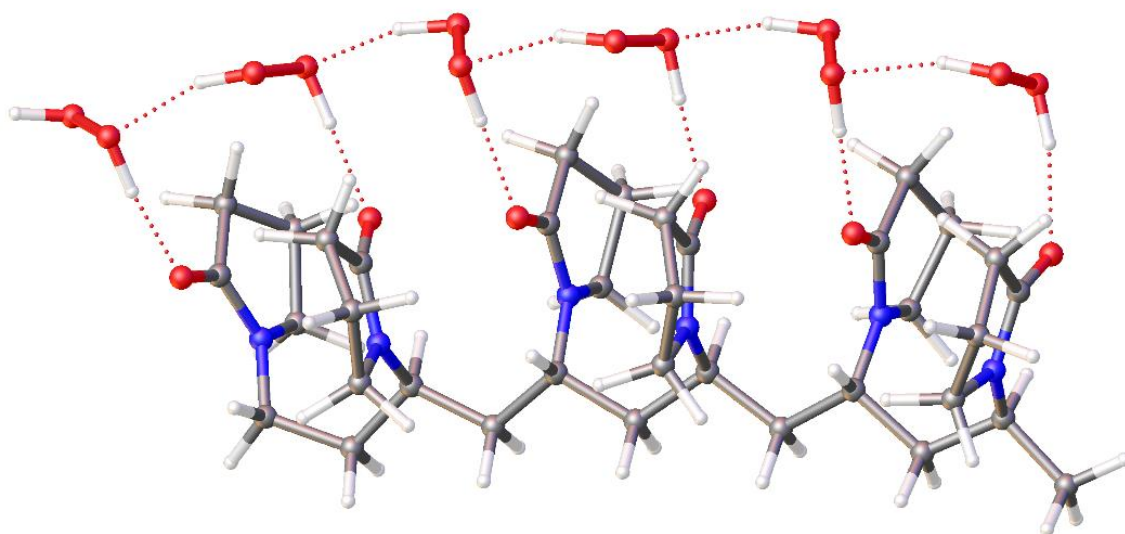


Figure 4.14: The DFT calculated structure of a hexamer model of PVP and six hydrogen peroxide molecules all in the A hydrogen bonding form.

Calculated  $^{13}\text{C}$  NMR chemical shifts based on the optimised geometries of uncomplexed PVP tetramer and both types of PVP tetramer-hydrogen peroxide models (A-type or AB-type) gave carbonyl carbon atom chemical shifts of 173.7, 178.1 and 177.8 ppm, respectively in very good agreement with observed resonances 175.7 and 177.8 ppm for PVP-K25 and PEX K-30 (Figure 4.6). The small 0.3 ppm difference in calculated chemical shift between the A and AB type tetramer models does not confirm one motif over another in PEX as the chemical shifts are averaged over a 3 ppm range of calculated resonances from non-identical CO groups in the optimised geometries.

#### 4.2.4 Peroxydone Structure

The  $\text{H}_2\text{bisVP}$  hydrogen peroxide co-crystal structures represent a plausible model for the structure of PEX because of the structural similarity between  $\text{H}_2\text{bisVP}$  and PVP as well as the similarity of the FTIR spectra of the co-crystal and PEX polymer. The crystal structures clearly show a 1:1 ratio of hydrogen peroxide to carbonyl units, close to the values obtained by analysis and titration suggesting the proposed 1:2 PEX structure (Figure 4.1) can be discounted. The previously proposed 1:1 PEX structure (Figure 4.1) is closer to the observed co-crystal and DFT results, however, this structure does not capture the additional hydrogen bonding between the hydrogen peroxide units. The structure suggestion by Panarin *et al.* only considers the hydrogen bonding with one vinylpyrrolidone unit so it does not suggest

the formation of chains of hydrogen peroxide units along the polymer. The DFT calculations suggest two potential structural models (Figure 4.15). One possibility involves a structure in which the hydrogen peroxide molecules are in a single environment A-type motif forming a repeating chain along a single polymer molecule. Alternatively, an AB-type motif may result in crosslinking between different polymer chains. The greater stability of  $\text{H}_2\text{O}_2$  in the A-type site suggests that the single site model shown in Figure 4.15a is more likely, although the cross-linking in the model shown in Figure 4.15b is likely to result in greater crystallinity and greater water tolerance. Hence, the real PEX material may involve regions of both types of interaction depending on crystallinity and water content. The experimental ratio of less than one  $\text{H}_2\text{O}_2$  molecule per pyrrolidone unit in PEX can be explained by the occurrence of water defects in the structure as exemplified by the partial substitution of peroxide by water in the crystal structures of  $\text{H}_2\text{bisVP}\cdot\text{H}_2\text{O}_2\cdot\text{H}_2\text{O}$  and  $\text{H}_2\text{bisVP}\cdot 1.7\text{H}_2\text{O}_2\cdot 0.3\text{H}_2\text{O}$ .

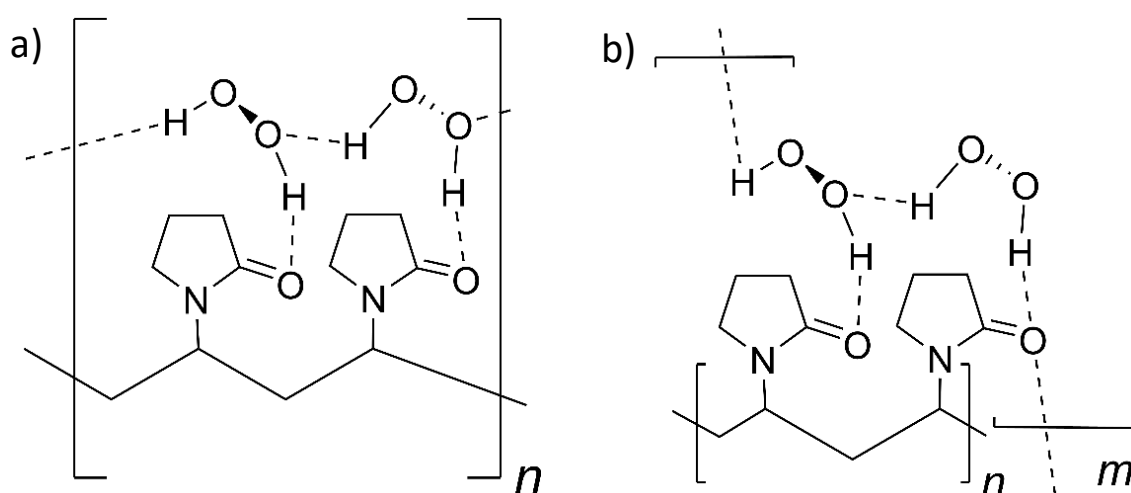


Figure 4.15: The two proposed structures of PEX (a) single type of hydrogen peroxide hydrogen bonded chain (A-type). (b) Hydrogen peroxide cross-linking between PVP molecules (AB-type).

### 4.3 Conclusion

In summary, co-crystal structures of  $\text{H}_2\text{bisVP}$  with varying amounts of hydrogen peroxide were used as model compounds for peroxydone to understand the bonding between PVP and hydrogen peroxide. FTIR data shows that this model system is closely comparable to peroxydone and in the ideal structure that the peroxydone carbonyl is hydrogen bonded to one hydrogen peroxide molecule. The hydrogen peroxide molecules in the co-crystal of  $\text{H}_2\text{bisVP}\cdot 2\text{H}_2\text{O}_2$  form AB dimeric pairs hydrogen bonding between carbonyl oxygen atoms.

This structure undergoes selective replacement of bridging B-type hydrogen peroxide molecules with water at low peroxide concentration. DFT calculations using 4- and 6-monomer segments of PVP with hydrogen peroxide show that a regular chain of hydrogen-bonded hydrogen peroxide molecules along the PVP chain is likely to be the most stable arrangement (Figure 4.15a) but cross linking between PVP chains may also occur depending on crystallinity and the amount of water present.

## 4.4 Experimental

### 4.4.1 Materials

PVP K-25, PVP K-90, PVP XL-10, PEX K-30, PEX K-90, PEX XL-10 and H<sub>2</sub>bisVP were supplied by Ashland LLC. Hydrogen peroxide 30 wt% was purchased from Sigma. All other reagents and solvents were purchased from standard commercial sources and used without further purification. Hydrogen peroxide was handled with care following strict procedures to limit the risk of explosion.<sup>41, 42</sup>

### 4.4.2 Analytical Methods

Fourier transform infrared spectra were recorded using a PerkinElmer Spectrum 100 with a  $\mu$ ATR attachment.

Solid-state NMR spectra were recorded at 100.63 MHz using a Bruker Avance III HD spectrometer and a 4 mm magic-angle spinning probe. Spectra were obtained using cross-polarisation with a 3 s recycle delay with 1 ms contact time at ambient probe temperature (approx. 25 °C) at a sample spin rate of 10 kHz with 400 repetitions. Spectral referencing was with respect to an external sample of neat tetramethylsilane.

Elemental analysis was performed by the University of Durham service using an Exeter CE-440 Elemental Analyser.

Single crystal X-ray crystallography data were collected at 120.0(2) (cocrystals H<sub>2</sub>bisVP·H<sub>2</sub>O<sub>2</sub>·H<sub>2</sub>O and H<sub>2</sub>bisVP·1.7H<sub>2</sub>O<sub>2</sub>·0.3H<sub>2</sub>O) and 100.0(2)K (cocrystal H<sub>2</sub>bisVP·2H<sub>2</sub>O<sub>2</sub>) on Bruker D8Venture diffractometers (PHOTON III C7 CPAD detector, I $\mu$ S microsource (H<sub>2</sub>bisVP·H<sub>2</sub>O<sub>2</sub>·H<sub>2</sub>O and H<sub>2</sub>bisVP·1.7H<sub>2</sub>O<sub>2</sub>·0.3H<sub>2</sub>O); PHOTON III C14 CPAD detector, I $\mu$ S 3.0 microsource (cocrystal H<sub>2</sub>bisVP·2H<sub>2</sub>O<sub>2</sub>); focusing mirrors,  $\lambda$ MoK $\alpha$ ,  $\lambda$  = 0.71073 Å) equipped with Cryostream (Oxford Cryostreams) open-flow nitrogen cryostats, and processed using

Bruker APEX-III software. The structures were solved using direct methods and refined by full-matrix least squares on  $F^2$  for all data using SHELXL<sup>43</sup> and OLEX2 software.<sup>44</sup> All non-hydrogen atoms in all structures were refined in anisotropic approximation, hydrogen atoms in structures of  $H_2bisVP \cdot 2H_2O_2$  and  $H_2bisVP \cdot H_2O_2 \cdot H_2O$  were located in the difference Fourier maps and refined isotropically. The i.d.p. of hydrogen atoms of water molecule in latter structure were restrained to be identical. Hydrogen atoms in structure  $H_2bisVP \cdot 1.7H_2O_2 \cdot 0.3H_2O$  were placed into calculated positions and refined in riding mode. OH-distances in this structure were constrained to be the same. The site occupancy factors of disordered atoms in  $H_2bisVP \cdot 1.7H_2O_2 \cdot 0.3H_2O$  structure were refined but then were rounded to one decimal place and fixed at these values at the final stages of refinement. The final Flack and Hooft parameters in all structures did not allow to establish the absolute structures reliably. X-seed was used to produce an image of the crystal structures.<sup>45</sup>

#### 4.4.3 Titration

Potassium permanganate (3 g) was dissolved in distilled water (250 mL) by heating at 100 °C for 1 hour. The solution was filtered, and the volume was made up to 500 mL with distilled water. Oxalic acid (0.05 g) was dissolved in 50 mL distilled water with sulfuric acid (98%, 0.25 mL) at 60-70 °C. The oxalic acid solution was titrated with the potassium permanganate solution to determine the concentration of the potassium permanganate solution.

The concentration of hydrogen peroxide was increased by storing hydrogen peroxide (20 mL, 30 wt%) in an open beaker in a desiccator (not under vacuum).<sup>46</sup> The desiccant was refreshed weekly. The hydrogen peroxide was left in the desiccator for 55 days with a final concentration of 80 wt%. The concentration was increased further by taking 0.5 mL of the 80 wt% solution and adding ethyl acetate (50 ml x 2) and then removing the solvent under vacuum, to give a final concentration of 85 wt%.

The hydrogen peroxide concentration of both the hydrogen peroxide solution and the PEX samples were determined by dissolving the sample in distilled water (71.25 mL) with sulfuric acid (98%, 3.75 mL). The amount of sample used for the hydrogen peroxide solution was 50  $\mu$ L and for the PEX sample 50 mg. The hydrogen peroxide solution was titrated with the potassium permanganate solution until the solution no longer remained colourless.

#### 4.4.4 H<sub>2</sub>bisVP H<sub>2</sub>O<sub>2</sub> cocrystal synthesis

The amorphous H<sub>2</sub>bisVP hydrogen peroxide complex was prepared by dissolving H<sub>2</sub>bisVP (200 mg) and hydrogen peroxide (80 wt%, 60  $\mu$ L) in ethyl acetate (10 mL). The solvent was removed under vacuum leaving an amorphous paste which was characterised by FTIR spectroscopy.

The crystalline H<sub>2</sub>bisVP·1.7H<sub>2</sub>O<sub>2</sub>·0.3H<sub>2</sub>O was prepared by mixing H<sub>2</sub>bisVP (50  $\mu$ L) with hydrogen peroxide (80 wt%, 10  $\mu$ L) (1:1.36 ratio of H<sub>2</sub>bisVP:H<sub>2</sub>O<sub>2</sub>) and stored at  $-28$  °C. After 2 weeks solid crystalline material formed and was analysed by FTIR spectroscopy. The same quantities of H<sub>2</sub>bisVP and hydrogen peroxide were dissolved in different amounts of ethanol (25, 50, 100  $\mu$ L) and the solid crystalline material was used as a seed crystal. After two hours small colourless block crystals formed. Crystal data: C<sub>12</sub>H<sub>24</sub>N<sub>2</sub>O<sub>5.7</sub> M = 287.53 g mol<sup>-1</sup>, 0.22  $\times$  0.05  $\times$  0.016 mm<sup>3</sup>, monoclinic, space group *P2*<sub>1</sub>, *a* = 6.9035(8) Å, *b* = 15.0032(17) Å, *c* = 7.0706(8) Å,  $\beta$  = 105.825(4)°, *V* = 704.58(14) Å<sup>3</sup>, *Z* = 2, *D*<sub>c</sub> = 1.355 g cm<sup>-3</sup>, *F*<sub>000</sub> = 311.0, 11274 reflections collected, 3733 unique (*R*<sub>int</sub> = 0.0440). Final GooF = 1.035, *R*<sub>1</sub> = 0.0456 (3158 reflections with *I*  $\geq$  2 $\sigma$ (*I*)), *wR*<sub>2</sub> = 0.1028 (all data); 205 parameters, 22 restraints,  $\mu$  = 0.107 mm<sup>-1</sup>.

An alternative non-disordered structure refinement was attempted in which the mixed H<sub>2</sub>O<sub>2</sub> site was treated as being occupied only by H<sub>2</sub>O<sub>2</sub>. This refinement resulted in unusually large a.d.p of oxygen atoms of peroxide molecule on the disordered site and an unfeasibly short O–O bond length of 1.315(6) Å and final *R*<sub>1</sub> = 0.0573. DFT calculations confirmed that such a short bond length is less stable than the equilibrium geometry by 9 kcal mol<sup>-1</sup> at the MP2/aug-cc-pvdz level. For these reasons the disordered model was adopted. This mixed model is also consistent with the isolation of the non-disordered H<sub>2</sub>bisVP·H<sub>2</sub>O<sub>2</sub>·H<sub>2</sub>O.

The crystalline H<sub>2</sub>bisVP·H<sub>2</sub>O<sub>2</sub>·H<sub>2</sub>O was prepared by mixing H<sub>2</sub>bisVP (100  $\mu$ L) with hydrogen peroxide (80 wt%, 10  $\mu$ L) (1:0.68 ratio of H<sub>2</sub>bisVP:H<sub>2</sub>O<sub>2</sub>), a single strand of hair was added to act a seed and the solution was stored at  $-28$  °C. After 1 week solid crystalline material formed and was analysed by FTIR spectroscopy. The same quantities of H<sub>2</sub>bisVP and hydrogen peroxide were dissolved in different amounts of ethanol (25, 50, 100  $\mu$ L) and the solid crystalline material was used as a seed crystal. After two hours small colourless plate crystals formed. Crystal data: C<sub>12</sub>H<sub>24</sub>N<sub>2</sub>O<sub>5</sub> M = 276.33 g mol<sup>-1</sup>, 0.19  $\times$  0.13  $\times$  0.09 mm<sup>3</sup>,



monoclinic, space group  $P2_1$ ,  $a = 6.9359(3) \text{ \AA}$ ,  $b = 14.9061(7) \text{ \AA}$ ,  $c = 6.9555(3) \text{ \AA}$ ,  $\beta = 105.7571(17)^\circ$ ,  $V = 692.12(5) \text{ \AA}^3$ ,  $Z = 2$ ,  $D_c = 1.326 \text{ g cm}^{-3}$ ,  $F_{000} = 300.0$ , 11754 reflections collected, 4014 unique ( $R_{int} = 0.0346$ ). Final GooF = 1.026,  $R_1 = 0.0448$ , (3711 reflections with  $I \geq 2\sigma(I)$ )  $wR_2 = 0.1136$  (all data); 267 parameters, 1 restraint,  $\mu = 0.102 \text{ mm}^{-1}$ .

The crystalline  $\text{H}_2\text{bisVP}\cdot 2\text{H}_2\text{O}_2$  was prepared by mixing  $\text{H}_2\text{bisVP}$  (25  $\mu\text{L}$ ) with hydrogen peroxide (85 wt%, 10.2  $\mu\text{L}$ ) (1:3.17 ratio of  $\text{H}_2\text{bisVP}:\text{H}_2\text{O}_2$ ) and storing at  $-28^\circ\text{C}$ . The solution was seeded using small crystals of  $\text{H}_2\text{bisVP}\cdot 1.7\text{H}_2\text{O}_2\cdot 0.3\text{H}_2\text{O}$ , causing the solution to crystallise. The solid crystalline material formed was analysed by FTIR spectroscopy. The same quantities of  $\text{H}_2\text{bisVP}$  and hydrogen peroxide were dissolved in different amounts of ethanol (25, 50  $\mu\text{L}$ ) and the solid crystalline material was used as a seed crystal. After two hours small colourless plate crystals formed. Crystal data:  $\text{C}_{12}\text{H}_{24}\text{N}_2\text{O}_6$   $M = 292.33 \text{ g mol}^{-1}$ ,  $0.21 \times 0.09 \times 0.04 \text{ mm}^3$ , monoclinic, space group  $P2_1$ ,  $a = 6.8700(2) \text{ \AA}$ ,  $b = 15.0114(4) \text{ \AA}$ ,  $c = 7.1364(2) \text{ \AA}$ ,  $\beta = 105.8830(10)^\circ$ ,  $V = 707.87(3) \text{ \AA}^3$ ,  $Z = 2$ ,  $D_c = 1.372 \text{ g cm}^{-3}$ ,  $F_{000} = 316.0$ , 16854 reflections collected, 4085 unique ( $R_{int} = 0.0322$ ). Final GooF = 1.056,  $R_1 = 0.0352$ , (3901 reflections with  $I \geq 2\sigma(I)$ ),  $wR_2 = 0.0858$  (all data); 277 parameters, 1 restraint,  $\mu = 0.109 \text{ mm}^{-1}$ .

#### 4.4.5 Computations

Geometry optimisations were carried out with the Gaussian 16 package.<sup>47</sup> Ground state ( $S_0$ ) geometries were fully optimised from starting geometries generated from the initial X-ray structure of  $\text{H}_2\text{bisVP}\cdot 2\text{H}_2\text{O}_2$  without symmetry constraints at the hybrid-DFT functional B3LYP<sup>48, 49</sup> with the 6-31(d) basis set<sup>50, 51</sup> and the Grimme dispersion factor, GD3BJ.<sup>52</sup> All fully optimised geometries were confirmed as true minima based on no imaginary frequencies found from frequency calculations. Simulated IR spectra were generated from frequency calculations using a scaling factor<sup>53</sup> of 0.95 to compare with experimental IR data. Carbon-13 NMR chemical shifts in ppm ( $\delta$ ) were converted<sup>54</sup> from sigma ( $\sigma$ ) values within the calculated GIAO-NMR data for the optimised geometries at B3LYP/6-31G(d)/GD3BJ using the equation  $\delta(^{13}\text{C}) = 196 - (\sigma(^{13}\text{C})/0.95)$  with tetramethylsilane (TMS) as external reference at 0.0 ppm.  $^{13}\text{C}$  NMR chemical shifts for CO groups were averaged from the inner non-equivalent CO groups of the geometries.

#### 4.4.5.1 Limitations of multimolecular models.

PVP/ H<sub>2</sub>bisVP solids contain many (hundreds) molecules where most molecules are in a very similar environment. Few molecules occupy the edges/surfaces of the solid particle/lattice. In the multimolecular models a proportionally high number of molecules are at the edges of the 'sheet'. This means the simulated IR spectra and NMR shifts can vary between those molecules in the 'centre' i.e. in the appropriate environment in solids and those on the edges. The simulated IR spectra of H<sub>2</sub>bisVP/PVP:H<sub>2</sub>O<sub>2</sub>/H<sub>2</sub>O complexes contain unusual O-H bands which can be due to dangling/edge H<sub>2</sub>O<sub>2</sub>/H<sub>2</sub>O molecules rather than be considered as representative of the solids.

Both hydrogens in a H<sub>2</sub>O<sub>2</sub> (and water) molecule are expected to be involved in intermolecular hydrogen bond interactions in the solids of H<sub>2</sub>bisVP/PVP:H<sub>2</sub>O<sub>2</sub>/H<sub>2</sub>O complexes. However, in these multimolecular models, several dangling H<sub>2</sub>O<sub>2</sub> (H<sub>2</sub>O) edge molecules exist where only one hydrogen bond interaction is present per molecule initially and some of these molecules will rearrange to form a second H-bond interaction. The AB motifs have more dangling/edge H<sub>2</sub>O<sub>2</sub>/H<sub>2</sub>O molecules thus less intermolecular hydrogen bond interactions overall and the overall total energy of the model would be higher than the A motifs where there are less dangling/edge molecules initially. So even though the A motifs are more stable energetically than AB motifs based on these models, the energy differences may be attributed to the different edge molecules within.

#### 4.5 References

1. W. T. Hess, *Hydrogen Peroxide*, in *Kirk-Othmer Encyclopedia of Chemical Technology*, Wiley, New York, 5th edn., 2000, vol. 13, pp. 470-485.
2. M. Sulieman, M. Addy, E. MacDonald and J. S. Rees, *J. Dent.*, 2004, **32**, 295-299.
3. M. V. Marshall, L. P. Cancro and S. L. Fischman, *J. Periodontol.*, 1995, **66**, 786-796.
4. H. Eimar, R. Siciliano, M.-N. Abdallah, S. A. Nader, W. M. Amin, P.-P. Martinez, A. Celemin, M. Cerruti and F. Tamimi, *J. Dent.*, 2012, **40**, e25-e33.
5. T. Jiang, Y. R. Guo, X. W. Feng, Y. Sa, X. Yang, M. Wang, P. Li and Y. N. Wang, *J. Dent. Res.*, 2018, **97**, 1339-1345.
6. C. J. Tredwin, S. Naik, N. J. Lewis and C. Scully, *Brit. Dent. J.*, 2006, **200**, 371-376.
7. B. A. Matis, M. A. Cochran, G. Wang and G. J. Eckert, *Oper. Dent.*, 2009, **34**, 142-149.
8. L. Féliz-Matos, L. M. Hernández and N. Abreu, *Open. Dent. J.*, 2015, **8**, 264-268.
9. I. Luque-Martinez, A. Reis, M. Schroeder, M. A. Muñoz, A. D. Loguercio, D. Masterson and L. C. Maia, *Clin. Oral Invest.*, 2016, **20**, 1419-1433.
10. J. H. Baxendale and J. A. Wilson, *T. Faraday Soc.*, 1957, **53**, 344-356.
11. E. S. Shanley and F. P. Greenspan, *Ind. Eng. Chem.*, 1947, **39**, 1536-1543.
12. C.-S. Lu, E. W. Hughes and P. A. Giguère, *J. Am. Chem. Soc.*, 1941, **63**, 1507-1513.

13. C. M. Carey, *J. Evid. Based Dent. Pr.*, 2014, **14**, 70-76.
14. A. C. Peixoto, S. C. Vaez, N. A. R. Pereira, C. N. D. S. Santana, K. D. A. Soares, A. C. T. R. Romão, L. F. Ferreira, P. R. S. Martins-Filho and A. L. Faria-E-Silva, *J. Appl. Oral Sci.*, 2018, **26**, e20170573-e20170573.
15. R. B. Login, J. J. Merianos, R. B. Biss and P. Garelick, Urea-Hydrogen Peroxide-Polyvinylpyrrolidone Process, U.S. Patent 5,206,385, 1993.
16. C. d. M. Bonesi, L. S. Ulian, P. Balem and V. W. Angeli, *Braz. J. Pharm. Sci.*, 2011, **47**, 719-724.
17. S. Okonogi, A. Kaewpinta, T. Rades, A. Müllertz, M. Yang, S. Khongkhunthian and P. Chaijareenont, *Pharmaceuticals*, 2020, **13**, 381.
18. E. F. Panarin, K. K. Kalninch and D. V. Pestov, *Eur. Polym. J.*, 2001, **37**, 375-379.
19. D. Modhave, B. Barrios and A. Paudel, *Pharmaceutics*, 2019, **11**, 457.
20. G. K. Surya Prakash, A. Shakhmin, K. E. Ginton, S. Rao, T. Mathew and G. A. Olah, *Green Chem.*, 2014, **16**, 3616-3622.
21. D. A. Shiraeff, Solid stabilized hydrogen peroxide compositions, U.S. Patent 3,376,110A, 1968.
22. D. A. Shiraeff, Solid stabilized hydrogen peroxide compositions, U.S. Patent 3,480,557, 1969.
23. Russell B. Biss, Jeffrey M. Cohen, John J. Merianos and P. D. Taylor, Process For Producing PVP-H<sub>2</sub>O<sub>2</sub> Products, WO. Patent 1,992,017,158A1, 1992.
24. J. J. Merianos, Anhydrous Complexes of PVP and Hydrogen Peroxide, U.S. Patent 5,008,093, 1991.
25. W. E. Prosis, Tooth Whitening Compositions, U.S. Patent 8,137,658 B2, 2012.
26. W. E. Prosis and J. B. Levine, Tooth Whitening Delivery System, U.S. Patent 2007/0183988 A1, 2007.
27. M. Prencipe, P. Mandadi and O. Garot, Peroxide-stable Oral Care Compositions, U.S. Patent 2015/0366766 A1, 2015.
28. K. Nacharaju, G. N. Onnembo, M. Rehmanji, A. Mola, B. Balasanmugam and J. Yapchulay, Methods of Treatment to Improve the Quality of Alcoholic Beverages Using Vinyl Lactam-Derived Polymer-Hydrogen Peroxide Complexes, U.S. Patent 9,920,146B2, 2018.
29. J. R. Davenport, O. M. Musa, M. J. Paterson, M.-O. M. Piepenbrock, K. Fucke and J. W. Steed, *Chem. Commun.*, 2011, **47**, 9891-9893.
30. M. J. Goodwin, B. W. Steed, D. S. Yufit, O. M. Musa, D. J. Berry and J. W. Steed, *Cryst. Growth Des.*, 2017, **17**, 5552-5558.
31. M. J. Goodwin, O. M. Musa, D. J. Berry and J. W. Steed, *Cryst. Growth Des.*, 2018, **18**, 701-709.
32. A. Perrin, M. J. Goodwin, O. M. Musa, D. J. Berry, P. Corner, K. Edkins, D. S. Yufit and J. W. Steed, *Cryst. Growth Des.*, 2017, **17**, 3236-3249.
33. O. N. Kavanagh, D. M. Croker, G. M. Walker and M. J. Zaworotko, *Drug Discov. Today*, 2019, **24**, 796-804.
34. M. Karimi-Jafari, L. Padrela, G. M. Walker and D. M. Croker, *Cryst. Growth Des.*, 2018, **18**, 6370-6387.
35. J. Sweit and J. B. Talbot, *J. Appl. Polym. Sci.*, 2003, **90**, 1153-1155.
36. S. Fitzpatrick, J. F. McCabe, C. R. Petts and S. W. Booth, *Int. J. Pharm.*, 2002, **246**, 143-151.

37. A. Perrin, M. J. Goodwin, S. Callear, A. K. Soper, O. M. Musa and J. W. Steed, *J. Phys. Chem. B*, 2018, **122**, 4901-4912.
38. M. Kurakula and G. S. N. K. Rao, *J. Drug Deliv. Sci. Tec.*, 2020, **60**, 102046-102046.
39. P. V. Prikhodchenko, A. G. Medvedev, T. A. Tripol'skaya, A. V. Churakov, Y. Wolanov, J. A. K. Howard and O. Lev, *CrystEngComm*, 2011, **13**, 2399-2407.
40. J. M. Savariault and M. S. Lehmann, *J. Am. Chem. Soc.*, 1980, **102**, 1298-1303.
41. O. Maass and W. H. Hatcher, *J. Am. Chem. Soc.*, 1920, **42**, 2548-2569.
42. Y. Wolanov, O. Lev, A. V. Churakov, A. G. Medvedev, V. M. Novotortsev and P. V. Prikhodchenko, *Tetrahedron*, 2010, **66**, 5130-5133.
43. G. Sheldrick, *Acta Crystallogr. C*, 2015, **71**, 3-8.
44. O. V. Dolomanov, L. J. Bourhis, R. J. Gildea, J. A. K. Howard and H. Puschmann, *J. Appl. Crystallogr.*, 2009, **42**, 339-341.
45. L. J. Barbour, *Supramol. Chem.*, 2001, **1**, 189-191.
46. K. V. Titova, V. P. Nikol'skaya, V. V. Buyanov and I. P. Suprun, *Russ. J. Appl. Chem.*, 2002, **75**, 1903-1906.
47. M. J. Frisch, G. W. Trucks, H. B. Schlegel, G. E. Scuseria, M. A. Robb, J. R. Cheeseman, G. Scalmani, V. Barone, G. A. Petersson, H. Nakatsuji, X. Li, M. Caricato, A. V. Marenich, J. Bloino, B. G. Janesko, R. Gomperts, B. Mennucci, H. P. Hratchian, J. V. Ortiz, A. F. Izmaylov, J. L. Sonnenberg, Williams, F. Ding, F. Lipparini, F. Egidi, J. Goings, B. Peng, A. Petrone, T. Henderson, D. Ranasinghe, V. G. Zakrzewski, J. Gao, N. Rega, G. Zheng, W. Liang, M. Hada, M. Ehara, K. Toyota, R. Fukuda, J. Hasegawa, M. Ishida, T. Nakajima, Y. Honda, O. Kitao, H. Nakai, T. Vreven, K. Throssell, J. A. Montgomery Jr., J. E. Peralta, F. Ogliaro, M. J. Bearpark, J. J. Heyd, E. N. Brothers, K. N. Kudin, V. N. Staroverov, T. A. Keith, R. Kobayashi, J. Normand, K. Raghavachari, A. P. Rendell, J. C. Burant, S. S. Iyengar, J. Tomasi, M. Cossi, J. M. Millam, M. Klene, C. Adamo, R. Cammi, J. W. Ochterski, R. L. Martin, K. Morokuma, O. Farkas, J. B. Foresman and D. J. Fox, Gaussian 16, Revision B.01, Gaussian, Inc., Wallingford, CT, 2016
48. A. D. Becke, *J. Chem. Phys.*, 1993, **98**, 5648-5652.
49. C. Lee, W. Yang and R. G. Parr, *Phys. Rev. B*, 1988, **37**, 785-789.
50. G. A. Petersson, A. Bennett, T. G. Tensfeldt, M. A. Al-Laham, W. A. Shirley and J. Mantzaris, *J. Chem. Phys.*, 1988, **89**, 2193-2218.
51. G. A. Petersson and M. A. Al-Laham, *J. Chem. Phys.*, 1991, **94**, 6081-6090.
52. S. Grimme, S. Ehrlich and L. Goerigk, *J. Comp. Chem.*, 2011, **32**, 1456-1465.
53. J. P. Merrick, D. Moran and L. Radom, *J. Phys. Chem. A*, 2007, **111**, 11683-11700.
54. A. E. Aliev, D. Courtier-Murias and S. Zhou, *J. Mol. Struct.: THEOCHEM*, 2009, **893**, 1-5.

## 5 Understanding the Interaction of Gluconamides and Gluconates with Amino Acids in Hair Care

### 5.1 Introduction

A human hair fibre is around 50-100  $\mu\text{m}$  in diameter and it is composed of three main parts: cuticle, cortex, and medulla.<sup>1, 2</sup> The cuticle is the outer barrier protecting the cortex from external damage<sup>1, 3-7</sup> The cortex makes up most of the hair mass and is responsible for the high tensile strength<sup>1, 8-13</sup> while the inner part of the hair fibre is the medulla which provides a negligible contribution to its mechanical strength.<sup>14, 15</sup> Overall, the main chemical component by weight is protein composing 65-95% of the hair.<sup>1</sup> The predominant proteins present are keratins which act as the structural building blocks of hair as well as other materials such as skin and nails.<sup>16</sup> Human hair is formed from alpha keratins which are in an alpha-helix conformation and can be divided into two types, type I which is smaller (44 – 46 kDa) and more acidic, and type II which is larger (50 – 60 kDa) and slightly basic or neutral.<sup>17</sup> Keratin proteins can also be divided into type “a” or type “b”, with type “a” being hard keratins found in hair and type “b” being soft keratins found in the skin.<sup>18</sup> Keratin proteins found in human hair contain more cysteine residues and fewer glycine residues compared to other keratins.<sup>19</sup> The higher cysteine content causes increased disulfide bridge formation, resulting in greater mechanical strength, and thermal and chemical resistance.<sup>20</sup> The strength of the structures formed from keratin is also related to the formation of hydrogen bonds, coulombic interactions, van der Waals forces and hydrophobic interactions present between the different amino acid residues.<sup>21</sup> These interactions can take place either between two separate chains or two portions of the same chain.

Hair can be damaged in a variety of ways including environmental, chemical, over-washing or thermal damage.<sup>20</sup> The amount and type of melanin pigments present determines the colour of the hair. Oxidising agents used in bleaching can oxidise and destroy the chromophore groups of melanin.<sup>22</sup> The oxidising agents also mechanically weaken hair by oxidising the cysteine residues into cysteic acid which breaks the disulfide bridge which is usually formed between two cysteine residues.<sup>23</sup> Table 5.1 shows the changes in amino acid composition between bleached and non-bleached hair. The two most significant changes are the drop in half cystine residues and the increase in cysteic acid residues.<sup>20</sup>

Table 5.1: Amino acids in bleached and non-bleached hair.<sup>20</sup>

Amino acid	Micromoles per gram of hair	
	Non-bleached hair	Bleached hair
Aspartic acid	437	432
Threonine	616	588
Serine	1085	973
Glutamic acid	1030	999
Proline	639	582
Glycine	450	415
Alanine	370	357
Half cystine	1509	731
Valine	487	464
Methionine	50	38
Isoleucine	227	220
Leucine	509	485
Tyrosine	183	146
Phenylalanine	139	129
Cysteic acid	27	655
Lysine	198	180
Histidine	65	55
Arginine	511	486

A hair treatment was reported in 2017 based on a range of gluconamides and their corresponding alkyl ammonium gluconate salts which were found to strengthen and repair damaged hair and prevent colour leaching during drying.<sup>24-26</sup> The compositions comprise *L*-gluconic acid (GLA) and a range of different amines including ethylenediamine, ethanolamine, 3-amino-1-propanol and tris(hydroxymethyl)aminomethane).<sup>24-26</sup> One of the compositions formed from 3-amino-1-propanol (3AP) and *L*-gluconic acid was shown to provide the greatest strength to hair fibres,<sup>24-26</sup> and the commercial product comprises a 50 wt % aqueous solution called fiberHance bm solution;<sup>27</sup> a mixture of hydroxypropyl-*L*-gluconamide (**1**), and hydroxypropylammonium *L*-gluconate (**2** and **3**) (Figure 5.1). The gluconamide **1** is initially in a 1:1 molar ratio with the gluconate salt but converts into **2** and **3** in solution, particularly under basic conditions.

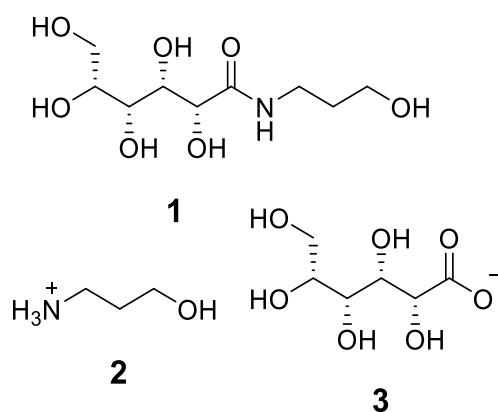


Figure 5.1. The components of the haircare mixture: hydroxypropyl-*L*-gluconamide (**1**), hydroxypropylammonium *L*-gluconate (**2** and **3**).

It has been shown previously that sugars such as sucrose stabilise the secondary structure of proteins which may be related to the hair strengthening properties of **1**.<sup>28</sup> Both the amide and the salt components are assumed to permeate the cuticle and reach the cortex.<sup>29</sup> The exact nature of how this mixture acts to strengthen hair is currently unknown but it is speculated that a range of intermolecular bonds including hydrogen bonds and ionic bonds are formed with amino acid residues in the keratin proteins.<sup>29</sup> This work aims to examine the assembly mode of **1** and identify potential interactions between **1**, **2** and **3** and the amino acids present in hair. This aim has been addressed by examination of the single-crystal structures of a range of molecules mimicking the substituent groups present in amino acid residues.

## 5.2 Results and Discussion

### 5.2.1 Cambridge Structural Database Search

Three crystal structures of 3AP have been reported in the CSD.<sup>30</sup> Pressure freezing was required to form the 3AP crystal structure with the three polymorphic forms determined at different pressures. The structures all display the same bonding pattern with each amine group forming two NH $\cdots$ O and one OH $\cdots$ N hydrogen bonds with three other alcohol groups on three different 3AP molecules.

The CSD also contains four salts of 3-hydroxypropyl ammonium. Three involve carboxylate anions, indicating the potential of **2** to form strong intermolecular bonds with amino acid groups containing a carboxylate in the substituent group.<sup>31-33</sup> The fourth salt involves

naphthalene-1,5-disulfonate and the crystal structure displays hydrogen bonds formed between the ammonium group and the sulfonate with  $N\cdots O$  distances of 2.768 Å.<sup>34</sup> The structure shows the potential of **2** to interact with cysteic acid residues present in bleached hair.

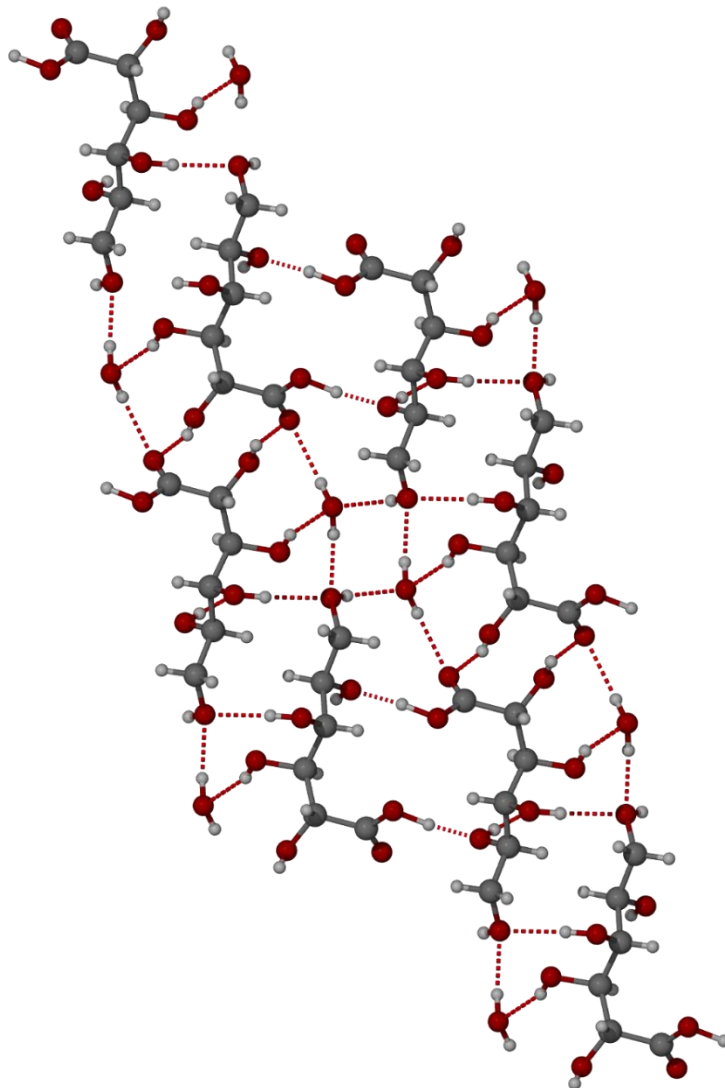


Figure 5.2: The X-ray crystal structure of D-gluconic acid monohydrate (CAKZAP) in the (010) crystallographic plane.

The CSD contains the structure of D-GLA monohydrate (CAKZAP)<sup>35</sup> (Figure 5.2) which forms an extensive hydrogen bonded network with one GLA molecule hydrogen bonded to eight other GLA molecules and four water molecules. The  $O\cdots O$  distance for the hydrogen bonds varies between 2.608 – 2.918 Å, with the largest distance of 2.918 Å between the carbonyl oxygen and an oxygen atom in a water molecule.



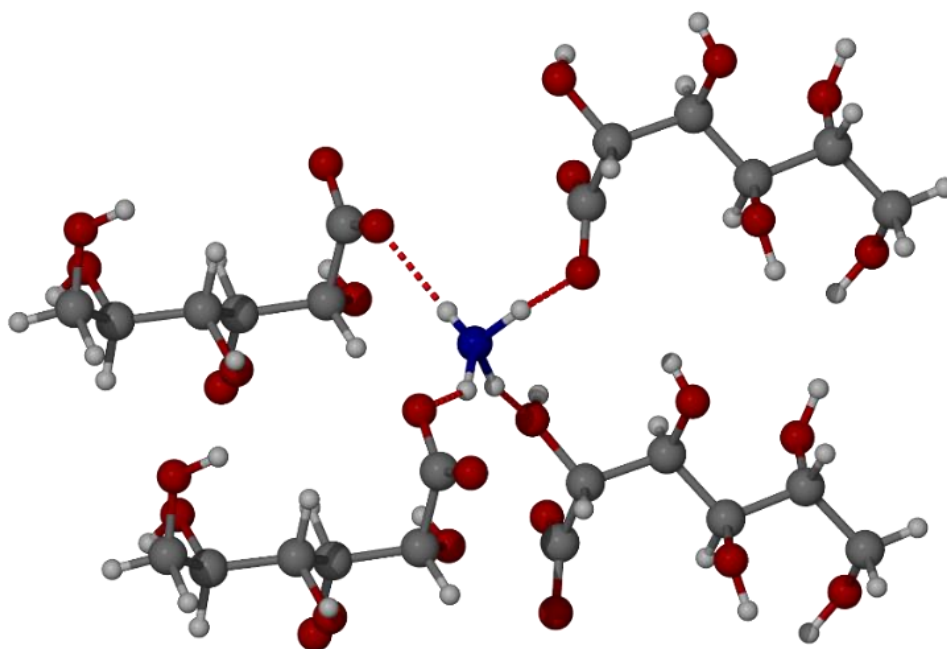


Figure 5.3: The X-ray crystal of ammonium gluconate (BAGDOC) showing a single  $\text{NH}_4^+$  interacting with four **3** anions.

The CSD contains a total of ten structures of the gluconate anion (**3**). Nine of the structures are metal salts including potassium, calcium, sodium, or rubidium. The other structure is the ammonium salt (BAGDOC)<sup>36</sup> (Figure 5.3). The structure shows the formation of four hydrogen bonds, three with the C=O bond and one with an OH group on **3**. The strongest bond is the charge-assisted interaction from an ammonium NH group to the carboxylate oxygen atom,  $\text{N}\cdots\text{O}$  distance 2.778 Å.

### 5.2.2 Gluconamide Structures

Compound **1** was separated from the commercial aqueous haircare mixture by slow evaporation which resulted in crystals of one of two polymorphs (form I) suitable for single-crystal X-ray diffraction (SXRD). The X-ray crystal structure is in the Sohncke space group  $P2_1$  consistent with a single enantiomer of the gluconamide and contains one molecule of amide **1** in the asymmetric unit. The molecular structure of form I (Figure 5.4) involves an intramolecular hydrogen bond, forming a five-membered ring between the hydrogen atom from the amide group and the oxygen atom on the alcohol group next to the carbonyl group. The intramolecular hydrogen bond is very short with an  $\text{N}\cdots\text{O}$  distance of 2.5984(19) Å. As a result, the amide NH proton is unavailable for intermolecular hydrogen bonding.

Form I displays extensive intermolecular hydrogen bonding from the OH groups with one molecule of **1** interacting with seven different neighbours. The alcohol groups form six different hydrogen bonds with other alcohol groups, the range of O...O distances are 2.7583(18) – 2.8448(18) Å. In addition, the carbonyl oxygen atom forms a strong hydrogen bond with an alcohol group on another molecule with an O...O distance of 2.6767(18) Å. An  $R_{1/2}^1(8)$  hydrogen bonding motif forms between two molecules of **1** which can be observed in the (001) crystallographic plane (Figure 5.4b). The opposite enantiomer of **1** was synthesised by mixing aqueous D-gluconic acid with 3AP in a 1:1 molar ratio and leaving the solution to evaporate producing crystals which were analysed via SXR. The SXR analysis revealed that the D-enantiomer forms an isomorphous crystal to form I under these conditions.

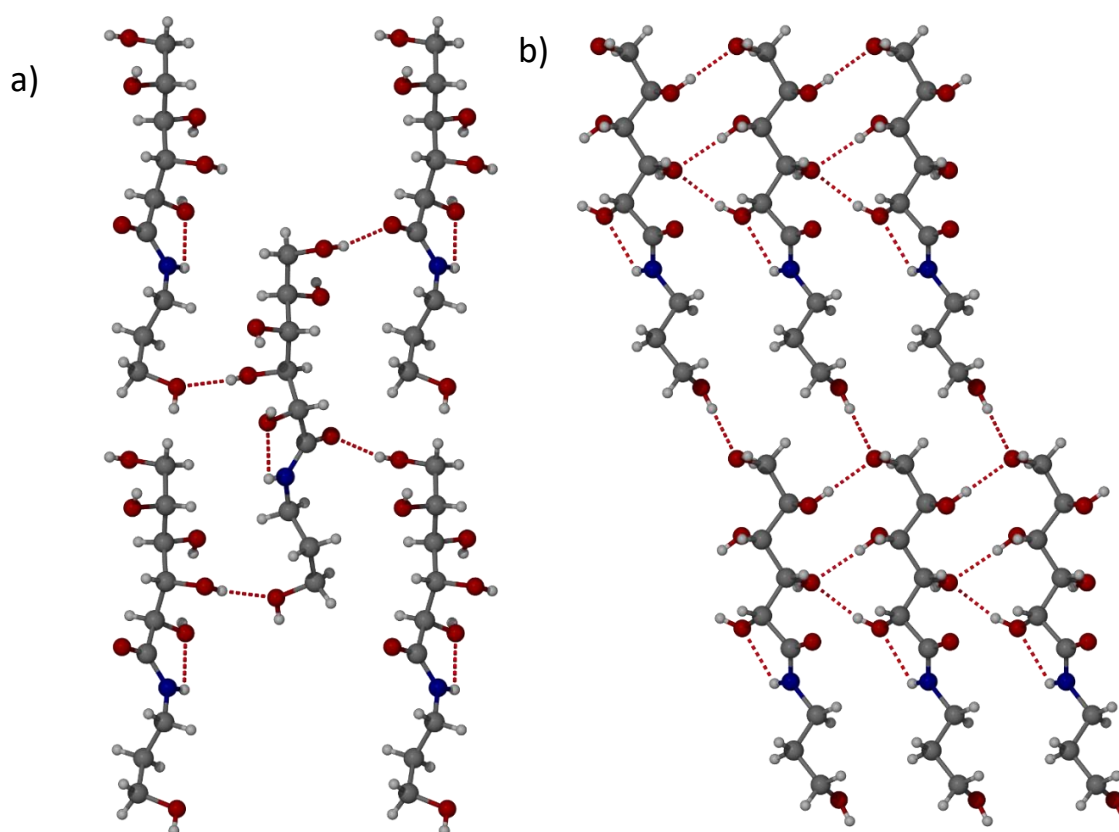


Figure 5.4: The X-ray crystal structure of **1** form I showing the hydrogen bonding in the a) (100) and b) (001) crystallographic planes.

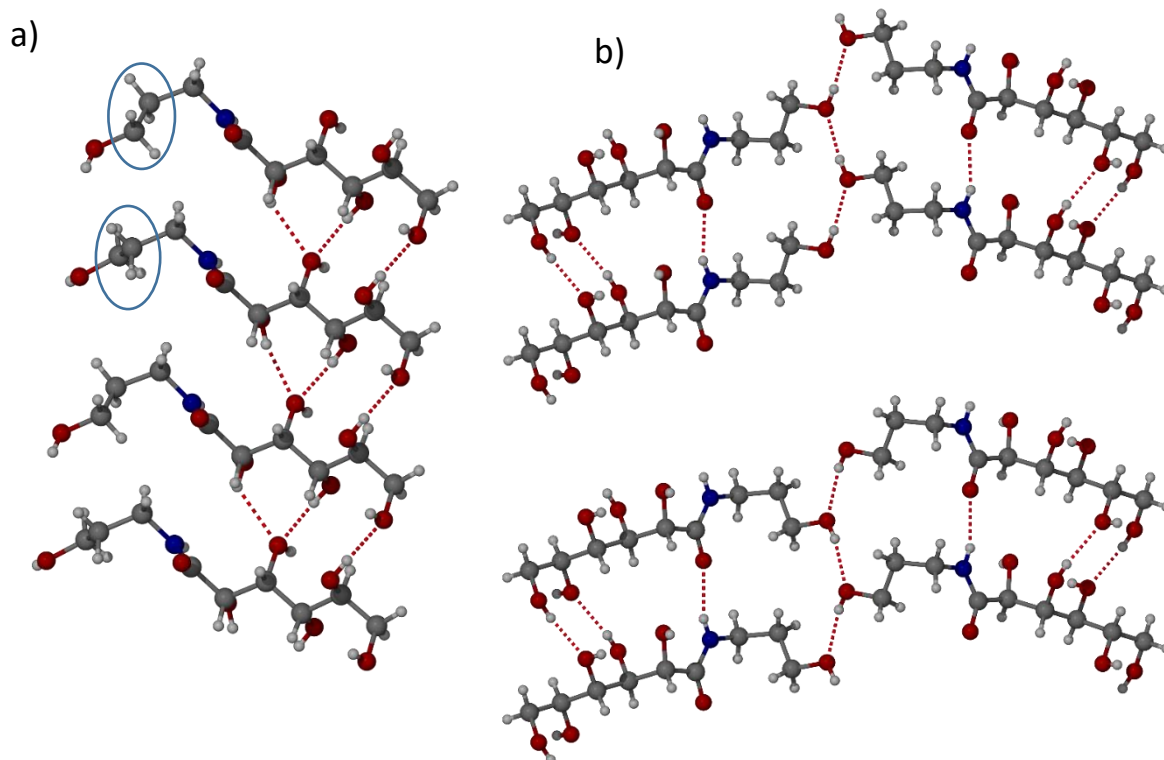


Figure 5.5: The X-ray crystal structure of **1** form II in a) crystallographic plane (120) with the C1-C2 bond highlighted in a blue circle. b) The two crystallographically independent molecules in the asymmetric unit form two separate chains along the end OH group, this is shown in the crystallographic plane (100).

A second polymorph of **1**, form II (Figure 5.5), was obtained by slow evaporation of an ethanol solution of **1** in the presence of aniline in a 1:5.5 molar ratio. Form II also adopts space group  $P2_1$  but the asymmetric unit contains two molecules of **1** in two different conformations (a conformational isomorph).<sup>37</sup> The difference between the two molecules is in the torsion angle from the carbonyl to the C1-C2 bond (O2 – C4 – C2 – C1) (Figure 5.5a) which is gauche in one (47.3 °) and anti-gauche in the other (164.9 °). Unlike form I, the amide NH group does not form an intramolecular hydrogen bond but instead takes part in an intermolecular interaction (Figure 5.5b) with the carbonyl group of an adjacent molecule with N $\cdots$ O distances of 2.840(4) and 2.834(4) Å for the two crystallographically independent molecules. The amide hydrogen bond gives an infinite chain, similar to the  $\beta$ -sheet structure of proteins. The alcohol group from the 3AP group of **1** forms a repeating chain of hydrogen bonds with O $\cdots$ O distances of 2.790(2) and 2.787(2) Å, in which each crystallographically unique molecule is part of a separate chain (Figure 5.5b). The other hydrogen bonds take

place between the other alcohol groups with O...O distances between 2.688(3) – 2.936(4) Å which are similar to form I. Each molecule of **1** is bonded to seven other molecules of **1** in the same way as form I. The same  $R_2^1(8)$  hydrogen bonding motifs observed in form I is also present in form II as shown in the (120) crystallographic plane (Figure 5.5a).

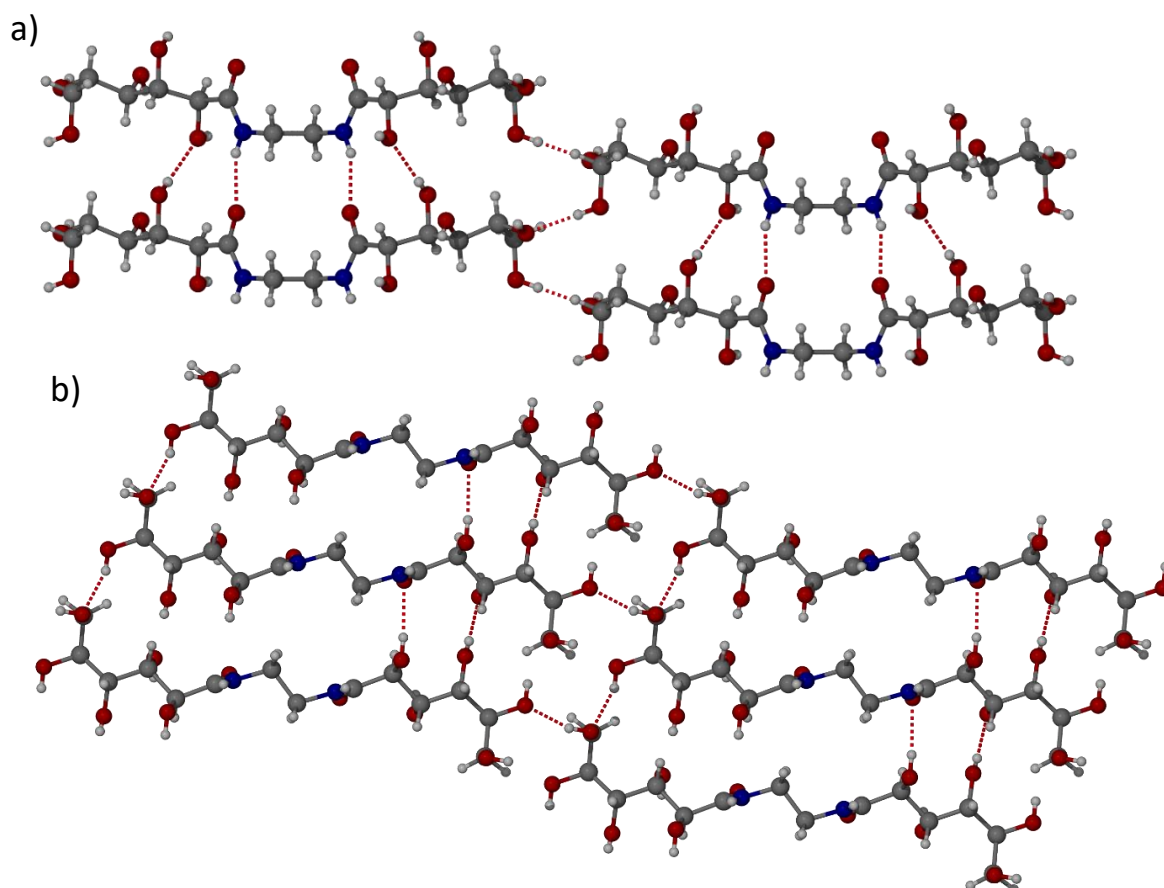


Figure 5.6: The X-ray crystal structure of *N,N'*-ethylene bis-*L*-gluconamide showing the amide hydrogen bond chain in the a) (100) and b) (010) crystallographic plane.

While compound **1** is used in the commercial product, related amides have similar properties.<sup>24-26</sup> For comparison, a related gluconamide *N,N'*-ethylene bis-*L*-gluconamide was prepared using the reported procedure.<sup>24-26</sup> A solution of ethylenediamine in methanol with *L*-gulonic acid  $\gamma$ -lactone was refluxed under nitrogen which produced a white powder of the diamide which was confirmed to be free of monoamide by <sup>1</sup>H NMR spectroscopy. This material was dissolved in water, and methanol was added as an antisolvent which resulted in the formation of single crystals suitable for SXRD analysis (Figure 5.6). XRPD established that the bulk material is phase pure and consistent with the pattern calculated from SXRD data (Figure 5.7). The X-ray crystal structure is in the Sohncke space group *C2* consistent

with a single enantiomer of the gluconamide and contains one *N,N'*-ethylene bis-*L*-gluconamide molecule in the asymmetric unit. The carbonyl oxygen atom is slightly disordered over two positions in a ratio of 90:10. The *N,N'*-ethylene bis-*L*-gluconamide is situated on a 2-fold axis passing through the central C-C bond and hence both halves of the molecule are equivalent. The hydrogen-bonding network is similar to form II of **1** with a hydrogen bonded amide chain, with a similar N...O distance of 2.7991(18) Å. Each molecule of *N,N'*-ethylene bis-*L*-gluconamide is hydrogen bonded to ten neighbours, showing the system forms an extensive hydrogen bonded network similar to **1**. The range O...O distances between alcohol groups is 2.6910(13) – 2.8061(15) Å.

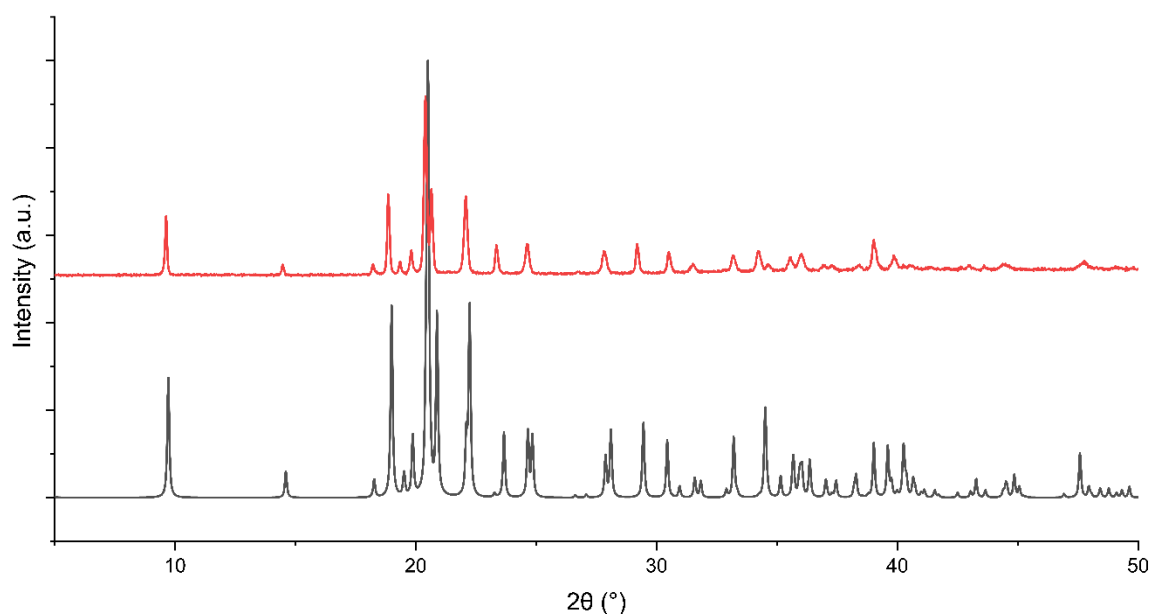


Figure 5.7: XRPD patterns of the *N,N'*-ethylene bis-*L*-gluconamide with the pattern calculated from the single crystal structure (black) and the bulk powder (red).

### 5.2.3 Amino Acid Salt Screen

Amino acids were selected as small molecule models of the protein structure present in hair, however, the amino acids do not take into account the amide bonding, the complex hydrogen bonding found in proteins and the long chain length. Nevertheless, the amino acid substituents may give insight into the interactions of hair care components with the amino acid residues in hair protein. COSMOquick was selected to screen the amino acids for cocrystal formation with each of **1**, 3AP and GLA screened separately. COSMOquick uses the Conductor like Screening Model for Real Solvents (COSMO-RS) method to create charge

density surfaces. The charge density surfaces describe each molecule and the surfaces of two different molecules can be used to calculate interaction energies including the excess enthalpy of mixing ( $\Delta H_{mix}$ ).<sup>38</sup> The neutral forms of **2** and **3** were used in COSMOquick because the software is only parameterised for a limited selection of precalculated ionic species.<sup>39, 40</sup> The components **1**, 3AP and GLA were screened individually as they exist as separate species when dissolved in water and the experiment aimed to understand the interactions of the amino acids with each individual component. The results of the COSMOquick screen (Table 5.2) showed **1** and GLA have similar interactions with amino acids and the combination of **1** or GLA with *L*-lysine gives the most negative  $\Delta H_{mix}$ . The top four amino acids (Table 5.2) with the most favourable excess enthalpy of mixing for each component were selected for co-crystal or salt screening. A range of experiments aimed at the preparation of co-crystals were performed with the selected systems including the use of mechanochemistry with grinding, liquid assisted grinding and a range of solution crystallisations including evaporation, antisolvent and cooling crystallisations. However, no new co-crystals or salts of **1**, 3AP or GLA with amino acids were produced, although a new dimethyl sulfoxide solvate with cysteic acid was formed (Figure 5.8). In the absence of amino acid cocrystals the combination of amide **1**, 3AP and GLA with small molecules that mimic the amino acid substituents, was examined. The small molecules were initially screened with COSMOquick (Table 5.3) and in all cases, the molecules selected to mimic the amino acid substituent groups showed more favourable  $\Delta H_{mix}$  with **1**, 3AP and GLA, compared to the corresponding amino acids. The substituent group mimics were, therefore, experimentally screened with **1**, GLA and 3AP.

Table 5.2: The potential excess enthalpy of mixing of the 3 components of the haircare solution with all the amino acids in hair calculated using COSMOquick.<sup>38</sup>

Hydroxypropyl-L-gluconamide		L-gluconic acid		3-Amino-1-propanol	
Co-former	$\Delta H_{mix}$	Co-former	$\Delta H_{mix}$	Co-former	$\Delta H_{mix}$
<i>L</i> -lysine	-3.088	<i>L</i> -lysine	-3.222	<i>L</i> -aspartic acid	-2.559
<i>L</i> -arginine	-1.378	<i>L</i> -arginine	-1.951	<i>L</i> -tyrosine	-1.353
<i>L</i> -threonine	-0.703	<i>L</i> -histidine	-1.249	<i>L</i> -glutamic acid	-1.321
<i>L</i> -cysteine	-0.617	<i>L</i> -threonine	-1.109	<i>L</i> -cysteic acid	-1.121
<i>L</i> -histidine	-0.572	<i>L</i> -proline	-1.107	<i>L</i> -serine	-0.999
<i>L</i> -proline	-0.330	<i>L</i> -cysteine	-0.872	<i>L</i> -cysteine	-0.528
<i>L</i> -aspartic acid	-0.286	<i>L</i> -alanine	-0.753	<i>L</i> -threonine	-0.318
<i>L</i> -valine	-0.053	<i>L</i> -valine	-0.749	<i>L</i> -histidine	-0.216

<i>L</i> -isoleucine	-0.019	<i>L</i> -isoleucine	-0.714	<i>L</i> -leucine	-0.196
<i>L</i> -alanine	-0.012	glycine	-0.671	<i>L</i> -methionine	-0.175
<i>L</i> -leucine	0.042	<i>L</i> -leucine	-0.629	<i>L</i> -valine	-0.164
<i>L</i> -serine	0.068	<i>L</i> -methionine	-0.523	<i>L</i> -phenylalanine	-0.149
glycine	0.070	<i>L</i> -phenylalanine	-0.495	<i>L</i> -isoleucine	-0.148
<i>L</i> -tyrosine	0.146	<i>L</i> -tyrosine	-0.206	<i>L</i> -arginine	-0.086
<i>L</i> -glutamic acid	0.199	<i>L</i> -glutamic acid	-0.158	<i>L</i> -alanine	-0.083
<i>L</i> -phenylalanine	0.231	<i>L</i> -serine	-0.110	<i>L</i> -proline	-0.076
<i>L</i> -methionine	0.232	<i>L</i> -aspartic acid	0.005	glycine	-0.040
<i>L</i> -cysteic acid	0.525	<i>L</i> -cysteic acid	0.284	<i>L</i> -lysine	0.065

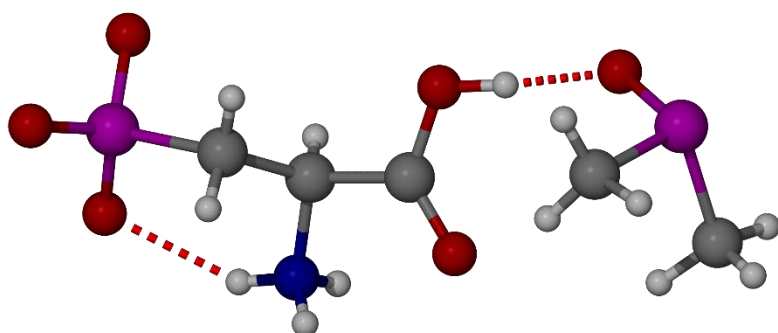


Figure 5.8: The X-ray crystal structure of a DMSO solvate of *L*-cysteic acid.

Table 5.3: The potential excess enthalpy of mixing of the 3 components of the haircare solution with the molecules that mimic the substituent groups of the amino acids calculated using COSMOquick.

Hydroxypropyl- <i>L</i> -gluconamide		<i>L</i> -gluconic acid		3-Amino-1-propanol	
Co-former	$\Delta H_{mix}$	Co-former	$\Delta H_{mix}$	Co-former	$\Delta H_{mix}$
Ethylenediamine	-4.764	Ethylenediamine	-5.073	Sulfuric acid	-9.654
Guanidine	-2.604	Guanidine	-2.773	Oxalic acid	-5.405
				Methanesulfonic acid	-3.919

Sulfuric acid (H<sub>2</sub>SO<sub>4</sub>) was chosen to mimic the sulfonic acid substituent group of cysteic acid due to the structural similarity and the large negative excess enthalpy of mixing with 3AP observed in the COSMOquick screen (Table 5.3). A slight excess of sulfuric acid (H<sub>2</sub>SO<sub>4</sub>) was slowly added to 3AP. The vial was sealed and after 15 days small plate crystals had formed which were analysed by SXR. The structure was found to be a 1:1 salt 3-hydroxypropylammonium hydrogen sulfate (**2**·HSO<sub>4</sub><sup>-</sup>) (Figure 5.9). Cation **2** forms intermolecular hydrogen bonds with five different hydrogen sulfate anions, with three hydrogen bonds forming between the N-H bonds and the S=O/S-O<sup>-</sup> oxygen atoms with O...N distances varying from 2.8486(13) to 2.868(2) Å. One hydrogen bond forms between the O-H group of **2** and a sulfate oxygen atom with an O...O distance of 2.8250(19) Å. The fifth hydrogen bond forms between the hydrogen sulfate OH group and the hydroxyl oxygen atom of the **2** with an O...O distance of 2.519(2) Å, which is similar to a comparable structure of a sulfate anion with 4-hydroxyanilinium which has an O...O distance of 2.642(2) Å.<sup>41</sup>



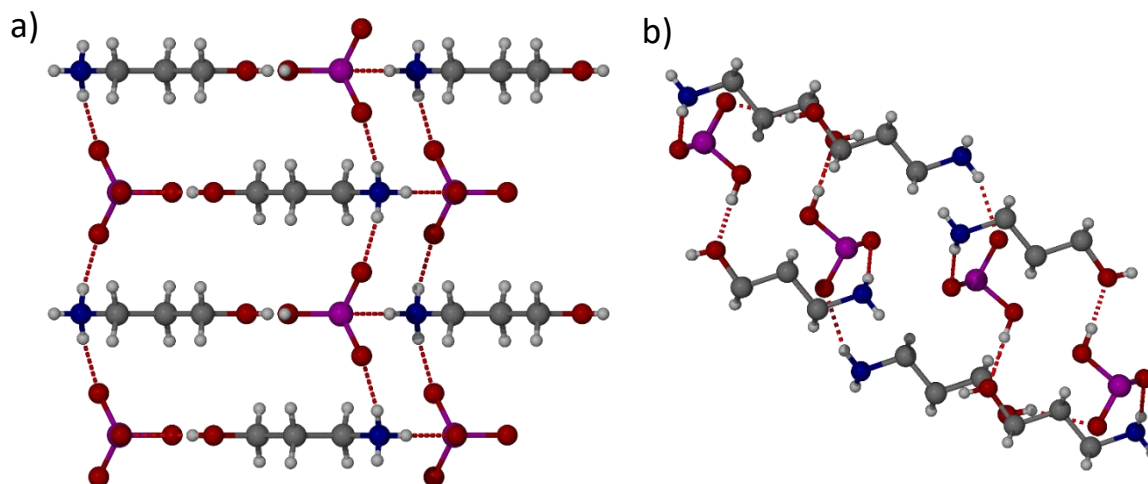


Figure 5.9: The X-ray crystal structure of **2**·HSO<sub>4</sub><sup>-</sup> showing the hydrogen bonding interactions in the a) (100) and b) (010) crystallographic planes.

Methane sulfonic acid (CH<sub>3</sub>SO<sub>3</sub>H) was identified as a better model for cysteic acid compared to sulfuric acid, due to CH<sub>3</sub>SO<sub>3</sub>H being more structurally similar to cysteic acid. 3AP was added to a solution of CH<sub>3</sub>SO<sub>3</sub>H and the temperature of the vial increased which was attributed to proton transfer. The system was then stored at 3 °C resulting in the formation of a white precipitate which was used as a seed crystal to produce a single crystal suitable for SXR analysis. The system was found to be the salt **2**·CH<sub>3</sub>SO<sub>3</sub><sup>-</sup> (Figure 5.10) formed from two independent ionic pairs. The ammonium moiety interacts similarly with all three of the N-H bonds interacting with S=O/S-O<sup>-</sup> oxygen atoms. The key difference between the CH<sub>3</sub>SO<sub>3</sub>H and H<sub>2</sub>SO<sub>4</sub> salt structures is that the alcohol group of **2** no longer forms hydrogen bonds with any S=O/S-O<sup>-</sup> or SOH oxygen atoms, instead it only forms hydrogen bonds with alcohol groups on other cations of **2** forming a repeating chain of alcohol groups. The change in the OH hydrogen bonding pattern can be attributed to the lack of SOH group limiting the hydrogen bond donor potential. The hydrogen bond between alcohol groups is quite strong with the O···O distance alternating between 2.769(11) and 2.778(10) Å. The hydrogen bond lengths between S=O and NH are similar to the lengths observed with the **3**·HSO<sub>4</sub><sup>-</sup> structure with the O···N distances varying from 2.832(11), 2.829(11), 2.899(14), 2.821(11), 2.901(14) and 2.850(11) Å.

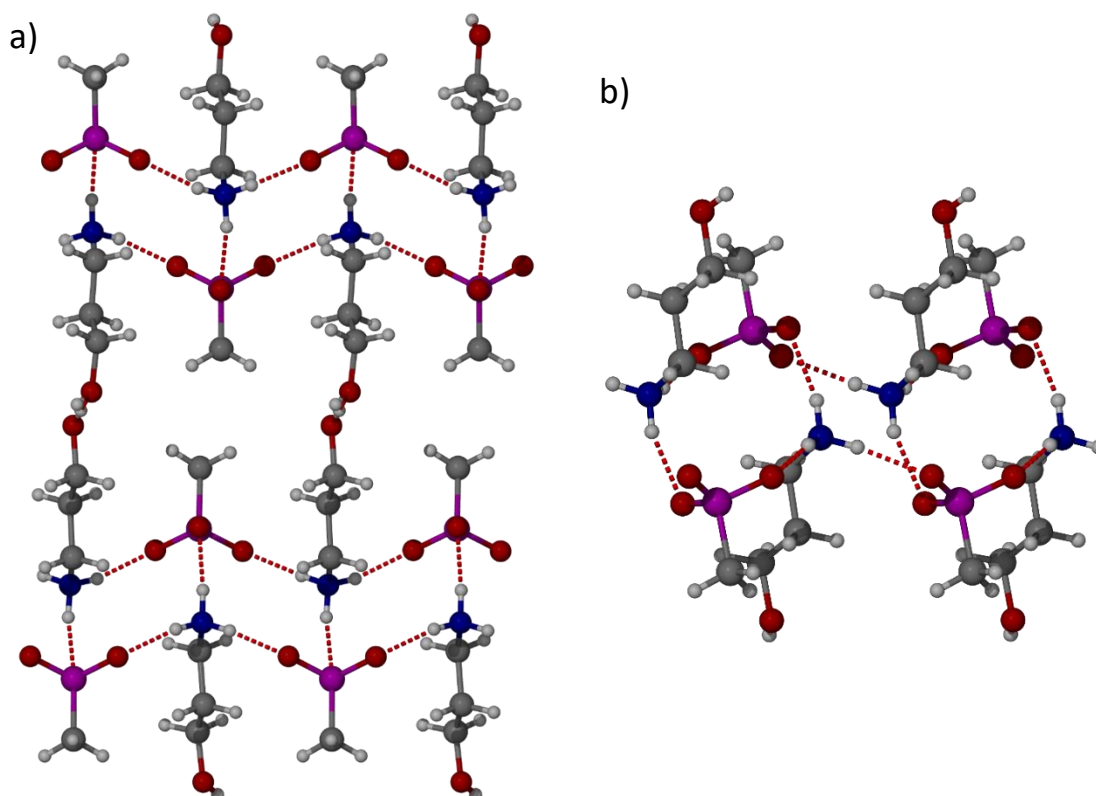


Figure 5.10: The X-ray crystal structure of  $2 \cdot \text{CH}_3\text{SO}_3^-$  in the a) (100) and b) (101) crystallographic planes.

The  $2 \cdot \text{HSO}_4^-$  and  $2 \cdot \text{CH}_3\text{SO}_3^-$  structures represent a plausible model for how cysteic acid could interact with **2**. From the two salt structures, it can be speculated that **2** could interact with two cysteic acid residues and produce a bridging interaction across the ammonium moiety. The bridging interaction between two cysteic acid residues with **2** could help strengthen damaged hair in a similar way to the original disulfide bridge which was present before the hair was damaged. The alcohol group could also interact with amino acids with substituent groups containing an alcohol group such as serine and threonine.

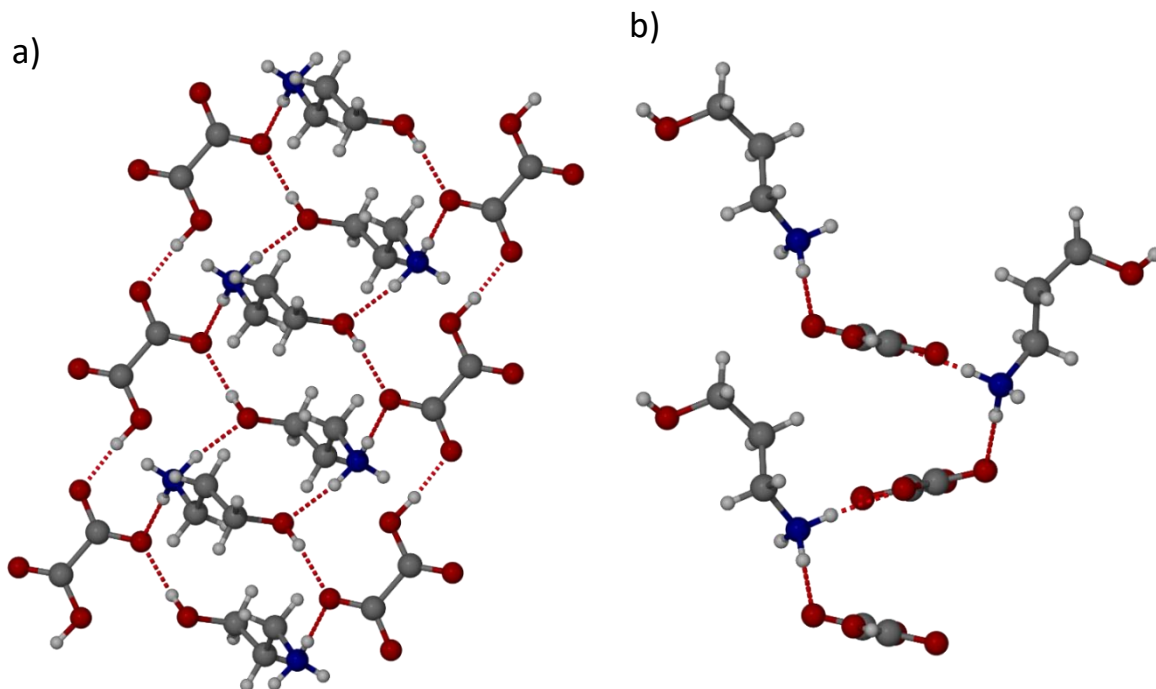


Figure 5.11: The X-ray crystal structure of  $2 \cdot \text{HC}_2\text{O}_4^-$  in the a) (010) and b) (100) crystallographic plane.

Oxalic acid ( $\text{C}_2\text{H}_2\text{O}_4$ ) was selected to mimic the glutamic acid and aspartic acid due to the structural similarity of  $\text{C}_2\text{H}_2\text{O}_4$  with the substituent group of the amino acids and the large negative excess enthalpy of mixing from the COSMOquick screen (Table S2).  $\text{C}_2\text{H}_2\text{O}_4$  was dissolved in ethanol and 3AP was added which resulted in the formation of crystals. The crystals were analysed by SXRD which determined the structure to be  $2 \cdot \text{HC}_2\text{O}_4^-$  (Figure 5.11). In the crystallisation experiment,  $\text{C}_2\text{H}_2\text{O}_4$  was in excess with over four molecules of oxalic acid per one molecule of 3AP to encourage the formation of a 1:1 stoichiometric salt. The structure of  $2 \cdot \text{HC}_2\text{O}_4^-$  shows only one of the carboxylic acid groups of the oxalic acid is deprotonated to give a hydrogen oxalate anion. The OH group on 3AP forms two hydrogen bonds, one via the hydrogen atom to the carboxylate anion side of  $\text{HC}_2\text{O}_4^-$  with an  $\text{O} \cdots \text{O}$  distance of 2.7040(13) Å and the other via the oxygen atom to an NH group on another cation of **2** with an  $\text{O} \cdots \text{N}$  distance of 2.8049(15) Å. The  $\text{NH}_3^+$  group of **2** forms two hydrogen bonds to the carboxylate anions of two different  $\text{C}_2\text{HO}_4^-$  atoms with standard  $\text{O} \cdots \text{N}$  distances of 2.7857(14) and 2.8414(15) Å. The  $\text{HC}_2\text{O}_4^-$  anions form a repeating hydrogen bonded chain from the OH of one  $\text{HC}_2\text{O}_4^-$  to the CO on another, the  $\text{O} \cdots \text{O}$  distances is very short at 2.5793(12) indicating it is a very strong bond (Figure 5.11A).

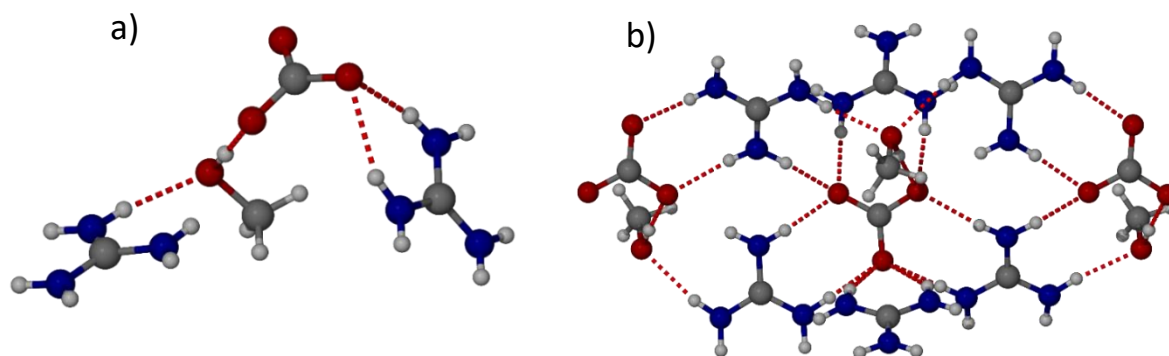


Figure 5.12: The X-ray crystal structure of guanidinium carbonate methanol solvate. a) the asymmetric unit and b) the (310) crystallographic plane.

Guanidine carbonate was chosen to mimic the interaction of the substituent group of arginine with **3**. *L*-gulonic acid  $\gamma$ -lactone was suspended in methanol with guanidine carbonate and the system was heated to reflux. The reaction produced a white powder suspended in a yellow solution. The white powder was separated by filtration, and found to be guanidine carbonate by FTIR. The yellow solution was sealed for three days which resulted in the formation of two different types of crystals. Both types of crystal were analysed via SXRD with one identified as a previously characterised structure of guanidine carbonate (GUANCB)<sup>42</sup> and the other proved to be a new methanol solvate of guanidine carbonate (Figure 5.12). The empirical formula of the methanol solvate contains two guanidine cations, one carbonate anion and one methanol molecule. The GUANCB guanidine carbonate structure contains three  $R_2^2(8)$  hydrogen bonding motifs formed around one guanidine cation with three carbonate anions, and six  $R_2^2(8)$  hydrogen bonding motifs formed around one carbonate anion with six guanidine cations.<sup>42</sup> The O $\cdots$ N distance of hydrogen bonds in GUANCB vary from 2.704 to 3.189 Å. In the methanol solvate structure, the methanol molecule hydrogen bonds strongly to the carbonate with an O $\cdots$ O distance of 2.635(2) Å. The strong methanol to carbonate hydrogen bond disrupts the bonding motifs found in the original GUANCB structure, the disruptions cause one of the hydrogen bonds between carbonate and guanidine to weaken and lengthen to 3.261(2) Å.

#### 5.2.4 Potential Interactions of **1**, **2** and **3** with Hair Protein

No cocrystal or salt structures were formed with **1** and any of the amino acids or model compounds. Attempts to form a co-crystal of **1** with 4,4'-biphenol in morpholine led to the

formation of a 1:2 co-crystal of 4,4'-biphenol and morpholine. Therefore, to help understand the potential interactions of **1** with amino acids in hair, the crystal structures of **1** were studied. Both polymorphs of **1** (Figure 5.4, Figure 5.5) show a large number of hydrogen bonds with up to 10 different hydrogen bonds from the alcohol groups, indicating the potential to form extensive hydrogen bonds with amino acids containing OH and NH groups in the substituents. Form II of amide **1** (Figure 5.5) has an amide linking interaction between molecules which could indicate the potential formation of similar amide linking interaction between the protein amide backbone which could change the overall structure. The new amide linking interactions could explain the increased strength of hair treated with the haircare mixture compared to unbleached hair. However, the amides in protein chains are usually heavily involved in forming hydrogen bonds with each other so it may not be possible for **1** to disrupt this structure. The potential bonding of **1** is displayed in Figure 5.13, showing the potential hydrogen bonding interactions formed between the alcohol groups in **1** and the alcohol groups present in the amino acids serine, threonine and tyrosine.

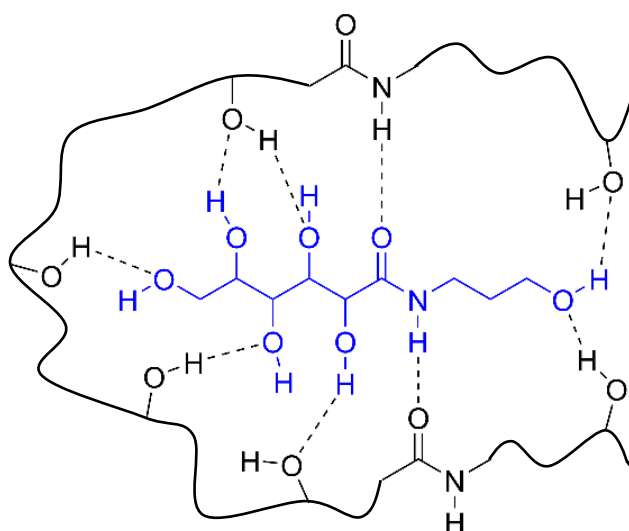


Figure 5.13: Model structure of the potential intermolecular interactions formed between **1** and the amino acid substituent groups on a simplified hair structure.

A range of structures found in the CSD and three new salt structures ( $\mathbf{2} \cdot \text{HSO}_4^-$ ,  $\mathbf{2} \cdot \text{CH}_3\text{SO}_3^-$ , and  $\mathbf{2} \cdot \text{HC}_2\text{O}_4^-$ ) were used to identify potential interactions formed between **2** and amino acids. The initial CSD search revealed the crystal structure of 3AP which displayed hydrogen bonds formed between amine and alcohol groups, suggesting **2** could form hydrogen bonds with amino acids containing OH groups like serine, threonine and tyrosine. The CSD search

for cation **2** found three salt structures with carboxylate anion groups containing charge assisted interactions formed between the ammonium moiety and the carboxylate anion. This is in agreement with the salt structure of  $\mathbf{2} \cdot \text{HC}_2\text{O}_4^-$  which also shows the interaction of ammonium moiety of cation **2** with a carboxylate anion. The four salt structures of **2** with carboxylate anions suggest **2** could form hydrogen bonds with amino acids containing carboxylate residues (glutamic and aspartic acid). The two salt structures of  $\mathbf{2} \cdot \text{HSO}_4^-$  and  $\mathbf{2} \cdot \text{CH}_3\text{SO}_3^-$  along with the salt structure  $(\mathbf{2})_2 \cdot \text{naphthalene-1,5-disulfonate}$  found in the CSD, shows the strong hydrogen bonding interactions that can form between sulfonic acid and **2**. The observed hydrogen bonding is speculated to be analogous to the potential hydrogen bonding that could take place between **2** and cysteic acid. The potential interactions formed between **2** and a range of amino acids have been summarised in Figure 5.14. Cation **2** shows the strongest charge assisted hydrogen bonding interactions, suggesting it is a very important part of the haircare mixture.

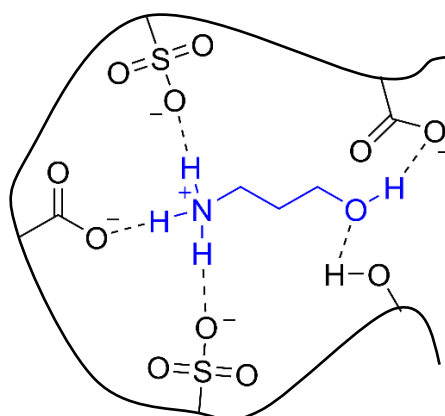


Figure 5.14: Model structure of the potential intermolecular interactions formed between **2** and the amino acid substituent groups on a simplified hair structure.

A range of potential interactions for **3** with the amino acids has been identified from the CSD and the crystal structure of the guanidine carbonate methanol solvate. The crystal structure of GLA monohydrate displays extensive hydrogen bonding formed between the alcohol groups of GLA and water molecules.<sup>35</sup> The hydrogen bonds observed in GLA monohydrate can be assumed to be analogous to the potential bonds that can form between **3** and amino acids with alcohol groups such as serine, threonine and tyrosine. The second structure of GLA located in the CSD search was the ammonium salt of anion **3**, the hydrogen bonding interactions that took place between **3** and the ammonium cation could

be related to potential interactions that could take place between **3** and lysine.<sup>36</sup> Attempts to form a salt of **3** with ethylenediamine proved unsuccessful and either led to the individual components or *N,N'*-ethylene bis-*L*-gluconamide. The guanidine carbonate methanol solvate displays extensive hydrogen bonds with the formation of  $R_2^2(8)$  hydrogen bonding motifs, it can be speculated that the carboxylate cation section of **3** could interact similarly with arginine, potentially forming a bridging interaction between two arginine residues. The combination of all these observations can be used to create a model structure of all the potential interactions between **3** and the amino acids in hair proteins (Figure 5.15).

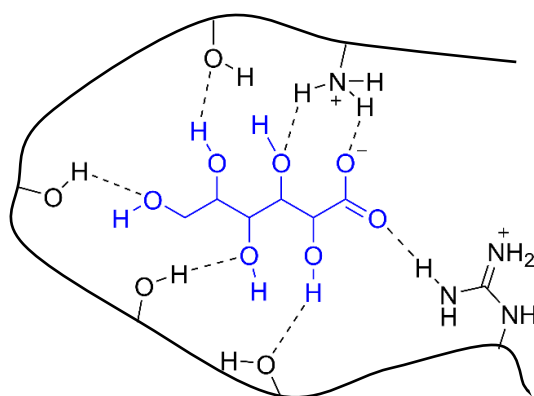


Figure 5.15: Model structure of the potential intermolecular interactions formed between **3** and the amino acid substituent groups on a simplified hair structure

### 5.3 Conclusion

Compounds **1**, **2** and **3** have been shown to form intermolecular hydrogen bonds with amino acid substituent group mimics. The CSD search for **2** revealed salt structures showing the interactions formed between the ammonium moiety of **2** with both carboxylate anions and sulfonate anions which suggests potential interactions with amino acids containing carboxylate and sulfonate residues. The salt structure of ammonium gluconate found in the CSD indicated the potential of **3** to interact with lysine. Two polymorphic forms of **1** were analysed by SXRD revealing an extensive network of hydrogen bonding taking place between the alcohol groups. One of the key differences between the two polymorphs was the NH group either forming an intramolecular hydrogen bond in form I and an intermolecular hydrogen bond in form II. The gluconamide *N,N'*-ethylene bis-*L*-gluconamide was crystallised and analysed by SXRD showing a similar extensive network of hydrogen bonds from the gluconic acid part of the molecule as seen in the crystal structures of both

polymorphs of **1**. The *N,N'*-ethylene bis-*L*-gluconamide also shows the same intermolecular hydrogen bond between amide units as observed in form II of **1**.

A COSMOquick screen was performed to identify the most energetically favourable co-crystals or salts that could form between **1**, **2** and **3**, with the amino acids present in hair. The most energetically favourable combinations of **1**, **2** and **3** with amino acids were screened experimentally using a variety of co-crystallisation techniques but no new structures were found. To simplify the potential interactions, smaller molecules were selected to mimic the amino acid substituent groups. The small molecules were screened using COSMOquick which showed the systems with the small molecules were more energetically favourable compared to the original amino acids. No co-crystal or salt structures were identified with **1** or **3**. A new methanol solvate of guanidine carbonate was discovered and used to speculate the potential interactions between the carboxylate anion of **3** and a guanidinium cation. Three new salt structures of **2** with sulfuric acid, methane sulfonic acid and oxalic acid were found. The three structures were used to speculate how **2** could interact with carboxylate and sulfonate residues on amino acids. The potential interactions of all three components with the amino acids were summarised in Figure 5.13, Figure 5.14, and Figure 5.15. To build upon the speculated bonding the next steps structural information in the interaction of compounds **1** – **3** with more sophisticated model oligopeptides is needed.

## 5.4 Experimental

### 5.4.1 Materials

FiberHance bm solution was supplied by Ashland LLC. 3-amino-1-propanol, aniline, chloroform, cysteic acid monohydrate, *D*-gluconic acid solution, dimethyl sulfoxide (DMSO), ethanol, ethylenediamine, guanidine carbonate salt, hydrochloric acid (37%), *L*-gulonic acid  $\gamma$  lactone, methanol, methane sulfonic acid, oxalic acid, sodium hydroxide and sulfuric acid were purchased from Merck and used without further purification.

### 5.4.2 Analytical Methods

$^1\text{H}$  and  $^{13}\text{C}$  solution NMR spectra were recorded using a Varian Mercury-400 spectrometer, operating at 400 MHz for  $^1\text{H}$  and 100 MHz for  $^{13}\text{C}$ , chemical shifts were reported in ppm ( $\delta$ ) and referenced to residual protic solvent.



FTIR spectra were measured with a Perkin-Elmer 100 FT-IR Spectrometer with an  $\mu$ ATR attachment. Data was recorded at a resolution of  $4\text{cm}^{-1}$  for 12 scans over a range of 4000 to  $550\text{cm}^{-1}$ .

XRPD measurements were performed using a Bruker D8 X-ray diffractometer (Billerica, Massachusetts) with  $\text{CuK}\alpha$  radiation ( $1.54187\text{ \AA}$ ), and acceleration voltage and current of 40 kV and 40 mA, respectively. The samples were scanned in reflectance mode between  $3^\circ$  and  $60^\circ 2\theta$  with a scan rate of  $0.01583^\circ 2\theta/\text{s}$  and a step size of  $0.02^\circ$ .

Elemental analysis was performed by the University of Durham service using an Exeter CE-440 Elemental Analyser.

The X-ray single crystal data for all compounds have been collected using  $\lambda\text{MoK}\alpha$  radiation ( $\lambda = 0.71073\text{ \AA}$ ) on Bruker D8Venture diffractometers at various configurations (Photon100 CMOS detector,  $\mu\text{S}$ -microsource, Helios focusing mirrors)/(Photon III MM C14 CPAD detector,  $\mu\text{S}$ -III-microsource, Helios focusing mirrors)/(Photon III MM C7 CPAD detector,  $\mu\text{S}$ -microsource, Helios focusing mirrors) equipped with Cryostream (Oxford Cryosystems) open-flow nitrogen cryostats at the temperature  $120.0(2)\text{K}$ .  $\lambda\text{CuK}\alpha$  radiation ( $\lambda = 1.54178\text{ \AA}$ ) was used in data acquisition for 4,4'-biphenol-morpholine (1:2) co-crystal. All structures were solved by direct method and refined by full-matrix least squares on  $F^2$  for all data using Olex2<sup>43</sup> and SHELXTL<sup>44</sup> software. All non-hydrogen atoms were refined anisotropically, hydrogen atoms in most of the structures were found in difference Fourier maps and refined in isotropic approximation. Hydrogen atoms in twinned structure of  $\mathbf{2}\cdot\text{CH}_3\text{SO}_3^-$  (TWINABS/HKLF 5 refinement) and those of  $\text{CH}_2$ -groups in the structure  $\mathbf{1}$  form  $\mathbf{2}$  ( $Z' = 2$ ) were placed in the calculated positions and refined in riding mode. Absolute structures of all chiral compounds (except *L*-cysteic acid dimethylsulfoxide solvate, where it was determined from experimental data by anomalous dispersion effects) were assigned on the basis of known configurations of starting materials.

#### 5.4.3 CSD Search

ConQuest was used to search the CSD (version 2021.1.0, build 319587). Five separate searches were performed 1) a gluconamide with an undefined amine, 2) a neutral GLA molecule, 3)  $\mathbf{3}$ , 4) neutral 3AP and 5)  $\mathbf{2}$ . The results were analysed using Mercury.

#### 5.4.4 The Crystallisation of **1** form I

FiberHance bm solution (2 mL) was left to slowly evaporate. After 1 week lath shaped crystals formed. Analysis calc. of  $C_9H_{19}NO_7$ : C 42.68, H 7.56, 5.54%, found: C 42.60, H 7.53, N 5.46 %; FTIR ( $\nu/cm^{-1}$ ): 3404, 3342, 3239, 2895, 1643, 1538, 1460, 1439, 1383, 1324, 1305, 1248, 1238, 1203, 1137, 1113, 1097, 1070, 1050, 1022, 971, 943, 927, 861, 775, 632, 576.  $^1H$  NMR (400 MHz,  $D_2O$ )  $\delta$  4.18 (d,  $J = 3.6$  Hz, 1H), 3.96 (t,  $J = 3.2$  Hz, 1H), 3.72- 3.68 (m, 2H), 3.64-3.61 (m, 2H), 3.56-3.50 (m, 2H), 3.2 (td,  $J = 6.9, 2.8$  Hz, 2H), 1.66 (p,  $J = 6.7$  Hz, 2H).

Crystal data:  $C_9H_{19}NO_7$   $M = 253.25$  g mol $^{-1}$ ,  $0.28 \times 0.18 \times 0.11$  mm $^3$ , monoclinic, space group  $P2_1$ ,  $a = 4.6468(2)$  Å,  $b = 13.9198(7)$  Å,  $c = 8.9183(5)$  Å,  $\alpha = 90^\circ$ ,  $\beta = 101.1403(19)^\circ$ ,  $\gamma = 90^\circ$ ,  $V = 565.99(5)$  Å $^3$ ,  $Z = 2$ ,  $D_c = 1.486$  g cm $^{-3}$ ,  $F_{000} = 272.0$ , 12795 reflections collected, 3305 unique ( $R_{int} = 0.0325$ ). Final GooF = 1.037,  $R_1 = 0.0325$  (3305 reflections with  $I \geq 2\sigma(I)$ ),  $wR_2 = 0.0823$  (all data), 230 parameters, 1 restraint,  $\mu = 0.128$  mm $^{-1}$ .

#### 5.4.5 Crystallisation of D-GLA **1** form I

D-gluconic acid solution was mixed with 3AP forming a viscous yellow solution. The solution was left to slowly evaporate forming colourless plank crystals. FTIR ( $\nu/cm^{-1}$ ): 3404, 3342, 3239, 2895, 1643, 1538, 1460, 1439, 1383, 1324, 1305, 1248, 1238, 1203, 1137, 1113, 1097, 1070, 1050, 1022, 971, 943, 927, 861, 775, 632, 576. Crystal data:  $C_9H_{19}NO_7$   $M = 253.25$  g mol $^{-1}$ ,  $0.29 \times 0.1 \times 0.$  mm $^3$ , monoclinic, space group  $P2_1$ ,  $a = 4.64620(10)$  Å,  $b = 13.9212(4)$  Å,  $c = 8.9163(3)$  Å,  $\alpha = 90^\circ$ ,  $\beta = 101.1335(11)^\circ$ ,  $\gamma = 90^\circ$ ,  $V = 565.86(3)$  Å $^3$ ,  $Z = 2$ ,  $D_c = 1.486$  g cm $^{-3}$ ,  $F_{000} = 272.0$ , 13525 reflections collected, 3268 unique ( $R_{int} = 0.0403$ ). Final GooF = 1.021,  $R_1 = 0.0366$  (3268 reflections with  $I \geq 2\sigma(I)$ ),  $wR_2 = 0.0934$  (all data), 230 parameters, 1 restraint,  $\mu = 0.128$  mm $^{-1}$ .

#### 5.4.6 Crystallisation of **1** form II

**1** (50 mg, 0.20 mmol) was suspended in ethanol (150 mL). Aniline (100  $\mu$ L, 1.11 mmol) was added, and the mixture was refluxed with stirring for 30 minutes. The solution was left to evaporate in a round bottom flask for 5 months. A white solid with an orange tinge was formed. The solid (4.6 mg) was dissolved in ethanol (100  $\mu$ L) and the solution was left to evaporate. Plank crystals of SXR quality formed after 3 days. FTIR ( $\nu/cm^{-1}$ ): 3405, 3239, 2895, 1648, 1536, 1459, 1439, 1386, 1320, 1300, 1248, 1237, 1208, 1134, 1113, 1107, 1047, 1021, 943, 924, 861, 813, 761, 763, 734, 670, 631, 580. Crystal data:  $C_9H_{19}NO_7$   $M = 253.25$  g mol $^{-1}$ ,  $0.15 \times 0.05 \times 0.01$  mm $^3$ , monoclinic, space group  $P2_1$ ,  $a = 9.5157(4)$  Å,  $b = 5.0795(2)$  Å,

$c = 24.2667(10) \text{ \AA}$ ,  $\alpha = 90^\circ$ ,  $\beta = 96.4629(14)^\circ$ ,  $\gamma = 90^\circ$ ,  $V = 1165.48(8) \text{ \AA}^3$ ,  $Z = 4$ ,  $D_c = 1.443 \text{ g cm}^{-3}$ ,  $F_{000} = 544.0$ , 19083 reflections collected, 6127 unique ( $R_{\text{int}} = 0.0501$ ). Final Goof = 1.028,  $R_1 = 0.0514$  (6127 reflections with  $I \geq 2\sigma(I)$ ),  $wR_2 = 0.1110$  (all data), 363 parameters, 1 restraint,  $\mu = 0.124 \text{ mm}^{-1}$ .

#### 5.4.7 Cosmoquick Screen

COSMOquick version 1.7 (COSMOlogic GmbH & Co. KG, Leverkusen, Germany) was used to calculate the excess enthalpy of mixing for each component of the haircare mixture with amino acids and a range of amino acids mimics.<sup>38</sup>

#### 5.4.8 $2 \cdot \text{HSO}_4^-$ salt

Sulfuric acid (80  $\mu\text{L}$ , 1.5 mmol) was slowly added to 3AP (50  $\mu\text{L}$ , 0.65 mmol). The sample released a vapour and was hot to the touch upon the addition of sulfuric acid. The vial was left sealed for 15 days until small plate-shaped crystals formed. Crystal data:  $\text{C}_3\text{H}_{11}\text{NO}_5\text{S}$   $M = 173.19 \text{ g mol}^{-1}$ ,  $0.15 \times 0.08 \times 0.01 \text{ mm}^3$ , monoclinic, space group  $P2_1/m$ ,  $a = 5.3514(3) \text{ \AA}$ ,  $b = 6.9661(4) \text{ \AA}$ ,  $c = 9.6220(5) \text{ \AA}$ ,  $\alpha = 90^\circ$ ,  $\beta = 98.976(2)^\circ$ ,  $\gamma = 90^\circ$ ,  $V = 354.30(3) \text{ \AA}^3$ ,  $Z = 2$ ,  $D_c = 1.623 \text{ g cm}^{-3}$ ,  $F_{000} = 184.0$ , 6372 reflections collected, 1104 unique ( $R_{\text{int}} = 0.0377$ ). Final Goof = 1.146,  $R_1 = 0.0306$  (1104 reflections with  $I \geq 2\sigma(I)$ ),  $wR_2 = 0.0708$  (all data), 83 parameters, 0 restraints,  $\mu = 0.426 \text{ mm}^{-1}$ .

#### 5.4.9 $2 \cdot \text{CH}_3\text{SO}_3^-$ salt

3AP (50  $\mu\text{L}$ , 0.65 mmol) was slowly added to methane sulfonic acid (90  $\mu\text{L}$ , 1.39 mmol). Upon the addition of 3AP, the temperature of the vial increased, and white gas was released. The sealed vial was stored at  $3^\circ\text{C}$  which resulted in the formation of a white precipitate after 2 hours. The white precipitate was used as a seed crystal and added to a solution of 3AP (50  $\mu\text{L}$ , 0.65 mmol), methane sulfonic acid (90  $\mu\text{L}$ , 1.39 mmol) and ethanol (200  $\mu\text{L}$ ) and stored at  $3^\circ\text{C}$ . After a few hours plate crystals formed. Crystal data:  $\text{C}_4\text{H}_{13}\text{NO}_4\text{S}$   $M = 171.21 \text{ g mol}^{-1}$ ,  $0.21 \times 0.07 \times 0.01 \text{ mm}^3$ , monoclinic, space group  $P2_1$ ,  $a = 5.1527(2) \text{ \AA}$ ,  $b = 21.5379(10) \text{ \AA}$ ,  $c = 7.1287(3) \text{ \AA}$ ,  $\alpha = 90^\circ$ ,  $\beta = 91.6578(19)^\circ$ ,  $\gamma = 90^\circ$ ,  $V = 790.80(6) \text{ \AA}^3$ ,  $Z = 4$ ,  $D_c = 1.438 \text{ g cm}^{-3}$ ,  $F_{000} = 368.0$ , 18888 reflections collected, 18888 unique ( $R_{\text{int}} = 0.1040$ ). Final Goof = 1.018,  $R_1 = 0.0665$  (18888 reflections with  $I \geq 2\sigma(I)$ ),  $wR_2 = 0.1757$  (all data), 187 parameters, 1 restraint,  $\mu = 0.372 \text{ mm}^{-1}$ .

#### 5.4.10 2·HC<sub>2</sub>O<sub>4</sub><sup>-</sup> salt

Oxalic acid (50 mg, 0.56 mmol) was dissolved in ethanol (250 μL). 3AP (10 μL, 0.13 mmol) was added to the vial which resulted in the formation of plate crystals. FTIR ( $\nu/\text{cm}^{-1}$ ): 3100, 1689, 1395, 1346, 1163, 779, 672, 652. Crystal data: C<sub>5</sub>H<sub>11</sub>NO<sub>5</sub>  $M = 165.15 \text{ g mol}^{-1}$ , 0.11 x 0.1 x 0.02 mm<sup>3</sup>, monoclinic, space group  $P2_1/n$ ,  $a = 5.6912(4) \text{ \AA}$ ,  $b = 7.1078(5) \text{ \AA}$ ,  $c = 19.2926(14) \text{ \AA}$ ,  $\alpha = 90^\circ$ ,  $\beta = 90.414(3)^\circ$ ,  $\gamma = 90^\circ$ ,  $V = 780.40(10) \text{ \AA}^3$ ,  $Z = 4$ ,  $D_C = 1.406 \text{ g cm}^{-3}$ ,  $F_{000} = 352.0$ , 12905 reflections collected, 2255 unique ( $R_{\text{int}} = 0.0450$ ). Final GooF = 1.061,  $R_1 = 0.0414$  (2255 reflections with  $I \geq 2\sigma(I)$ ),  $wR_2 = 0.0993$  (all data), 144 parameters, 0 restraints,  $\mu = 0.126 \text{ mm}^{-1}$ .

#### 5.4.11 Guanidine Carbonate Methanol Solvate

*L*-Gulonic acid  $\gamma$ -lactone (1g, 5.6 mmol) and guanidine carbonate (2 g, 22.2 mmol) was suspended in methanol (10 mL). The mixture was degassed with nitrogen for 30 minutes and then refluxed under nitrogen for 3 hours. The mixture was cooled, and it contained a white powder in a light yellow transparent solution. The solid powder was removed via filtration and identified by FTIR as guanidine carbonate. The yellow solution was left sealed for 3 days and crystals formed. The vial contained two different types of lath shaped crystal with one crystal identified as guanidine carbonate (GUANCB)<sup>42</sup> and the other a new structure of guanidine carbonate methanol solvate. Crystal data: C<sub>4</sub>H<sub>16</sub>N<sub>6</sub>O<sub>4</sub>  $M = 212.23 \text{ g mol}^{-1}$ , 0.21 x 0.06 x 0.01 mm<sup>3</sup>, orthorhombic, space group  $P2_12_12_1$ ,  $a = 7.1149(3) \text{ \AA}$ ,  $b = 11.6098(4) \text{ \AA}$ ,  $c = 13.7967(5) \text{ \AA}$ ,  $\alpha = 90^\circ$ ,  $\beta = 90^\circ$ ,  $\gamma = 90^\circ$ ,  $V = 1139.64(7) \text{ \AA}^3$ ,  $Z = 4$ ,  $D_C = 1.237 \text{ g cm}^{-3}$ ,  $F_{000} = 456.0$ , 20652 reflections collected, 3319 unique ( $R_{\text{int}} = 0.0471$ ). Final GooF = 1.103,  $R_1 = 0.0415$  (3319 reflections with  $I \geq 2\sigma(I)$ ),  $wR_2 = 0.0985$  (all data), 180 parameters, 0 restraints,  $\mu = 0.107 \text{ mm}^{-1}$ .

#### 5.4.12 N,N'-ethylene bis-*L*-gluconamide

Ethylenediamine (0.53 mL, 9.8 mmol) was mixed with methanol (20 mL) and *L*-gulonic acid  $\gamma$ -lactone (2.852 g, 16.0 mmol) was added.<sup>24</sup> The solution was refluxed with stirring under nitrogen for 2 hours. A white powder forms during the reaction which was separated by filtration. 10 mg of the powder was dissolved in water (20 μL), methanol (20 μL) was added and the sample formed crystals after a few hours. FTIR ( $\nu/\text{cm}^{-1}$ ): 3289, 2933, 2879, 1642, 1538, 1434, 1315, 1077, 1043, 878. Crystal data: C<sub>14</sub>H<sub>28</sub>N<sub>2</sub>O<sub>12</sub>  $M = 416.38 \text{ g mol}^{-1}$ , 0.21 x 0.17 x 0.12 mm<sup>3</sup>, monoclinic, space group  $C2$ ,  $a = 9.7045(4) \text{ \AA}$ ,  $b = 5.0273(2) \text{ \AA}$ ,  $c = 18.1838(7) \text{ \AA}$ ,  $\alpha$

$\alpha = 90^\circ$ ,  $\beta = 90.9710(10)^\circ$ ,  $\gamma = 90^\circ$ ,  $V = 887.01(6) \text{ \AA}^3$ ,  $Z = 2$ ,  $D_C = 1.559 \text{ g cm}^{-3}$ ,  $F_{000} = 444.0$ , 10231 reflections collected, 2537 unique ( $R_{\text{int}} = 0.0260$ ). Final GooF = 1.105,  $R_1 = 0.0252$  (2537 reflections with  $I \geq 2\sigma(I)$ ),  $wR_2 = 0.0665$  (all data), 187 parameters, 1 restraint,  $\mu = 0.137 \text{ mm}^{-1}$ .

#### 5.4.13 L-Cysteic acid dimethylsulfoxide solvate synthesis

**1** (5.8 mg, 0.023 mmol) and cysteic acid monohydrate (4.3 mg, 0.023 mmol) were dissolved in dimethylsulfoxide (400  $\mu\text{L}$ ). Chloroform (1.2 mL) was vapour diffused into the solution resulting in the formation of small prism crystals. Crystal data:  $\text{C}_5\text{H}_{13}\text{NO}_6\text{S}_2$   $M = 247.28 \text{ g mol}^{-1}$ ,  $0.45 \times 0.34 \times 0.14 \text{ mm}^3$ , monoclinic, space group  $P2_1$ ,  $a = 6.5483(3) \text{ \AA}$ ,  $b = 7.9607(3) \text{ \AA}$ ,  $c = 9.8718(4) \text{ \AA}$ ,  $\alpha = 90^\circ$ ,  $\beta = 93.5090(19)^\circ$ ,  $\gamma = 90^\circ$ ,  $V = 513.64(4) \text{ \AA}^3$ ,  $Z = 2$ ,  $D_C = 1.599 \text{ g cm}^{-3}$ ,  $F_{000} = 260.0$ , 8225 reflections collected, 2839 unique ( $R_{\text{int}} = 0.0388$ ). Final GooF = 1.056,  $R_1 = 0.0337$  (2839 reflections with  $I \geq 2\sigma(I)$ ),  $wR_2 = 0.0881$  (all data), 179 parameters, 1 restraint,  $\mu = 0.523 \text{ mm}^{-1}$ .

#### 5.4.14 4,4'-Biphenol·Morpholine (1:2) co-crystal synthesis

**1** (6.1 mg, 0.024 mmol) and 4,4'-biphenol (2.3 mg, 0.012 mmol) were dissolved in morpholine (0.5 mL). Hexane (1 mL) was vapour diffused slowly into the system and small prism crystals formed after 8 days. Crystal data:  $\text{C}_{20}\text{H}_{28}\text{N}_2\text{O}_4$   $M = 360.44 \text{ g mol}^{-1}$ ,  $0.15 \times 0.06 \times 0.04 \text{ mm}^3$ , monoclinic, space group  $P2_1/c$ ,  $a = 5.9841(3) \text{ \AA}$ ,  $b = 10.7325(6) \text{ \AA}$ ,  $c = 14.8852(8) \text{ \AA}$ ,  $\alpha = 90^\circ$ ,  $\beta = 97.666(4)^\circ$ ,  $\gamma = 90^\circ$ ,  $V = 947.45(4) \text{ \AA}^3$ ,  $Z = 2$ ,  $D_C = 1.263 \text{ g cm}^{-3}$ ,  $F_{000} = 388.0$ , 10710 reflections collected, 1821 unique ( $R_{\text{int}} = 0.0792$ ). Final GooF = 1.099,  $R_1 = 0.0525$  (1821 reflections with  $I \geq 2\sigma(I)$ ),  $wR_2 = 0.1413$  (all data), 174 parameters, 0 restraints,  $\mu = 0.713 \text{ mm}^{-1}$ .

## 5.5 References

1. C. F. Cruz, C. Costa, A. C. Gomes, T. Matamá and A. Cavaco-Paulo, *Cosmetics*, 2016, **3**, 26.
2. M. Feughelman, *J. Appl. Polym. Sci.*, 2002, **83**, 489-507.
3. M. S. Birbeck and E. H. Mercer, *J. Biophys. Biochem. Cytol.*, 1957, **3**, 215-222.
4. S. Tokunaga, H. Tanamachi and K. Ishikawa, *Cosmetics*, 2019, **6**.
5. L. N. Jones, *Clin. Dermatol.*, 2001, **19**, 95-103.
6. S. D. Bringans, J. E. Plowman, J. M. Dyer, S. Clerens, J. A. Vernon and W. G. Bryson, *Exp. Dermatol.*, 2007, **16**, 951-960.
7. M. Feughelman and B. K. Willis, *J. Cosmet. Sci.*, 2001, **52**, 185-193.
8. D. P. Harland, R. J. Walls, J. A. Vernon, J. M. Dyer, J. L. Woods and F. Bell, *J. Struct. Biol.*, 2014, **185**, 397-404.

9. J. E. Plowman, L. N. Paton and W. G. Bryson, *Exp. Dermatol.*, 2007, **16**, 707-714.
10. R. C. Marshall, D. F. G. Orwin and J. M. Gillespie, *Electron Microsc. Rev.*, 1991, **4**, 47-83.
11. M. A. Rogers, L. Langbein, S. Praetzel-Wunder, H. Winter and J. Schweizer, *Int. Rev. Cytol.*, 2006, **251**, 209-263.
12. S. Thibaut, P. Barbarat, F. Leroy and B. A. Bernard, *Int. J. Dermatol.*, 2007, **46**, 7-10.
13. Y. Liu, L. Hong, K. Wakamatsu, S. Ito, B. Adhyaru, C.-Y. Cheng, C. R. Bowers and J. D. Simon, *Photochem. Photobiol.*, 2005, **81**, 135-144.
14. D. W. Deedrick and S. L. Koch, *Forensic Sci. Commun.*, 2004, **6**.
15. R. L. Harrison, *Wildl. Soc. Bull.*, 2002, **30**, 412-419.
16. B. Wang, W. Yang, J. McKittrick and M. A. Meyers, *Prog. Mater. Sci.*, 2016, **76**, 229-318.
17. M. L. Huggins, *Proc. Nat. Acad. Sci. U. S. A.*, 1957, **43**, 204-209.
18. J. F. Conway and D. A. D. Parry, *Int. J. Biol Macromol*, 1988, **10**, 79-98.
19. J. Yu, D.-w. Yu, D. M. Checkla, I. M. Freedberg and A. P. Bertolino, *J. Investig. Dermatol.*, 1993, **101**, S56-S59.
20. C. R. Robbins, *Chemical and Physical Behavior of Human Hair*, Springer-Verlag Berlin Heidelberg, 5 edn., 2012.
21. L. J. Wolfram, *J. Am. Acad. Dermatol.*, 2003, **48**, S106-S114.
22. T. Imai, *Okajimas Folia Anat. Jpn.*, 2011, **88**, 1-9.
23. L. Wolfram, K. Hall and I. Hui, *J. Soc. Cosmet. Chem.*, 1970, **21**, 875-900.
24. E. P. J. M. Everaert, G. Kroon and X. Zhang, Method of strengthening hair fibers and protecting dyed hair color from fading or wash-out, US20170007518A1, 2017.
25. E. P. J. M. Everaert, G. Kroon and T. D. T. Tran, Method for coloring or bleaching hair fibers, US20180193242A1, 2018.
26. R. V. Moorsel-Murerikaite, T. D. T. Tran and G. Kroon, Method of strengthening non-keratinous fibers, and uses thereof, WO2020150384A1, 2020.
27. Ashland, are you ready to bond?, <https://www.ashland.com/industries/personal-and-home-care/fiberhance#>, (accessed 16 June 2021).
28. G. Graziano, *Int. J. Biol. Macromol.*, 2012, **50**, 230-235.
29. Ashland, strengthen hair from the inside, <https://www.ulprospector.com/documents/1519442.pdf?bs=4989&b=718145&st=20&r=eu&ind=personalcare>, (accessed 16 June 2021).
30. R. Gajda and A. Katrusiak, *Acta Crystallogr. B*, 2008, **64**, 476-482.
31. M. W. Büttner, C. Burschka, J. O. Daiss, D. Ivanova, N. Rochel, S. Kammerer, C. Peluso-Iltis, A. Bindler, C. Gaudon, P. Germain, D. Moras, H. Gronemeyer and R. Tacke, *ChemBioChem*, 2007, **8**, 1688-1699.
32. Y. Chumakov, Y. Simonov, M. Grozav, M. Crisan, G. Bocelli, A. Yakovenko and D. Lyubetsky, *Open Chem. J.*, 2006, **4**, 458-475.
33. L. Fang, S. Numajiri, D. Kobayashi, H. Ueda, K. Nakayama, H. Miyamae and Y. Morimoto, *J. Pharm. Sci*, 2004, **93**, 144-154.
34. Y. Jin, *Acta Crystallogr. E*, 2012, **68**, o212.
35. T. Lis, *Carbohydr. Res.*, 1983, **122**, 23-29.
36. T. Lis, *Acta. Crystallogr. B.*, 1981, **37**, 1957-1959.
37. J. Bernstein, *Polymorphism In Molecular Crystals*, Oxford University Press, Oxford, UK, 1st edn., 2002.
38. A. Klamt, *Wires Comput. Mol. Sci.*, 2018, **8**, e1338.

39. COSMObase - The compound collection for COSMOtherm, <https://www.3ds.com/products-services/biovia/products/molecular-modeling-simulation/solvation-chemistry/cosmobase/>, (accessed 11 October 2021).
40. COSMOlogic GmbH & Co KG, 2018, COSMOquick User Guide, Version 1.7
41. N. Benali-Cherif, A. Kateb, H. Boussekine, Z. Boutobba and A. Messai, *Acta Crystallographica Section E*, 2007, **63**, o3251.
42. J. M. Adams and R. W. H. Small, *Acta. Crystallogr. B.*, 1974, **30**, 2191-2193.
43. O. V. Dolomanov, L. J. Bourhis, R. J. Gildea, J. A. K. Howard and H. Puschmann, *J. Appl. Crystallogr.*, 2009, **42**, 339-341.
44. G. Sheldrick, *Acta Crystallogr. C*, 2015, **71**, 3-8.

## 6 Supramolecular Gelation Properties of Hydroxypropyl-L-gluconamide

### 6.1 Introduction

Gels have a wide range of uses in many fields including food, materials, pharmaceuticals, and personal care.<sup>1-5</sup> To form a gel a small amount of a gelator (0.1 – 10 wt%) is dissolved in a hot solvent.<sup>6,7</sup> The solution is then cooled to the temperature of gelation and the gel forms by trapping solvent molecules in place with an elastic cross-linked network, forming a viscoelastic solid-like material.<sup>8</sup> In the case of supramolecular gels the cross-linked network is formed from the self-aggregation of low molecular weight gelators held together by intermolecular interactions.<sup>5,9</sup> The intermolecular interactions involved include hydrogen bonding, halogen bonding,  $\pi$ - $\pi$  stacking, metal coordination, hydrophobic forces, van der Waals interactions and coordination interactions.<sup>10-12</sup> For a gel fibre to form the intermolecular interactions need to be strong and directional to produce one-dimensional chains, these chains form the primary structure of the gel.<sup>4,13,14</sup> The secondary structure involves the aggregation of the molecular chain into fibres which then entangle to form the gel network which is classed as the tertiary structure (Figure 6.1).<sup>7,9</sup>

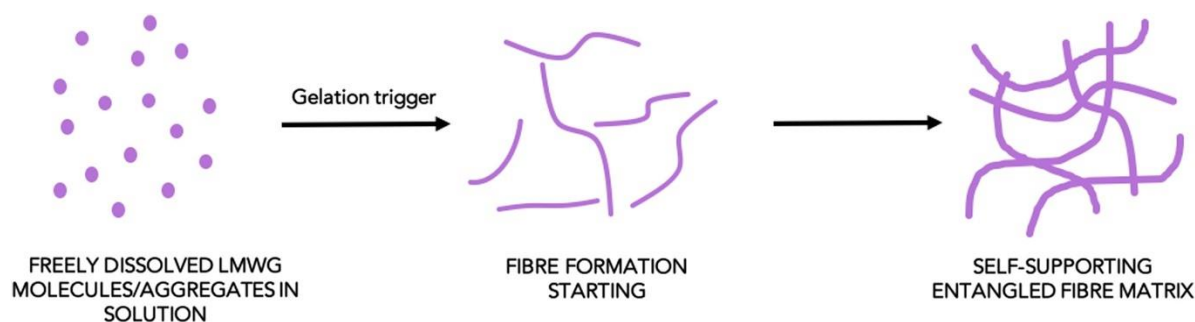


Figure 6.1: Gel formation process. Reproduced with permission from Draper *et al.*<sup>9</sup>

Characterisation of supramolecular gels is difficult due to the dynamic nature of the intermolecular interactions formed between gelator molecules. However, a variety of characterisation methods are available.<sup>15,16</sup> The initial test is a visual test that involves inverting a vial and if the sample does not flow it is assumed to be a gel. However, this method does not distinguish well between gels and viscous liquids. Therefore, a more reliable test is to perform rheology on the sample.<sup>17</sup> Gels are viscoelastic meaning they have both “solid-like” and “liquid-like” behaviour. The “solid-like” behaviour is shown by the



elastic storage modulus ( $G'$ ) and the “liquid-like” behaviour is shown by the elastic loss modulus ( $G''$ ).<sup>18, 19</sup> For a system to be classed as a gel the value of  $G'$  has to be approximately one order of magnitude higher than  $G''$ . Also, the values of  $G'$  and  $G''$  should not change when constant stress and varying frequency is applied. Two main experimental rheology procedures are performed with gels, an oscillatory frequency sweep and an oscillatory amplitude sweep. The frequency sweep involves varying the frequency whilst maintaining a fixed small amplitude of stress. The amplitude sweep involves using a fixed frequency and varying the amplitude of stress. The relative strength of a gel can be found using the magnitude of  $G'$  and from the yield stress which is identified in the amplitude sweep. The yield stress is the point at which  $G''$  becomes larger than  $G'$  indicating the sample is more “liquid-like”.<sup>20</sup>

Scanning electron microscopy (SEM) produces an image of the gel fibres by scanning over them with a focused beam of electrons.<sup>16</sup> The interaction between the electrons in the beam and the electrons in the sample produces various signals that provide information about the samples topography and produces high-resolution images.<sup>21</sup> To produce samples for SEM the samples are dried to remove the solvent which leaves behind the gel fibres in the form of a xerogel. The drying process may cause the xerogel to not be representative of the gel fibre due to potential structural changes including crystallisation of the sample.<sup>15</sup>

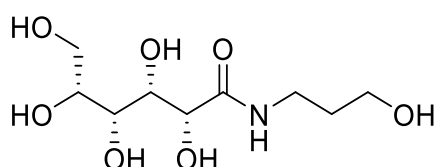


Figure 6.2: The structure of hydroxypropyl-*L*-gluconamide (**1**).

Hydroxypropyl-*L*-gluconamide (**1**) (Figure 6.2) was introduced in Chapter 5 as part of the hair care mixture fiberHance bm.<sup>22-26</sup> In Chapter 5 the crystal structure of two polymorphs of **1** showed a large number of hydrogen bonds which was speculated to help strengthen hair fibres when used as part of a hair care formulation. In this chapter, a polymorph screen was carried out with **1** which led to the discovery that **1** acts as a low molecular weight gelator forming supramolecular gels in aniline and benzyl alcohol. Amides are known to act as supramolecular gelators due to the strong directional bonding forming one-dimensional fibres which may be what causes **1** to act as a gelator.<sup>27-29</sup> Gluconamides with hydrophobic

groups have been shown to form gels in water and a range of organic solvents with gel formation speculated to be due to hydrogen bonding and hydrophobic interactions.<sup>30-36</sup> The **1** gel formation process was investigated to determine the conditions required to form the gels. Furthermore, the different gels were characterised in a variety of ways including rheology of the gels to determine the strength of the gel, SEM to visualize the gel fibres, and NMR, FTIR and XRPD to determine if **1** had chemically changed during the gelation process.

## 6.2 Results and Discussion

### 6.2.1 Initial Gel Screen

A polymorph screen was performed on **1** with a range of 26 solvents based on covering the majority of the 15 solvent groups described by Gu *et al.*<sup>37</sup> The screen involved making up 2 weight percent (wt%) solutions, heating to the boiling point, sonicating, and then leaving them to cool. The screen (Table 6.1) did not lead to any new polymorphs but it was found that the system with aniline formed a supramolecular gel and the system with benzyl alcohol formed a partial gel. A partial gel is when not all of the solvent is trapped by the gelator network.<sup>38</sup> To form a gel of **1** in benzyl alcohol the concentration was increased to 5 wt% and the same process was repeated which resulted in a gel. The **1** aniline gel is translucent and has a dark orange colour and the **1** benzyl alcohol gel is opaque and a cloudy white colour (Figure 6.3).

Table 6.1: The results of the polymorph screen of **1** with a range of solvents at 2 wt%. G = gel, PG = partial gel, S = solution, ND = not dissolved, P = precipitate.

Solvent	Result	Solvent	Result
1,4-Dioxane	ND	Ethylene glycol	P
Acetic acid	S	Formic acid	S
Acetone	ND	Hexane	ND
Acetonitrile	ND	Methanol	S
Aniline	G	Morpholine	S
Benzene	ND	<i>N,N</i> -Dimethylacetamide	S
Benzyl alcohol	PG	Nitromethane	ND
Chlorobenzene	ND	<i>N</i> -Methyl pyrrolidone	S
Chloroform	ND	Pyridine	S
Diethyl ether	ND	Tetrahydrofuran	ND
Diethylamine	ND	Toluene	ND
Ethanol	P	Triethylamine	S
Ethyl acetate	ND	Water	S

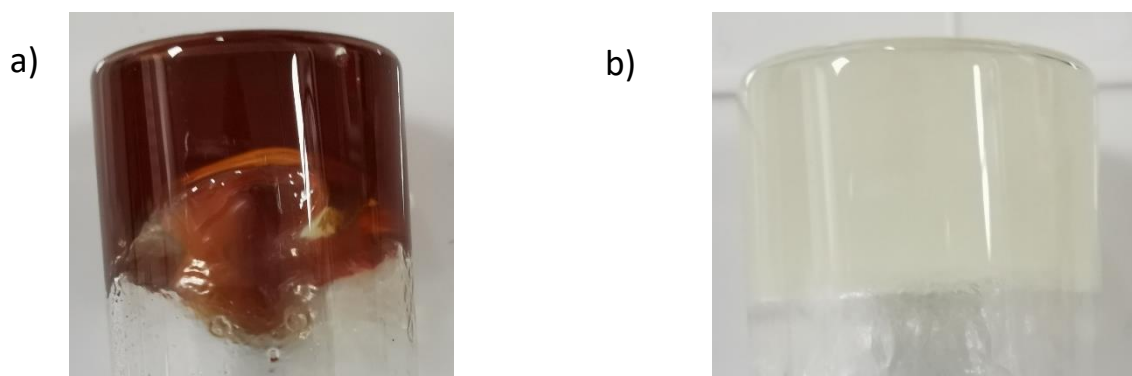


Figure 6.3: Images of the two supramolecular **1** gels with a) aniline and b) benzyl alcohol.

### 6.2.2 Gel Formation Conditions

A study was carried out to determine the temperature required to form the gel. The study involved making up 2 wt% **1** aniline solutions and 5 wt% **1** benzyl alcohol solutions and sonicating them for one minute. The solutions were then heated for two minutes at a range of different temperatures (60, 80, 100 and 120 °C), sonicated for 1 minute and then cooled to room temperature. At 60 °C no gels formed and **1** did not dissolve in either solvent. At 80 °C both solvents gel but the gels are significantly weaker than the gels formed in the original polymorph screen and break when the vials are gently shaken. At 100 °C both solvents again

form gels and they appear to be slightly stronger than the gel at 80 °C but still break easily. At 120 °C both solvents form gels which only break down when the vial is vigorously shaken. Therefore 120 °C was selected as the temperature to use, to form the gels, for the rest of the study.

It was determined that sonication after heating is essential for the formation of the **1** benzyl alcohol gel, however, it was not essential for the **1** aniline gel, but it did speed up gel formation. In the case of aniline, two 2 wt% solutions of **1** were made, and both were heated to 120 °C for 2 minutes, then one solution was sonicated for 1 minute whilst the other was not. The solution that was sonicated formed a gel within five minutes, however, the sample that was not sonicated formed a gel within four to five hours. The longer gelation time for the sample that was not sonicated may be due to the more gradual drop in temperature due to the sonicated sample being submerged in the room temperature water tank of the sonicator. The same process was repeated with 5 wt% **1** benzyl alcohol solutions, and it was found that the sonicated sample undergoes gelation during the sonication process and the sample that was not sonicated undergoes precipitation. The need for sonication suggests the gel fibres in benzyl alcohol are not the most thermodynamically stable product and sonication induces the formation of a kinetically metastable state.<sup>39-41</sup>

The critical gelling concentration of both gels was identified by heating and sonicating solutions with a range of different concentrations and observing if gels formed. For aniline, it was found that the critical gelling concentration is 0.5 wt%, with a concentration of 0.4 wt% and below forming partial gels. For benzyl alcohol, the critical gel concentration is 4.5 wt%. The lower critical gelling concentration of **1** in aniline shows it is a more potent gelator in aniline.

The thermoreversible properties of both gels were assessed which involved heating the gel until it dissolves and then cooling the solution to see if the gel reforms. It was found using the ball drop technique that the breakdown temperature of the 2 wt% aniline gel is between 65 – 70 °C and the gel quickly reforms when cooled. The breakdown temperature of the 5 wt% benzyl alcohol gel is around 80 °C and the gel does not reform unless it is sonicated after heating.

### 6.2.3 Gel Screen of Aniline and Amine Derivatives

To investigate the structural characteristics of solvent that promote gelation with **1** as the gelator, a second gel screen was performed with a range of aniline and amine derivatives (Scheme 6.1). The gel screen was performed with 5 mg of **1** dissolved in the minimum amount of solvent when heating to the boiling point of the solvent. The solution was sonicated for one minute if **1** dissolved. The gel screen is summarised in Table 6.2. Three gels formed with **1** in 2,4-dimethylaniline, 3,4-difluoroaniline and 4-butyl aniline, and four partial gels formed with 2,6-dimethylaniline, 2-methoxyaniline, 3,5-dimethylaniline and *N*-methylaniline. All of the aniline derivatives apart from *N,N*-dimethylaniline formed gels or partial gels. It is possible that *N,N*-dimethylaniline does not form a gel or partial gel because it does not contain any N-H bonds available to undergo hydrogen bonding. All of the aliphatic amine derivatives do not form any gels or partial gels suggesting the aniline group is key for gel formation. Neither benzylamine or cyclohexylamine formed a gel or partial gel indicating the aromatic phenyl group is essential for the formation of the gel network. Therefore, the gel screen indicates a phenyl group that is directly connected to a primary or secondary amine group is required for gel formation to take place.

Scheme 6.1: Aniline, benzyl alcohol and the aniline and amine derivatives used for the second gel screen.

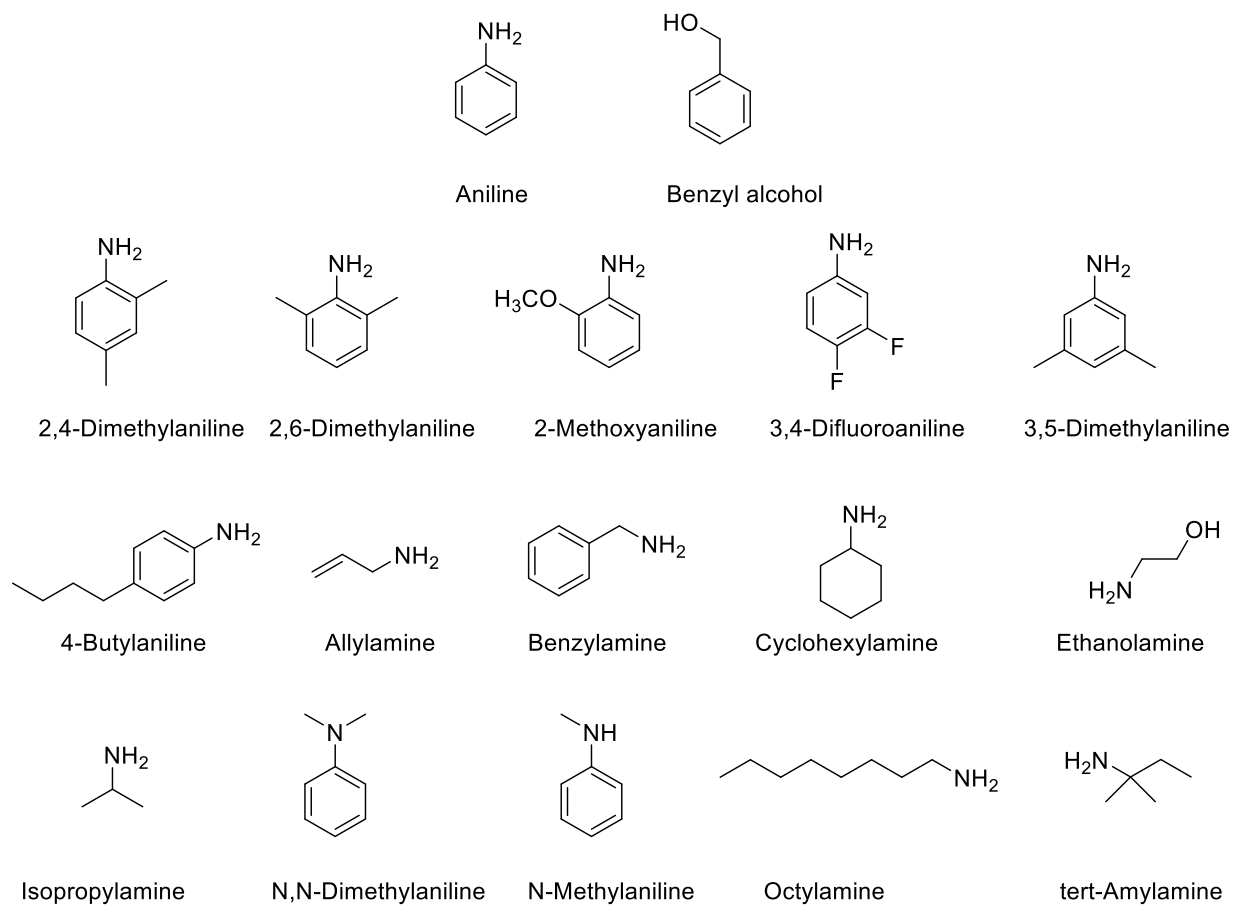


Table 6.2: Gel screen of **1** with a range of aniline and amine derivatives with varying wt%. G = gel, PG = partial gel, S = solution, ND = not dissolved, P = Precipitate, VL = viscous liquid.

Solvent	Result	wt%	Solvent	Result	wt%
2,4-Dimethylaniline	G	2.5	Cyclohexylamine	P	19
2,6-Dimethylaniline	PG	2.5	Ethanolamine	VL	5
2-Methoxyaniline	PG	2.5	Ethylene diamine	S	2
3,4-Difluoroaniline	G	2	Isopropylamine	L	22
3,5-Dimethylaniline	PG	15	<i>N,N</i> -Dimethylaniline	P	5
4-Butylaniline	G	2.5	<i>N</i> -Methylaniline	PG	17
Allylamine	S	2	Octylamine	P	15
Benzylamine	P	17	<i>Tert</i> -amylamine	S	2

#### 6.2.4 Rheology

The strength of a range of different concentrations of the **1** aniline gel were assessed by oscillatory rheology. The gels were made at 0.75, 1, 1.5 and 2 wt% by heating the mixture to 120 °C and sonicating for 1 minute. To place the gel into the well on the rheometer plate the sample was heated using a heat gun to dissolve the gel and then it was pipetted onto the plate where it reformed within a few minutes. The oscillatory frequency sweep at a constant oscillatory stress of 10 Pa confirmed that  $G'$  and  $G''$  do not change with frequency and  $G'$  is at least one magnitude higher than  $G''$  for all gels (Figure 6.4). The oscillatory frequency sweep shows that the gel is strongest around 1.5 – 2 wt% due to the higher  $G'$  and  $G''$  values compared to the lower concentrations (Figure 6.5). The oscillatory stress sweep involves testing the sample at a constant angular frequency of 10 rad/s with increasing oscillatory stress. The gel strength increases with concentration, reaching a plateau at 1.5 – 2 wt% (Figure 6.6).

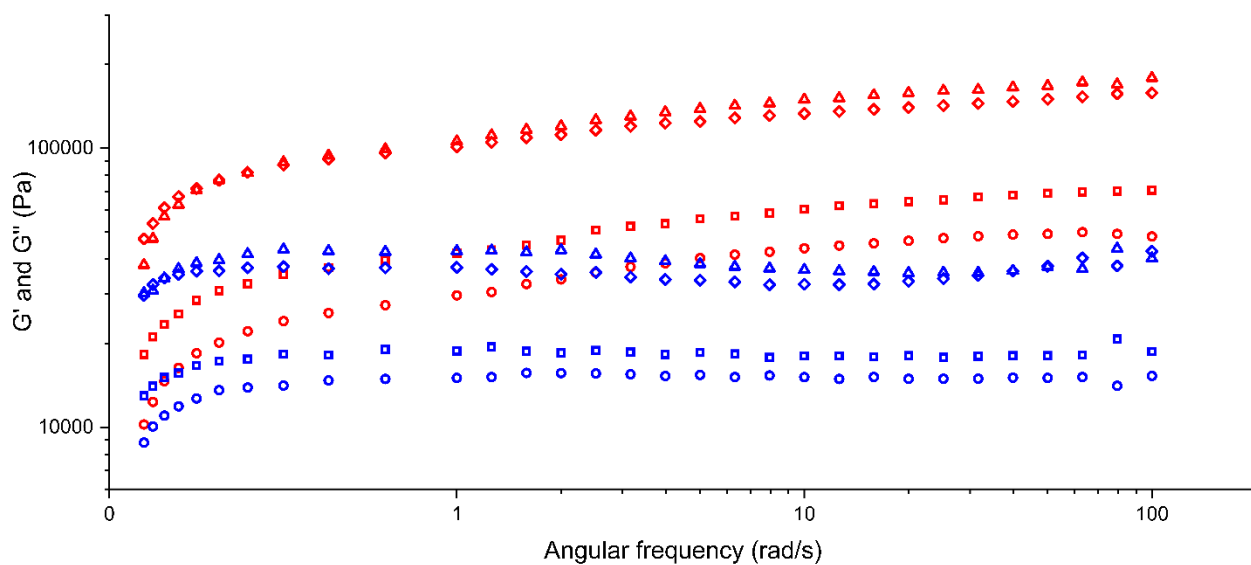


Figure 6.4: The oscillatory frequency sweep for different concentrations of **1** in aniline at 10 Pa. G' is shown in red and G'' is shown in blue. The different concentrations are 0.75 wt% (circle), 1 wt% (square), 1.5 wt% (diamond) and 2 wt% (triangle).

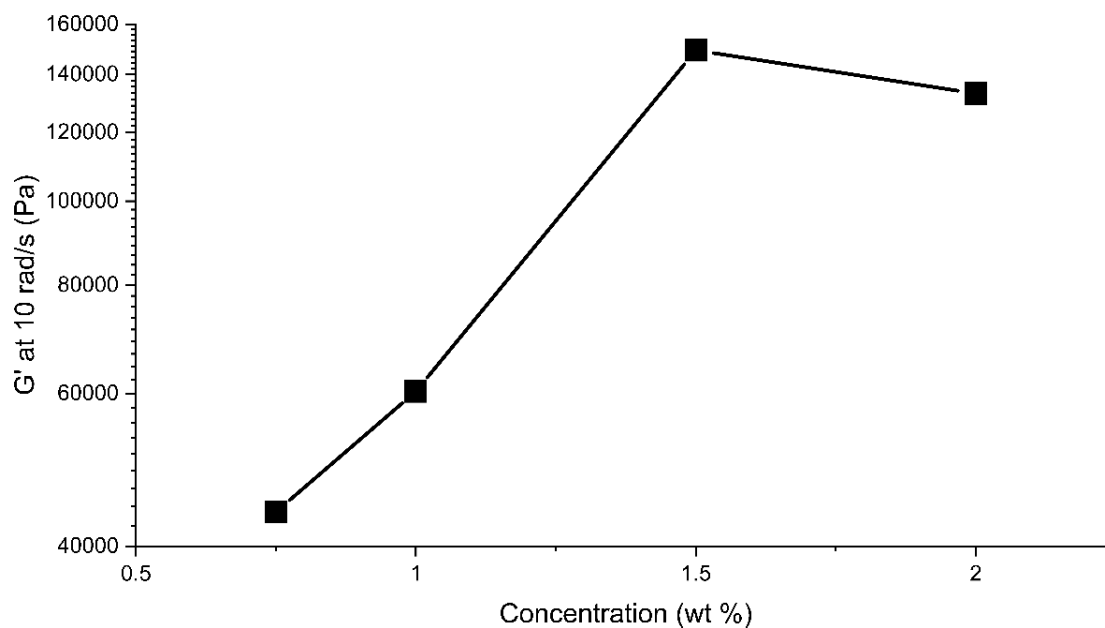


Figure 6.5: The variation of G' at 10 rad/s from the oscillatory frequency sweep for different concentrations of compound **1** in aniline.



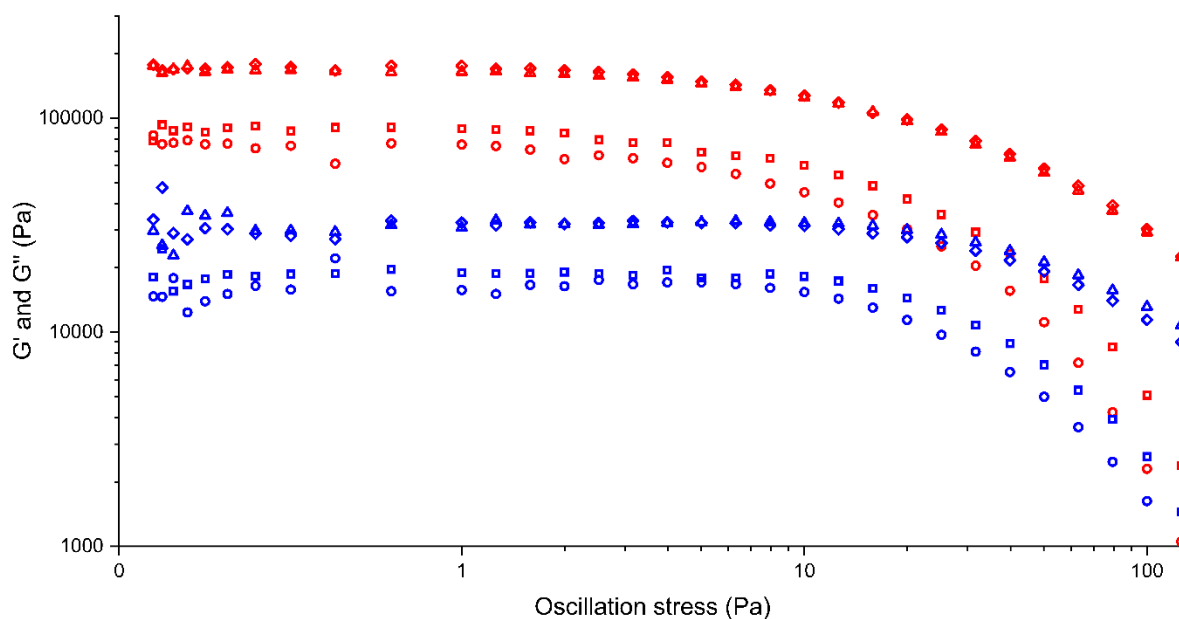


Figure 6.6: The oscillatory stress sweeps for a range of different concentrations of **1** in aniline at 10 rad/s.  $G'$  is shown in red and  $G''$  is shown in blue. The different concentrations are 0.75 wt% (circle), 1 wt% (square), 1.5 wt% (diamond) and 2 wt% (triangle).

### 6.2.5 Xerogel Analysis

Xerogels of a 1 wt% **1** aniline gel and a 5 wt% **1** benzyl alcohol gel were produced by leaving the solvent to slowly evaporate. The xerogel was initially analysed by FTIR spectroscopy and compared to the FTIR spectra of both polymorphs of **1** (Chapter 5). The FTIR spectra (Figure 6.7) shows the xerogel is identical to form I of **1** and establishes that **1** has not reacted with the solvent or decomposed and the gel fibre structure may be similar to the crystal structure of form I.

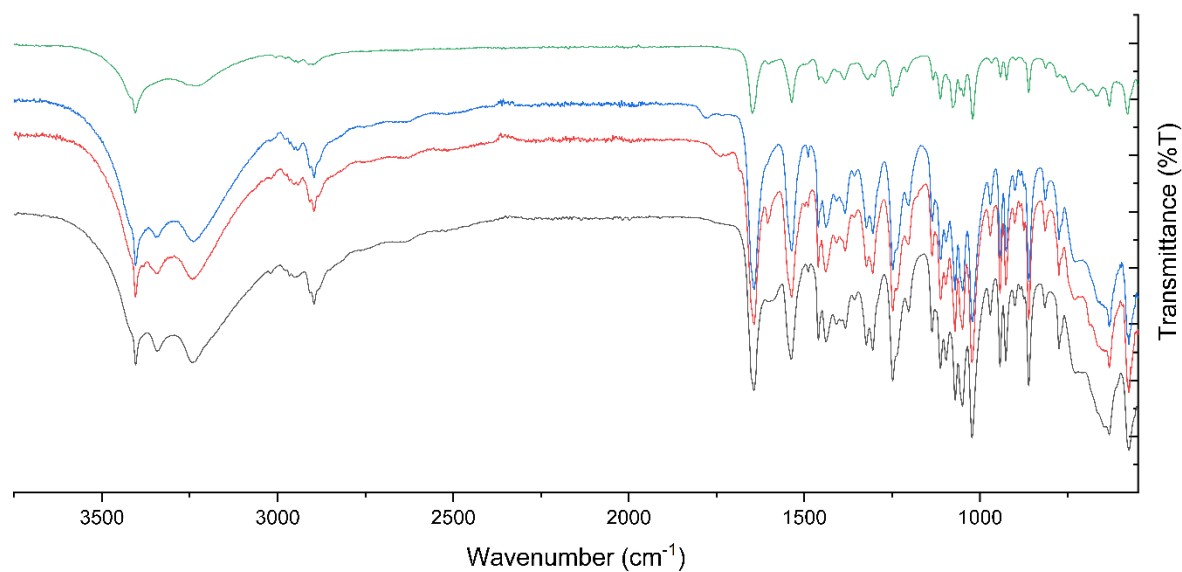


Figure 6.7: FTIR spectra of **1** form I (black), form II (green), **1** aniline xerogel (red) and **1** benzyl alcohol xerogel (blue).

The xerogels of the **1** aniline and benzyl alcohol gels were analysed by powder X-ray diffraction (XRPD). The XRPD patterns (Figure 6.8) of the two xerogels are very similar to each other and the majority of their peaks match the peaks from **1** form I. The XRPD is consistent with the FTIR data suggesting the gel fibre is structurally similar to form I. A few extra peaks are observed which are shown to match up with the calculated XRPD pattern of the frozen solvent, suggesting the xerogel is not completely dry.

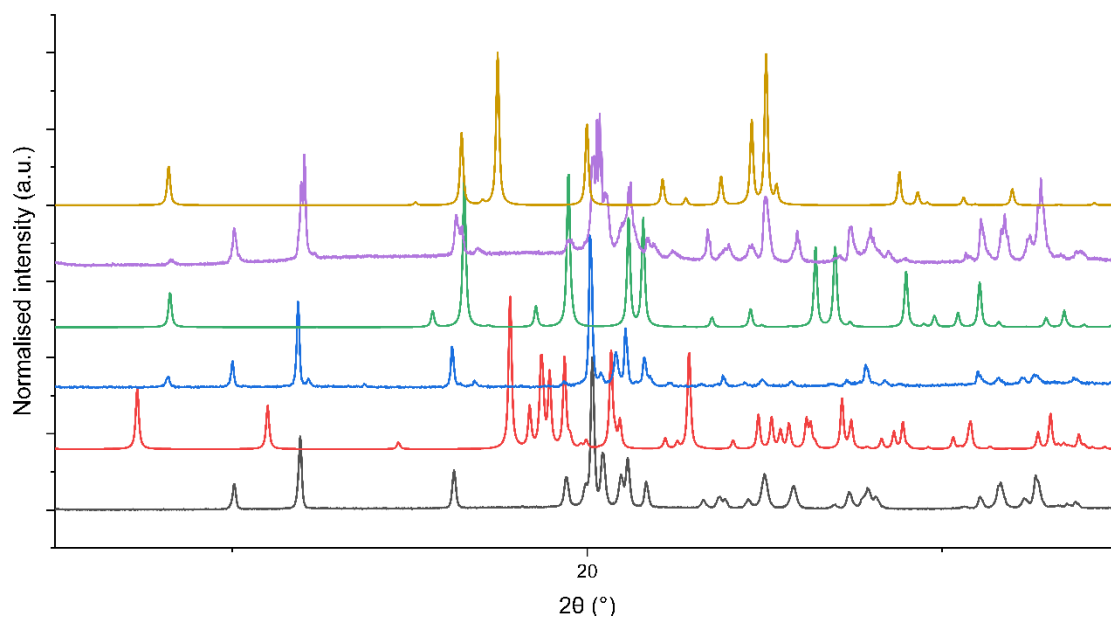


Figure 6.8: The XRPD patterns of **1** form I (black), **1** form II (red), **1** aniline xerogel (blue) and **1** benzyl alcohol xerogel (purple). The calculated patterns from published crystal structures of aniline (green) and benzyl alcohol (orange) are shown.<sup>42, 43</sup>

The solution <sup>1</sup>H NMR spectra (Figure 6.10) of the aniline xerogel and pure **1** are identical indicating **1** has not reacted with the aniline or decomposed into the gluconate salt. The spectra of the benzyl alcohol, however, shows partial hydrolysis with the sample containing 88% **1** and 12% gluconate salt. The partial hydrolysis may have been caused by the heating step to form the gel, the presence of moisture or during the slow evaporation of the solvent.

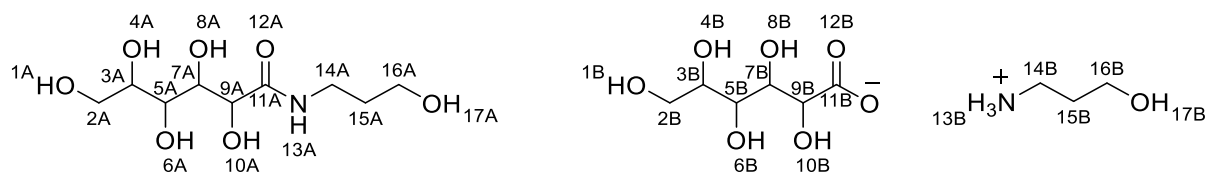


Figure 6.9: The labelled diagram of **1** and the gluconate salt for NMR assignment.

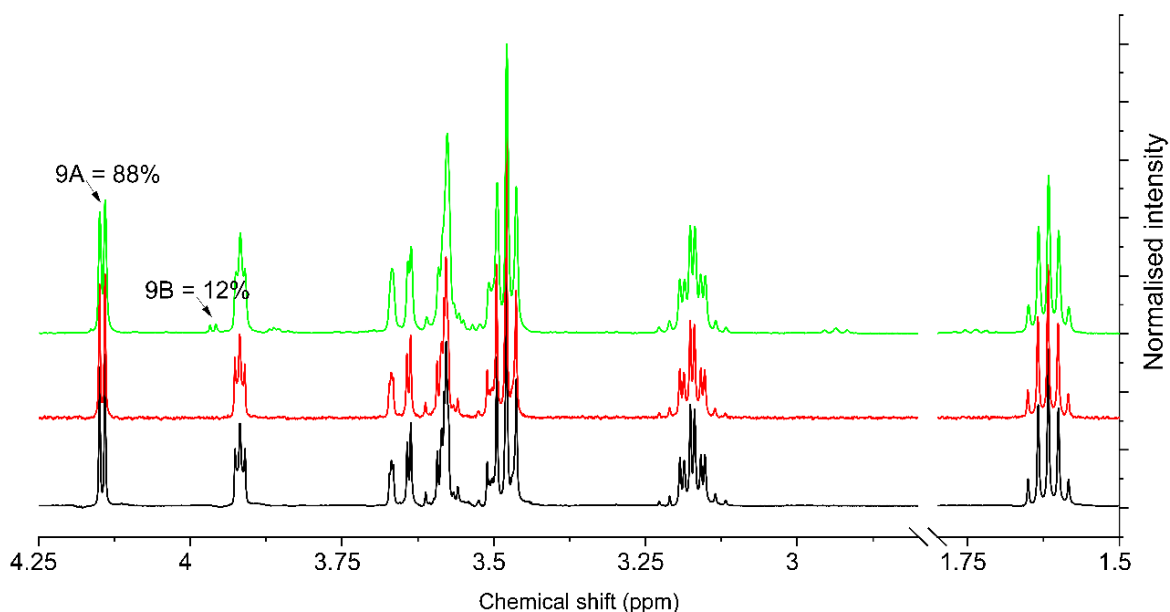


Figure 6.10: The <sup>1</sup>H NMR spectrum of **1** (black), **1** aniline xerogel (red) and **1** benzyl alcohol xerogel (green). Two peaks are assigned based on the labelling in Figure 6.9 to show the ratio of **1** to the salt decomposition product.

The xerogels were analysed via scanning electron microscopy (SEM) to visualize the fibres formed in the gels. The SEM images of the **1** aniline xerogel (Figure 6.11) show a fibrillar network which is characteristic of gels. The gel fibres are relatively large with a width of between 0.35 – 2  $\mu\text{m}$ . The SEM images of the **1** benzyl alcohol xerogel (Figure 6.12) do not show the characteristic gel fibres instead they show small plank-shaped crystals with a larger width of 3.5 – 7.5  $\mu\text{m}$ . These crystalline-appearing fibres features suggest the gel fibres in the benzyl alcohol gel are not very stable (as indicated in the sonication study) and they start to recrystallise when the solvent is removed.



Figure 6.11: SEM micrographs of the dried xerogel of **1** aniline at 1 wt%.

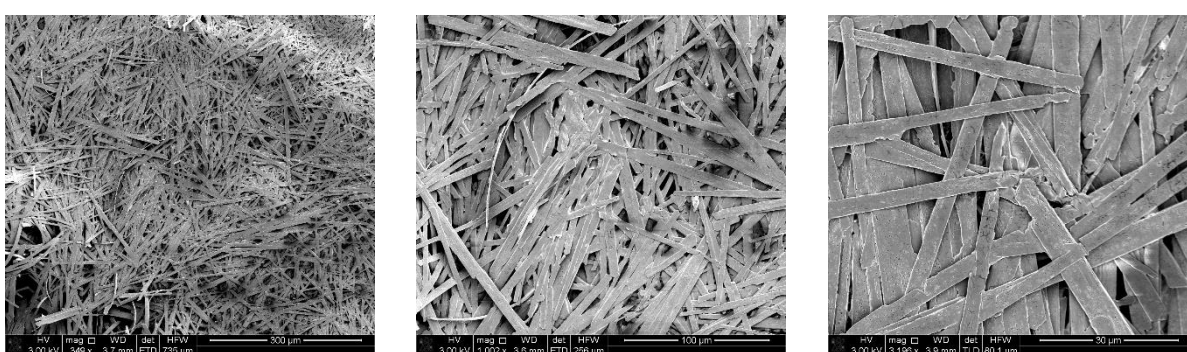


Figure 6.12: SEM micrographs of the dried xerogel of **1** benzyl alcohol at 5 wt%.

### 6.3 Conclusion

Hydroxypropyl-*L*-gluconamide was found to act as a supramolecular gelator in benzyl alcohol, aniline, and a range of aniline derivatives. The temperature required to form stable gels of **1** with aniline and benzyl alcohol is 120 °C. Sonication was required to form the **1** benzyl alcohol gel but it was not required to form the **1** aniline gel, indicating the **1** benzyl alcohol gel fibres are in a metastable state. The critical gelling concentration is 0.5 wt% for the **1** aniline gel and 4.5 w % for the **1** benzyl alcohol gel. The **1** aniline gel is thermoreversible without any sonication, however, the **1** benzyl alcohol gel requires sonication after heating to re-form the gel. The rheological properties of the **1** aniline gel were assessed at four different concentrations and it was found to be the strongest between 1.5 and 2 wt%. The low wt% of **1** required to form strong gels could be related to its ability to strengthen hair fibres when added in small quantities.<sup>22-24</sup>

The xerogels of both the **1** aniline and **1** benzyl alcohol gel were produced and analysed. FTIR, XRPD and <sup>1</sup>H NMR showed that, apart from minimal conversion to the salt

decomposition product in the **1** benzyl alcohol gel, the **1** molecule had not changed throughout the gelation process. It was also found that xerogel was more similar to the form I of **1** suggesting the gel fibres structure is similar to the structure in form I. The gel fibres of the xerogels were analysed via SEM which showed the **1** aniline gel displayed characteristic gel fibres. However, the SEM of the **1** benzyl alcohol gel showed small crystals had formed indicating the metastable gel fibres had recrystallized when the solvent was removed.

## 6.4 Experimental

### 6.4.1 Materials

FiberHance bm solution was supplied by Ashland LLC. 2,4-dimethylaniline, 2,6-dimethylaniline, 2-methoxyaniline, 3,4-difluoroaniline, 3,5-dimethylaniline, 4-butylaniline, allylamine, aniline, benzene, benzyl alcohol, benzylamine, cyclohexylamine, diethylamine, ethylenediamine, ethylene glycol, formic acid, isopropylamine, morpholine, *N,N*-dimethylaniline, *N*-methylaniline, octylamine, tert-amylamine and triethylamine were purchased from Merck and used without further purification. 1,4-Dioxane, acetic acid, acetone, acetonitrile, chlorobenzene, chloroform, diethyl ether, ethanol, ethanolamine, ethyl acetate, hexane, methanol, nitromethane, *N,N*-dimethylacetamide, *N*-methyl-2-pyrrolidone, pyridine, tetrahydrofuran and toluene were purchased Thermo Fisher Scientific and used without further purification.

### 6.4.2 Analytical Methods

XRPD measurements were performed using a Bruker D8 X-ray diffractometer (Billerica, Massachusetts) with CuK $\alpha$  radiation (1.54187 Å), and acceleration voltage and current of 40 kV and 40 mA, respectively. The samples were scanned in reflectance mode between 3° and 60° 2 $\theta$  with a scan rate of 0.01583° 2 $\theta$ /s and a step size of 0.02°.

FTIR spectra were measured with a Perkin-Elmer 100 FT-IR Spectrometer with an  $\mu$ ATR attachment. Data was recorded at a resolution of 4cm<sup>-1</sup> for 12 scans over a range of 4000 to 550 cm<sup>-1</sup>.

<sup>1</sup>H solution NMR spectra were recorded using a Varian Mercury-400 spectrometer, operating at 400 MHz for <sup>1</sup>H, chemical shifts were reported in ppm ( $\delta$ ) and referenced to residual protic solvent.

Oscillatory rheometry measurements were performed using a TA Instruments AR 2000, on a rough Peltier top plate, with a 25 mm rough plate geometry and 2.5 mm gap, and a bottom plate containing a small well with a diameter of 26 mm and a depth of 2.5 mm. Samples were prepared by heating pre-prepared gels until they dissolved. A portion of the solution was then pipetted into the well of the rheometer plate, which was set to maintain a temperature of 20 °C throughout the formation and analysis of the gels. The solution was covered with a watch glass during gel formation to limit evaporation. The gels were allowed to form over 10 minutes before analysis. Oscillatory frequency sweep experiments were performed with a constant applied stress of 10 Pa, and oscillatory stress sweep experiments with a constant frequency of 10 rad/s.

Scanning electron microscopy (SEM) samples were prepared on silicon wafers, dried in air for 2 days and coated with 2.5 nm of platinum using a Cressington 328 Ultra High Resolution EM Coating System. The images were obtained using a FEI Helios Nanolab 600 microscope.

#### 6.4.3 Gel Screening Procedure

The gelation behaviour of **1** was initially tested in a range of solvents by producing a 2 wt% sample. The sample was sonicated for 1 minute, then heated to the boiling point of the solvent using a heat gun in a sealed glass vial. The sample was then sonicated for one minute and left to cool in an insulating wooden block. A similar process was followed for the amine and aniline derivative gel screen with 5 mg of **1** added to a vial and solvent added and heated to boiling point until it fully dissolves. If **1** had not started to dissolve by 1 wt% the sample was labelled as not dissolved.

#### 6.4.4 The Temperature of Gel Formation Study

To test the temperature required to form a gel, solutions were made of **1** at 2 wt % in aniline and 5 wt % in benzyl alcohol with 1 mL of solvent. The solutions were sonicated for one minute then heated at a set temperature for five minutes, then sonicated for one more minute. The temperatures analysed were 60 80, 100 and 120 °C. The samples were then monitored visually for gelation.

#### 6.4.5 Sonication Study

To test if sonication is required for gel formation two 2 wt% solutions of **1** in aniline were made and heated to 120 °C for five minutes. One of the solutions was left to cool and the

other was sonicated for one minute. The samples were then monitored visually for gelation. The same process was repeated for 5 wt% solutions of **1** in benzyl alcohol.

#### 6.4.6 Critical Gelling Concentration Study

To identify the critical gelling concentration of the gels a 2 wt% solution of aniline was gelled using the previously described method. Then the wt% of the solution was gradually decreased with the addition of aniline and the gel formation method was repeated with the sample visually analysed for gel formation. If a gel formed more aniline was added and the process was repeated until no gel or a partial gel formed and the last concentration to result in the formation of a gel was recorded as the critical gelling concentration. The process was repeated with a 5 wt% solution of **1** in benzyl alcohol.

#### 6.4.7 Gel Breakdown Temperature

A 2 wt% gel of **1** in aniline was formed with 2 mL of aniline in a small vial. A small stainless-steel ball with a diameter of 5 mm was carefully placed on top of the gel. The sample was slowly heated on a hot plate and the temperature at which the ball drops and touches the bottom of the vial is recorded as the gel breakdown temperature. The same process is repeated with a 5 wt% gel of **1** in benzyl alcohol.

#### 6.4.8 Xerogel Formation

To form the dried xerogels a 2 wt% gel of **1** in 1 mL of aniline was formed in a small vial and the lid was left open allowing the solvent to slowly evaporate over a few weeks leaving behind the xerogel. The same process was repeated with a gel of 5 wt% **1** in 1 mL of benzyl alcohol.

### 6.5 References

1. S. Banerjee and S. Bhattacharya, *Crit. Rev. Food Sci. Nutr.*, 2012, **52**, 334-346.
2. S. Banerjee, R. K. Das and U. Maitra, *J. Mater. Chem.*, 2009, **19**, 6649-6687.
3. A. Dawn, K. S. Andrew, D. S. Yufit, Y. Hong, J. P. Reddy, C. D. Jones, J. A. Aguilar and J. W. Steed, *Cryst. Growth Des.*, 2015, **15**, 4591-4599.
4. X. Du, J. Zhou, J. Shi and B. Xu, *Chem. Rev.*, 2015, **115**, 13165-13307.
5. J. W. Steed, *Chem. Commun.*, 2011, **47**, 1379-1383.
6. L. E. Buerkle and S. J. Rowan, *Chem. Soc. Rev.*, 2012, **41**, 6089-6102.
7. L. A. Estroff and A. D. Hamilton, *Chem. Rev.*, 2004, **104**, 1201-1218.
8. N. M. Sangeetha and U. Maitra, *Chem. Soc. Rev.*, 2005, **34**, 821-836.
9. E. R. Draper and D. J. Adams, *Chem*, 2017, **3**, 390-410.



10. E. R. Triboni, T. B. F. Moraes and M. J. Politi, *3 - Supramolecular Gels*, in *Nano Design for Smart Gels*, eds. R. Bacani, F. Trindade, M. J. Politi and E. R. Triboni, Elsevier, 2019, pp. 35-69.
11. P. Dastidar, *Gels*, 2019, **5**, 15.
12. G. O. Lloyd and J. W. Steed, *Nat. Chem.*, 2009, **1**, 437-442.
13. P. Terech and R. G. Weiss, *Chem. Rev.*, 1997, **97**, 3133-3160.
14. P. Dastidar, *Chem. Soc. Rev.*, 2008, **37**, 2699-2715.
15. G. Yu, X. Yan, C. Han and F. Huang, *Chem. Soc. Rev.*, 2013, **42**, 6697-6722.
16. E. R. Draper and D. J. Adams, *Chem. Soc. Rev.*, 2018, **47**, 3395-3405.
17. M.-O. M. Piepenbrock, G. O. Lloyd, N. Clarke and J. W. Steed, *Chem. Rev.*, 2010, **110**, 1960-2004.
18. A. Dawn and H. Kumari, *Chem. Eur. J.*, 2018, **24**, 762-776.
19. A. Noro, M. Hayashi and Y. Matsushita, *Soft Matter*, 2012, **8**, 6416-6429.
20. J. S. Weston, J. H. Harwell and B. P. Grady, *Soft Matter*, 2017, **13**, 6743-6755.
21. K. D. Vernon-Parry, *III-Vs Review*, 2000, **13**, 40-44.
22. E. P. J. M. Everaert, G. Kroon and X. Zhang, Method of strengthening hair fibers and protecting dyed hair color from fading or wash-out, US20170007518A1, 2017.
23. E. P. J. M. Everaert, G. Kroon and T. D. T. Tran, Method for coloring or bleaching hair fibers, US20180193242A1, 2018.
24. R. V. Moorsel-Murerikaite, T. D. T. Tran and G. Kroon, Method of strengthening non-keratinous fibers, and uses thereof, WO2020150384A1, 2020.
25. Ashland, are you ready to bond?, <https://www.ashland.com/industries/personal-and-home-care/fiberhance#>, (accessed 16 June 2021).
26. Ashland, strengthen hair from the inside, <https://www.ulprospector.com/documents/1519442.pdf?bs=4989&b=718145&st=20&r=eu&ind=personalcare>, (accessed 16 June 2021).
27. F. Fages, F. Vögtle and M. Zinic, *Top Curr. Chem.*, 2005, **256**, 77-131.
28. L. Liao, X. Jia, H. Lou, J. Zhong, H. Liu, S. Ding, C. Chen, S. Hong and X. Luo, *RSC Adv.*, 2021, **11**, 11519-11528.
29. X. Feng, C. Liu, X. Wang, Y. Jiang, G. Yang, R. Wang, K. Zheng, W. Zhang, T. Wang and J. Jiang, *Front. Chem.*, 2019, **7**.
30. Y. Siva Prasad, S. Manikandan, K. Lalitha, M. Sandeep, R. Vara Prasad, R. Arun Kumar, C. S. Srinandan, C. Uma Maheswari, V. Sridharan and S. Nagarajan, *Nano Select*, 2020, **1**, 510-524.
31. P. Lin, N.-X. Zhang, J.-J. Li, J. Zhang, J.-H. Liu, B. Zhang and J. Song, *Chin. Chem. Lett.*, 2017, **28**, 771-776.
32. K. Yabuuchi, A. E. Rowan, R. J. M. Nolte and T. Kato, *Chem. Mater.*, 2000, **12**, 440-443.
33. X. Zhang, J. Liu, Y. Gao, J. Hao, J. Hu and Y. Ju, *Soft Matter*, 2019, **15**, 4662-4668.
34. S. Sun and P. Wu, *Soft Matter*, 2011, **7**, 6451-6456.
35. R. J. H. Hafkamp, M. C. Feiters and R. J. M. Nolte, *J. Org. Chem.*, 1999, **64**, 412-426.
36. L. E. Buerkle, R. Galleguillos and S. J. Rowan, *Soft Matter*, 2011, **7**, 6984-6990.
37. C.-H. Gu, H. Li, R. B. Gandhi and K. Raghavan, *Int. J. Pharm.*, 2004, **283**, 117-125.
38. G. Sathyanarayanan, M. Rodrigues, D. Limón, R. Rodriguez-Trujillo, J. Puigmartí-Luis, L. Pérez-García and D. B. Amabilino, *ACS Omega*, 2017, **2**, 8849-8858.
39. D. Bardelang, *Soft Matter*, 2009, **5**, 1969-1971.
40. G. Cravotto and P. Cintas, *Chem. Soc. Rev.*, 2009, **38**, 2684-2697.

41. C. Deng, R. Fang, Y. Guan, J. Jiang, C. Lin and L. Wang, *Chem. Commun.*, 2012, **48**, 7973-7975.
42. S. K. Nayak, R. Sathishkumar and T. N. G. Row, *Cryst. Eng. Comm.*, 2010, **12**, 3112-3118.
43. M. Fukuyo, K. Hirotsu and T. Higuchi, *Acta Crystallogr. B*, 1982, **38**, 640-643.

## 7 Concluding Remarks

### 7.1 Conclusion

#### 7.1.1 Introduction

This work was based around three clear sections which are linked together by the overall theme of multi-component solid forms. Section one is based around co-amorphous systems and was covered in Chapters 2 and 3. Section two was based on understanding the structure of a poly(vinylpyrrolidone) hydrogen peroxide complex and was covered in Chapter 4. Section three was based around the hair care formulation made from a gluconamide and the corresponding gluconate and 3-hydroxypropylammonium salt, and it was covered in Chapters 5 and 6.

#### 7.1.2 Section One – Co-amorphous Systems in Pharma

The aim of Chapter 2 was to produce a method to select a suitable co-former for a co-amorphous system. To achieve this a prediction model was created by selecting 36 variables to describe each system in a previous co-amorphous screen containing 120 systems made from six different APIs with all twenty amino acids.<sup>1</sup> Partial least squares – discriminant analysis was used to reduce the 36 variables to seven key variables including  $\Delta H_{hb}$ ,  $\Delta H_{mix}$ ,  $\Sigma HBC_{self}$ , *AV. MW*,  $\Delta TPSA$ ,  $\Delta\mu$  and  $\Delta(\delta h)$ .<sup>2,3</sup> The prediction model suggests co-amorphous formation is related to a large *AV. MW* and a small or negative value of  $\Delta H_{hb}$ ,  $\Delta H_{mix}$  and  $\Delta(\delta h)$ . The three variables  $\Sigma HBC_{self}$ ,  $\Delta TPSA$ ,  $\Delta\mu$  do not seem to have a large effect on co-amorphous formation but removing them lowered the prediction hit rate. A large *AV. MW* correlates with co-amorphous formation due to the slower diffusion which would inhibit recrystallisation. A negative value of  $\Delta H_{mix}$  favours co-amorphous formation, as a negative value indicates that the mixed system has a lower free energy state due to stronger intermolecular interaction formed between the mixed molecules compared to the individual components. A negative value of  $\Delta H_{hb}$ , favours co-amorphous formation due to the stronger hydrogen bonding formed between the mixed molecules compared to the individual components. A small value of  $\Delta(\delta h)$  favours co-amorphous formation due to molecules with similar hydrogen-bonding potential being more likely to interact and stabilise the co-amorphous system. The prediction model was tested using a new dataset of mebendazole

with 29 different co-formers and compared to the results of the experimental screen, with 90% of systems correctly predicted.

The model was further tested in Chapter 3 with the specific co-former bisVCap, which has previously been shown to produce a few co-amorphous systems with APIs.<sup>4</sup> The prediction model was initially tested with the published co-amorphous screen produced by Goodwin *et al.*, with 71% of systems correctly predicted.<sup>4</sup> An extensive co-amorphous screen was then performed with bisVCap and 13 different APIs. The systems were experimentally produced by co-melting and rapid solvent evaporation to reduce any formation method related issues, such as decomposition during melting or differing solubilities. The systems were analysed by hot-stage microscopy, XRPD, DSC and FTIR to determine if the systems were co-amorphous and the results were compared to the predicted results. It was found that 85% of the systems were correctly predicted, suggesting the prediction model is a viable method to pre-screen combinations of an API and bisVCap to determine the likelihood of producing a co-amorphous system. Overall, the model seems to be useful at predicting co-amorphous systems even when the component screened are not related to the training set. The prediction model produces a COAM value using Equation 2.1 with a value below 0.5 indicating the system is predicted to be not co-amorphous and above 0.5 it is predicted to be co-amorphous. Therefore, it was speculated that the higher the number the more stable the co-amorphous system, however upon testing the stability of three co-amorphous systems of bisVCap with indomethacin, paracetamol and simvastatin this was shown not to be the case.

Analysing the FTIR spectra of the co-amorphous systems with bisVCap revealed the formation of new hydrogen bonding interactions with the bisVCap carbonyl groups, suggesting the system is stabilised by favourable intermolecular interactions.<sup>5</sup> A study was performed with the bisVCap furosemide systems which involved testing ratios with more API and it was found that the highest ratio achieved whilst remaining co-amorphous is 1:2, with higher ratio systems displaying crystallisation. The 1:2 limit agrees with the suggested stabilisation method of favourable intermolecular interactions due to the bisVCap only containing two carbonyl groups limiting the potential bonding.

The results from section one demonstrates that the newly produced prediction model successfully predicts the formation of co-amorphous systems with a high hit rate as shown

by the three tests (90, 71 and 85%). Chapter 3 also shows bisVCap is a good co-former for co-amorphous formation with it forming a co-amorphous system with 10 out of 13 APIs and displaying a clear stabilisation method.

### 7.1.3 Section Two – Solvates and Hydrates in Dental Care

The aim of Chapter 4 was to gain an understanding of the structure of a poly(vinylpyrrolidone) hydrogen peroxide complex (peroxydone).<sup>6, 7</sup> To achieve the aim three different molecular weight pairs of peroxydone and PVP polymers were initially analysed by FTIR spectroscopy and SS-NMR which revealed clear hydrogen bonding interaction taking place between the carbonyl on PVP and the hydrogen peroxide molecule. The three peroxydone complexes were analysed by elemental analysis and permanganate titrations which revealed that the ratio of PVP monomer to hydrogen peroxide molecule was just below 1:1 indicating that each carbonyl is likely to interact with only one hydrogen peroxide molecule with some vacant or water sites.

A hydrogenated dimeric model compound of vinylpyrrolidone ( $H_2bisVP$ ) was selected to help understand the interactions between PVP and hydrogen peroxide due to  $H_2bisVP$ 's similarity to a small section of PVP. Three isomorphous crystal structures were produced including  $H_2bisVP \cdot 2H_2O_2$ ,  $H_2bisVP \cdot H_2O_2 \cdot H_2O$  and  $H_2bisVP \cdot 1.7H_2O_2 \cdot 0.3H_2O$  with two bonding sites A and B, with A always occupied by hydrogen peroxide and B containing either a hydrogen peroxide molecule or a water molecule. The crystal structures were used as a starting point for DFT calculations of larger sections of PVP including 4- and 6-monomer segments. The DFT calculations along with the crystal structures revealed two potential structures of peroxydone, model one which contains a repeating A bonding motif along the polymer chain which was shown with the 6-monomer segment, and model two which contains a repeating AB bonding motif forming a crosslinking interaction between multiple polymer chains. The A bonding site shows greater stability suggesting the A bonding motif is more likely, however the AB bonding motif is likely to lead to greater crystallinity and water tolerance. Therefore, the real peroxydone structure may involve regions of both bonding types depending on crystallinity and water content.

#### 7.1.4 Section Three – Salts, Polymorphs and Supramolecular Gels in Hair Care

The aim of Chapter 5 was to understand how the hair care treatment, formed from a gluconamide and the corresponding gluconate salt, strengthens hair fibres.<sup>8-10</sup> The gluconamide was crystallised in two polymorphic forms, with both forms displaying a network of extensive hydrogen bonding. The three components of the hair care treatment were screened with a range of amino acids to mimic the interactions between the three components and a keratin protein in hair fibre, with the aim of producing co-crystals or salts. However, the screen proved unsuccessful, therefore the individual components were screened with molecules that mimicked the substituent groups of the amino acids to simplify the interactions and encourage crystallisation. The screen led to three new salt structures of 3-hydroxypropylammonium with sulfuric acid, methane sulfonic acid and oxalic acid. The new crystal structures and similar structures found in the CSD were used to produce simplified models to describe the potential interactions taking place between the hair care components and the keratin protein. The overall aim was achieved as a range of potential intermolecular interactions which could form between the hair care mixture and the keratin proteins were identified.

The polymorph screening with the gluconamide from the hair care mixture led to the discovery of supramolecular gels with aniline and benzyl alcohol. The low concentration of the gluconamide in the gel formation can be related to the hair strengthening properties of the gluconamide, with the gluconamide forming extensive hydrogen bonding networks which stabilise the solvent molecules in a gel structure. The xerogel of both the aniline and benzyl gels were analysed via FTIR, <sup>1</sup>H NMR and XRPD which revealed the xerogel matched the structure found in the form I polymorph of the gluconamide, suggesting the gel fibre is similar to the crystal structure. The gel properties were analysed, and it was found by rheology that the strongest gel with aniline formed at 1.5 – 2 wt%. The aniline and benzyl alcohol gels were analysed via SEM which showed the aniline gel formed characteristic fibres whereas the benzyl gel had crystallised in the drying process, suggesting the gel formed with aniline is more thermodynamically stable.

## 7.2 Future Work

### 7.2.1 Section One – Co-amorphous Systems in Pharma

The prediction model produced in Chapter 2 is very effective at predicting the formation of co-amorphous systems, however, the model could still be improved. One way to improve the model would be to increase the size of the training set, which was originally 120 systems, also it could be improved by using more varied systems as the original training set only contained APIs with amino acid co-formers. Another way to improve the model would be to test a larger range of initial variables and hopefully identify more key variables, such as the glass transition temperature which provides information on how stable a co-amorphous system would be. The model could be tested with a co-crystal screen to check if the model could be applied to co-crystals or identify if it is specialised at predicting co-amorphous systems. Furthermore, the model could also be tested with the monomer units of polymers used in PASDs and APIs to see if the model could predict polymeric amorphous solid dispersion formation.

In Chapter 3 bisVCap was shown to be a good co-former for co-amorphous systems however solubility studies need to be carried out with the bisVCap co-amorphous systems to determine if the co-amorphous systems have improved solubility characteristics compared to the commercial form of the API. Furthermore, a smaller range of APIs with poor aqueous solubility should be focused on with the aim of eventually forming a viable commercial product. The stability of the co-amorphous systems needs to be checked in higher humidity and temperature environments, to achieve this work needs to be undertaken using dynamic vapour sorption. The toxicity of the bisVCap would need to be checked to confirm it is safe for ingestion as a tablet. Eventually, the synthesis of the co-amorphous system will need to be scaled up, with the rapid solvent evaporation having the potential to be scaled up by using spray drying.

### 7.2.2 Section Two – Solvates and Hydrates in Dental Care

Two potential models of the bonding taking place in peroxydone were identified in Chapter 4, however, it was not possible to clearly state which model was the best representation of the PVP hydrogen peroxide complex. Therefore, the future work should be based on identifying which model is most likely or creating a new model to describe the bonding. In

Chapter 4 most of the analysis was based on the production of crystal structures of H<sub>2</sub>bisVP with hydrogen peroxide, which did not provide clarity about what would happen with a longer chain length. Therefore, a clear next step would be to produce a larger vinylpyrrolidone system containing 4- and 6-monomer units and then crystallise with hydrogen peroxide, allowing a direct comparison with the results from the DFT calculations.

### 7.2.3 Section Three – Salts, Polymorphs and Supramolecular Gels in Hair Care

Chapter 5 involved the synthesis of a range of crystal structures to identify the hair strengthening properties of a hair care mixture containing a gluconamide and gluconate and 3-hydroxypropylammonium salt. The next steps will be to expand the study performed with amino acid substituent mimics such as attempting to form a crystal structure with gluconic acid and guanidine to display the potential bonding that could take place with *L*-arginine and gluconic acid. No co-crystals or salt were formed with amino acids but larger peptide sections of 3 to 4 amino acids were not tested which would provide a better model for a keratin fibre. Protein crystallisation could also be utilised to form large crystal structures showing the interactions formed between the hair care components with a model protein.

Further studies that could be performed to understand the action of hair strength include testing which of the individual components are the most important in the hair strengthening process. To achieve this the individual component could be washed into hair fibres and the tensile strength could be tested.<sup>8-10</sup> Another interesting study would involve analysing the hair fibre by SEM before and after washing with the hair care mixture to check if there are any clear changes in the structure of the hair fibre. Furthermore, dynamic vapour sorption studies could be carried out to see if the hair care mixture altered the water sorption and desorption of hair fibres. Additionally, the amount of the hair care mixture retained in the original washing process and subsequent washing cycles could be determined to understand how long the hair strengthening effect last.

In Chapter 6 the gluconamide from the hair care mixture was identified as a supramolecular gelator in the solvent's aniline and benzyl alcohol. The next steps would be to further examine what causes the gluconamide to act as a gelator. To achieve this a solvent screen should be performed with solvents similar to benzyl alcohol to identify which properties of the solvent enhance gel formation. Furthermore, DFT calculations could be performed on



small systems containing a few molecules of gluconamide surrounded by aniline or benzyl alcohol molecules to visualize the potential aggregation of the structures. Additionally, the formation of a single crystal from aniline could be attempted as it would provide a direct image of how aniline affects the intermolecular interactions between each gluconamide molecule.

### 7.3 References

1. G. Kasten, H. Grohgan, T. Rades and K. Lobmann, *Eur. J. Pharm. Sci.*, 2016, **95**, 28-35.
2. R. G. Brereton and G. R. Lloyd, *J. Chemom.*, 2014, **28**, 213-225.
3. D. Ruiz-Perez, H. Guan, P. Madhivanan, K. Mathee and G. Narasimhan, 2018.
4. M. J. Goodwin, O. M. Musa, D. J. Berry and J. W. Steed, *Cryst. Growth Des.*, 2018, **18**, 701-709.
5. K. Löbmann, R. Laitinen, C. Strachan, T. Rades and H. Grohgan, *Eur. J. Pharm. Biopharm.*, 2013, **85**, 882-888.
6. D. A. Shiraeff, Solid stabilized hydrogen peroxide compositions, U.S. Patent 3,376,110A, 1968.
7. D. A. Shiraeff, Solid stabilized hydrogen peroxide compositions, U.S. Patent 3,480,557, 1969.
8. E. P. J. M. Everaert, G. Kroon and T. D. T. Tran, Method for coloring or bleaching hair fibers, US20180193242A1, 2018.
9. E. P. J. M. Everaert, G. Kroon and X. Zhang, Method of strengthening hair fibers and protecting dyed hair color from fading or wash-out, US20170007518A1, 2017.
10. R. V. Moorsel-Murerikaite, T. D. T. Tran and G. Kroon, Method of strengthening non-keratinous fibers, and uses thereof, WO2020150384A1, 2020.

## 8 Appendices

### 8.1 Full Crystallographic Information for Structures in Chapter 4

Table 8.1: Crystallographic information for BisVP·1.7H<sub>2</sub>O<sub>2</sub>·0.3H<sub>2</sub>O.

Crystal Information	
Empirical formula	C <sub>12</sub> H <sub>24</sub> N <sub>2</sub> O <sub>5.7</sub>
Formula weight	287.53
Temperature/K	120.0
Crystal system	monoclinic
Space group	P2 <sub>1</sub>
a/Å	6.9035(8)
b/Å	15.0032(17)
c/Å	7.0706(8)
α/°	90
β/°	105.825(4)
γ/°	90
Volume/Å <sup>3</sup>	704.58(14)
Z	2
ρ <sub>calc</sub> /g/cm <sup>3</sup>	1.355
μ/mm <sup>-1</sup>	0.107
F(000)	311.0
Crystal size/mm <sup>3</sup>	0.22 × 0.05 × 0.016
Radiation	MoKα (λ = 0.71073)
2θ range for data collection/°	5.988 to 57.998
Index ranges	-9 ≤ h ≤ 9, -20 ≤ k ≤ 20, -9 ≤ l ≤ 9
Reflections collected	11274
Independent reflections	3733 [R <sub>int</sub> = 0.0440, R <sub>sigma</sub> = 0.0570]
Data/restraints/parameters	3733/22/204
Goodness-of-fit on F <sup>2</sup>	1.035
Final R indexes [I ≥ 2σ (I)]	R <sub>1</sub> = 0.0456, wR <sub>2</sub> = 0.0970
Final R indexes [all data]	R <sub>1</sub> = 0.0586, wR <sub>2</sub> = 0.1028
Largest diff. peak/hole / e Å <sup>-3</sup>	0.23/-0.22
Flack parameter	0.2(5)

Table 8.2: Crystallographic information for BisVP·H<sub>2</sub>O<sub>2</sub>·H<sub>2</sub>O.

Crystal Information	
Empirical formula	C <sub>12</sub> H <sub>24</sub> N <sub>2</sub> O <sub>5</sub>
Formula weight	276.33
Temperature/K	100.0
Crystal system	monoclinic
Space group	P2 <sub>1</sub>
a/Å	6.9359(3)
b/Å	14.9061(7)
c/Å	6.9555(3)
α/°	90
β/°	105.7471(17)
γ/°	90
Volume/Å <sup>3</sup>	692.12(5)
Z	2
ρ <sub>calc</sub> /cm <sup>3</sup>	1.326
μ/mm <sup>-1</sup>	0.102
F(000)	300.0
Crystal size/mm <sup>3</sup>	0.19 × 0.13 × 0.09
Radiation	MoKα (λ = 0.71073)
2θ range for data collection/°	6.086 to 60
Index ranges	-9 ≤ h ≤ 9, -20 ≤ k ≤ 20, -9 ≤ l ≤ 9
Reflections collected	11754
Independent reflections	4014 [R <sub>int</sub> = 0.0346, R <sub>sigma</sub> = 0.0410]
Data/restraints/parameters	4014/1/267
Goodness-of-fit on F <sup>2</sup>	1.026
Final R indexes [I >= 2σ (I)]	R <sub>1</sub> = 0.0448, wR <sub>2</sub> = 0.1103
Final R indexes [all data]	R <sub>1</sub> = 0.0490, wR <sub>2</sub> = 0.1136
Largest diff. peak/hole / e Å <sup>-3</sup>	0.46/-0.26
Flack parameter	0.5(4)

Table 8.3: Crystallographic information for BisVP·2H<sub>2</sub>O<sub>2</sub>.

Crystal Information	
Empirical formula	C <sub>12</sub> H <sub>24</sub> N <sub>2</sub> O <sub>6</sub>
Formula weight	292.33
Temperature/K	120.0
Crystal system	monoclinic
Space group	P2 <sub>1</sub>
a/Å	6.8700(2)
b/Å	15.0114(4)
c/Å	7.1364(2)
α/°	90
β/°	105.8830(10)
γ/°	90
Volume/Å <sup>3</sup>	707.87(3)
Z	2
ρ <sub>calc</sub> /cm <sup>3</sup>	1.372
μ/mm <sup>-1</sup>	0.109
F(000)	316.0
Crystal size/mm <sup>3</sup>	0.21 × 0.09 × 0.04
Radiation	MoKα (λ = 0.71073)
2θ range for data collection/°	5.936 to 59.976
Index ranges	-9 ≤ h ≤ 9, -21 ≤ k ≤ 21, -10 ≤ l ≤ 10
Reflections collected	16854
Independent reflections	4085 [R <sub>int</sub> = 0.0322, R <sub>sigma</sub> = 0.0300]
Data/restraints/parameters	4085/1/277
Goodness-of-fit on F <sup>2</sup>	1.056
Final R indexes [I ≥ 2σ (I)]	R <sub>1</sub> = 0.0352, wR <sub>2</sub> = 0.0845
Final R indexes [all data]	R <sub>1</sub> = 0.0373, wR <sub>2</sub> = 0.0858
Largest diff. peak/hole / e Å <sup>-3</sup>	0.30/-0.18
Flack parameter	0.3(3)

## 8.2 Full Crystallographic Information for Structures in Chapter 5

Table 8.4: Crystallographic information for hydroxypropyl-*L*-gluconamide (**1**) form I.

Crystal Information	
Empirical formula	C <sub>9</sub> H <sub>19</sub> NO <sub>7</sub>
Formula weight	253.25
Temperature/K	120.0
Crystal system	monoclinic
Space group	P2 <sub>1</sub>
a/Å	4.6468(2)
b/Å	13.9198(7)
c/Å	8.9183(5)
α/°	90
β/°	101.1403(19)
γ/°	90
Volume/Å <sup>3</sup>	565.99(5)
Z	2
ρ <sub>calc</sub> /cm <sup>3</sup>	1.486
μ/mm <sup>-1</sup>	0.128
F(000)	272.0
Crystal size/mm <sup>3</sup>	0.28 × 0.18 × 0.11
Radiation	Mo Kα (λ = 0.71073)
2θ range for data collection/°	4.656 to 59.998
Index ranges	-6 ≤ h ≤ 6, -19 ≤ k ≤ 19, -12 ≤ l ≤ 12
Reflections collected	12795
Independent reflections	3305 [R <sub>int</sub> = 0.0325, R <sub>sigma</sub> = 0.0294]
Data/restraints/parameters	3305/1/230
Goodness-of-fit on F <sup>2</sup>	1.037
Final R indexes [I ≥ 2σ (I)]	R <sub>1</sub> = 0.0325, wR <sub>2</sub> = 0.0805
Final R indexes [all data]	R <sub>1</sub> = 0.0367, wR <sub>2</sub> = 0.0823
Largest diff. peak/hole / e Å <sup>-3</sup>	0.31/-0.23
Flack parameter	-0.5(7)

Table 8.5: Crystallographic information for hydroxypropyl-D-gluconamide (**1**).

Crystal Information	
Empirical formula	C <sub>9</sub> H <sub>19</sub> NO <sub>7</sub>
Formula weight	253.25
Temperature/K	120.0
Crystal system	monoclinic
Space group	P2 <sub>1</sub>
a/Å	4.64620(10)
b/Å	13.9212(4)
c/Å	8.9163(3)
α/°	90
β/°	101.1335(11)
γ/°	90
Volume/Å <sup>3</sup>	565.86(3)
Z	2
ρ <sub>calc</sub> /cm <sup>3</sup>	1.486
μ/mm <sup>-1</sup>	0.128
F(000)	272.0
Crystal size/mm <sup>3</sup>	0.29 × 0.1 × 0.03
Radiation	Mo Kα (λ = 0.71073)
2θ range for data collection/°	5.852 to 60
Index ranges	-6 ≤ h ≤ 6, -19 ≤ k ≤ 19, -12 ≤ l ≤ 12
Reflections collected	13525
Independent reflections	3268 [R <sub>int</sub> = 0.0403, R <sub>sigma</sub> = 0.0332]
Data/restraints/parameters	3268/1/230
Goodness-of-fit on F <sup>2</sup>	1.021
Final R indexes [I >= 2σ (I)]	R <sub>1</sub> = 0.0366, wR <sub>2</sub> = 0.0924
Final R indexes [all data]	R <sub>1</sub> = 0.0375, wR <sub>2</sub> = 0.0934
Largest diff. peak/hole / e Å <sup>-3</sup>	0.34/-0.18
Flack parameter	0.0(8)

Table 8.6: Crystallographic information for hydroxypropyl-*L*-gluconamide (**1**) form II.

Crystal Information	
Empirical formula	C <sub>9</sub> H <sub>19</sub> NO <sub>7</sub>
Formula weight	253.25
Temperature/K	120.0
Crystal system	monoclinic
Space group	P2 <sub>1</sub>
a/Å	9.5157(4)
b/Å	5.0795(2)
c/Å	24.2667(10)
α/°	90
β/°	96.4629(14)
γ/°	90
Volume/Å <sup>3</sup>	1165.48(8)
Z	4
ρ <sub>calc</sub> /cm <sup>3</sup>	1.443
μ/mm <sup>-1</sup>	0.124
F(000)	544.0
Crystal size/mm <sup>3</sup>	0.15 × 0.05 × 0.01
Radiation	MoKα (λ = 0.71073)
2θ range for data collection/°	4.308 to 57.99
Index ranges	-12 ≤ h ≤ 12, -6 ≤ k ≤ 6, -33 ≤ l ≤ 33
Reflections collected	19083
Independent reflections	6127 [R <sub>int</sub> = 0.0501, R <sub>sigma</sub> = 0.0686]
Data/restraints/parameters	6127/68/363
Goodness-of-fit on F <sup>2</sup>	1.028
Final R indexes [I >= 2σ (I)]	R <sub>1</sub> = 0.0514, wR <sub>2</sub> = 0.0951
Final R indexes [all data]	R <sub>1</sub> = 0.0944, wR <sub>2</sub> = 0.1110
Largest diff. peak/hole / e Å <sup>-3</sup>	0.29/-0.23
Flack parameter	0.7(7)

Table 8.7: Crystallographic information for 3-hydroxypropylammonium hydrogen sulfate.

Crystal Information	
Empirical formula	C <sub>3</sub> H <sub>11</sub> NO <sub>5</sub> S
Formula weight	173.19
Temperature/K	120.0
Crystal system	monoclinic
Space group	P2 <sub>1</sub> /m
a/Å	5.3514(3)
b/Å	6.9661(4)
c/Å	9.6220(5)
α/°	90
β/°	98.976(2)
γ/°	90
Volume/Å <sup>3</sup>	354.30(3)
Z	2
ρ <sub>calc</sub> /cm <sup>3</sup>	1.623
μ/mm <sup>-1</sup>	0.426
F(000)	184.0
Crystal size/mm <sup>3</sup>	0.15 × 0.08 × 0.01
Radiation	MoKα (λ = 0.71073)
2θ range for data collection/°	4.286 to 59.982
Index ranges	-7 ≤ h ≤ 7, -9 ≤ k ≤ 9, -13 ≤ l ≤ 13
Reflections collected	6372
Independent reflections	1104 [R <sub>int</sub> = 0.0377, R <sub>sigma</sub> = 0.0262]
Data/restraints/parameters	1104/0/83
Goodness-of-fit on F <sup>2</sup>	1.146
Final R indexes [I >= 2σ (I)]	R <sub>1</sub> = 0.0306, wR <sub>2</sub> = 0.0693
Final R indexes [all data]	R <sub>1</sub> = 0.0343, wR <sub>2</sub> = 0.0708
Largest diff. peak/hole / e Å <sup>-3</sup>	0.45/-0.41



Table 8.8: Crystallographic information for 3-hydroxypropylammonium sulfonate.

Crystal Information	
Empirical formula	C <sub>4</sub> H <sub>13</sub> NO <sub>4</sub> S
Formula weight	171.21
Temperature/K	120.0
Crystal system	monoclinic
Space group	P2 <sub>1</sub>
a/Å	5.1527(2)
b/Å	21.5379(10)
c/Å	7.1287(3)
α/°	90
β/°	91.6578(19)
γ/°	90
Volume/Å <sup>3</sup>	790.80(6)
Z	4
ρ <sub>calc</sub> /cm <sup>3</sup>	1.438
μ/mm <sup>-1</sup>	0.372
F(000)	368.0
Crystal size/mm <sup>3</sup>	0.21 × 0.07 × 0.01
Radiation	MoKα (λ = 0.71073)
2θ range for data collection/°	3.782 to 55.998
Index ranges	-6 ≤ h ≤ 6, -28 ≤ k ≤ 28, -9 ≤ l ≤ 9
Reflections collected	18888
Independent reflections	18888 [R <sub>int</sub> = 10.40, R <sub>sigma</sub> = 0.1016]
Data/restraints/parameters	18888/1/187
Goodness-of-fit on F <sup>2</sup>	1.018
Final R indexes [I >= 2σ (I)]	R <sub>1</sub> = 0.0665, wR <sub>2</sub> = 0.1600
Final R indexes [all data]	R <sub>1</sub> = 0.0940, wR <sub>2</sub> = 0.1757
Largest diff. peak/hole / e Å <sup>-3</sup>	1.13/-0.62
Flack parameter	0.58(9)

Table 8.9: Crystallographic information for 3-hydroxypropylammonium hydrogen oxalate.

Crystal Information	
Empirical formula	C <sub>5</sub> H <sub>11</sub> NO <sub>5</sub>
Formula weight	165.15
Temperature/K	120.0
Crystal system	monoclinic
Space group	P2 <sub>1</sub> /n
a/Å	5.6912(4)
b/Å	7.1078(5)
c/Å	19.2926(14)
α/°	90
β/°	90.414(3)
γ/°	90
Volume/Å <sup>3</sup>	780.40(10)
Z	4
ρ <sub>calc</sub> /cm <sup>3</sup>	1.406
μ/mm <sup>-1</sup>	0.126
F(000)	352.0
Crystal size/mm <sup>3</sup>	0.11 × 0.1 × 0.02
Radiation	MoKα (λ = 0.71073)
2θ range for data collection/°	4.222 to 59.996
Index ranges	-8 ≤ h ≤ 8, -9 ≤ k ≤ 10, -27 ≤ l ≤ 27
Reflections collected	12905
Independent reflections	2255 [R <sub>int</sub> = 0.0450, R <sub>sigma</sub> = 0.0351]
Data/restraints/parameters	2255/0/144
Goodness-of-fit on F <sup>2</sup>	1.061
Final R indexes [I >= 2σ (I)]	R <sub>1</sub> = 0.0414, wR <sub>2</sub> = 0.0925
Final R indexes [all data]	R <sub>1</sub> = 0.0553, wR <sub>2</sub> = 0.0993
Largest diff. peak/hole / e Å <sup>-3</sup>	0.42/-0.32

Table 8.10: Crystallographic information for guanidine carbonate methanol solvate.

Crystal Information	
Empirical formula	C <sub>4</sub> H <sub>16</sub> N <sub>6</sub> O <sub>4</sub>
Formula weight	212.23
Temperature/K	120.0
Crystal system	orthorhombic
Space group	P2 <sub>1</sub> 2 <sub>1</sub> 2 <sub>1</sub>
a/Å	7.1149(3)
b/Å	11.6098(4)
c/Å	13.7967(5)
α/°	90
β/°	90
γ/°	90
Volume/Å <sup>3</sup>	1139.64(7)
Z	4
ρ <sub>calc</sub> /cm <sup>3</sup>	1.237
μ/mm <sup>-1</sup>	0.107
F(000)	456.0
Crystal size/mm <sup>3</sup>	0.21 × 0.06 × 0.01
Radiation	MoKα (λ = 0.71073)
2θ range for data collection/°	4.586 to 59.998
Index ranges	-10 ≤ h ≤ 10, -16 ≤ k ≤ 16, -19 ≤ l ≤ 19
Reflections collected	20652
Independent reflections	3319 [R <sub>int</sub> = 0.0471, R <sub>sigma</sub> = 0.0326]
Data/restraints/parameters	3319/0/180
Goodness-of-fit on F <sup>2</sup>	1.103
Final R indexes [I ≥ 2σ (I)]	R <sub>1</sub> = 0.0415, wR <sub>2</sub> = 0.0956
Final R indexes [all data]	R <sub>1</sub> = 0.0487, wR <sub>2</sub> = 0.0985
Largest diff. peak/hole / e Å <sup>-3</sup>	0.19/-0.23
Flack parameter	0.3(6)

Table 8.11: Crystallographic information for *N,N'*-ethylene bis-*L*-gluconamide.

Crystal Information	
Empirical formula	C <sub>14</sub> H <sub>28</sub> N <sub>2</sub> O <sub>12</sub>
Formula weight	416.38
Temperature/K	120.0
Crystal system	monoclinic
Space group	C2
a/Å	9.7045(4)
b/Å	5.0273(2)
c/Å	18.1838(7)
α/°	90
β/°	90.9710(10)
γ/°	90
Volume/Å <sup>3</sup>	887.01(6)
Z	2
ρ <sub>calc</sub> /cm <sup>3</sup>	1.559
μ/mm <sup>-1</sup>	0.137
F(000)	444.0
Crystal size/mm <sup>3</sup>	0.21 × 0.17 × 0.12
Radiation	MoKα (λ = 0.71073)
2θ range for data collection/°	8.658 to 59.996
Index ranges	-12 ≤ h ≤ 13, -7 ≤ k ≤ 7, -25 ≤ l ≤ 25
Reflections collected	10231
Independent reflections	2537 [R <sub>int</sub> = 0.0260, R <sub>sigma</sub> = 0.0223]
Data/restraints/parameters	2537/1/187
Goodness-of-fit on F <sup>2</sup>	1.105
Final R indexes [I >= 2σ (I)]	R <sub>1</sub> = 0.0252, wR <sub>2</sub> = 0.0662
Final R indexes [all data]	R <sub>1</sub> = 0.0256, wR <sub>2</sub> = 0.0665
Largest diff. peak/hole / e Å <sup>-3</sup>	0.34/-0.15
Flack parameter	0.0(2)

Table 8.12: Crystallographic information for *L*-cysteic acid dimethylsulfoxide solvate.

Crystal Information	
Empirical formula	C <sub>5</sub> H <sub>13</sub> NO <sub>6</sub> S <sub>2</sub>
Formula weight	247.28
Temperature/K	120.0
Crystal system	monoclinic
Space group	P2 <sub>1</sub>
a/Å	6.5483(3)
b/Å	7.9607(3)
c/Å	9.8718(4)
α/°	90
β/°	93.5090(13)
γ/°	90
Volume/Å <sup>3</sup>	513.64(4)
Z	2
ρ <sub>calc</sub> /cm <sup>3</sup>	1.599
μ/mm <sup>-1</sup>	0.523
F(000)	260.0
Crystal size/mm <sup>3</sup>	0.45 × 0.34 × 0.14
Radiation	Mo Kα (λ = 0.71073)
2θ range for data collection/°	6.234 to 59.998
Index ranges	-9 ≤ h ≤ 9, -11 ≤ k ≤ 11, -13 ≤ l ≤ 13
Reflections collected	8225
Independent reflections	2839 [R <sub>int</sub> = 0.0388, R <sub>sigma</sub> = 0.0419]
Data/restraints/parameters	2839/1/179
Goodness-of-fit on F <sup>2</sup>	1.056
Final R indexes [I >= 2σ (I)]	R <sub>1</sub> = 0.0337, wR <sub>2</sub> = 0.0880
Final R indexes [all data]	R <sub>1</sub> = 0.0337, wR <sub>2</sub> = 0.0881
Largest diff. peak/hole / e Å <sup>-3</sup>	0.33/-0.29
Flack parameter	0.03(7)

Table 8.13: Crystallographic information for 4,4'-biphenol·morpholine (1:2).

Crystal Information	
Empirical formula	C <sub>20</sub> H <sub>28</sub> N <sub>2</sub> O <sub>4</sub>
Formula weight	360.44
Temperature/K	120.0
Crystal system	monoclinic
Space group	P2 <sub>1</sub> /c
a/Å	5.9841(3)
b/Å	10.7325(6)
c/Å	14.8852(8)
$\alpha$ /°	90
$\beta$ /°	97.666(4)
$\gamma$ /°	90
Volume/Å <sup>3</sup>	947.45(9)
Z	2
$\rho_{\text{calc}}$ /cm <sup>3</sup>	1.263
$\mu$ /mm <sup>-1</sup>	0.713
F(000)	388.0
Crystal size/mm <sup>3</sup>	0.15 × 0.06 × 0.04
Radiation	Mo K $\alpha$ ( $\lambda$ = 1.54178)
2 $\Theta$ range for data collection/°	10.192 to 141.948
Index ranges	-7 ≤ h ≤ 7, -13 ≤ k ≤ 13, -17 ≤ l ≤ 18
Reflections collected	10710
Independent reflections	1821 [R <sub>int</sub> = 0.0792, R <sub>sigma</sub> = 0.0516]
Data/restraints/parameters	1821/0/174
Goodness-of-fit on F <sup>2</sup>	1.099
Final R indexes [I ≥ 2 $\sigma$ (I)]	R <sub>1</sub> = 0.0525, wR <sub>2</sub> = 0.1302
Final R indexes [all data]	R <sub>1</sub> = 0.0741, wR <sub>2</sub> = 0.1413
Largest diff. peak/hole / e Å <sup>-3</sup>	0.24/-0.28